UNIVERSIDAD AUTONOMA DE MADRID

ESCUELA POLITECNICA SUPERIOR

PROYECTO FIN DE CARRERA

"Antenas híbridas con array y doble reflector de tipo Imaging"

"Hybrid antennas with an array and double reflector of Imaging type"

Bogdana Tsonevska Lachezarova
Octubre 2011

"Hybrid antennas with an array and double reflector of imaging type"

Antena híbrida con array y doble reflector de tipo Imaging

AUTOR: Bogdana Tsonevska Lachezarova
TUTOR: Piero Angeletti
PONENTE: Bazil Taha Ahmed

Departamento de Tecnología Electrónica y de las Comunicaciones

Escuela Politécnica Superior
Universidad Autónoma de Madrid
mes de 2011

European Space Agency ESTEC Noordwijk
TEC-ETP

Universitá "La Sapienza" Roma
Dipartimento di Ingegneria Elettronica

Abstract

The topic of this work is interdisciplinary and covers theoretical electromagnetism and advanced antenna architectures. It is proposed the analysis and design of hybrids antennas with an array and double reflector of imaging type in view of potential applications to satellite systems for Earth observation. The considered frequency is 30 GHz and the implementation is for geostationary satellite. For such high frequencies the applied theories are Geometrical Optics (G.O.) and Physical Optics (P.O.).

These antennas systems are capable to provide magnified imaging of the array on the main aperture with minimal aberrations. Different array shapes are presented.

One of them is an antenna with square configuration, which was constructed in the 80' s from Fitzgerald [1] and Pearson [10]. The patent was registered in 1993 by Corado Dragon [3]. They considered the G.O. theory as a method of analysis with plane wave excitation. In this thesis to their work is added more detailed phase and path length study, as well as the scan characteristics, the aperture images and polarization. Another two configurations are considered: hexagon and triangle. Serious improvements are made related to the side lobe level and the beam width, as well as power gain for scan angles.

On the other hand, spherical wave excitation is applied to the phase array. It is observed that for entire illumination of the main reflector the array should be placed below it.

All the discussed parameters are implemented in specially designed software. The obtained results are contrasted with existing works in this field.

The application of the studied hybrid antenna is for Earth Observation, more concrete as a synthetic radiometer. It is demonstrated that with Synthetic Radiometry is possible to obtained better accuracy in the observation: narrower beams. The cost is the high computational effort. The procedure of obtaining the Visibility function is explained. The equivalence between Y shaped and hexagon arrays is verified.

Key words

Hybrid antenna, Gregorian antenna, array, offset feed, reflectors, imaging, Physical Optics, Geometrical Optics, plane and spherical wave, power pattern, pencil beam, polarization phase, aberration, scan, antenna temperature, brightness temperature, Visibility function, baseline, G matrix, ray tracing, potential magnetic, path length, grating lobes, main lobe, side lobe, Far Field, focal point, caustic region, blocking, payload, upward, downward, elevation plan, azimuth plane, spillover, aberration, first null beam width.

Resumen

El trabajo realizado es interdisciplinar y cubre electromagnetismo y sistemas de antenas avanzados. Se ha propuesto el análisis y diseño de antenas híbridas con array y doble reflector de tipo Imaging para aplicaciones satelitales, como por ejemplo la Observación de la Tierra. La frecuencia considerada es de 30GHz y la implementación es pensada para un satélite geoestacionario. Para dicha frecuencia las aplicadas teorías son Óptica Geométrica y Óptica Física.

El presente Proyecto Fin de Carrera tiene como objetivo analizar teóricamente las propiedades y el funcionamiento del dicho sistema con mínimo de aberraciones. Se presentan diferentes antenas híbridas con un array plano y doble reflector de tipo imaging.

Una de ellas es la antena con alimentadores distribuidos en forma de cuadrado, que fue construida en los 80 por Fitzgerald [1] y Pearson [10]. El patente fue registrado en 1993 por Corado Dragon [3]. Ellos hicieron el estudio teórico con G.O. con onda incidente plana. En este trabajo se ha añadido mas detalladamente el estudio de la distribución de la fase y de el trayecto de los rayos., como también las características de barrido, las imágenes en la apertura y la polarización.

Se han considerado otras dos configuraciones diferentes del array: triangular y hexagonal. Se han conseguido unas mejoras considerables en el nivel de los lóbulos secundarios, el ancho del haz, como también ganancia en potencia para los ángulos de barrido.

A parte se ha aplicado onda esférica al array, se ha observado que para iluminar enteramente el main reflector el array debe ser debajo de él.

Todos los parámetros discutidos son implementados en un software diseñado. Los resultados obtenidos son contrastados con trabajos ya existentes en este campo.

La aplicación de la antena híbrida es para Observación de la Tierra, mas concretamente se utilizará como un radiómetro sintético. Está demostrado que con Radiometría Sintética es posible obtener mejor precisión en la observación: un haz más estrecho. El coste es el alto esfuerzo computacional. El proceso de obtener la

función de Visibility es expuesta. La equivalencia entre el array en forma de Y y la configuración hexagonal es verificada.

Palabras Clave

Antena híbrida, antena Gregoriana, array, alimentador de offset, reflectores, Imaging, Óptica Física y Geométrica, onda plana y esférica, haz de radiación, haz pincel, polarización, fase, aberraciones, barrido, temperatura de la antena y de brillo, función Visiblity, lóbulo principal, lóbulo secundario, punto focal, campo lejano, región cáustica, bloqueo, payload

Agradecimientos

Бих искала да благодаря за безусловната подкрепата на родителите ми Лъчезар Цоневски и Цветана Мирчева. Голяма част от постигнатото в живота ми дължа на тях. Благодаря.

Quiero agradecer a mi Profesor José Luis Masa de la Universidad Autónoma de Madrid las horas dedicadas a mi Proyecto Fin de Carrera. También a mi ponente Bazil Taha por la disponibilidad y apoyo, facilitando mi labor con sus consejos. Aprecio con afecto los conocimientos que me ha aportado mi Profesor Jesús Bescós.

Desidero innanzitutto ringraziare il Professore Fabrrizio Frezza della Università “La Sapienza” Roma per la opportunità di svolggere la mia tesi in ESA/ESTEC. Reingrazio sentitamente il Dr. Piero Angeletti ,il Dr. Giovanni Toso ed il Dr. Salvatore D’Addio della Agenzia Spaziale Europea, che sono stati sempre disponibili a dirimere i miei dubbi durante la stesura di questo lavoro. Inoltre, vorrei esprimere la mia sincera gratitudine al mio compagno Fabio Pelorossi.

Quiero dar las gracias a mi compañero Ignacio Palacios, que ha compartido con migo muchas horas de estudios. También a todos mis compañeros durante los años pasados en la Universidad Autónoma de Madrid.

Thanks Teo!

A mi novio Pablo Secades, quiero darle las gracias, por estar siempre a mi lado durante mi carrera universitaria, ayudándome con todo. A su familia quiero agradecerles el apoyo durante el período de la escritura del presente Proyecto Fin de Carrera.

Content

Content

List of figures

List of tables

1. Introduction

1.1. English version

1.1.1. Motivation

In satellite communication, phase array of large aperture diameter is used, but it has a lot of inconveniences like the weight, the complexity of the long interconnections required by the large spacing between the array elements. Thus, in this work the use of small array combined with two reflectors is proposed. The reflectors are arranged so that a magnification image of the array with minimal aberrations is formed over the aperture of the main reflector. Using this architecture minimization of the used area and reduction of the difficulty of deployment is obtained.

Offset parabolic reflectors offer illumination without blockage, because the feed is mounted out of the line of sight of the aperture.

There was need of software in order to study the system. At the current moment, the commercial software either does not support this architecture or there is no computational capability for its simulation. The designed software is optimized in time.

1.1.2. Goals

The following are the principal goals of this work:

- The theoretical analysis and synthesis of dual reflector offset Gregorian antennas with double reflector and excited with planar arrays, with the potential to scan narrow beams over a limited field of view for earth observation from space and for telecommunications applications.
- Exploiting the advantages provided from the use of an imaging system, to reduce the high complexity given from the use of a large array.
- Studying the electromagnetic characteristics of the payload system with the use of *Geometrical Optics* (G.O.) and *Physical Optics* (P.O.) theories.
- Investigating the best computing modelization applicable to the antenna system. Some numerical analysis software is created for the analysis of these antenna architectures.

-Appling the *Synthetic Radiometry* theory to the defined system. Clarify theoretical concepts like Visibility function and antenna temperature are discussed.

1.1.3. Report Structure

In **Chapter 2 on page 7** the current state of the art is exposed. We mention the field theory. The basic principles of operation of hybrid antenna with an array and double reflector are described. We discuss notions from Radiometry. The two main theories Geometrical and Physical Optics are contrasted.

In **Chapter 3 on page 25** is described the operation of the proposed antenna architecture, described with Geometrical Optics theory. The fundaments of ray tracing are explained. The antenna configuration with a feed of square configuration exited with plane wave is represented. Images on the main aperture are plotted for different cases. It is explained the scan performance of the system. The distortion in phase and path length error is described. The scalar power pattern and the polarization are studied.

In **Chapter 4 on page 81** are proposed two different array's configurations: hexagon and triangle. Some improvements for the scalar power pattern are made. The comparison between the different feed distributions is examined.

In **Chapter 5 on page 99** Physical Optics is applied with the assumption of incident plane wave. The study of the induced currents on the two metal dishes applying triangle meshing is provided. The computational problem releated to the nature of the structure is discussed.

In **Chapter 6 on page 109** the hexagon array is excited by spherical wave, which is simulated using a cone that emerges from the feed. First, it is considered just one feed, explaining the best position for it to obtain full main dish coverage. Second, the entire array is considered. The cone that emerges from every single feed, illuminates just a part of the sub reflector. The best position is decided and the power patterns are represented for boresight and scan angles.

In **Chapter 7 on page 133** the concepts that concerns Interferometric Synthetic Radiometry are exposed and the obtained results are presented for Y shape array and for the hexagon array. The different results are contrasted.

In **Chapter 8 on page 143** it is explained in detail the conclusions obtained from the developed work and speaks about possible future work and interesting paths to follow, in case the work done in this project would be continued.

1.2. Spanish version

1.2.1. Motivación

En las comunicaciones satelitales se utiliza phased array de una apertura grande, dichas antenas tienen muchos inconvenientes, como por ejemplo el peso y la complejidad de interconexiones necesarias para el espaciado entre los elementos. Este es el motivo por el cual, en este trabajo se propone el uso de un array pequeño combinado con dos reflectores. Estos están distribuidos de tal manera que se forma una imagen magnificada con el mínimo de aberraciones después de la doble reflección. De esta forma se obtiene **una minimización del área** usada y una **despliegue mas sencillo**.

Los reflectores parabólicos de tipo offset ofrecen **iluminación sin bloqueo**, porque el alimentador está montado fuera de la línea de iluminación de la apertura. La eficiencia es mayor comparada con el caso de un reflector centrado.

Para el estudio de la arquitectura propuesta ha sido necesaria la creación de un software. En el presente momento, los programas comerciales no soportan esta arquitectura o no hay capacidad computacional para realizar la simulación. El software creado está optimizado en tiempo.

El sistema estudiado va a ser implementado como radiómetro, hasta ahora solo han sido utilizados arrays desplegables para la Observación de la Tierra. La Radiometría Sintética aplicada puede dar lugar a un haz de radiación más pequeño, la mayor precisión significa mayor densidad de potencia en menos área, lo que es una clara ventaja para las comunicaciones satelitales.

1.2.2. Objetivos

Los siguientes objetivos son los principales de este trabajo:
- El análisis y síntesis teórico de offset antena de tipo Gregoriano con doble reflectores parabólicos y excitado con un array plano, con el potencial de barrido con un haz estrecho en un campo limitado para la observación de la tierra desde el espacio y las aplicaciones de telecomunicaciones satelitales
-Explorar las ventajas obtenidas del uso de un sistema de Imaging puede reducir la complejidad producida por un array largo.
- El estudio de las características electromagnéticas del sistema de payload usando la Geométrica Óptica (G.O.) y la Óptica Física (P.O.).
-Investigar la mejor modelización computacional que se puede aplicar para el sistema de antena. Es creado un software numérico para el análisis de la arquitectura.
- Aplicar Radiometría Sintética al sistema definido. Conceptos teóricos como la función de visibilidad y la temperatura de la antena son descritos.

1.2.3. Estructura

La memoria consta de los siguientes capítulos:

En el **Capítulo 2, página 7** el actual estado del arte es expuesto. Se habla de la teoría de los campos. Se describen los principios básicos del funcionamiento de la antena. También se discuten nociones de Radiometría. Las dos principales teorías de Óptica y Física Geométrica son contrastadas.

En el **Capítulo 3, página 25** se describe el funcionamiento de la arquitectura propuesta con un array cuadrado. Los fundamentos del recorrido de los rayos son explicados. Se examina el comportamiento del sistema, alimentando el array con una onda plana. Las imágenes en la apertura son representadas para diferentes casos. Diversos casos de barrido son considerados. Se expone la distorsión de la fase y el error en la longitud del trazadp de los rayos. El haz de radiación escalar y la polarización es estudiada.

En el **Capítulo 4, página 81** vienen propuestos dos diferentes configuraciones de los alimentadores: hexagonal y triangular. Algunas mejoras para el haz de potencia escalar están observadas. Se examina la comparación entre las diferentes distribuciones.

En el **Capítulo 5, página 99** se aplica la Óptica Física, asumiendo que hay una onda plana incidente sobre el sub reflector. El estudio de las corrientes inducidas en los dos reflectores mallados en triángulos es propuesto. Se discute un problema computacional relacionado con el mallado triangular.

En el **Capítulo 6, página 109** el array con forma hexagonal se excita con una onda esférica, que es simulada mediante un cono que emerge del alimentador. Primero, es considerado solo un alimentador, explicando la posición óptima para obtener una cobertura completa del reflector principal. Segundo, se considera todo el array. El cono que emerge desde un solo elemento, ilumina una parte del sub reflector. Se elige la mejor posición y el haz de radiación es representado para el caso de boresight.

En el **Capítulo 7, página 133** los conceptos de la Radiometría Sintética son expuestos y los resultados obtenidos son representados para una array en forma Y y hexagonal. Los diferentes resultados son contrastados.

En el **Capítulo 8, página 143** se explica en detalle las conclusiones obtenidas del trabajo desarrollado. Se discuten los posibles futuros trabajos y caminos de interés que pueden ser realizados en el caso de que este trabajo se continúe.

2. State of the art

2.1. *Reflector antenna*

The reflector antenna uses metal (p.e.c) reflector to concentrate radiation which comes from a feed into very directive pattern [6].

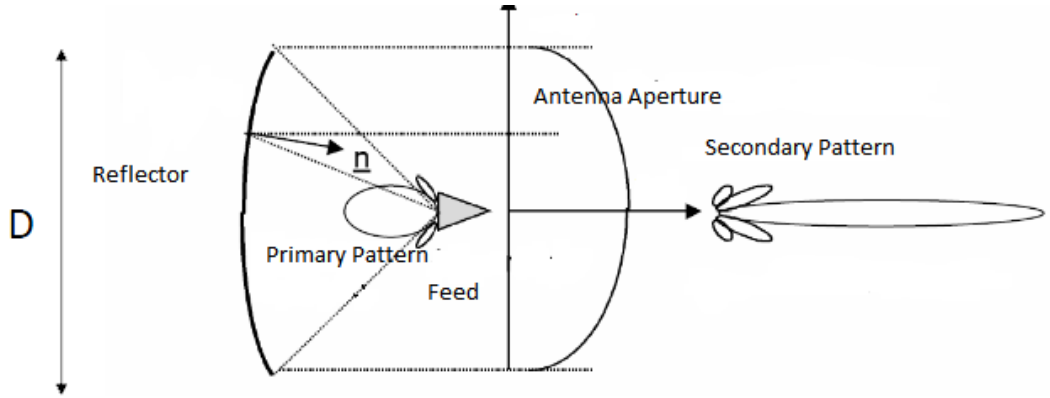

Fig 2.1: Reflector antenna general description

The beam width at the aperture is calculated by the equation in circle aperture:

$$\Delta\theta_{-3dB} \approx 70\frac{\lambda}{D}\ \Delta\theta_{-3dB} \approx 70\frac{\lambda}{D}\ \text{[Degree]}\quad [8] \qquad (2.1)$$

2.1.1. *Important concepts*

Spillover- Some of the radiation from the feed antenna falls outside the edge of the dish and so it does not contribute to the beam formation.

Feed illumination taper- The maximum gain for any aperture antenna is only achieved when the intensity of the radiated beam is constant across the entire aperture area. However, as the radiation pattern from the feed antenna usually tapers off toward the outer part of the dish, the outer parts of the dish are "illuminated" with a lower intensity of radiation. Even if the feed provided constant illumination across the angle subtended by the dish, the outer parts of the

dish are further away from the feed antenna than the inner parts, so the intensity would drop off with distance from the centre. So the intensity of the beam radiated by the antenna is maximum at the centre of the dish and falls off with distance from the axis, reducing the efficiency.

Aperture blockage– If the feed antenna is located in front of the dish in the beam path, the feed structure and its supports block some of the beam. To prevent this problem these types of antennas often use an off-axis feed, where the feed antenna is located to one side - outside the beam area

Aberrations– are departures of the performance of a system from the predictions. Aberration leads to the blurring of the image produced by an image-forming optical system. It occurs when light from one point of an object after transmission through the system does not converge into (or does not diverge from) a single point.

2.1.2. *Paraboloid reflector*

The most used reflector is the parabola. The parabola has the valuable property that rays of light or RF emanating from the focus are all reflected to parallel paths, forming a narrow beam. All paths from the focus to a plane across the aperture, or a parallel plane at any distance, have the same length. Since all the rays have the same path length, they are all in phase and the beam is coherent. This behaviour is reciprocal — rays from a distant source are reflected to a point at the focus.

The most known types of reflector antenna are listed below:

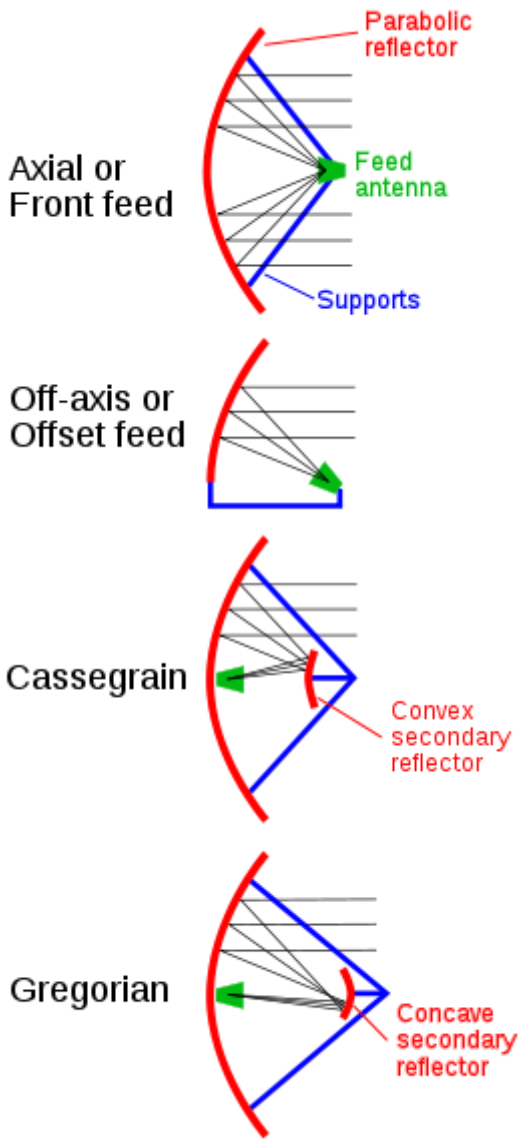

Fig. 2.2: Different type of antenna’s configurations

The most used configuration is Cassegrain (the sub reflectoris formed from the rotation of hyperbola) and Gregorian (ellipse). The both system have similar performance.

The multiple-reflector systems were originally developed as optical telescopes long before radio. All of them have the same important property — ray paths must all have the same length. For more information about the functionality of this type of antennas see Appendix A. In this work Gregorian configuration is discussed with paraboloid as a subreflector.

Just as an ***offset-fed*** parabola has the advantage of reduced feed blockage, Cassegrain and Gregorian antennas can use an offset configuration to reduce or eliminate both sub reflectorand feed blockage.

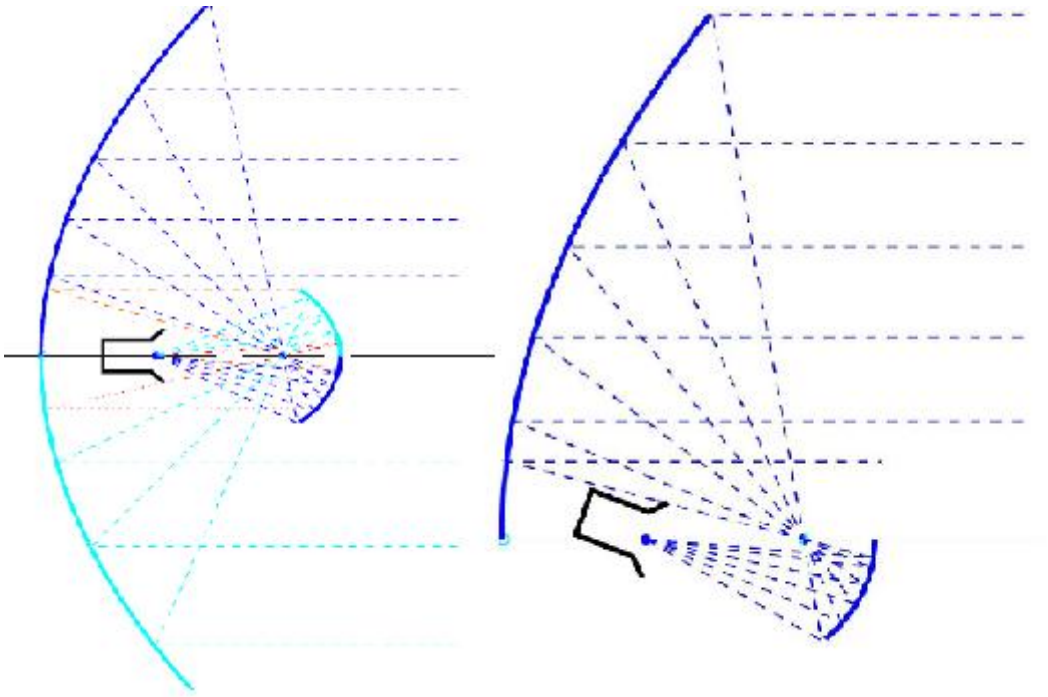

Fig. 2.3: Gregorian antennas difference between centred (right) and offset (left) configurations.

A problem with offset reflectors is that they produce an asymmetric polarization distribution across their aperture and this gives rise to a significant cross-polar component when excited by a linearly polarized feed. The variation in the cross-polarization generated as a function of the offset angle.

2.2. Radiation pattern

The radiation pattern is defined like the mathematical function or graphic representation of the antenna's radiation property considering special coordinates. The far field pattern is considered when the distance where the field is measured is more than $\frac{2D}{\lambda}$, where D is the antenna's diameter and λ is the wave length typically $\lambda = \frac{c}{f}[m]$ and $c = 3 \cdot 10^8 \ [m/s]$ speed of light in vacuum f[Hz] frequency

It is possible to represent the radiation pattern in 3D or for different plane cuts. The coordinate system is usually spherical coordinates defined of: r the radio, θ is the polar angle and φ azimuth angle.

-r (radius) is the distance between P and the origin.

-φ (azimuth, it is defined between 0º and 360º) it is the angle between axis X and the line that connects the origin with the projection of the P point in the XY plane.

-θ (polar angle, it is defined between 0º and 90º) it is the angle between the axis z and the line that connects the origin and the point P.

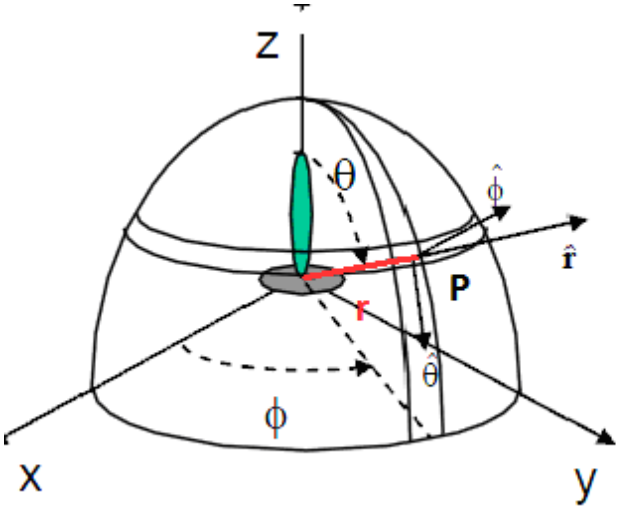

Fig 2.4: Spherical coordinate system [7]

The main beam it's the diagram's zone of radiation delimited of less strong radiation and defines the direction of maximum directivity. The beams around the main beam are with less amplitude and they are named side lobes. The beam width at -3dB is the angular separation of the direction in which is the halved mean beam far field pattern; it is very useful to visualize the directivity.

There are a lot of pattern types classified by their directivity:

- Isotropic: the same power density is radiated in all directions
- Omnidirectional: it represents symmetry in one axis (it has toroidal form)
- Directive: the maximum of radiation is concentrated in one direction.

If we consider the type of graphics there are three possibilities: 3D, colour map and plots for plane cuts (θ and φ are constant).

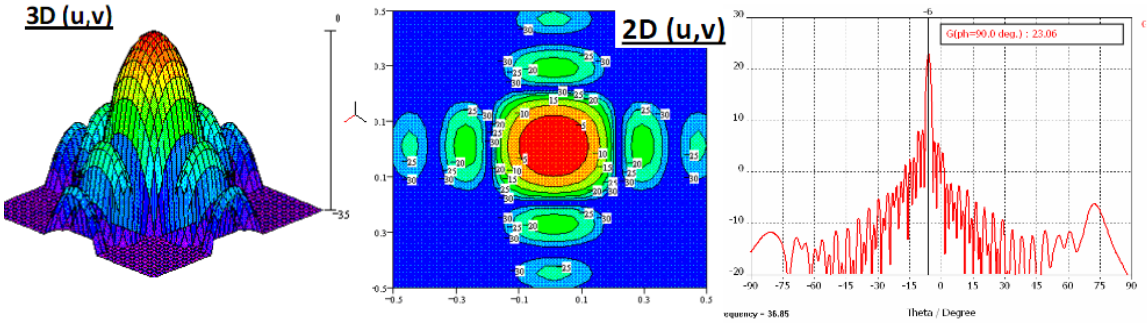

Fig.2.5: Different representations: a) 3D, b) colour map, c) plot for plane cuts [7]

In 3D and color map it is possible to represent them for u and v:

$$u = sen\theta \cos\varphi$$
$$v = sen\theta sen\varphi \qquad (2.2)$$

2.3. *Planar phase array*

If the main lobe of one element is very wide, the gain and the directivity are low. In the satellite communication there is a need of very directive patterns. This is possible using bigger antenna or coupling the radiating elements. This new antenna is formed of many elements and is known like array.

The array consists of identical radiating elements in regular order. The most used reticular arrays configurations are:

1. *Square shape* [7]

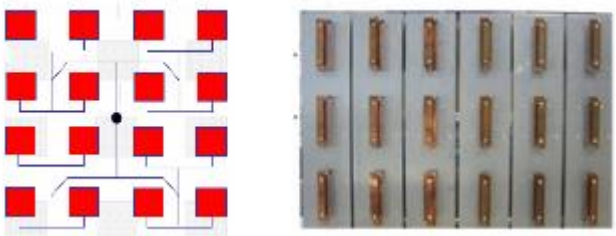

2. *Triangle (hexagonal)*

3. *Circle*

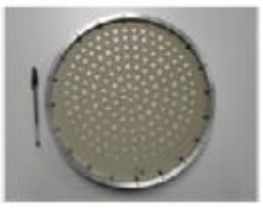

In a typical array antenna, all the elements radiate coherently along a desired direction [6]. This is particularly true for a pencil beam array where a linear phase progression between the elements is set to accomplish this coherent radiation. A pencil beam array is generally referred to as an array that produces narrow beams. Thus, a pencil beam array exhibits maximum possible gain in a desired direction. Typically, the amplitude *taper* of such an array is decided by the side lobe requirement; thus only the element phase is adjusted to maximize the array gain.

For a shaped beam array, however all the elements do not radiate coherently at a given direction. The shape of the beam decides the amplitude and phase distribution of the array, which is usually nonlinear.

The radiated field emanating from radiating sources has two mutually orthogonal components along θ and φ, respectively.

For linearly polarized radiation the ***co-polarization vector*** essentially is the preferred electric field vector. The ***cross-polarization vector*** is orthogonal to both the co-polarization vector and the direction of radiation. One can define the preferred polarization direction.

The radiated field of an array essentially is the summation of the individual element field.

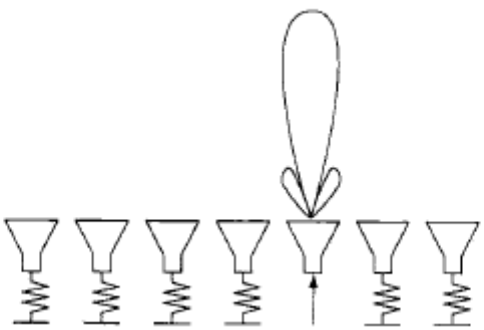

Fig. 2.6: Linear Feed Array

The scan loss has a very important role in designing a scan beam array. A phased array may have several radiating lobes of peak intensities comparable with that of the desired beam. Such undesired radiating lobes are known as ***grating lobes.*** The grating lobes should not be confused with the **side lobes**. Usually, a side lobe has much lower peak intensity than that of grating lobe. See Chapter 3 for more information. For quantitative understanding of grating lobes, when we consider the pattern, the function is periodic function of $k_0 a \sin\theta$ of period 2π, where is the wave length and a is the space between elements.

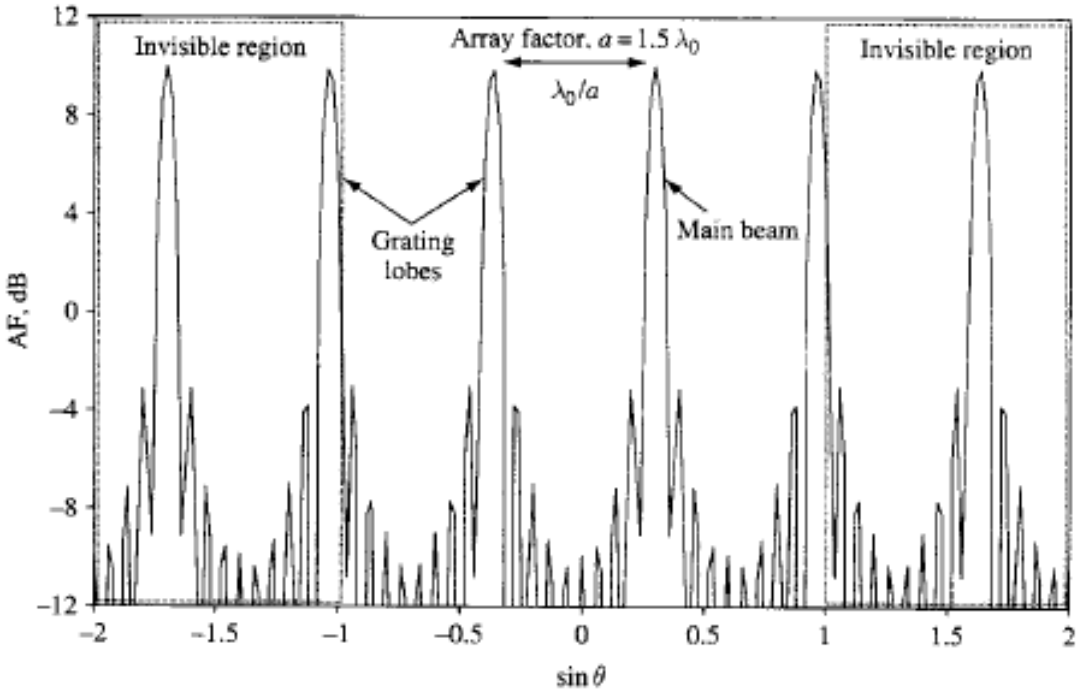

Fig. 2.7: Grating lobes [6]

The *radiated field* of an array essentially is the summation of the individual element fields. It can be shown that the far-field pattern of an array of identical elements can be represented by a product of two quantities, namely *the element pattern* and the *array factor*. The element pattern signifies the radiation behaviour of an individual element and the array factor signifies the arraying effect, including array architecture and relative excitation of the elements.

To explain the array factor the reticular array is taken in consideration, with N elements with the same space between them with complex coefficient A_i. The resulting pencil beams are orientated to any direction (d_y, φ). The elements are

positioned in square of MxN element in XY plane, with the same distance d_x and d_y.

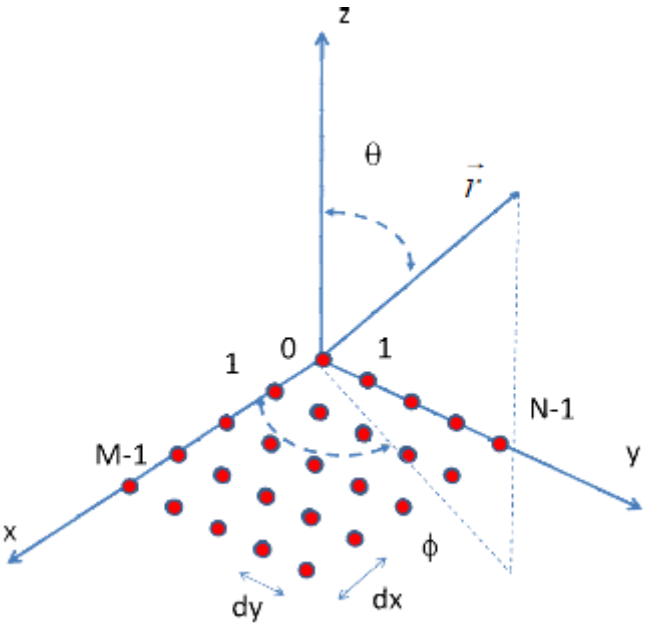

Fig. 2.8: Reticular planar phased array [7]

The array factor is given by the formula:

$$F_A(\theta,\phi) = \sum_{m=1}^{M-1}\sum_{n=1}^{N-1} A_{mn} \cdot e^{jk_0 \hat{r}\vec{r}_{mn}} = \sum_{m=1}^{M-1}\sum_{n=1}^{N-1} A_{mn} \cdot e^{jmk_0 d_x sen\,\theta\cos\phi} \cdot e^{jnk_0 d_y sen\,\theta sen\,\phi} \quad (2.3)$$

In order to estimate the radiated power of an array antenna in the *far-field* region, it is necessary to understand the radiated field intensity of an element in the far-field region. The element pattern is defined as the field intensity of an element in the far-field region. The element pattern is defined as the field intensity of an element in the far-field region. The element pattern is defined as the field intensity distribution of a radiating element as a function of two far-field coordinates, while the radial distance remains constant. In spherical coordinate systems the radiated electric field in the far-field location can be expressed as:

$$\vec{E}(r,\theta,\varphi) = A\frac{\exp^{(-jk_0 r)}}{r}\vec{e}(\theta,\varphi) \quad (2.4)$$

In the above A is a constant which is related to the input excitation of the antenna $\vec{e}(\theta,\varphi)$ is the element patter, k_0 is the wave number in free space. The component $k_0 r$ is known as relative phase.

It is possible to obtain transversal radiation (***boresight***) to the array's axis. If the array is in XY plane the principal radiation is obtained for $\theta = 0^\circ$.

Important concept is boresight, it is the axis of maximum gain (maximum radiated power) of a directional antenna. For most antennas the boresight is the axis of symmetry of the antenna. For example, for axial-fed dish antennas, the antenna boresight is the axis of symmetry of the parabolic dish, and the antenna radiation pattern (the main lobe) is symmetrical about the boresight axis. Most antennas boresight axis is fixed by their shape and cannot be changed.

However, phased array antennas can electronically steer the beam, changing the angle of the boresight by shifting the relative phase of the radio waves emitted by different antenna elements, this property is named ***scanning.***

2.4. Geometrical Optics and Physical Optics

Geometrical optics (G.O.) or ray optics, describes light propagation in terms of "rays". The "ray" in geometric optics is an abstraction, or "instrument", which can be used to approximately model how light will propagate. It is more useful technique for the system under study. It is a good approximation for electromagnetic systems where the wavelength is considerably smaller than the objects that interact with it. G.O. requires only to know the field along a ray path. The theory is quite simple and the computational effort results, in general, are not heavy.

Physical optics *(*P.O.) is more accurate than G.O. in terms of field distributions, but has stronger computational requirements. There is a need of meshing in small planar surfaces the reflectors dishes in order to obtain certain accuracy. It is necessary to calculate the induced currents on the reflector and the scattered field for every small surface, for all possible combinations.

2.5. Hybrid approach (G.O.)

In this chapter we discussed the plane wave excitation of the array viewed of the perspective of Geometrical Optics.

The phase array and paraboloidal reflector are combined into what is known as a ***hybrid antenna.*** The phased array is employed to illuminate a large parabolic reflector, with the help of a small parabolic sub reflector. A symmetrical sub reflector and array feed structure would present unacceptable levels of **blocking** with this type of configuration hence an **offset** is used.

The aim of the antenna system is to increase the gain of a phased array by using an imaging arrangement, as shown in the figure:

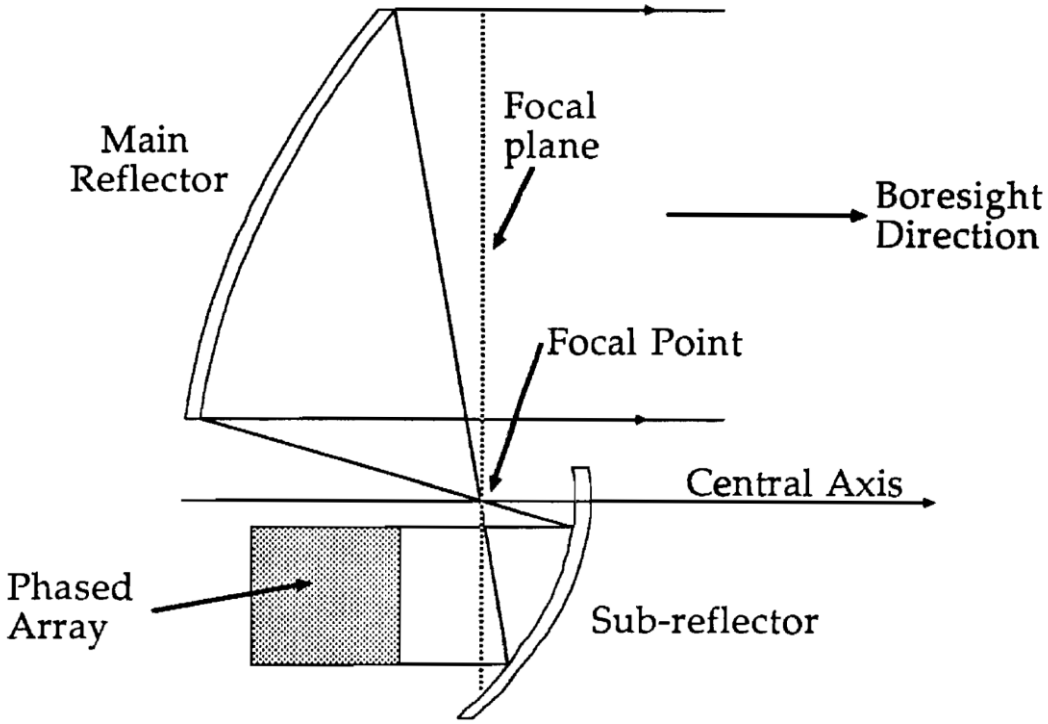

Fig. 2.9: Gregorian configuration. Offset feed [10]

Applying the *Fresnel law*, the field radiated by the phased array feed can be approximate to single **plane wave**.

2.6. *Operation*

The first paraboloid transforms a plane wave propagating in the direction of the paraboloid axis, into a spherical wave converging toward the Focal Point. This spherical wave is then transformed into plane wave, by the second paraboloid, which is large enough to intercept all incident rays. After the second reflection, the reflected rays illuminate the aperture of the antenna with magnified image. This is the principal of operation in case of transition. In case of reception the procedure is dual.

Since the illuminated area corresponds to the projection of the first paraboloid, its diameter Ds is determined by the diameter of the main dish D_m. The **magnification factor** is:

$$M = \frac{D_m}{D_s} = \frac{f_m}{f_s} \qquad (2.5)$$

Where f_m and f_s are axial focal lengths of the two paraboloids.

The main reflector and the array are a **conjugate element** that means that the rays originally from a point of one element are transformed, by the optical system, into rays which pass trough a corresponding point of the other element.

Another important property of the arrangements described here is that the transformation relating the field over the array aperture to the field over the main reflector aperture is essentially **frequency independent**, and therefore it can be approximated by its asymptotic behaviour at high frequency.

The position of the parabolic sub reflectors is very important: they must be deposed **coaxially** to achieve both paraxial and geometric surface co focally while positioning the feed array at the **conjugate plane** relative to the exit aperture of the reflector system. The reflectors are co focal and co axial, in this conditions we have perfect imaging and aberration free performance.

2.6.1. Fourier Transform

Hybrid systems are classified according to the number of Fourier Transform or FT [5].The number of FT's determines whether an antenna is fed by an array of individual feed which are arranged in a group, i.e. a multiple beam antenna (M.B.A) with an array feed where all the elements contribute to one beam, which

might be possible to be scanned. It is well known that a Fourier transform relation exist between the field distribution over an antenna aperture and its far field radiation pattern, but approximate FT relation holds between the aperture distribution and the focal plane field of a parabolic reflector.

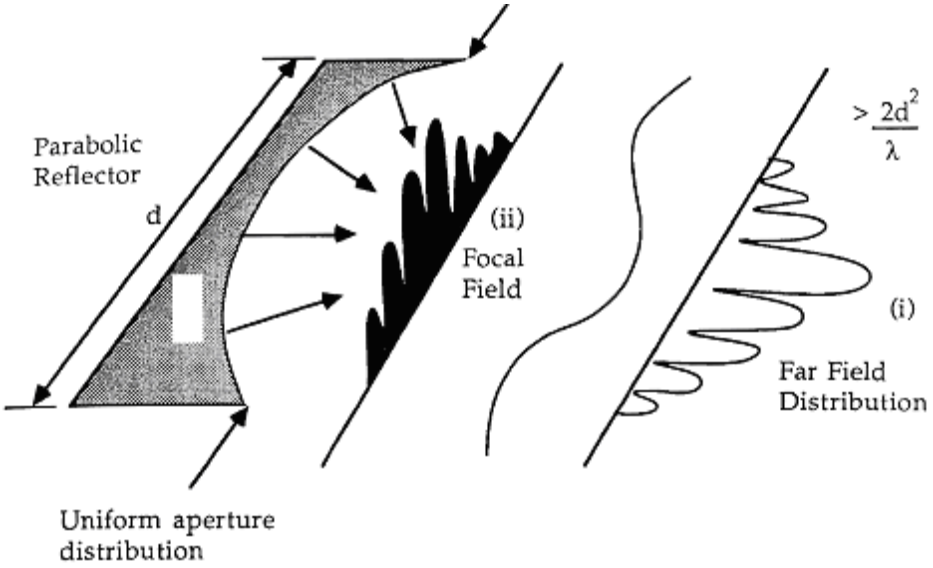

Fig.2.10: A schematic view of the FT relationship between the aperture distribution of a parabolic reflector and (i) its far field pattern,(ii) its focal plane distribution.[10]

Hybrid antenna can be classified as having an odd or even number of Furrier transforms: with an odd number of FT's: one input corresponds to a single beam, whereas an even number of FT's signifies a number of elements contributing to single pattern. In this work the chosen system is double FT system. The sub –dish is used to produce a second Fourier transform.

2.7. Field theory (P.O)

It is possible to describe an antenna in terms of its equivalent radiating currents in free space. We represent the electric field generated by these current's distributions, considering Maxwell equations in linear, isotropic, no dispersion and homogeneous space, characterized by a dielectric constant ε and magnetic permeability μ, in presence of electric current J, magnetic current M and of electric charges ρ and magnetic ρ_m in one determine region.

$$\nabla \cdot E = \frac{\rho}{\varepsilon} \qquad (2.6)$$

$$\nabla \cdot H = \frac{\rho_m}{\mu} \tag{2.7}$$

$$\nabla \times E = -j\omega\mu H - M \tag{2.8}$$

$$\nabla \times H = j\omega\varepsilon E + J \tag{2.9}$$

Considering zeros the currents and the magnetic charge. As $\nabla \cdot (\mu H) = 0$ we can write the H like rotor vector field, so there is a vector A, named potential magnetic vector that

$$\Rightarrow \mu H = \nabla \times A \Rightarrow H = \frac{1}{\mu}\nabla A \tag{2.10}$$

Substituting (2.5) in (2.3):

$$\nabla \times E = -j\omega\nabla \times A \Rightarrow \nabla \times (E + j\omega A) = 0 \tag{2.11}$$

The first member of equation (6) makes clear that $(E + j\omega A)$ is not rotational and that's way there is need of scalar ϕ , named scalar potential:

$$E + j\omega A = -\nabla\phi \tag{2.12}$$

With this choice the Maxwell equations are satisfied. We determined two equations which will help to reconstruct easily E and H:

$$\begin{cases} E = -j\omega A - \nabla\phi \\ H = \frac{1}{\mu}\nabla \times A \end{cases} \tag{2.13}$$

We consider a generic uniform currents' distribution J(r') over an surface S

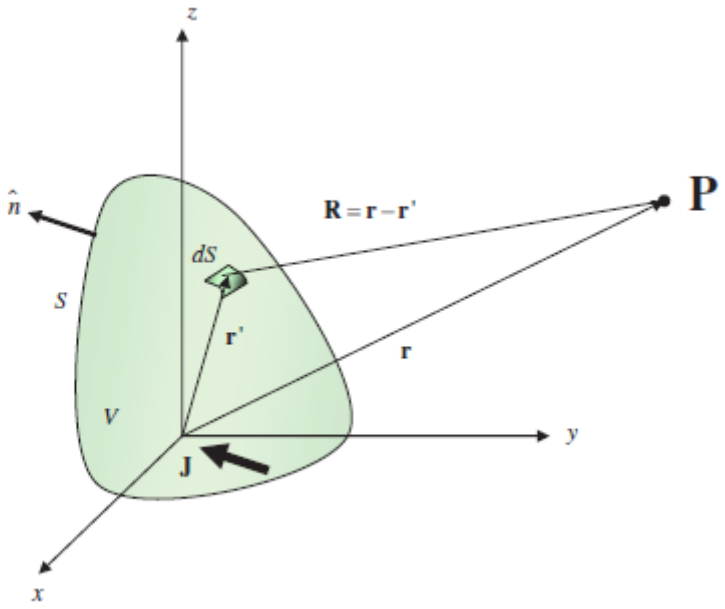

Fig 2.11 Uniform currents' distribution over a surface [12]

The radiated electric field coming from this current's distribution at a distance r form the point P is given by:

(2.15)

$$E(r) = \iint_S J(r') \cdot G_E(r, r') dS \quad (2.14)$$

$G_E(r, r')$ is Green's function. We substitute the expression for the potential magnetic vector in (9)

$$A(r) = \mu \iint_S J(r') \cdot G_0(r, r') dS \quad (2.16)$$

The (10) is obtained from the Maxwell's equation with annulations tangent currents of the total field.

From the boundary condition on a p.e.c. the induced electric and magnetic current densities vectors are related to the incident field to the metallic surface:

$$\mathbf{J} = 2\mathbf{n} \times \mathbf{H} = \mathbf{y} h_x + \mathbf{x} h_y$$
$$\mathbf{M} = -2\mathbf{n} \times \mathbf{E} = 0$$

From [8] we define:

(2.17)

$$\mathbf{F} = \frac{\varepsilon e^{-j\beta r}}{4\pi r}\mathbf{L}$$
$$\mathbf{A} = \frac{\mu e^{-j\beta r}}{4\pi r}\mathbf{N} \tag{2.18}$$

2.8. Obtaining:

$$\mathbf{N} = \iint_S \mathbf{J}_s e^{j\beta r' \cos\psi} dS' = \iint_S (\mathbf{a}_x J_x + \mathbf{a}_y J_y + \mathbf{a}_z J_z) e^{j\beta r' \cos\psi} dS'$$
$$\mathbf{L} = \iint_{S'} \mathbf{M}_s e^{j\beta r' \cos\psi} dS' = \iint_{S'} (\mathbf{a}_x \mathbf{M}_x + \mathbf{a}_y \mathbf{M}_y + \mathbf{a}_z \mathbf{M}_z) e^{j\beta r' \cos\psi} dS' = 0 \tag{2.19}$$

Where $\mathbf{r}$ is the observation vector, $\mathbf{r}'$ is the source vector and ψ is the angle between.

Using the rectangular-to-spherical transformations:

$$\begin{bmatrix} \mathbf{a}_x \\ \mathbf{a}_y \\ \mathbf{a}_z \end{bmatrix} = \begin{bmatrix} \sin\theta\cos\phi & \cos\theta\cos\phi & -\sin\phi \\ \sin\theta\sin\phi & \cos\theta\sin\phi & \cos\phi \\ \cos\theta & -\sin\theta & 0 \end{bmatrix} \begin{bmatrix} \mathbf{a}_r \\ \mathbf{a}_\theta \\ \mathbf{a}_\phi \end{bmatrix} \tag{2.20}$$

We can reduce to:

$$N_\theta = \iint_S (J_x \cos\theta\cos\phi + J_y \cos\theta\sin\phi - J_z \sin\theta) e^{j\beta r' \cos\psi} dS'$$
$$N_\phi = \iint_S (-J_x \sin\phi + J_y \cos\phi) e^{j\beta r' \cos\psi} dS'$$
$$L_\theta = \iint_S (M_x \cos\theta\cos\phi + M_y \cos\theta\sin\phi - M_z \sin\theta) e^{j\beta r' \cos\psi} dS' \tag{2.21}$$
$$L_\phi = \iint_S (-M_x \sin\phi + M_y \cos\phi) e^{j\beta r' \cos\psi} dS'$$

Thus, we obtain:

$$E_r \approx 0$$
$$E_\theta \approx -\frac{j\beta e^{-j\beta r}}{4\pi r}(L_\phi + \eta N_\theta)$$
$$E_\phi \approx +\frac{j\beta e^{-j\beta r}}{4\pi r}(L_\theta - \eta N_\phi)$$
$$H_r \approx 0 \tag{2.22}$$
$$H_\theta \approx +\frac{j\beta e^{-j\beta r}}{4\pi r}(N_\phi - \frac{L_\theta}{\eta})$$

$$H_\phi \approx -\frac{j\beta e^{-j\beta r}}{4\pi r}(N_\theta + \frac{L_\phi}{\eta})$$

where η is the characteristic impedance of vacuum (377 Ohm) , $\beta = \frac{2\pi}{\lambda_0}$

2.9. Radiometry

Radiometry is the scientific discipline that measures the electromagnetic radiation flux produced by a thermal source.

Interferometric aperture synthesis for Earth observation was first proposed in the 80's by D. Le Vine as an alternative to real aperture radiometry, in order to overcome antenna size problems in high spatial resolution applications, especially at low frequencies.

The described antenna is used as synthetic aperture interferometric radiometer. The current state of the art in this sector is represented by MIRAS (Microwave Imaging Radiometer with Aperture Synthesis) the payload of ESA's "SMOS" (*soil moisture and ocean* salinity) mission, one of the six satellites designed for the "Living Planet Program" of ESA to operate remote sensing of Earth parameters related to the hydrological cycle. The SMOS is measuring the microwave radiation emitted from Earth's surface within the L-bans at 1.413 GHz. MIRAS is formed of Y-shaped array of 69 elementary antennas, deployed in space, which are equivalent to a classical antenna 8m in diameter. This is the first ever two-dimensional interferometric radiometer in space. Obviously, there is clear disadvantage coming from the complexity of the deployment of the shields and the big dimensions of the structure. This is the reason why the Gregorian antenna is attractive for future applications as interferometric radiometer.

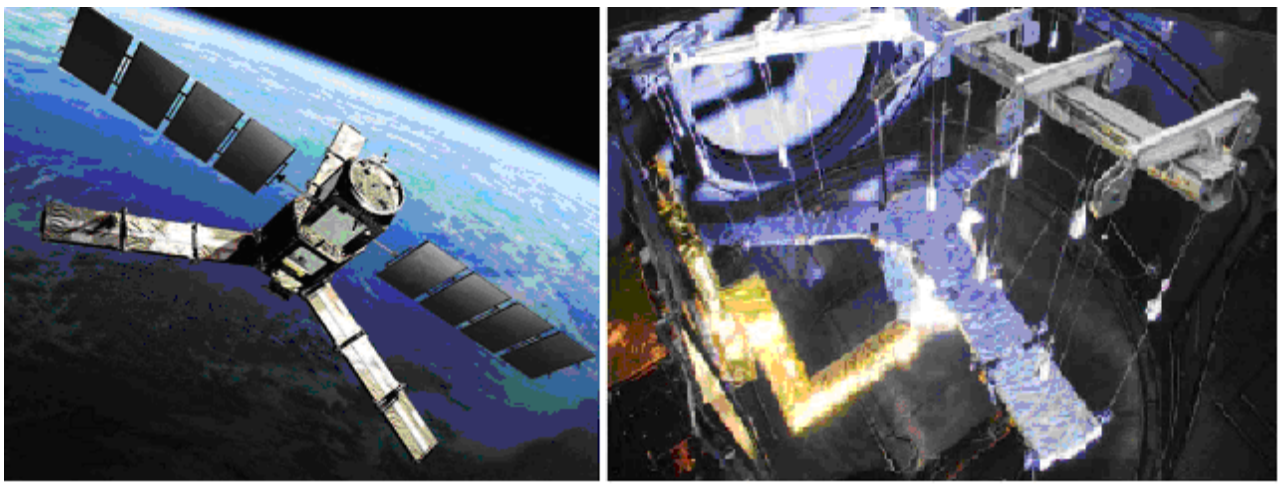

Fig. 2.12: a)SMOS b) MIRAS inside ESA's largest Space Simulator [13]

Actual studies on radiometry have led to periodic antenna configurations adopting the technique of two-dimensional aperture synthesis which are analyzed through traditional Fourier techniques.
On the other hand, the synthetic radiometry is preferred to the classic radiometry theory due to its pattern accuracy.

3. Square configuration (GO).Plane wave

3.1. Introduction

The analysis is based on the assumption that the fields in the near-zone region of the array can be accurately determined by the methods of the Geometric Optics.
Three different configurations of the array are discussed: squares, triangles and hexagonal. The purpose is to evaluate the scanning capabilities of the system. The applied equations are deduced from the paper of D. W. Fitzgerald [1]
The main characteristics of the system are discussed in Chapter 2.4. To summarize them: The antenna is offset-feed Gregorian geometry, both reflectors are offset sections of confocal coaxial paraboloids the projection of which is circular into the XY plane. The main reflector is that portion of the compete paraboloids intersected by the cylinder:

$$[x-\frac{f_m}{f_s}h]^2+y^2=\left[\frac{f_m}{f_s}\frac{d}{2}\right]^2$$

As for the sub reflector, it is intersected by:

$$[x+h_2]^2+y^2=\left[\frac{d_2}{2}\right]^2$$

Very important concept is that just one ray comes out from any feed (see Fig.3.1).The main aperture is complexly defined for boresight. The sub reflectoris illuminated with a linear phase front by placing it well into the near field of the array. In condition of scanning the beam is generated with a linear tilt on the array. If θ and φ are the coordinates which define the phase tilt of the array, and θ' and φ' are the spherical coordinates defining the secondary beam position, then for small angles:

$$\theta=\frac{fm}{fs}\theta' \qquad (3.1)$$
$$\varphi=\varphi'+\pi$$

Unfortunately, these equations are not applied for all beam widths scans from boresight. See Chapter 3 and its paragraph 4.5. The coordinate system is orientated by the figure below:

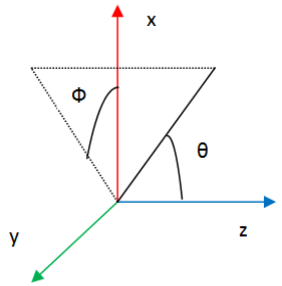

Fig.3.1: Coordinate system

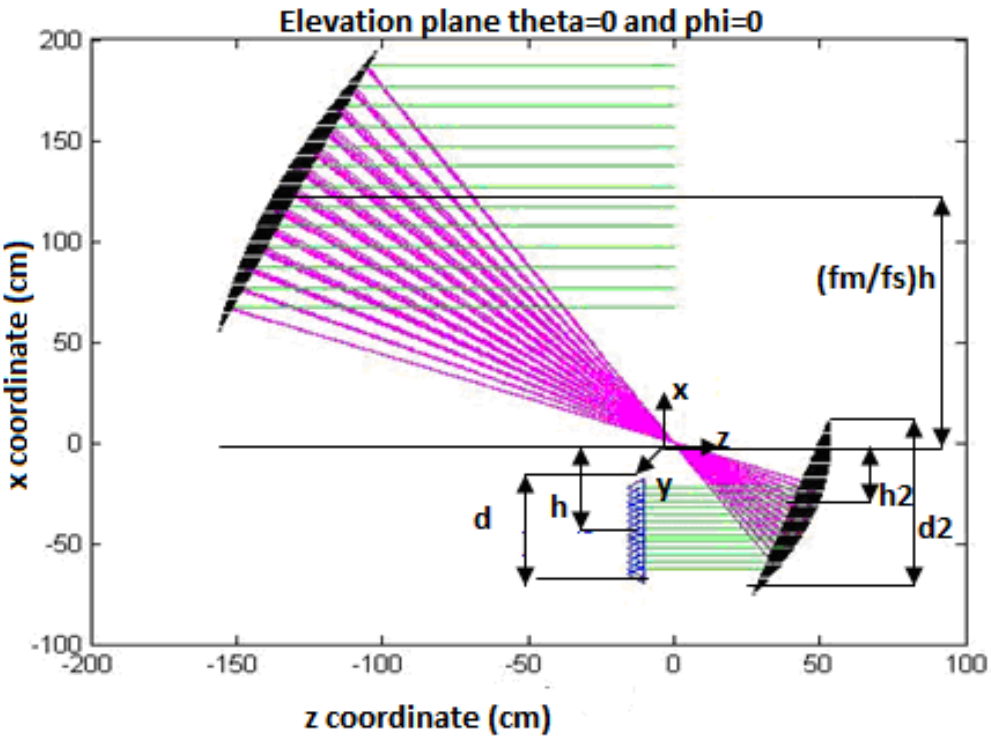

Fig. 3.2: General configuration boresight

As can be observed in the figure, the sub reflector is oversized in the upper part and the center of the array does not match with the sub reflector's center. For each pair of coordinate points xm and yn (See Eq. (3.20)) and for given θ and φ the coordinates of the points of the reflection, which describe the passage of the ray through the system, are computed and then used to determine the optical path length $L_{m,n}$. The parameters d, h, l, h_2, d_2 and the coordinates of points on the array and sub reflector are normalized

to f_s. The coordinates of the main reflector and the assumed aperture plane are normalized to f_m.

The calculations are parametric for the wave length. The system is studied for 30GHz, which means wave length of 1 cm. ($\lambda = \frac{c}{f}$)

3.2. Ray tracing

The ray tracing is applied to demonstrate the variation in the scanning properties of the antenna as a function of the beam deflection angle. A very important part of the solution is the coordinates of the array, sub reflector and the main reflector. The origin of the coordinates system coincides with the focal point of both reflectors. The main aperture plane is arbitrarily chosen to be in the focal plane. A points of the sub reflector is denoted (xs,ys,zs), of the array (x0,y0,z0). Similarly (xm,ym,zm) defines a point on the main reflector:

$$zm = \frac{xm^2 + ym^2}{4\,fm} - fm \tag{3.2}$$

And the equation of the sub reflectoris:

$$zs = fs - \frac{xs^2 + ys^2}{4\,fs} \tag{3.3}$$

The spherical coordinates θ and φ define the direction of the general ray emerging from the aperture. This ray is perpendicular to the assumed linear phase tilt and hence is parallel to:

$$\bar{a}\bar{b} = \bar{i}\sin\theta\cos\varphi + \bar{j}\sin\theta\sin\varphi + \bar{k}\cos\theta \tag{3.4}$$

Lower-case letters denote unit vectors, and i,j and k are the unit vectors parallel to the coordinate axes.

The component ray form point A on the array to the point B on the sub reflectoris given by:

$$\bar{A}\bar{B} = \bar{i}(xs - x0) + \bar{j}(ys - y0) + \bar{k}(zs + z0) \tag{3.5}$$

The unit vector $\overline{AB}/|AB|$ is equated with Eq. (4.3). This yields three equations that define a line in three-dimensional space. Only two of these equations are independent:

$$\tan\varphi(xs - x0) = ys - y0$$
$$\frac{1}{\tan\varphi\cos\varphi}(xs - x0) = zs + z0 \qquad (3.6)$$

Solving Equations. (4.5) and (4.2) give the coordinate of the first point of reflection B:

$$xs = \frac{-B \pm \sqrt{B^2 - 4AC}}{2A} \qquad (3.7)$$
$$ys = y0 + (xs - x0)\tan\varphi$$
$$zs = fs - \frac{xs^2 + ys^2}{4\,fs}$$

Where:

$$A = (1 + \tan^2\varphi)$$
$$B = (2y0\tan\varphi - 2x0\tan^2\varphi + \frac{4\,fs}{\tan\theta\cos\varphi})$$
$$C = (y0^2 + x^2\tan^2\varphi - \frac{4\,fsx0}{\tan\theta\cos\varphi} - 4\,fs(fs + z0) - 2x0\,y0\tan\varphi)$$

Snell's law of reflection relates the incident, reflected, and normal unit vectors at the point xs, ys, zs on the subreflector:

$$\overline{bc} = \overline{ab} - 2\overline{n_s}(\overline{n_s}\,\overline{ab}) \qquad (3.8)$$

The unit vector $\overline{n_s}$ on the sub reflectorsurface is:

$$\overline{n_s} = -\left(\frac{\bar{i}xs + \bar{j}ys + \bar{k}(2\,fs)}{\sqrt{xs^2 + ys^2 + 4\,fs^2}}\right) \qquad (3.9)$$

By using Eq. (4.3) the components of the unit vector $\overline{bc}$ are:

$$(bc)_x = \sin\theta\cos\varphi - \frac{2xs}{xs^2 + ys^2 + 4\,fs^2}(xs\sin\theta\cos\varphi + ys\sin\theta\sin\varphi + 2\,fs\cos\theta)$$
$$(bc)_y = \sin\theta\sin\varphi - \frac{2ys}{xs^2 + ys^2 + 4\,fs^2}(xs\sin\theta\cos\varphi + ys\sin\theta\sin\varphi + 2\,fs\cos\theta)$$
$$(bc)_z = \cos\theta - \frac{2\,fs}{xs^2 + ys^2 + 4\,fs^2}(xs\sin\theta\cos\varphi + ys\sin\theta\sin\varphi + 2\,fs\cos\theta)$$

The component ray $\overline{BC}$:

$$\overline{BC} = \bar{i}(xm - xs) + \bar{j}(ym - ys) + \bar{k}(zm - zs)$$

With the equation the unit vector $\overline{BC}/|BC| = \overline{bc}$, once again there are three equations defining line in space, only two of which being independent. Thus:

$$\begin{aligned} &\frac{(bc)_y}{(bc)_x}(xm - xs) = ym - ys \\ &\frac{(bc)_z}{(bc)_x}(xm - xs) = zm - zs \end{aligned} \qquad (3.10)$$

Solving Equations (3.10) and (3.2) gives the coordinates on the main equation:

$$\begin{aligned} xm &= \frac{-B' \pm \sqrt{B' - 4A'C'}}{2A'} \ * \\ ym &= ym + \frac{(bc)_y}{(bc)_x}(xm - xs) \\ zm &= \frac{xm^2 + ym^2}{4\,fm} - fm \end{aligned} \qquad (3.11)$$

*we use + per upward and – per downward

3.3. Computational results

The next figure illustrates how the array aperture is divided into a two dimensional lattice of equally spaced sampling point. The difference between elements is of 3λ

$$\begin{aligned} x_m &= [\frac{2(m-1)}{N-1} - 1]\frac{d}{2\,f_s} - \frac{h}{f_s} \\ y_n &= [\frac{2(n-1)}{N-1} - 1]\frac{d}{2\,fs} \end{aligned} \qquad (3.12)$$

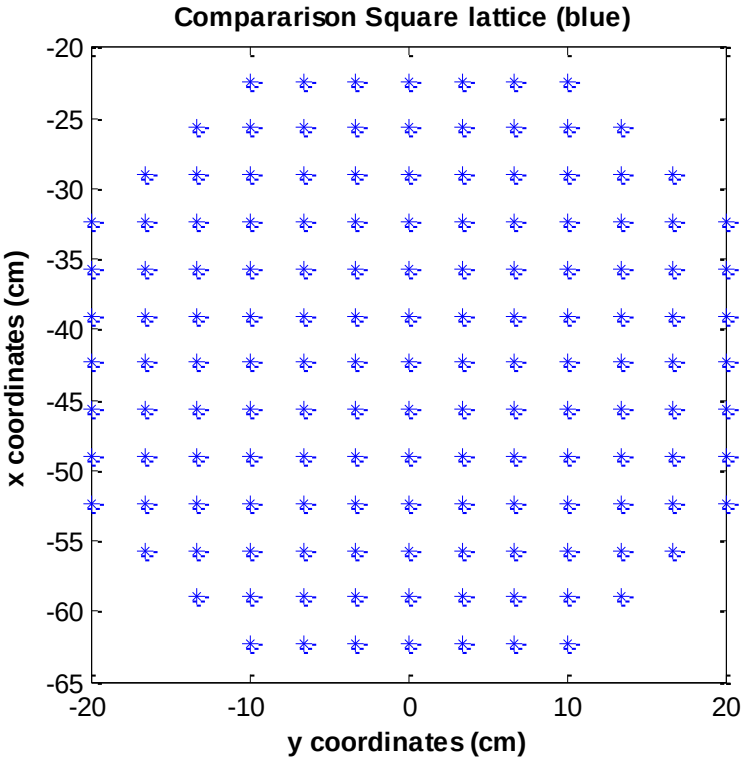

Fig. 3.3: Circle cut of square configuration

The next figure shows the cross section of the example considered. The main reflector size given by:

$$d_m = 2 \cdot 69,2 \cdot \lambda \qquad [14]$$

139.8λ corresponds to a 1° as First Null Beam Width [2]. The frequency considered is 30GHz. The magnification factor is M=3. The offset distance is of 56 λ. The table lists the input parameters to the computer program.

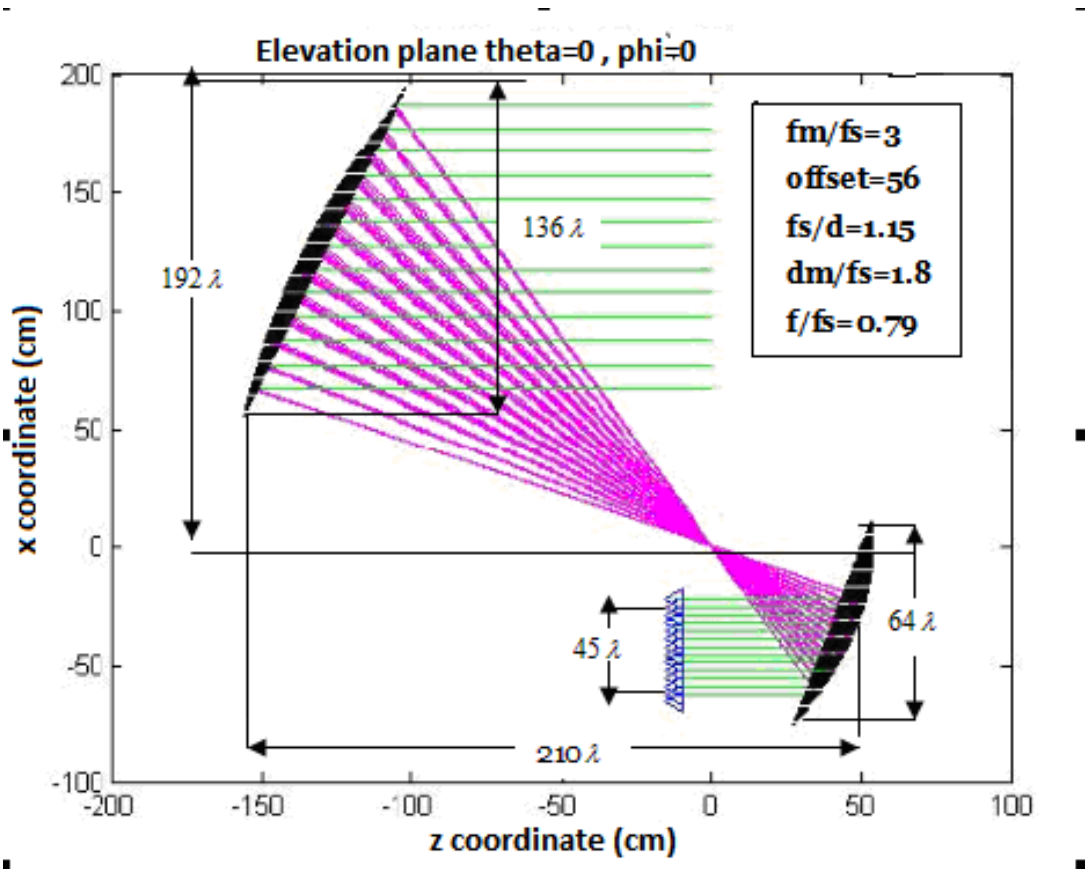

Fig. 3.4: Cross section elevation plane for boresight

The software program is parametric as shown in the Table 1 below.

3.3.1. Inputs

The geometrical parameters determine the size and positioning of the array as well as the two reflectors. The constraint, which defines the outline of the main reflector, can be modified or removed to investigate the effects of an oversized main reflector. For boresight the main reflector is completely utilized.

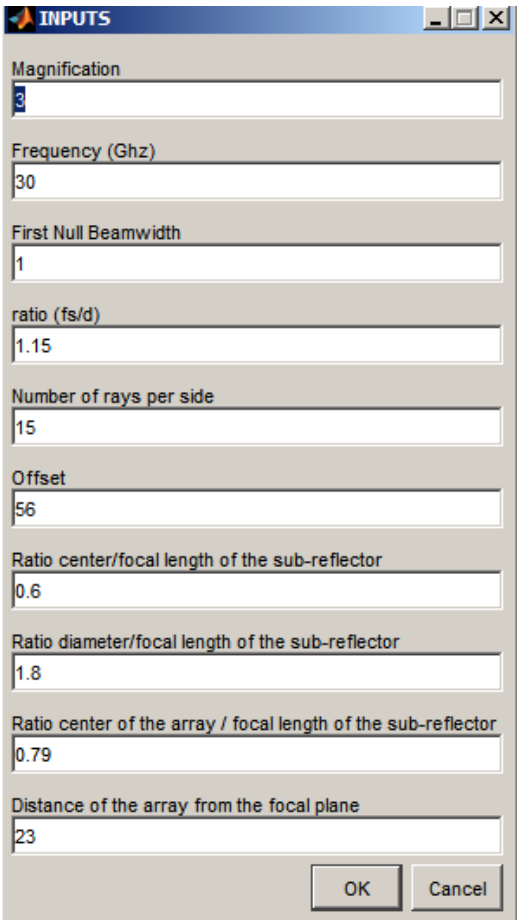

Table 1. Inputs for the square system

Variation of N

N is the number of sampling points (feed) per side, equivalent in this case of the number of rays per side mentioned in the previous figure. For example, there is a square with NxN elements. It is difficult to determine N as we have to consider the grating lobes. A value of N=15 is generally used. The total numbers of elements its not 15x15=225 because the square is cut in circle as shown in the Fig.3.3, therefore the real number of feeds is 145.
If N=30 the number of rays feeds the circle cut would be 648.

Variation of f/d

With the array the same distance behind the focal plane in each case, the longer f/d ratio antenna has significant blocking problems, owing to rays reflected from the sub dish back into the array feed. This implies that the array needs to be repositioned further back into the array feed. Although the former, as already said, implies that the array needs to be

repositioned further back, the already significant problems of spillover around the sub reflector will be increased.

On balance a small f/d ratio antenna, offering a more compact configuration with a smaller sub dish is probably preferable to the longer f/d ratio, because the reduction in phase and aberration errors offered are not particularly big and blocking effects are reduced.

The system is represented in the next figures for f/d=1 and f/d=1.5. As [1] in more of the cases discussed in this work f/d=1.15.

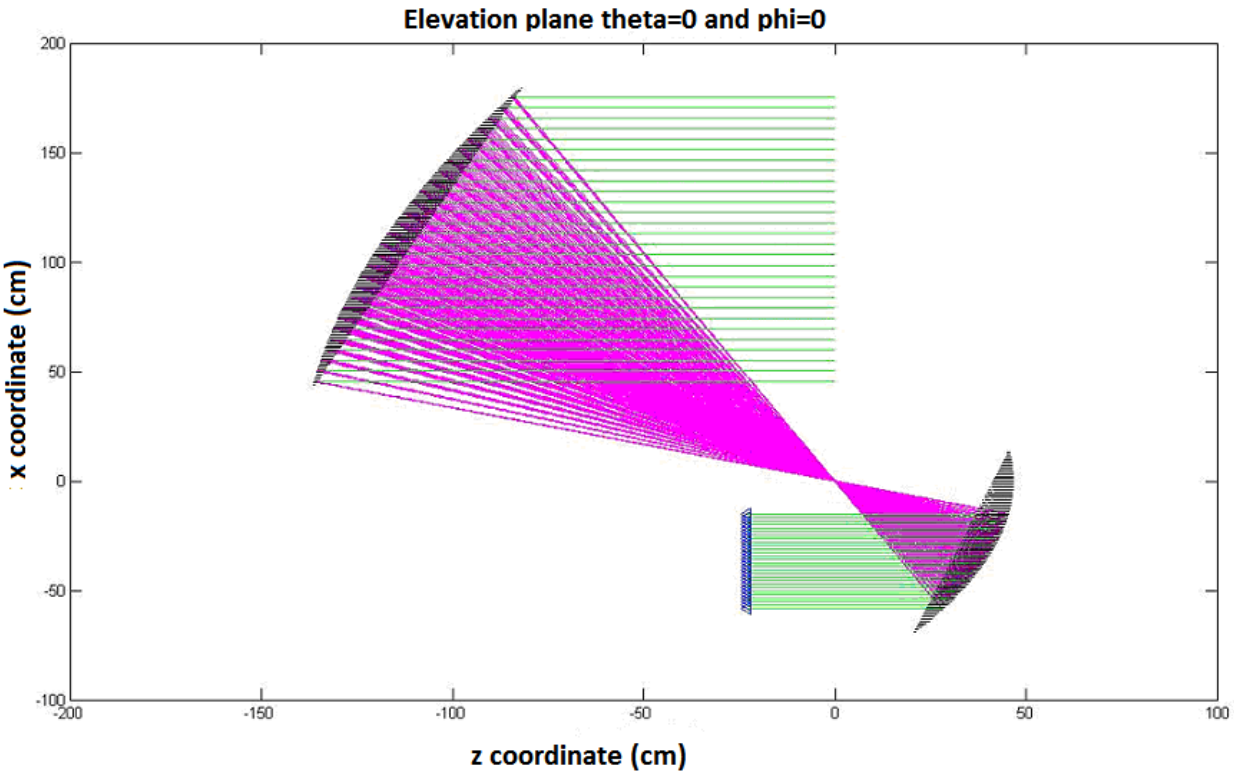

Fig.3.5 a): System representation f/d=1 boresight

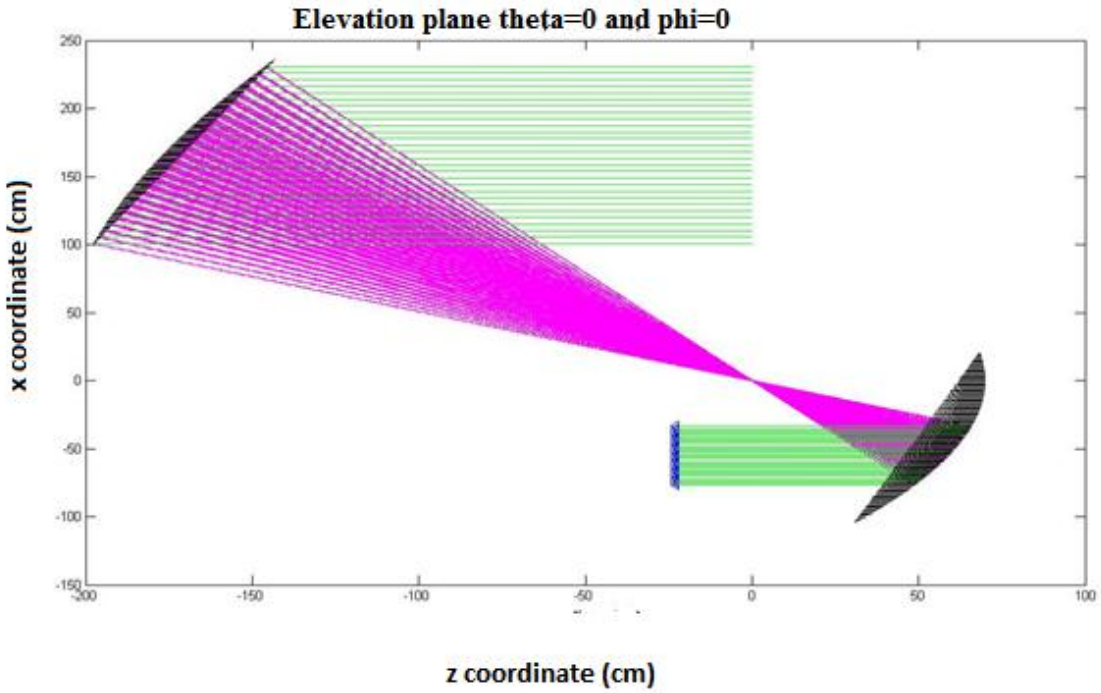

Fig.3.5 b)System representation: f/d=1.5 boresight

Variation of scan angles

The software program was designed to introduce different angles of θ and φ. The relationship of the reflected and induced angles is provided in Eq.3.1. For better understanding see Fig. 2.4. Scan in the elevation plane is considered for φ=0° (upward), φ=180°, downward φ=90° azimuth and φ=45° diagonal scan. The boresight direction is considered for θ=0°.

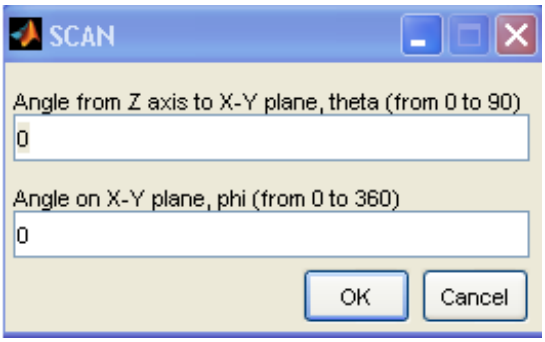

Table 2. Inputs for the scan angles

3.3.2. Aperture representation

Considering the Ray Tracing, an interesting aspect of the system would be the rays represented in the aperture. The observation is done considering boresight and different scan angles. In this representation the number of feed per side is 15, and the magnification

factor is 3. To make the computation less complex, a square aperture is represented, although the true aperture shape is circular.

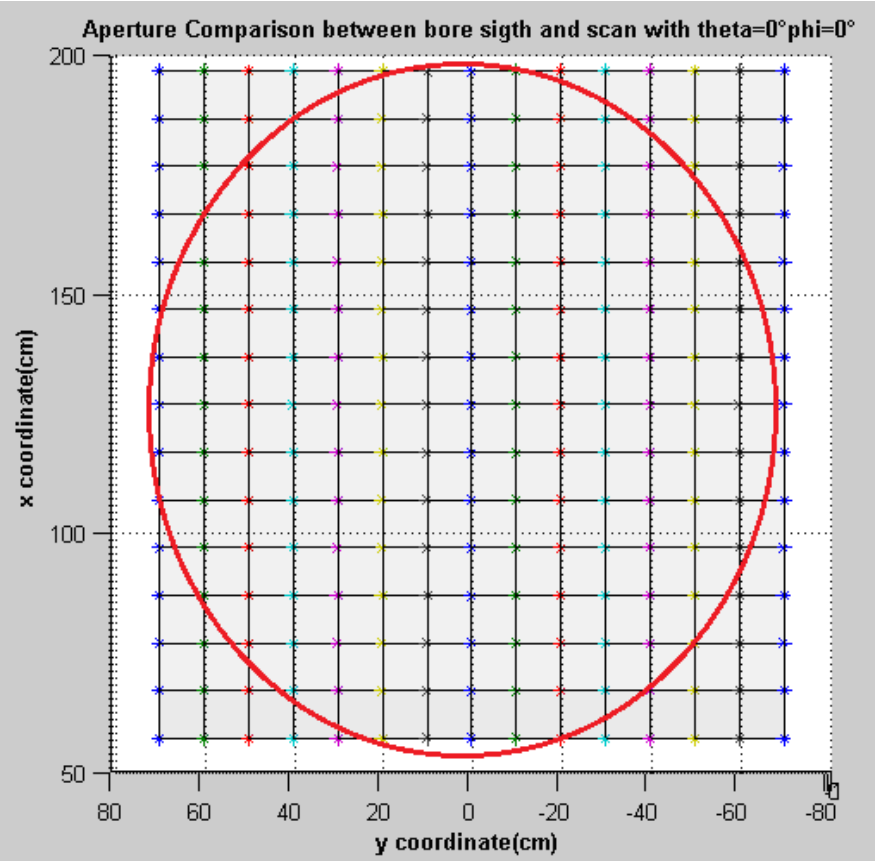

Fig. 3.6: Aperture the boresight case XY plane

As expected and comparing it with Fig. 3.3, there is a magnified mirror image of the array. For the scan we observed that there is an expansion of the image for downward while there is a reduction in the case of upward. The blue part is the boresight case meanwhile the multicolor stars represents the rays in case of scan.

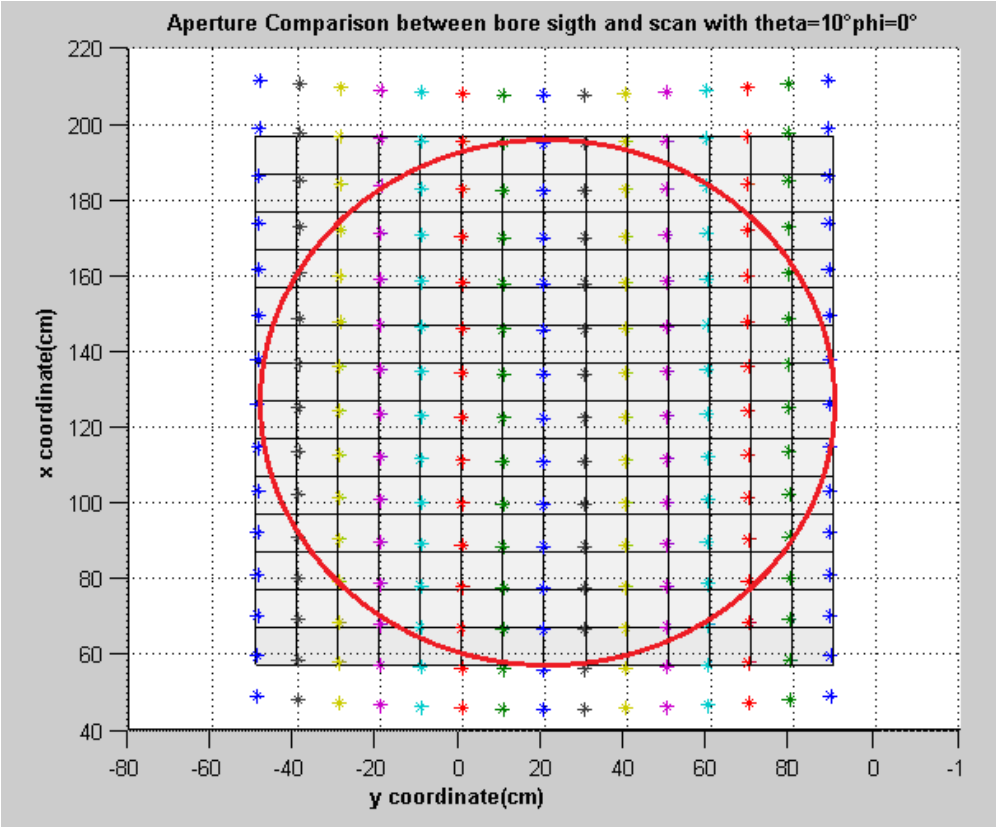

Fig. 3.7: a) Aperture Distribution downward

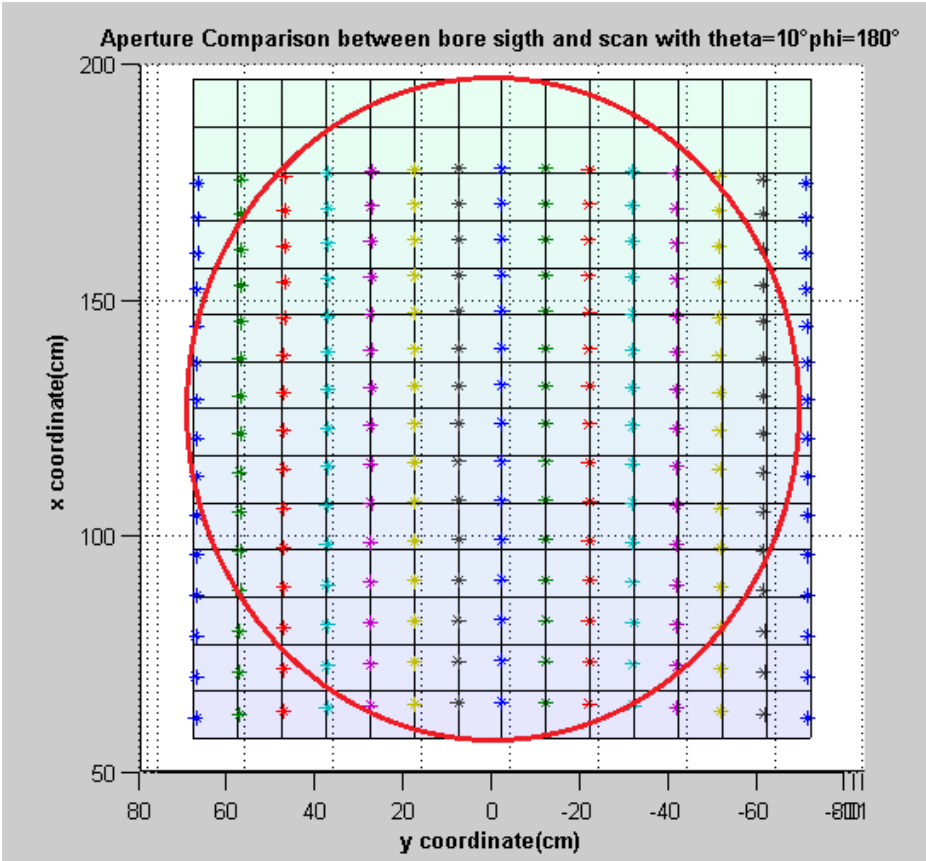

Fig. 3.7: b) Aperture Distribution upward scanning

If we consider the images, provided in [10], the array distribution image in reception, studied by R.A Pearson gives a verification of the observed aperture image. Obviously, the comparison is just qualitative.

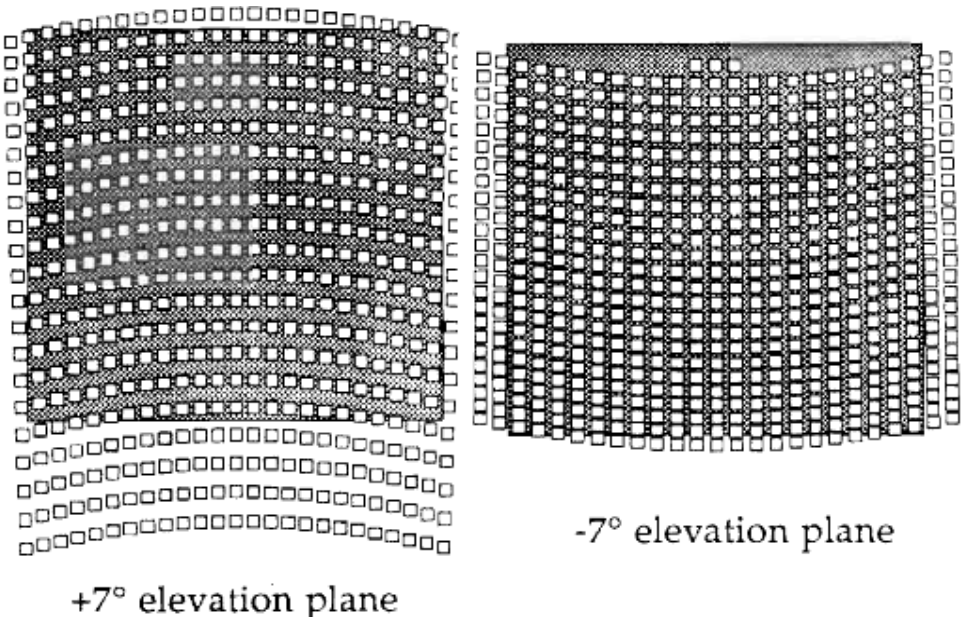

Fig. 3.8: Array Distribution studied by R.A Pearson [10]

The variation in the ray density corresponds to asymmetries in the amplitude distribution produced across the main reflector aperture.

Another important aperture is for the diagonal scan ($\theta = 45^{\circ}$ and $\varphi = 45^{\circ}$).

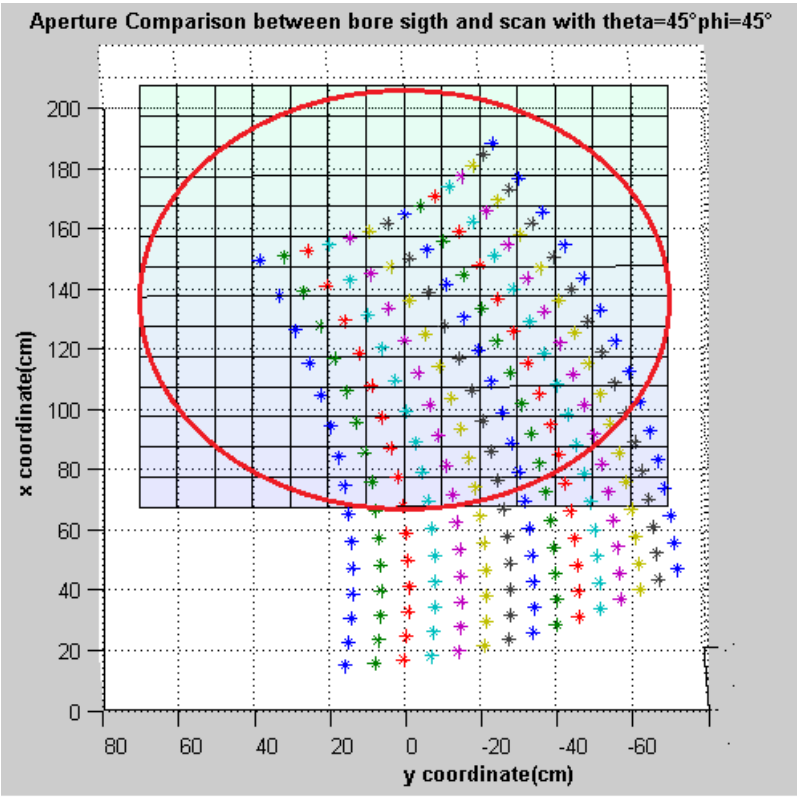

Fig. 3.9: Aperture image, diagonal scanning

If the number of feeds is increased, it is observed that the number of reflected ray increases as can be seen from Fig. 5 in Appendix A. In boresight all the emitted rays are reflected.

3.3.3. System representation

The designed software gives the opportunity to represent the system in 2 dimensions (in two different cuts azimuth Fig. 3.10 and elevation plane Fig. 3.1) and in 3 dimensions. The equation form Chapter 3.2 of ray tracing are used.

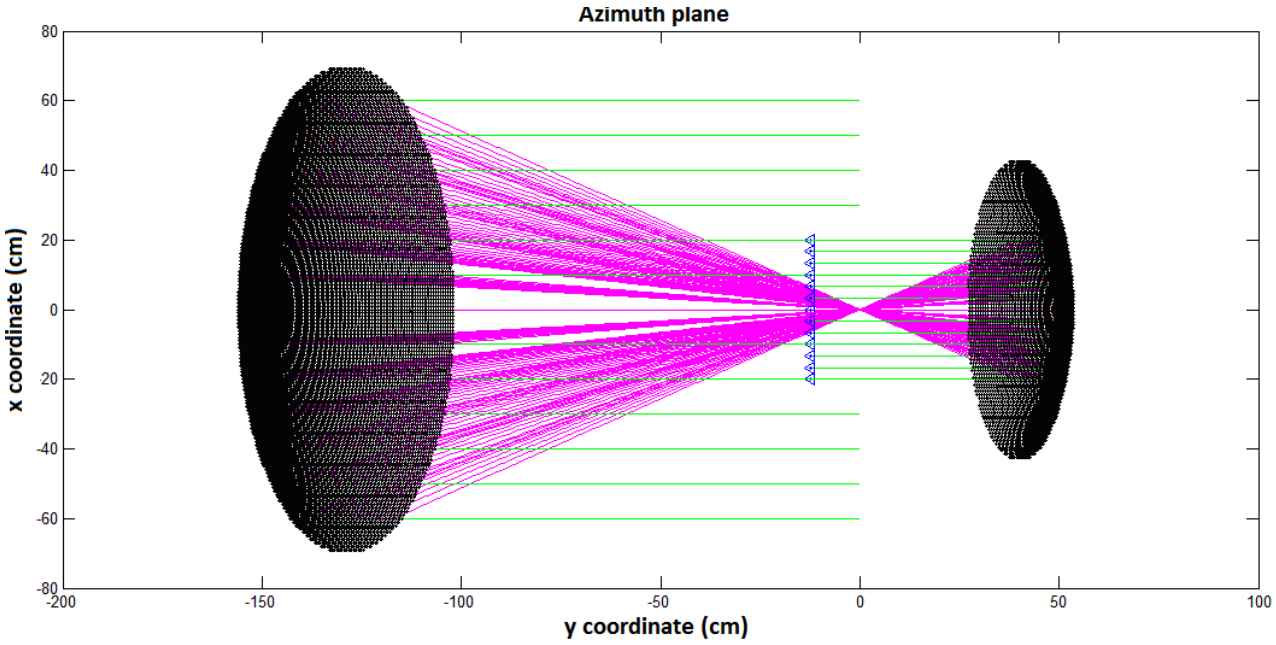

Fig. 3.10: Azimuth plane boresight

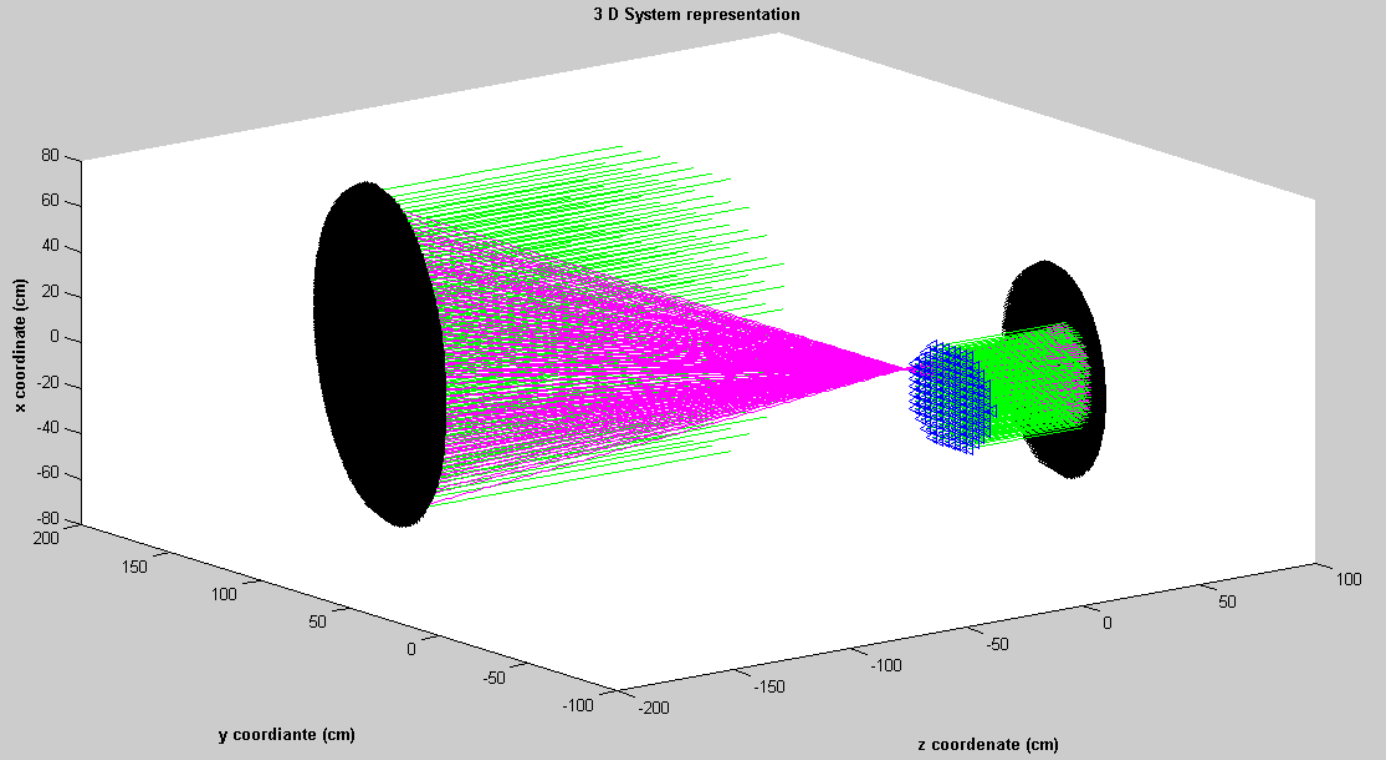

Fig. 3.11: 3D representation of boresight

3.3.4. System representation in case of scan

Scanning the phase array beam from boresight can be represented by a type of rays incident on the sub reflector at an angle to the central axis. The array field is shifted across the sub reflectorso the focal spot is distorted and moved along the focal plane. As can be seen from Fig. 3.13 as the array beam is scanned from boresight the distortion caused by the response of the main reflector in the displaced focus, is approximately compensated by the phase error introduced at the main reflector to the displaced focus. However, the phase distribution as calculated from the overall ray path length has departed to some extent from a plane wave front. The rays across the main reflector aperture are not uniformly spaced, which indicates a slight asymmetry in the amplitude distribution. Interestingly the proportion of the main reflector aperture illuminated is dependent on the array scan angle and direction. Further it is shown that this is the major factor governing the variation in the antenna gain as the beam is scanned through its coverage sector.

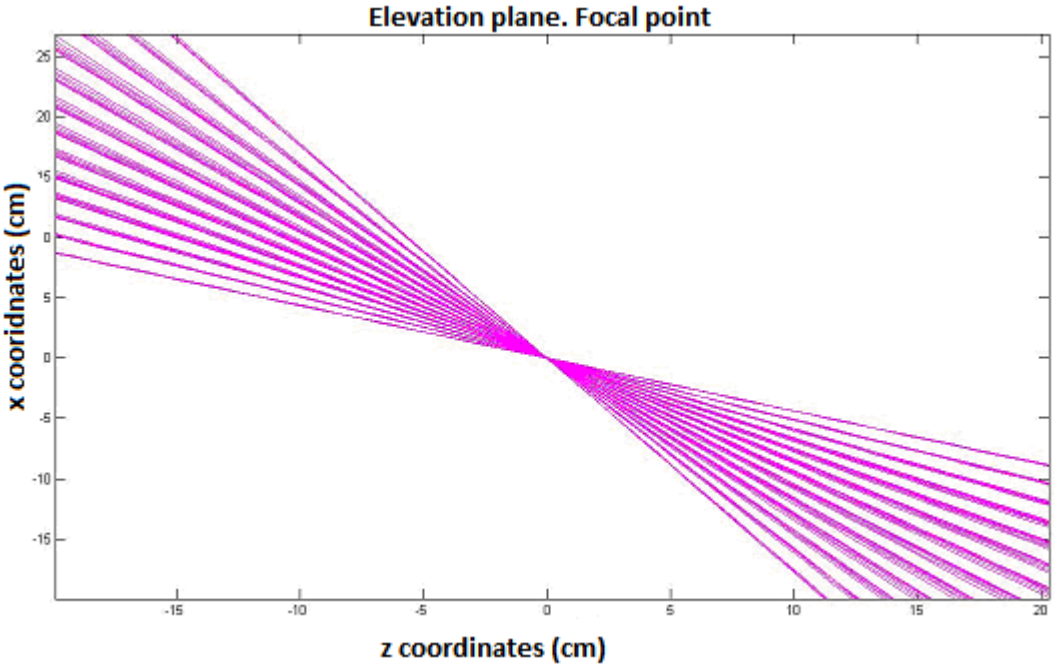

Fig. 3.12: Focal Point boresight case

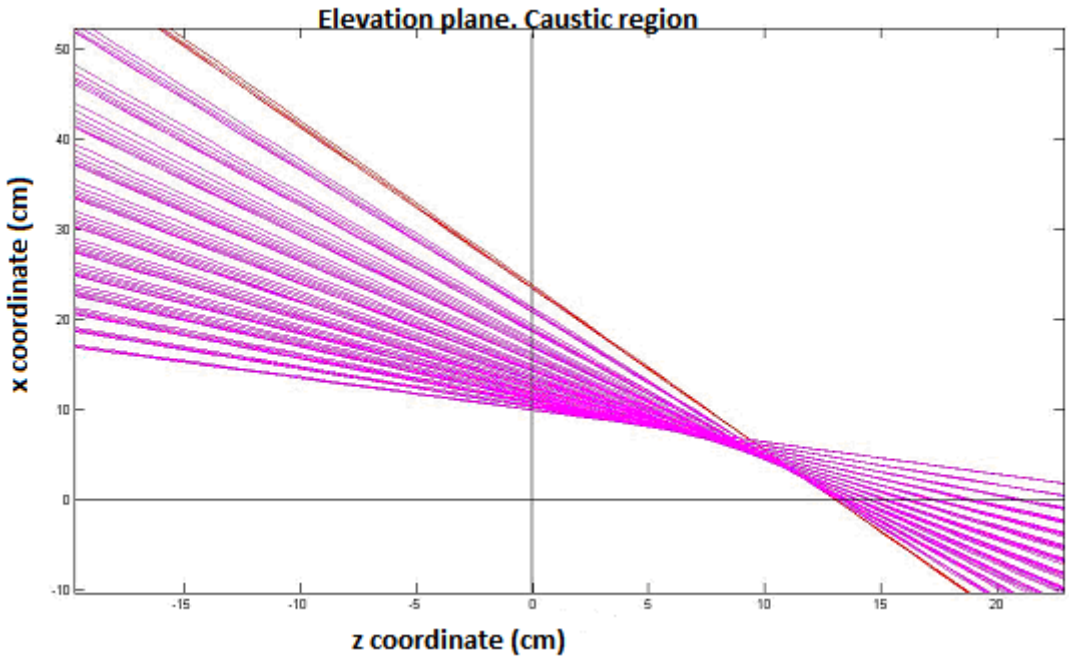

Fig.3.13: Caustic region for elevation scan

The black line shows the focal point, because the coordinate system is placed on it.

Elevation scan

Shifting the phase with θ=10° and φ=0° we have scan in the elevation plane, the rays are directed upwards and after the double transformation as seen in the figure below are pointing downwards.

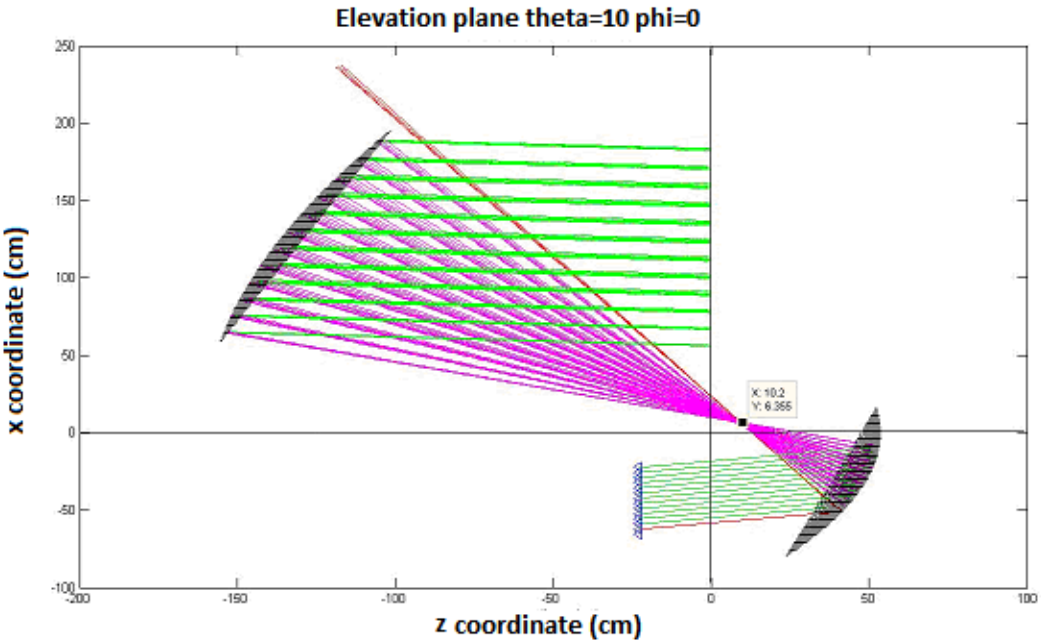

Fig. 3.14: Scan θ=10° and φ=0°

The percentage of spillover is obtained as the ratio between rays that are reflected from the system and those, which go out of it. Percentage of spill-over in this case is 11.6438%. We observe that in this case, just a spillover the main reflector is observed, but for other cases, for example in case of the diagonal scan, there is a spillover not just over the main reflector but over the sub reflector as well.

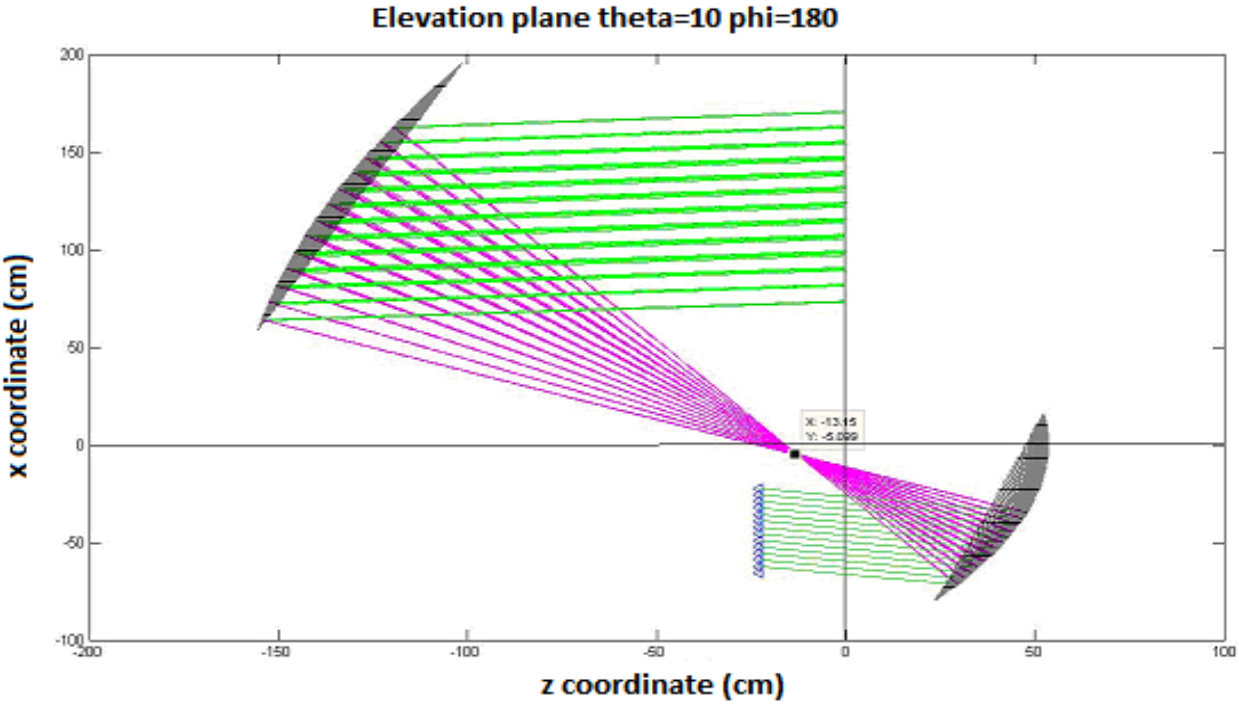

Fig. 3.15: Scan with θ=10° and φ=180°

There is a spillover in the case of upwards meanwhile there is no spillover in the case of downwards, for this reason the upper part of the sub reflector is oversized. An explication to this phenomenon would be the fact that when there is a concentration of the rays in the downward scan meanwhile there is expansion for the upward scan.(Chapter 3.5.1)

In upward the entire main reflector is illuminated, in contrast for the downward where the main reflector is not completely illuminated. This latter will have an effect to the phase distribution and the beam formation.

Azimuth scan

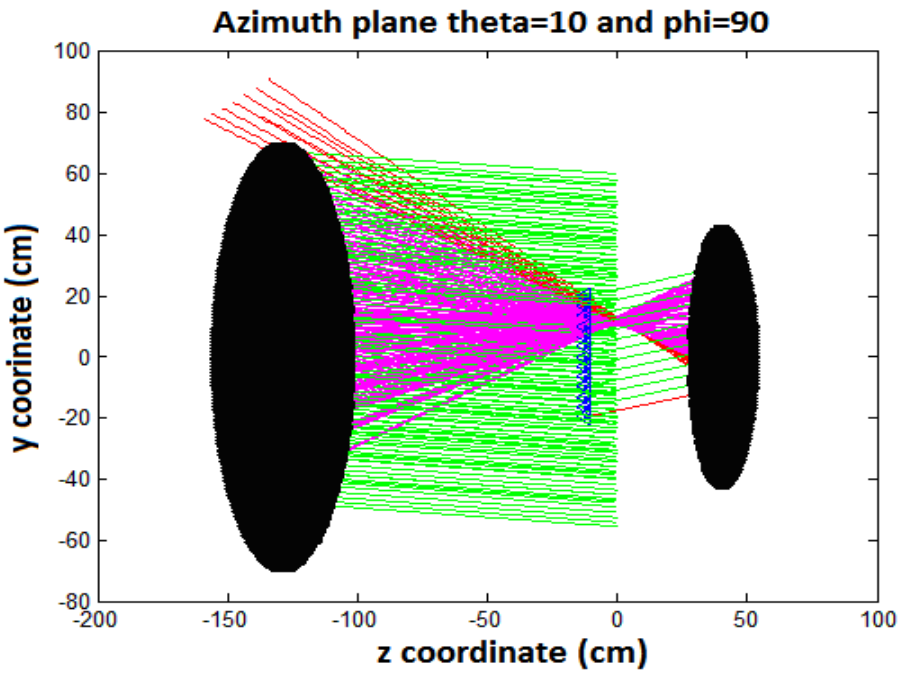

Fig.3.16. Scan with θ=10° and φ=90°

Here the spillover is of 6.8493%. For more scan angles see Appendix B. For the diagonal scan ($\varphi = 45^{\circ}$ and $\theta = 45^{\circ}$) the spillover is of 57,3%.

3.3.5. Phase contributes and Path length

The phase distribution over the main aperture is given by:

$$\Phi(x'_{m,n}, y'_{m,n}) = 2\pi \frac{f_s}{\lambda}[\sin\theta[(xm + \frac{h}{f_2})\cos\varphi + yn\sin\varphi] + \frac{f_m}{f_s}\frac{L_{m,n}}{f_m}] \qquad (3.13)$$

This phase function is simply the sum of the linear phase shift applied to the array and the electrical path length as determined by ray tracing.

Analysis 3D

The path length is simply the sum between the ray procures from the array to the sub reflector and then to the main reflector. In the boresight case the length error is 0°, meanwhile if we apply phase shift, we observe variation of the length. This phenomenon is illustrated plotting the length all over the main aperture. The circular cut is omitted to reduce computational cost.

The path length error is not lineal.

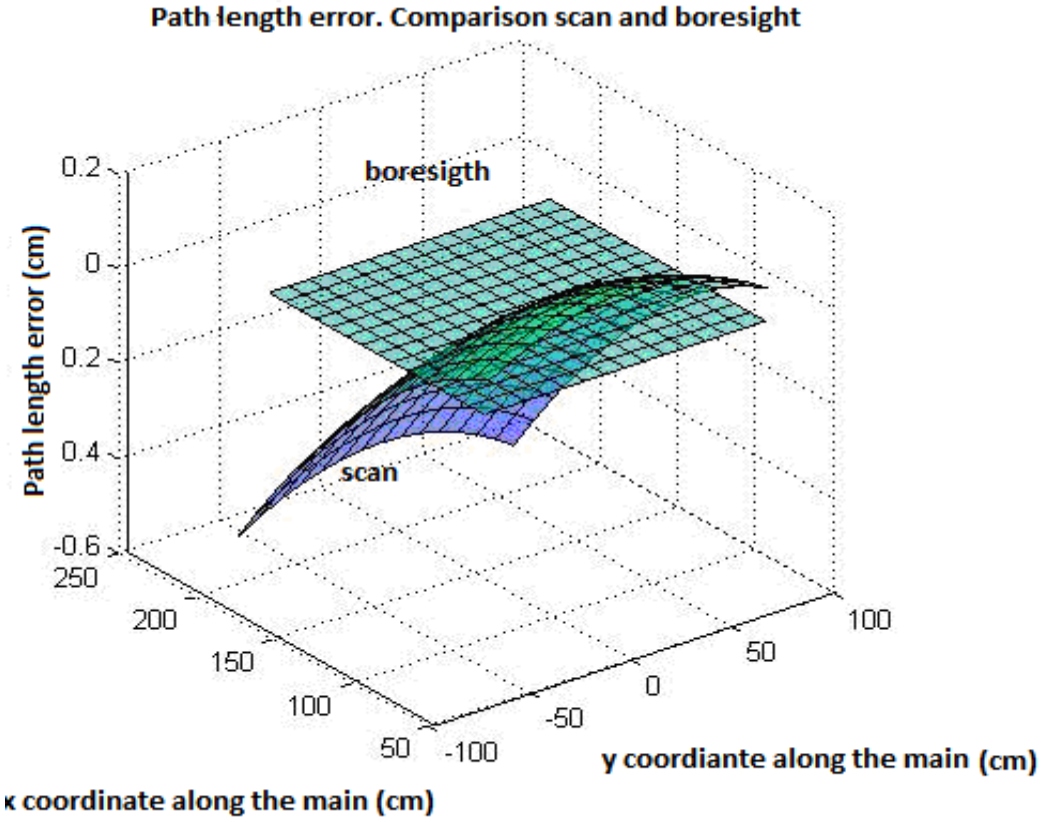

Fig. 3.17: Path length error

The differences between the path lengths for any ray are illustrated. As seen in Eq. 3.12 this path length affects and the phase distribution. The dimensions are in cm.

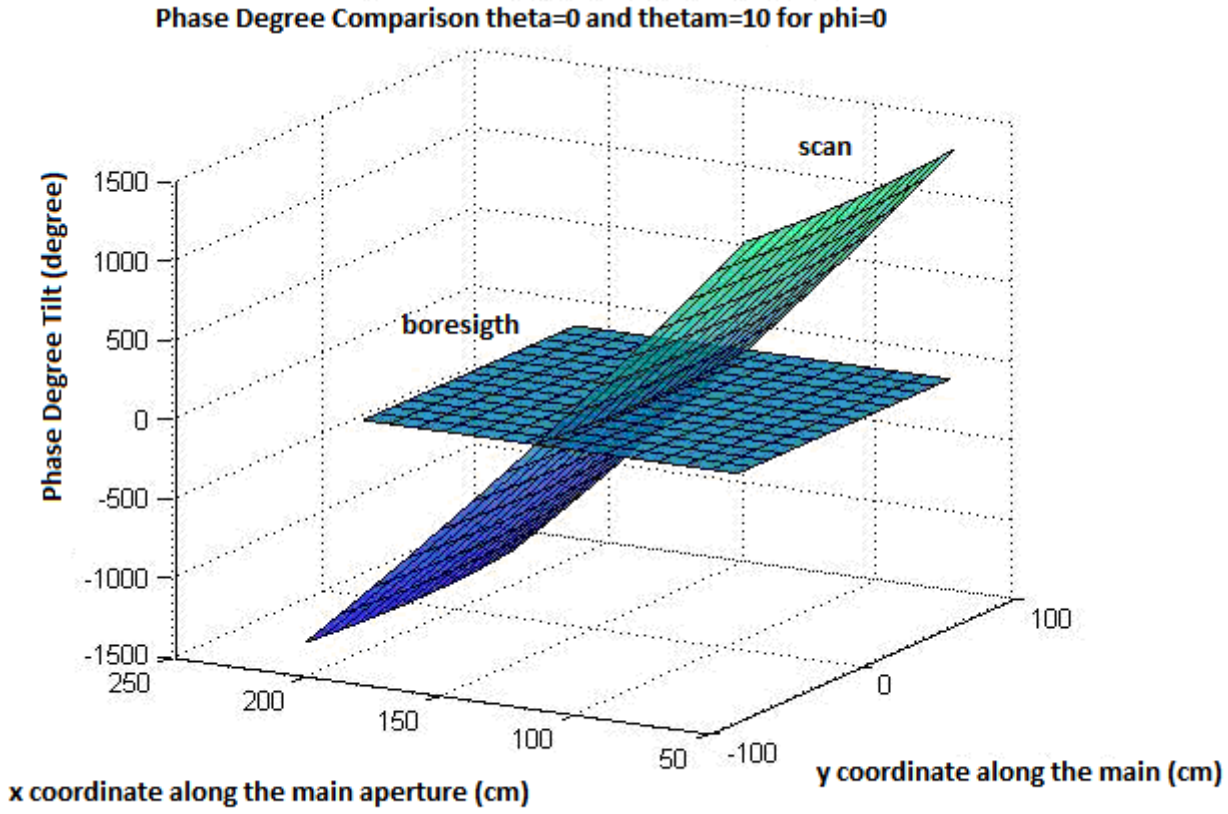

Fig. 3.18: Phase Degree Tilt

The phase tilt is in the direction of scan. In the figure a scan in elevation plane with $\theta = 0^{\circ}$ is considered. The measure is for the entire aperture where the circular cut is not applied. The expression is in degrees.

The **phase aberration distortion** is calculated like the difference between the boresight and the shifted phase. The phase error is not linear, corresponding to a slightly diverging wave front. The whole wave front has been plotted.

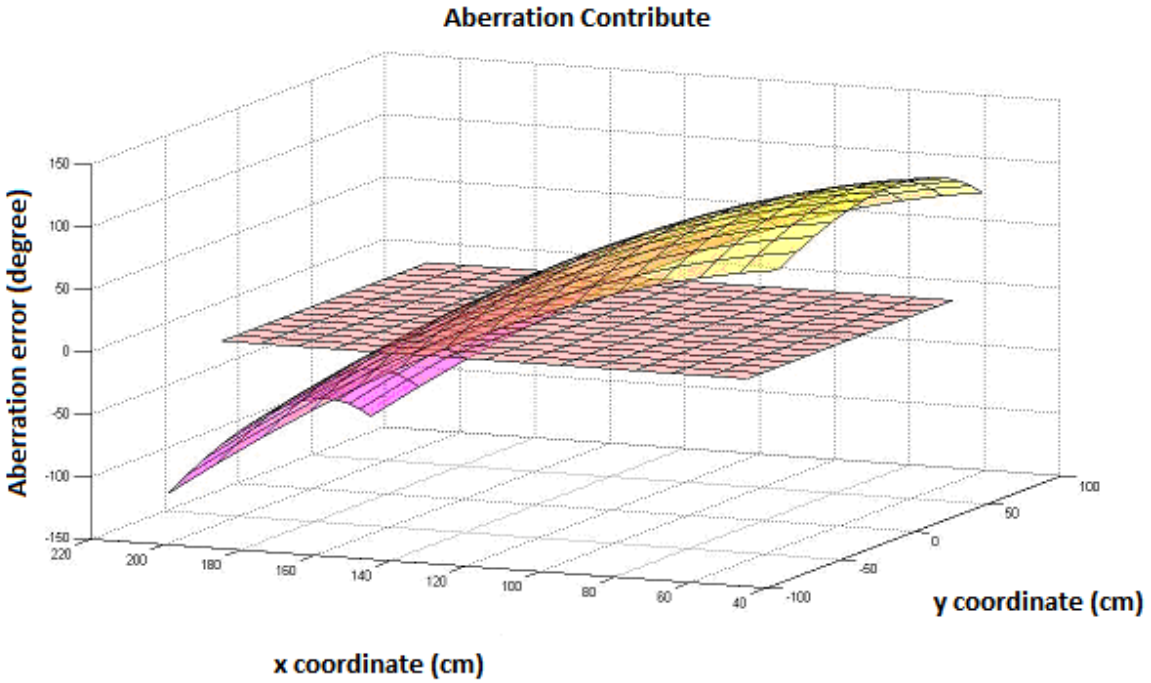

Fig. 3.19: Aberration Contribute Scanning with θ= 10 ° and φ= 0 ° comparison with boresight

As the scan angle is increased the aberrations are major.

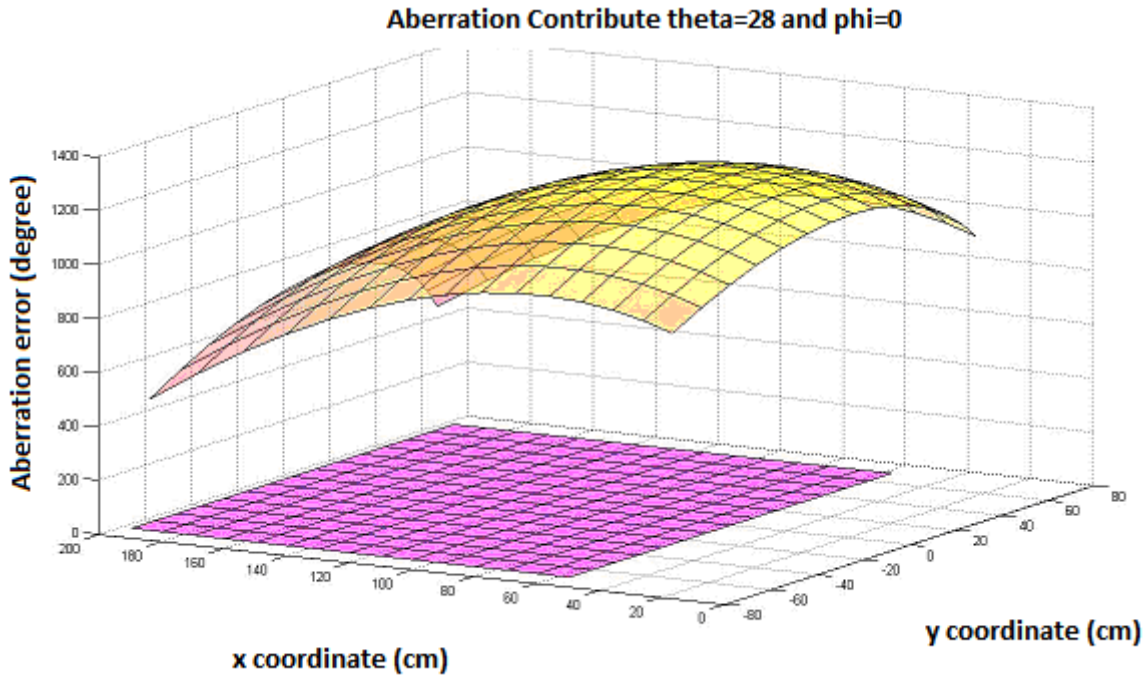

Fig.3.20: Aberration Contribute with θ= 20 ° and φ= 0 ° comparison with boresight

Analysis 2D

The same parameters are discussed but just for the central string of the main aperture. This representation permits a better comparison when the input parameters are changed.
The path length error is represented in cm for the component x. For elevation scan the error is more linear.

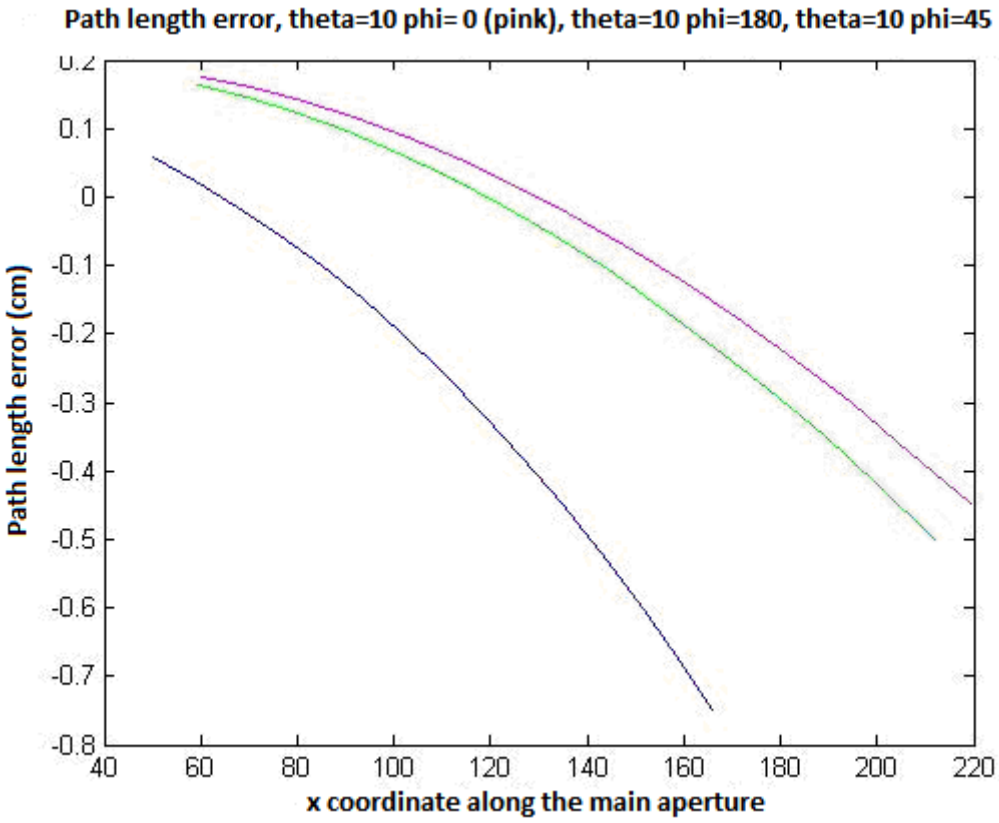

Fig. 3.21: Comparison path length error for different scan angles

The phase tilt is represented in degrees. For better understanding it is represented in the range of 1500 to -1500 degrees. Different scan planes are considered.

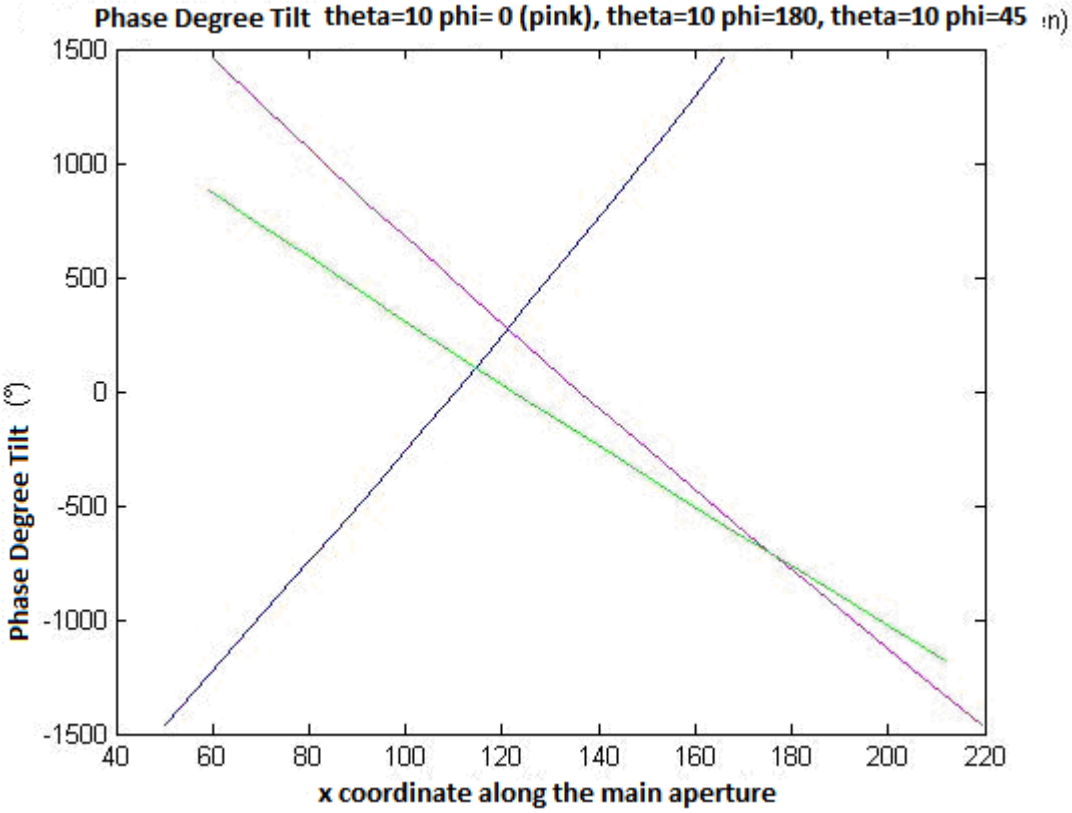

Fig. 3.22: Phase Degree Tilt for different scan angles

The aberrations are calculated in the same way as in the previous chapter.

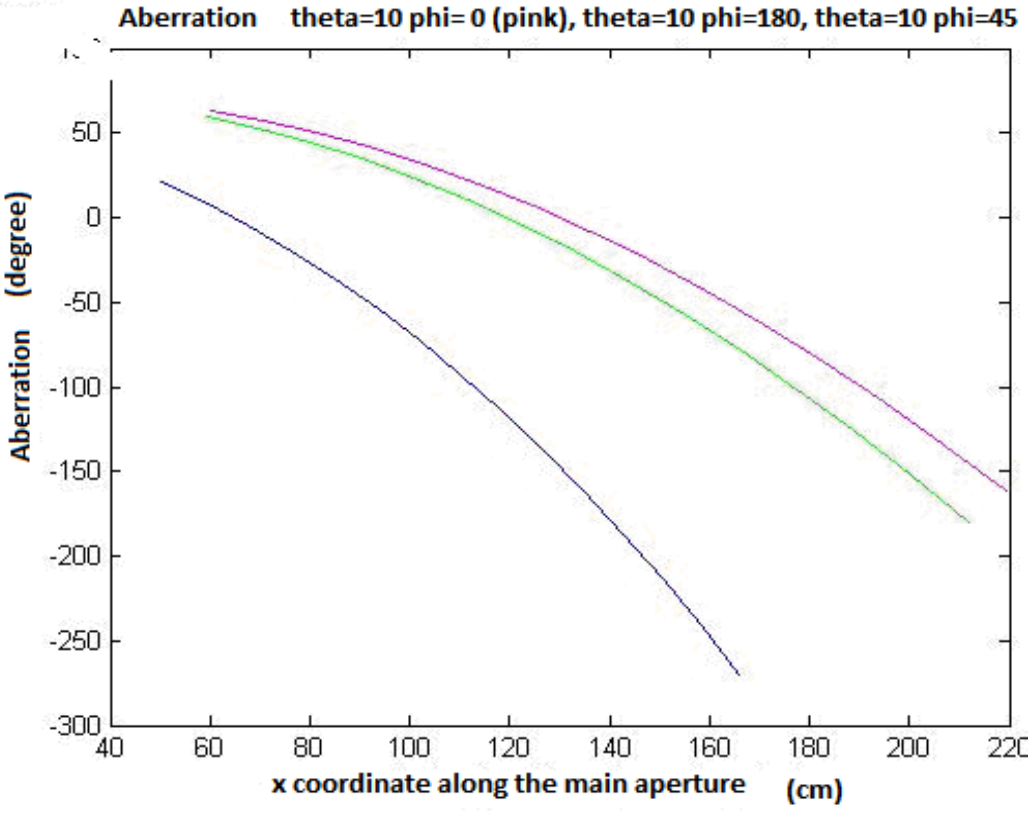

Fig.3.23: Contribution of aberrations for different scan angles.

As a conclusion, the phase tilt or shift is contrasted with the aberration distortion. The observed parameters are considered for the central string of the main aperture. Positively the phase tilt is predominant.

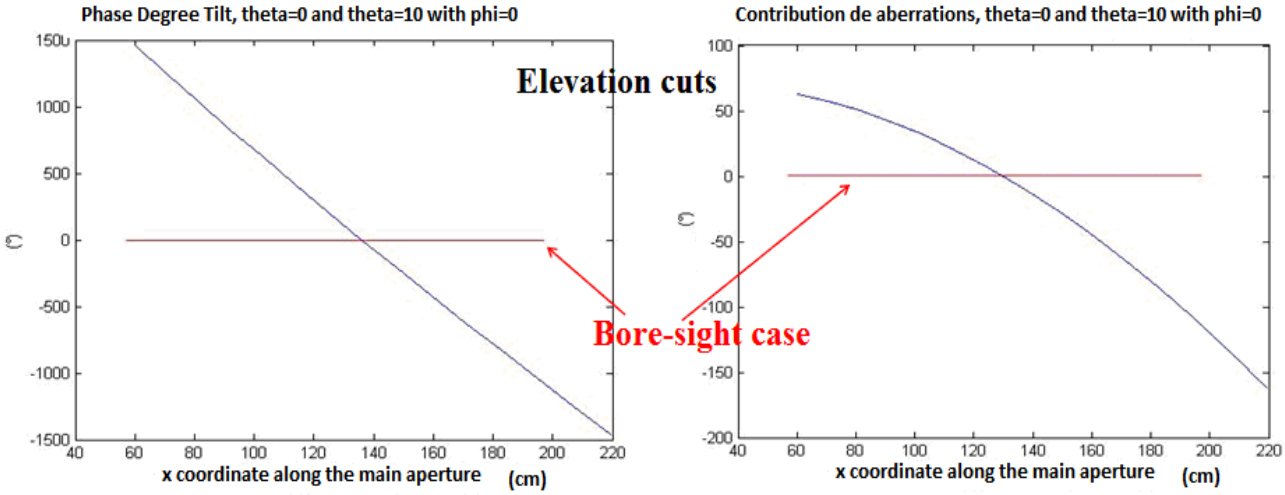

Fig. 3.24: Comparison the phase tilts (right) and the aberration distortion (left)

The f/d and magnification ratios are altered and the corresponding change in characteristics are discussed with respect to phase and path length distortions, the aperture illumination and the ratio of the main beam to phase array scan angle.

Variation of the f/d ratio

It is clear for the larger f/d ratio configuration, that the antenna is longer for a given height and the reflector surface is less curved.

The asymmetry in the aperture amplitude illumination is also reduced with the longer f/d ration. Owning to the longer focal length of the system, there is some blocking of the main reflector by the sub dish. The phase error and the asymmetry in the phase length are all more severe with smaller ratio configuration.

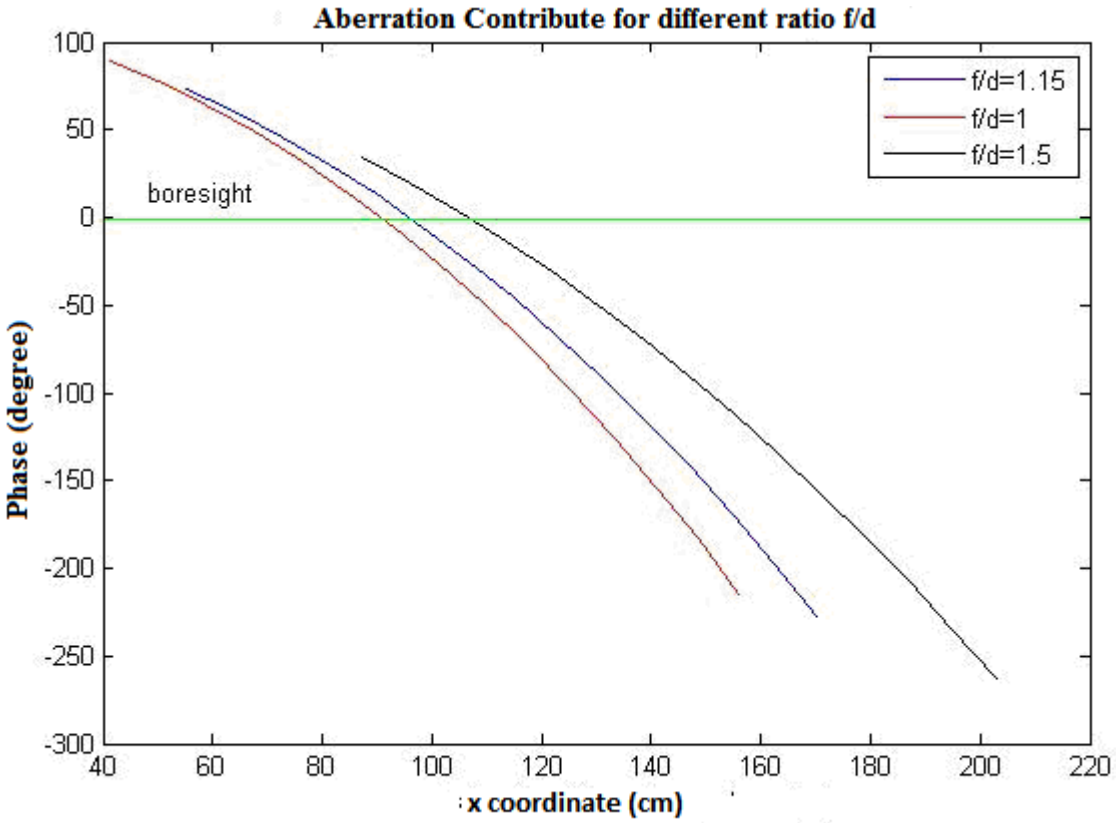

Fig. 3.25: Aberration Contribute for different ratio f/d

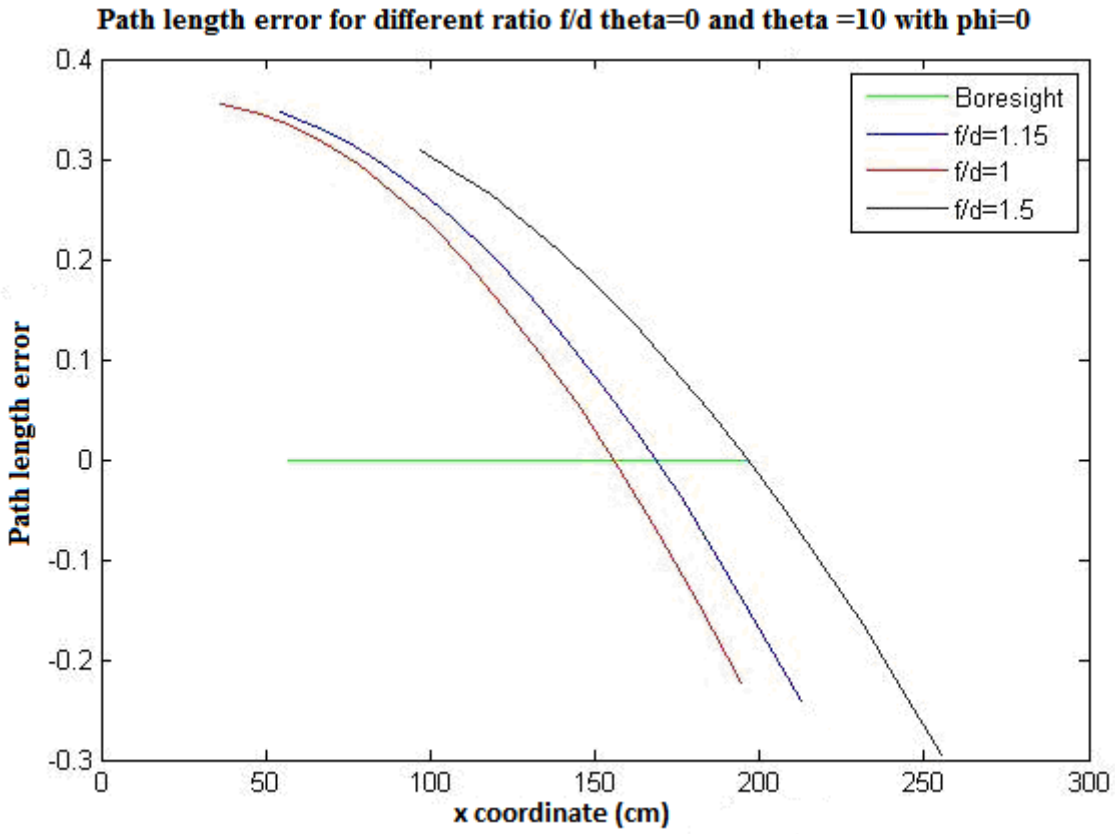

Fig. 3.26: Path length error for different ratio f/d

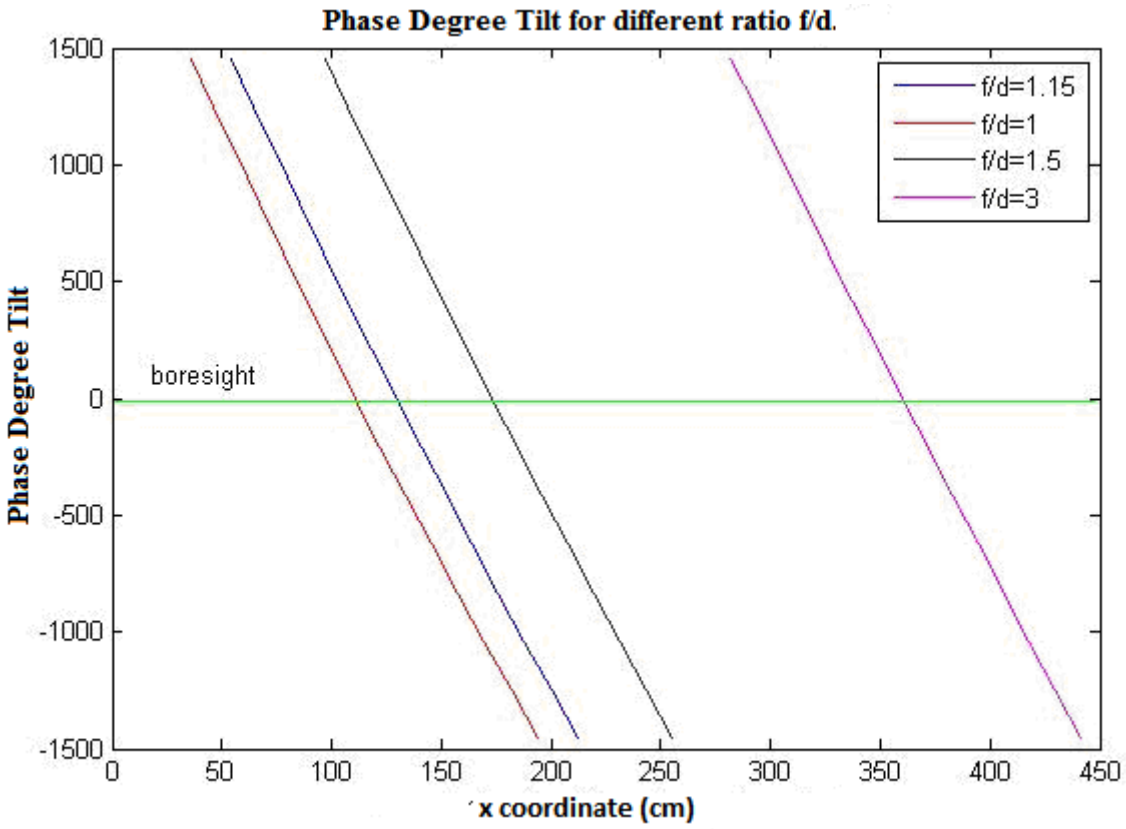

Fig.3.27: Phase Degree Tilt for different ratio f/d.

In conclusion bigger dimension leads to less phase distortion. Nevertheless, as well, the smaller the system is, the more cost effective it is. Therefore a compromise between the two parameters should be considered.

Different magnification factor

Fewer aberrations are observed by increasing the magnification factor, so the phase is more linear, but in this way there are less scan capabilities. As shown in the figure below the phase degree tilt is more linear for M=4 than M=3.

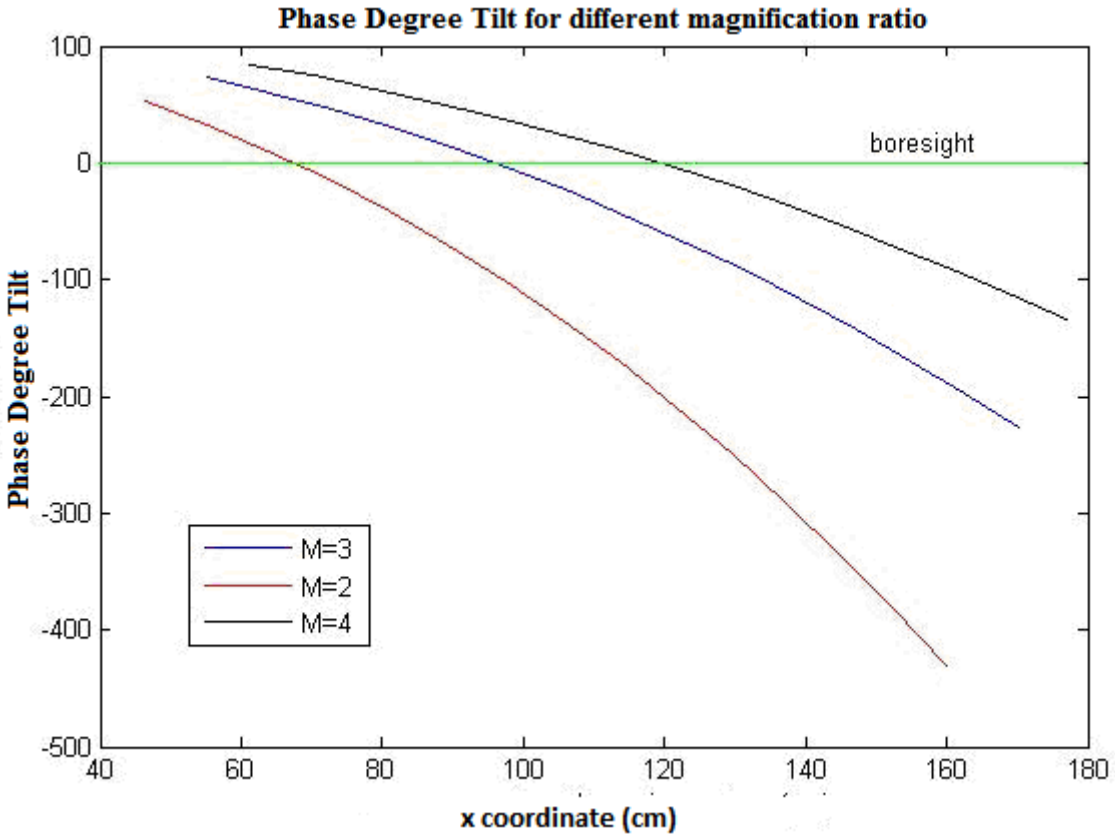

Fig. 3.28: Phase Degree Tilt for different magnification ratio

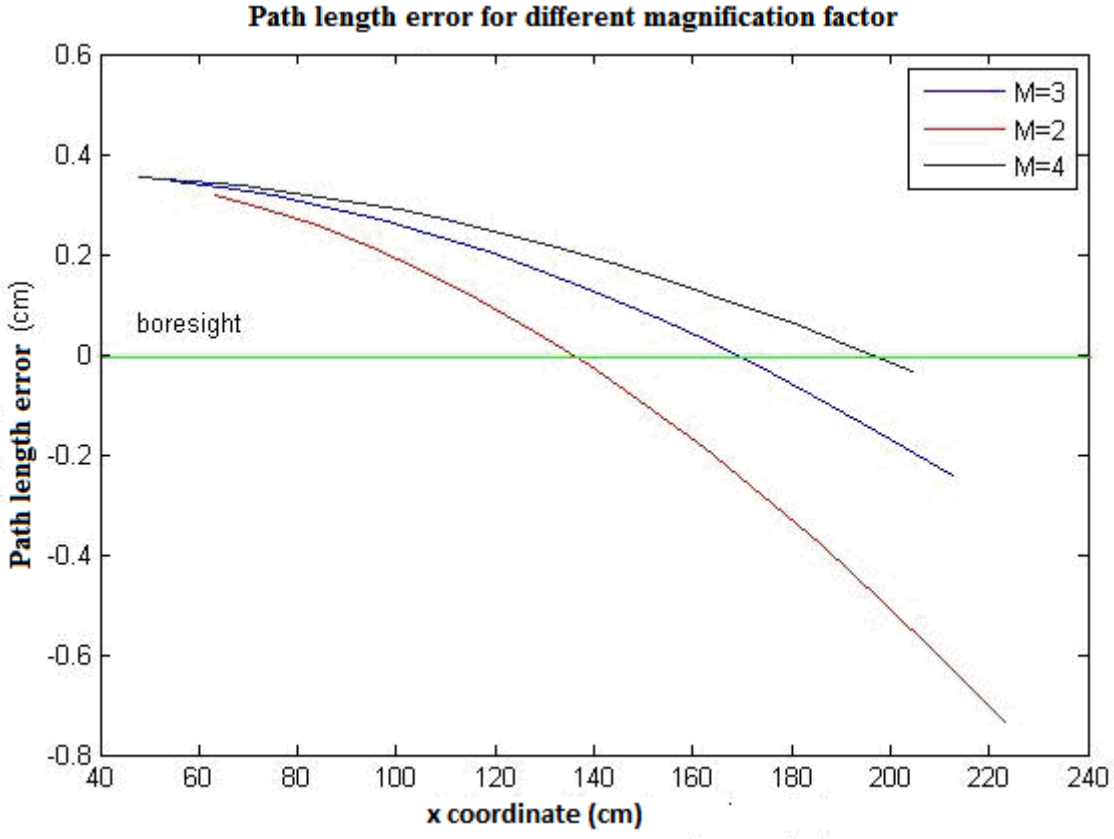

Fig. 3.29: Path length error for different magnification factor

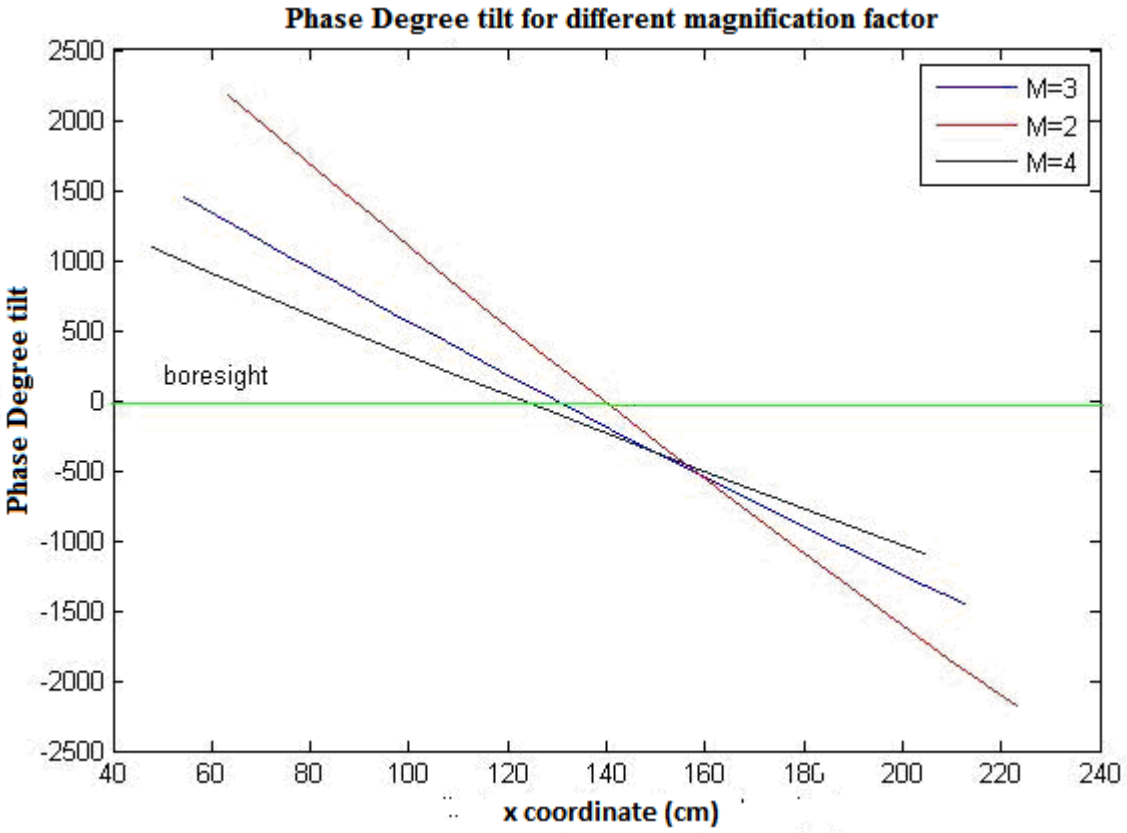

Fig.3.30. Phase Degree tilt for different magnification factor

3.3.6. Scalar Power Pattern

The amplitude distribution over the main aperture planes, denoted $E(x'_{m,n}, y'_{m,n})$ is related to the assumed distribution on the array by conservation of energy in G.O.

Thus,

$$A_{array}E^2(xm, yn) = \frac{fm}{fs} A_{aperture}E'^2(x'_{m,n}, y'_{m,n}) \qquad (3.14)$$

Where A_{array} is the area between elements in the array, $A_{aperture}$ is the area between rays after the double reflection in the aperture. Notice that $\Delta x \Delta y$ and $\Delta x'_{m,n}\,\Delta y'_{m,n}$ are the areas between elements of the array and the area formed from the passing reflected rays in the aperture. In the first case the area is a square area. See Fig. 3.3 for array configuration and Fig.3.15 for aperture configuration. The components are given from the equation below:

$$\Delta x'_{m,n} = x_{m+1}' - x_m' \qquad (3.15)$$

$$\Delta y'_{m,n} = y_{n+1}' - y_n'$$

The intensity of the field across the main reflector aperture is not uniform, this is because (i) the amplitude is proportional to the square root of the ray spacing and (ii) the rays at the top of the aperture are more widely spaced then those at the bottom.

The scalar pattern $P(\theta',\varphi')$ is computed with the expression from scalar diffraction theory in summation form:

$$P(\theta',\varphi') = A_{aperture} E'(x'_m, y'_n)\, e^{-j\Phi(x'_{m,n}, y'_{m,n})}\, e^{j2\pi \frac{fm}{\lambda} \sin\theta'(x'_{m,n}\cos\varphi' + y'_{m,n}\sin\varphi')} \qquad (3.16)$$

By combining the equations and omitting unnecessary constants:

$$\left|P(\theta',\varphi')\right| = \left|\sum_{m=1}^{M}\sum_{n=1}^{M} \sqrt{A_{aperture}} E(x_{m,} y_n)\, e^{-j\Phi(x_{m,n}' y_{m,n}')}\, e^{j2\pi(fm/\lambda)\sin\theta'(x'_{m,n}\cos\varphi' + y'_{m,n}\sin\varphi')}\right| \qquad (3.17)$$

$E(x_{m,} y_n)$ is the amplitude of the electric field in the array, as expressed in equation (3.19). As it was explained in Chapter 2.4.1 the far field is the Fourier Transform of the field in the aperture. In the double summation m represents the row and n is the column index. The array factor of the image of the array in the aperture is considered and simplification of the element factor is done in this formula.

If we consider uniform distributed amplitude, for example $E(x_{m,} y_n) = 1$, the obtained scalar power pattern is shown below:

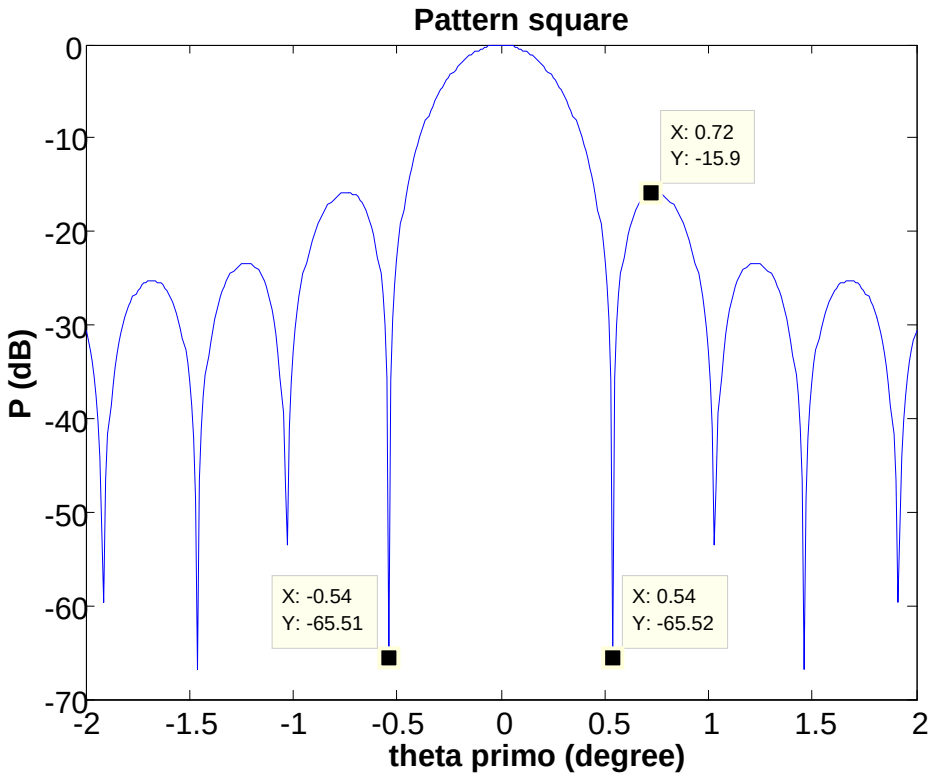

Fig. 3.31: Single Pattern Boresight without taper

It can be seen that the beam width is wider than the imposed 1 degree. This is due to the fact that the main diameter is smaller than a circle with diameter 139λ, as the array configuration is not a perfect circle (see Fig 3.3). The side lobes are at -15.01dB and according to the theory [8] we have the result that the side lobes must be at -17dB. We can observe that if we increase the number of arrays, we have more similarity to the theorical model which means that the beam is narrow and the side lobes are at -16.69dB, as shown in the figure where N=30.

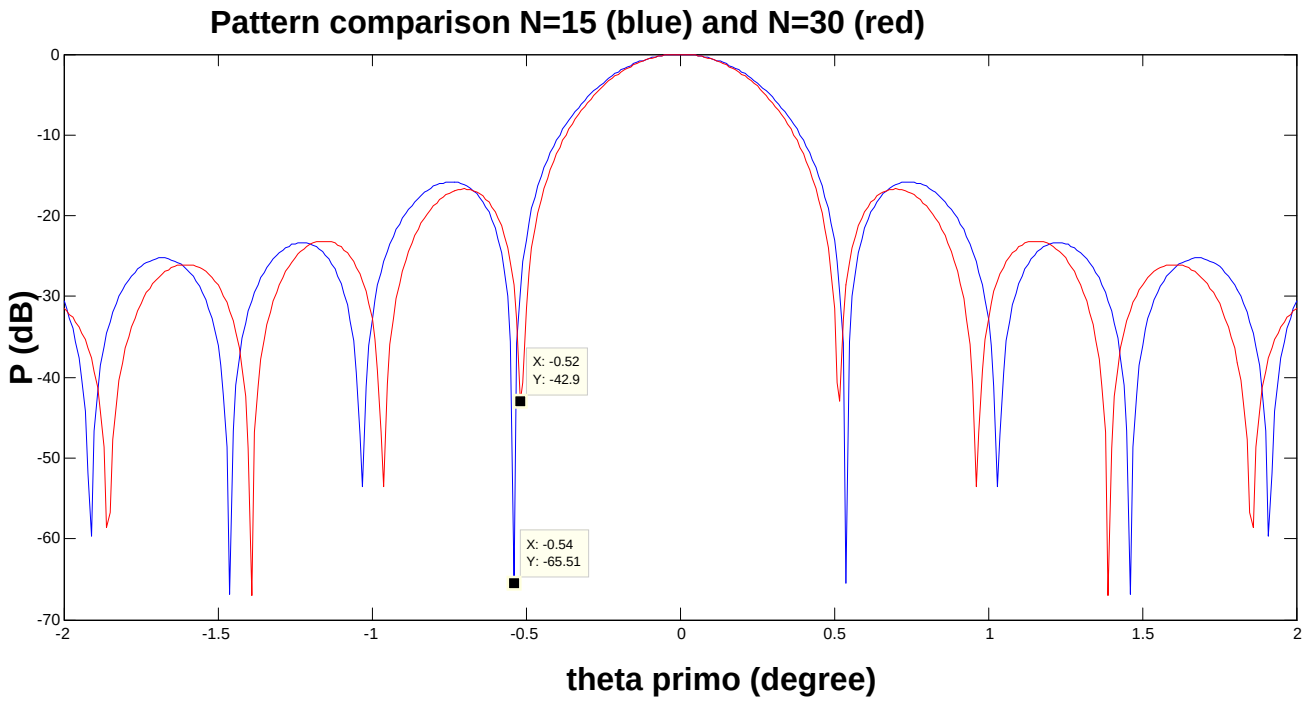

Fig. 3.32: Comparison of Pattern. Different feed number

In this case the ray number is equivalent to the array number. In case of scan, the rays, which are spilled over, are excluded. The far field scalar power pattern is represented considering the formula:

$$20\log(|P(\theta',\varphi')|)\,.$$

Taper

The parameters K and C determine the form of the amplitude distribution applied to the array. The expression used is:

$$E(x_{m,}y_n)=\left\{1-\frac{\left[\left(x_m+\frac{h}{f_s}\right)^2+y_n{}^2\right]}{\left(\frac{d}{2f_s}\right)}\right\}^K+C \qquad (3.18)$$

In the software program different values of K and C can be determine with the following prompt:

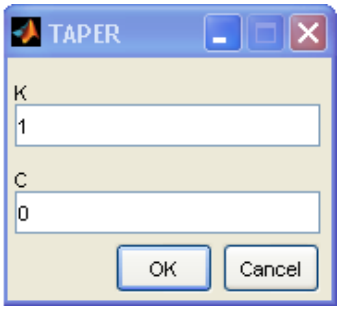

Table 3. Software prompt for K and C

If we consider the taper, we observe the next figure:

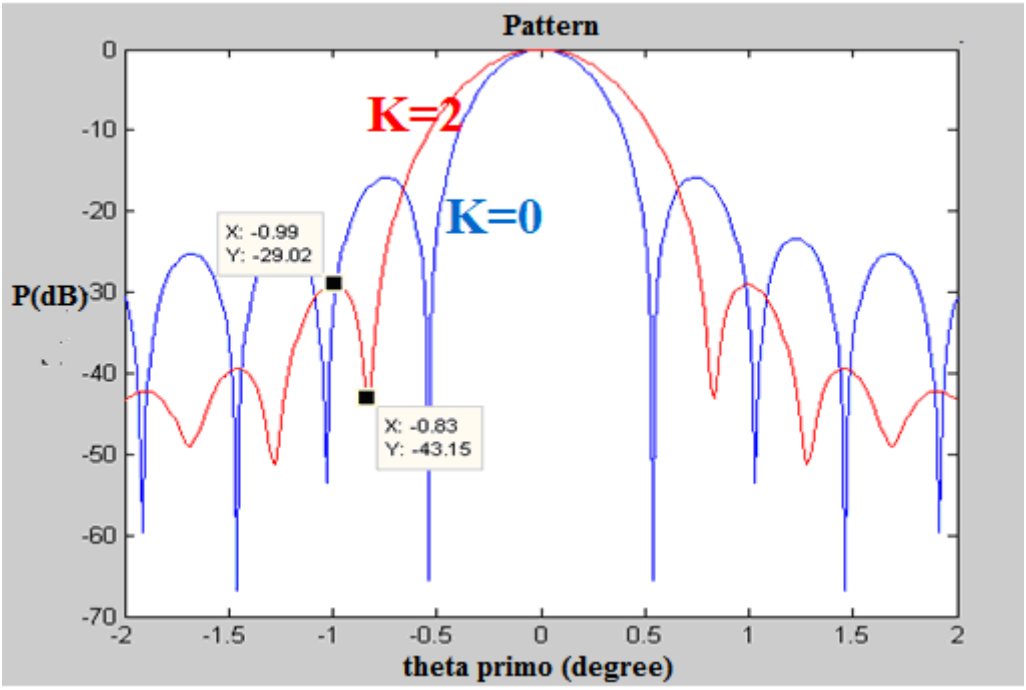

Fig. 3.33: Comparison K=2 and K=0

Hence K=0 and C=0 correspond to a uniform distribution. For K=1 and K=0 is a $(1-\rho^2)$ distribution. The taper is applied to the field distribution over the feed array. The pattern is generated applying the equation for scalar pattern (3.17).

3.3.7. Grating Lobes

But to illustrate the concept of grating lobes, a plot where N=15 and N=30 is represented.

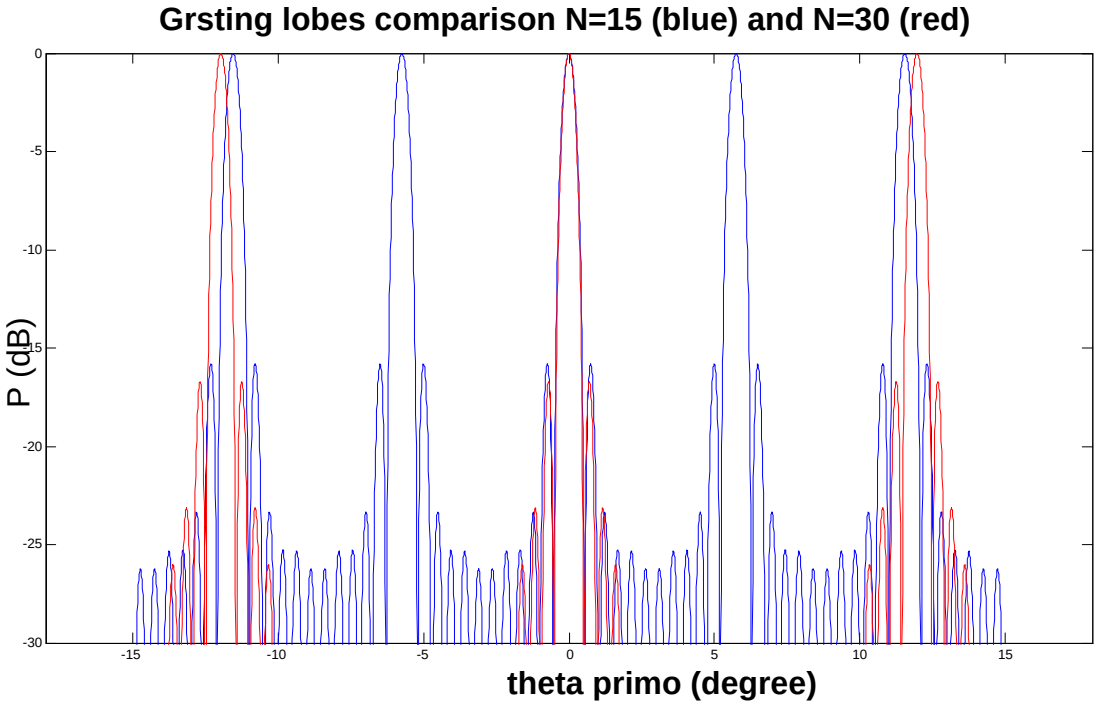

Fig. 3.34: Pattern for N=15 and N=30

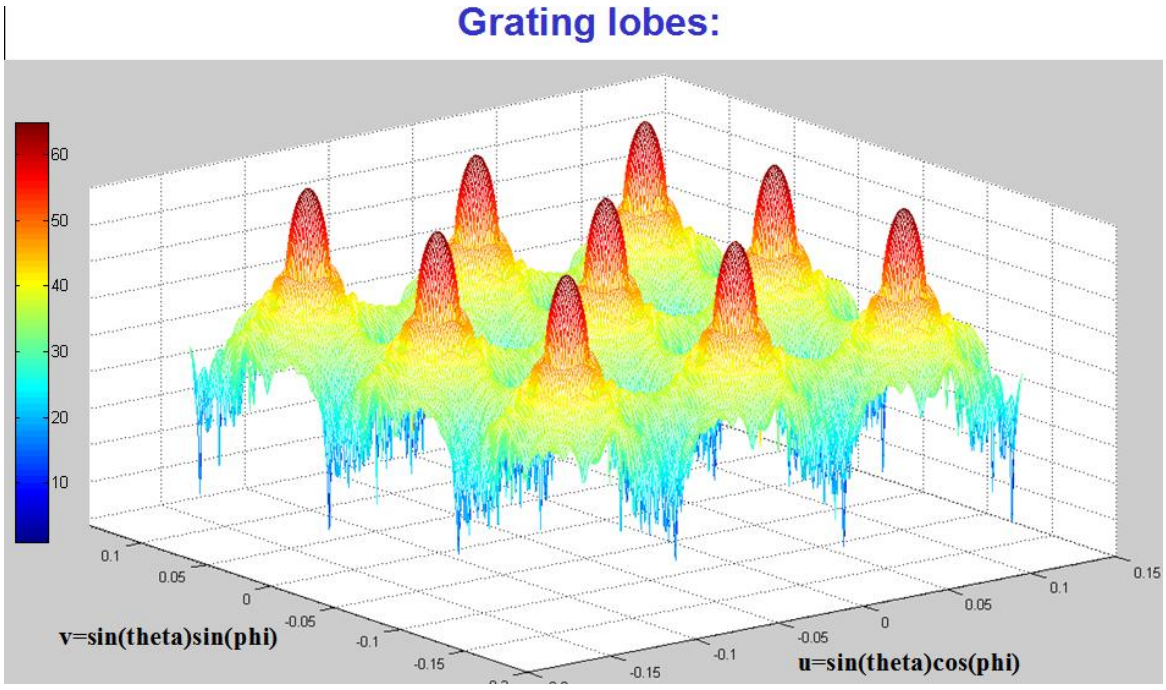

Fig. 3.35: 3D Power Pattern

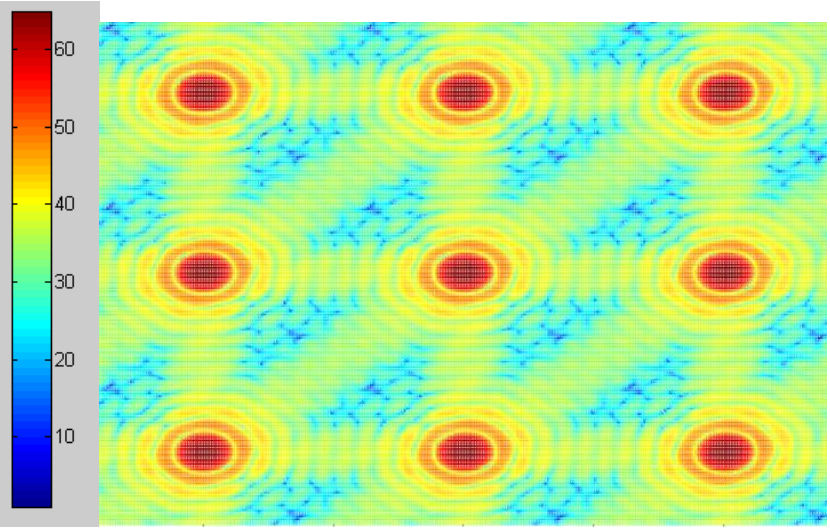

Fig. 3.36: 3D Power Pattern Azimuth plane

The representation is done considering the Eq.3.18 in tension.

3.3.8. Scalar Power Pattern in case of Scan

If the pattern is evaluated for $\theta = 10^{o}$, the relation between θ' and θ of the equation (3.1) is verified with small error due to the aberrations discussed in the previous Chapter 2.

The phase error will increase the antenna side lobes, small differences are observed in the two sides of the main beam. Nevertheless, this does not cause serious beam distortion.

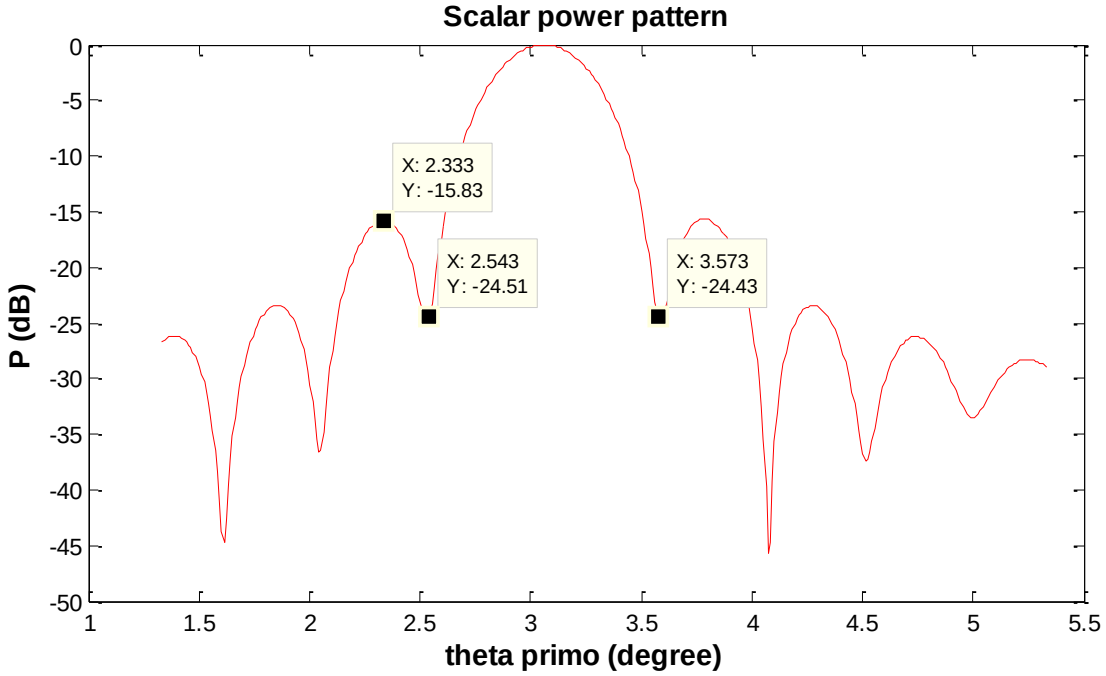

Fig. 3.37: Scanning with θ= 10 ° and φ= 0°

There is a significant difference in the beam, with each direction of scan. For the beam scanned downward there is a substantial broadening of the main lobe and a corresponding loss in gain. For the downward scan though the energy has bunched up over a smaller region of the main reflector. This effect becomes more pronounced towards the top of the dish. The overall ray density has almost doubled.

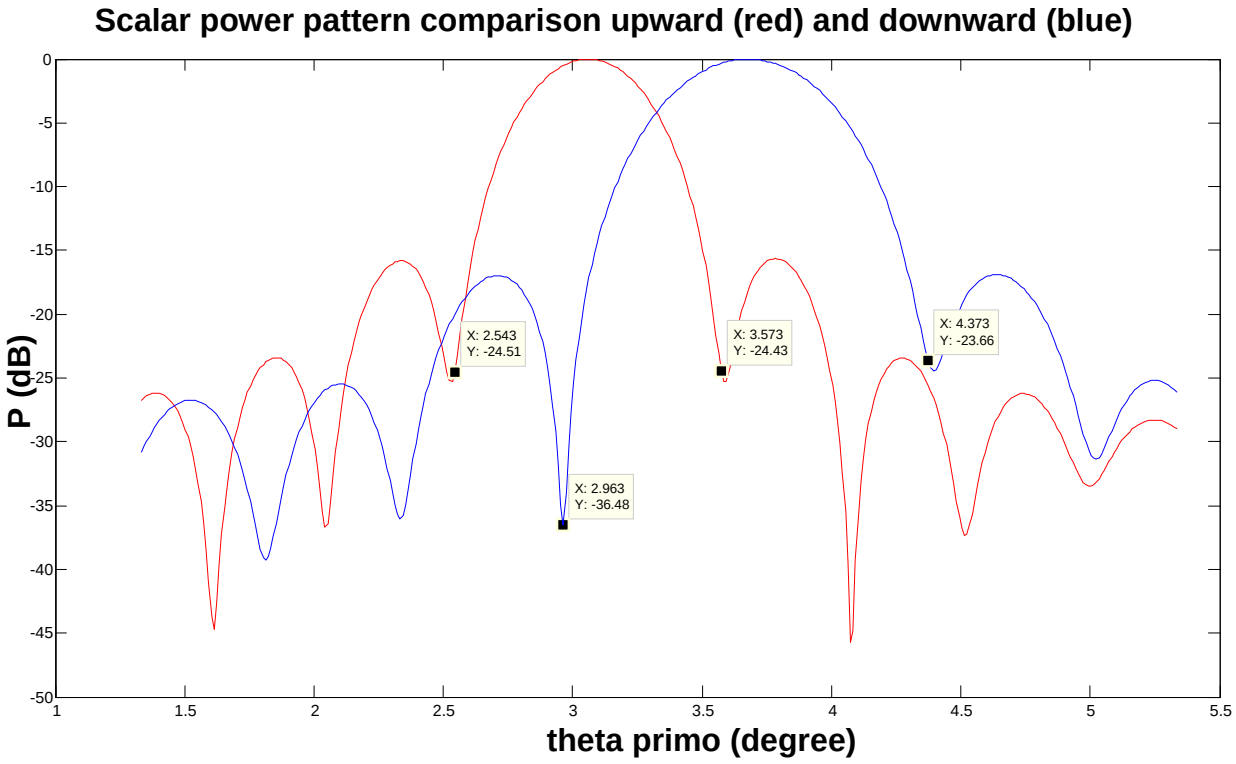

Fig. 3.38: Comparison scanning with θ= 10 ° changing φ= 0 ° upward (red) to φ =180 ° downward (blue)

3.3.9. Multiple power patterns

To illustrate the scan the pattern is represented for angle θ incremented with step of 4° for upward ($\varphi = 0^{\circ}$) is from 0 ° to 29 ° and downward ($\varphi = 180^{\circ}$) is from 0 ° to 25 ° . The punctual line fixes the level where beam width is at -3dB and as said before it is the angular separation of the direction in which is the halved mean beam far field pattern. For the negative part of the figure $\varphi = 0^{\circ}$ and for the positive $\varphi = 180^{\circ}$. For the plotted patterns correction angles are used which means that the linear relation between the incident angles and the reflected ones is not conserved. More precise study is provided in Chapter 3.3.10.

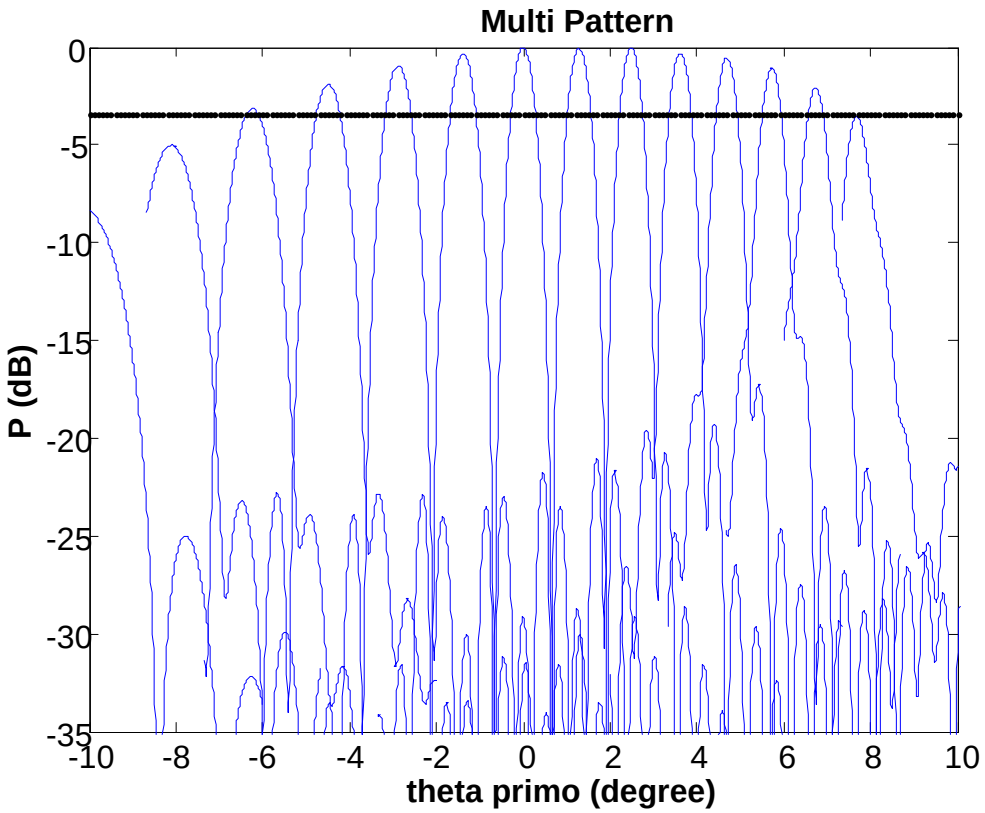

Fig. 3.39: Multiple beam for different scan angles of θ

There is a 3dB of gain loss between the boresight and downward with θ=28°. To be sure of the result, it is contrasted with the graphic of the paper [1] and the conclusion is that they are the same.

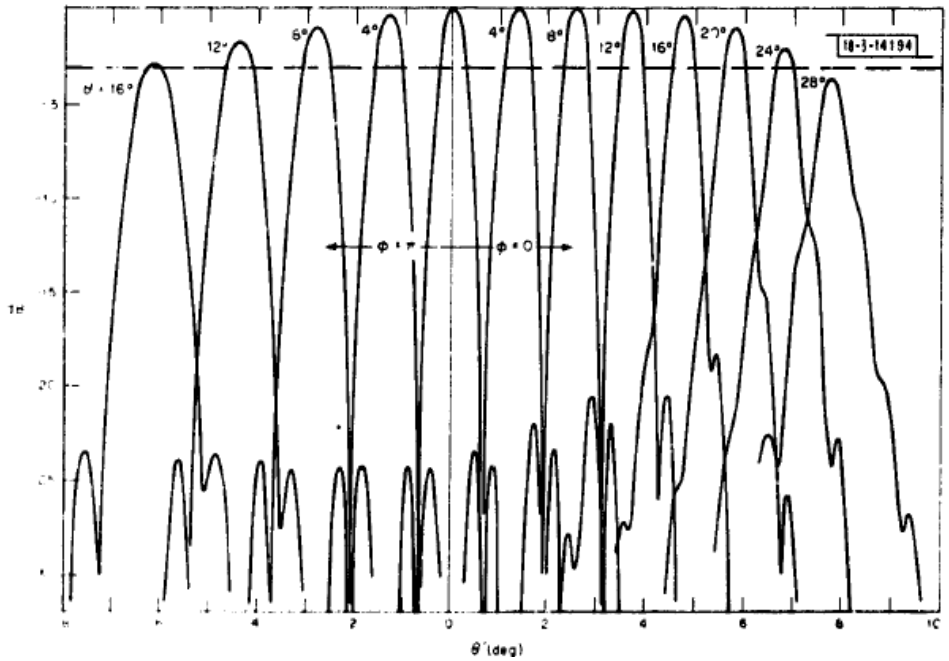

Fig. 3.40: Multiple beam from paper of D.W.Fitzgerald for K=1 and C=0

6The excitation was made using linear phase excitations and a uniform amplitude distribution. As it is to be expected the elevation beam shows a clear symmetry in terms of the overall variation in gain and beam width as a function of deflection angles. The azimuth symmetry leads to an equal fall-off in the gain as the beam is scanned in each direction from boresight. From the fist main lobe beam through the main and to the last one there is a drop in gain of 4.6dB. However, the beam width remains almost constant throughout the coverage sector. The next two figure describe elevation and diagonal scan.

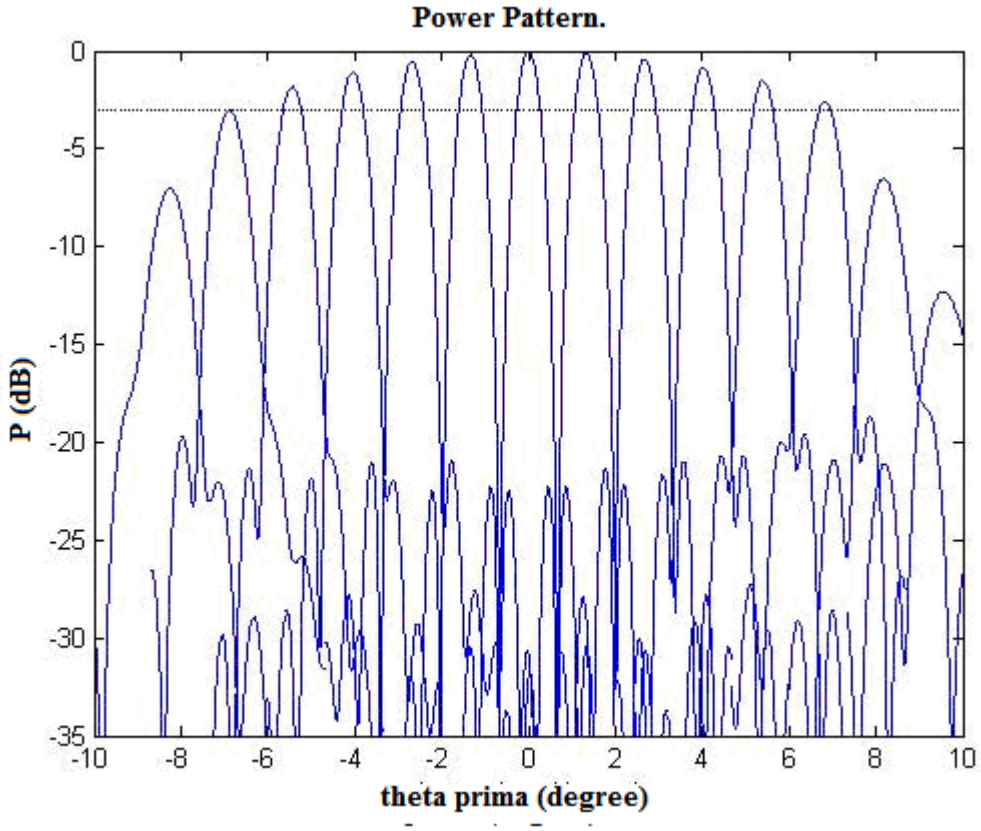

Fig. 3.41: Azimuth scan φ=90° and φ=270°

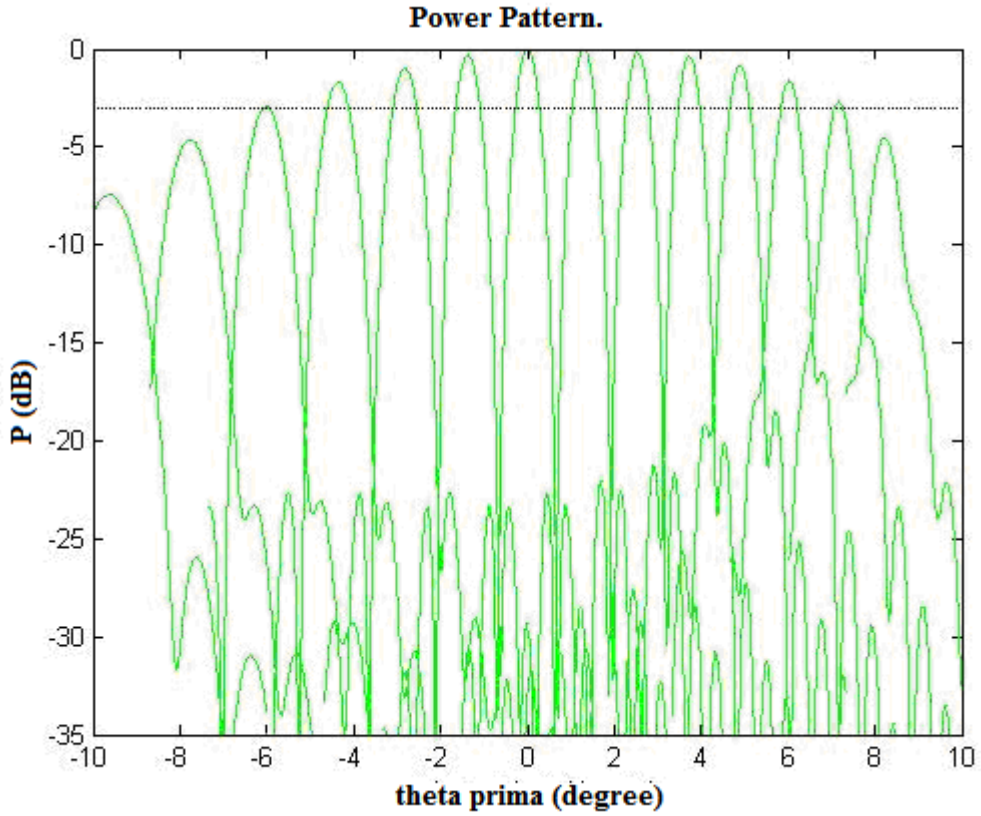

Fig. 3.42: φ=45° and φ=225° Diagonal scan

The implication is that scan range is limited by phase aberrations. For φ=π Fig.3.41 , the beam broadens with very little distortion as scan is increased, indicating that spillover and aperture reduction are principal causes of scan loss. Diagonal plane patterns (see Fig 3.42) are very similar to the vertical ones. The patterns in the horizontal plane – the only plane of symmetry – apparently have a measure of both spillover and phase aberrations. Note that in this plane the patterns are well - defined and usable beyond the -3dB scan-loss. Computed patterns with different distributions show similar characteristics.

3.3.10. Nonlinearity and phase distortion

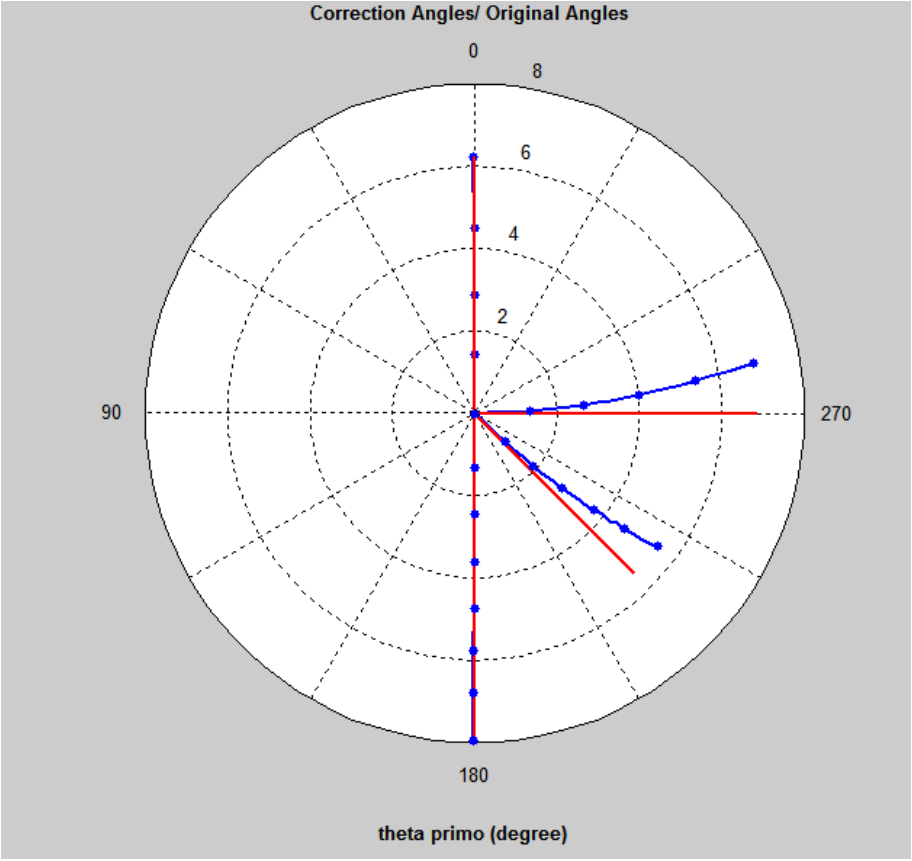

Fig. 3.43: The projection of coordinates θ' and φ' showing nonlinear relationship between coordinate system and scan-coverage contours for M=3

In boresight beam (θ=0°), a real image is created at the focal point of the reflectors. All power transmitted by the array is contained within an area on the order of a wavelength in diameter. We have linear relationship for the reflected angles as Eq.3.1. As the array is scanned in the plane φ=π, this high-energy concentration, although somewhat diffused, approaches the top edge of the array. The stars correspond to different θ.

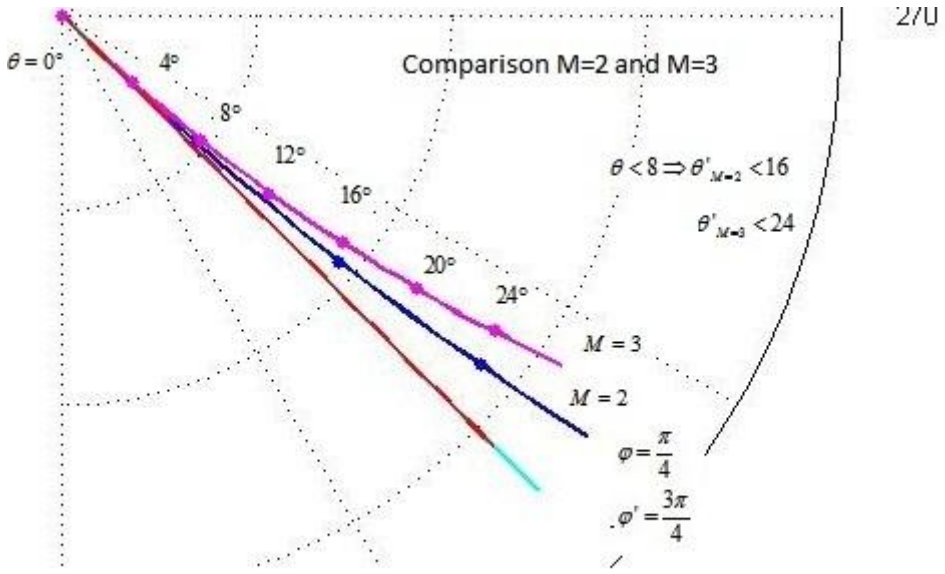

a)

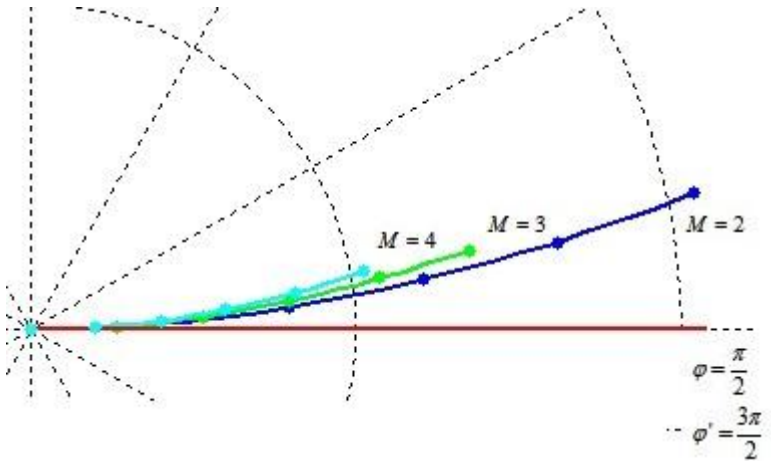

b)

Fig. 3.44: Comparison M=2, M=3, M=4 a) φ =45° b) φ =90°

The above figure shows the comparison between the different magnification factors. It is clear that for some angles there is an expansion of the curves. We considered cases for θ<8°. For boresight there is no difference between the expected angles and the observed ones.

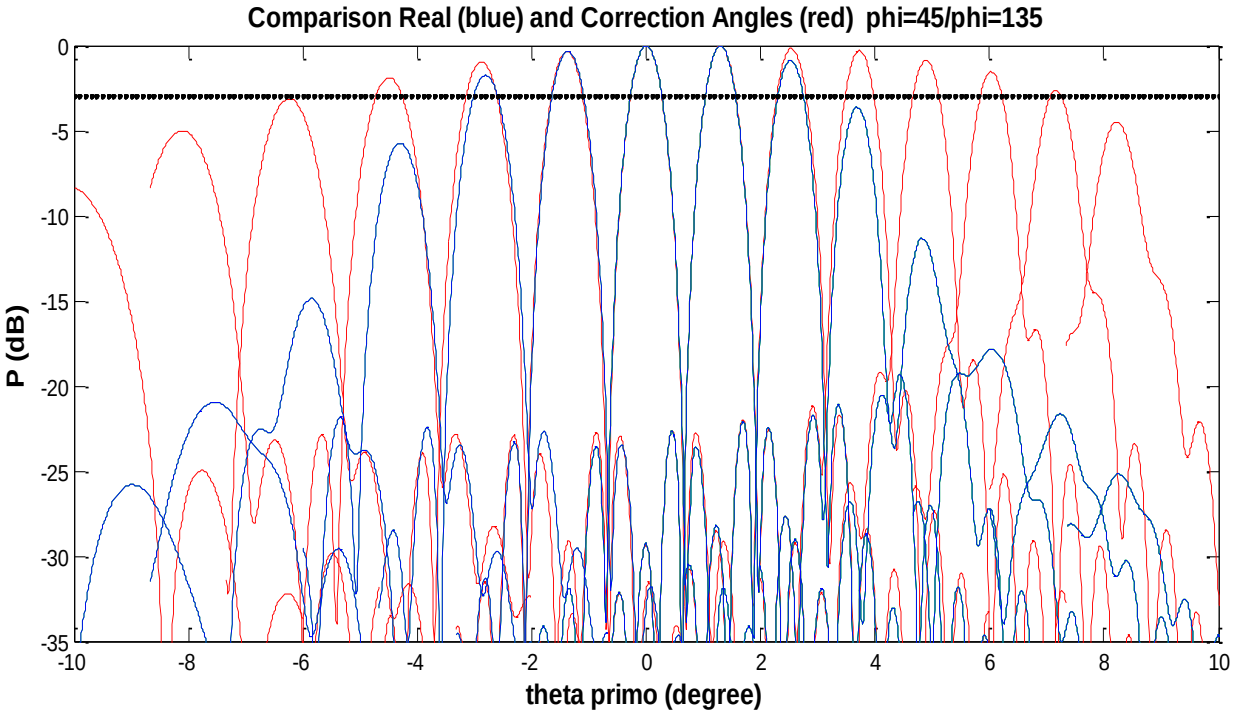

Fig. 3.45: Distortion in the pattern due to angles non linearity

In Fig.45 the patterns for diagonal scan are represented for M=3: φ=45° for θ=0°:25° and φ=135° for θ=0°:28° with the linear relationship for θ' and φ' (blue line). There is clear evidence of pattern distortion. Over most of the usable scan range the relationship between θ and θ' is not linear. Therefore we represent the pattern with the correction angles (red line). Those angles are calculated searching the maximum value for θ' in a range of 20° around θ'.

In this plane the half power beam widths are constant, even beyond the -3dB scan-loss point, but there is clear evidence of phase distortion.

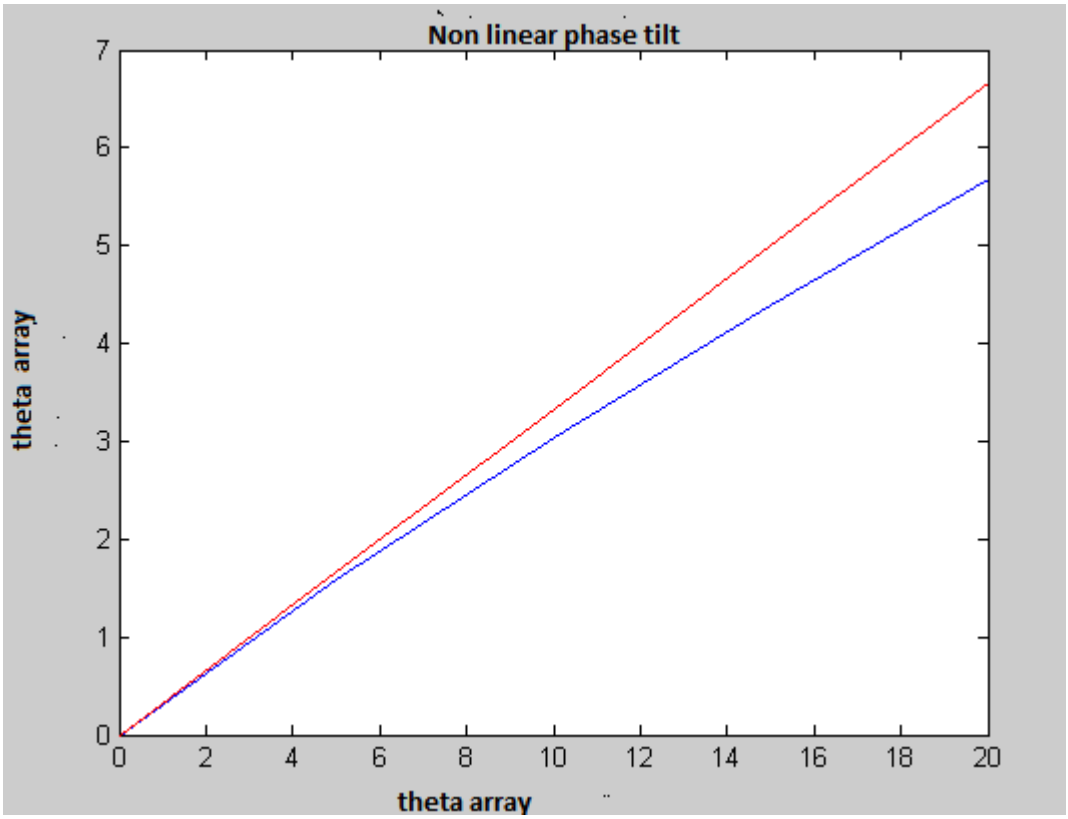

Fig. 3.46: Non lineal phase distortion

The developed software also provides a polynomial interpolation to simulate the reflected angles curves. The interpolation is represented in the figure below with a green line:

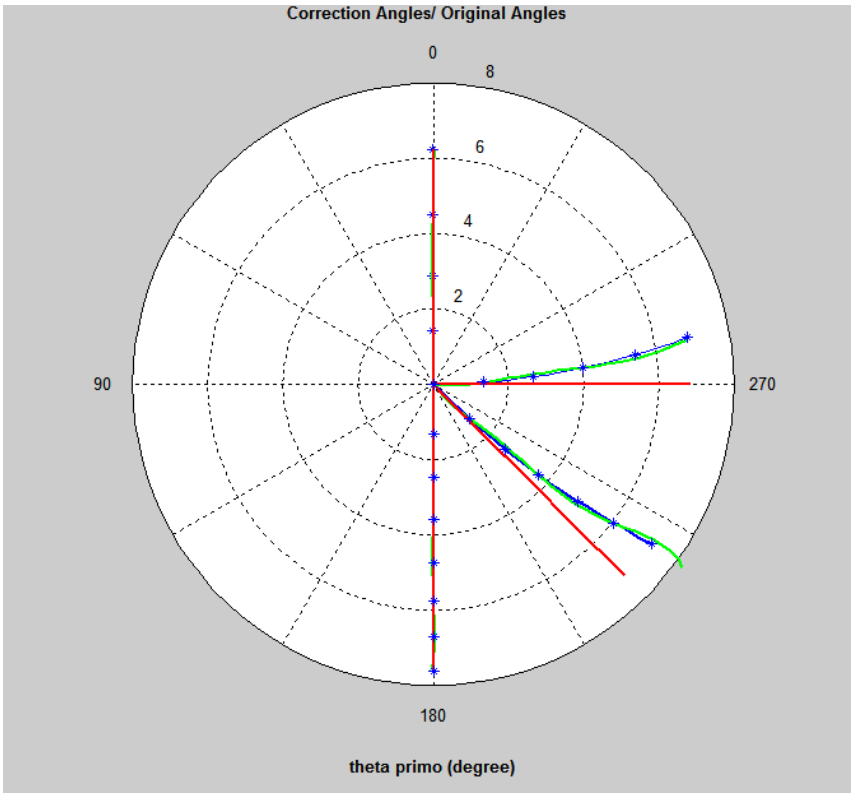

Fig. 3.47: A polynomial interpolation

The equations are fifth grade polynomials:

$$\varphi' = -0.0712\theta'^4 + 1.284\theta'^3 - 7.8371\theta'^2 + 18.3067\theta' + 100.9245 \text{ for } \varphi = 0^\circ$$
$$\varphi' = -0.0004\theta'^4 + 0.0055\theta'^3 - 0.0347\theta'^2 + 0.1080\theta' + 0.0312186 \text{ for } \varphi = 180^\circ$$
$$\varphi' = -0.1614\theta'^4 + 2.3481\theta'^3 - 11.5536\theta'^2 + 23.3953\theta' - 47.2252 \text{ for } \varphi = 45^\circ$$
$$\varphi' = -0.0002\theta'^4 + 0.0054\theta'^3 - 11.5536\theta'^2 + 0.0097\theta' - 89.9940 \text{ for } \varphi = 90^\circ$$

The polynomials are verified with the numbers of angles in Table B in Appendix B.

3.3.11. Polarization

The polarization of the array is parallel (Vertical of H) – see Fig. 3.48 below [8]:

$$ex_{m,n} = 1$$
$$ey_{m,n} = 0 \qquad (3.17)$$
$$ez_{m,n} = 0$$

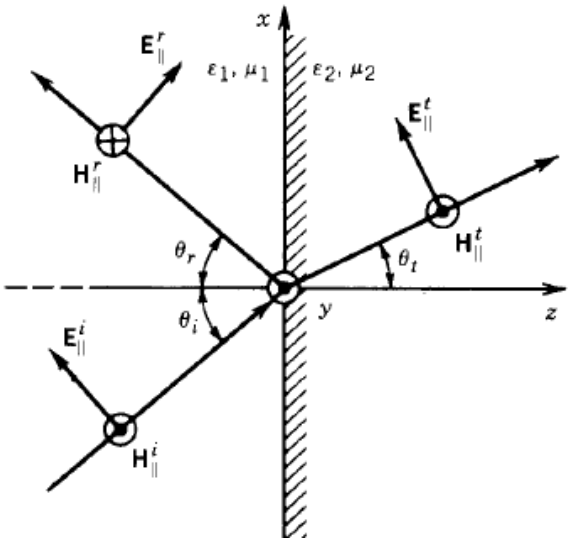

Fig. 3.48: Parallel (vertical) polarized uniform plane wave incident at an oblique angle on interface [8]

The near field (on the aperture) is calculated with method used in [10]

$$\Delta s_{m,n}=(xs_{m,n}{}^2+ys_{m,n}{}^2+4f_s{}^2)$$

$$\alpha_{m,n}=\frac{2(xs_{m,n}ex_{m,n}+ys_{m,n}ey_{m,n}-2f_s ez_{m,n})}{\Delta s_{m,n}}$$

$$\Delta m_{m,n}=((-2\frac{xm_{m,n}}{(4f_m)})^2+(-2\frac{ym_{m,n}}{(4f_m)})^2+1)$$

$$\beta_{m,n}=2((ex_{m,n}-\alpha_{m,n}xs_{m,n})(-2\frac{xm_{m,n}}{(4f_m)})+(ey_{m,n}-\alpha_{m,n}ys_{m,n})(-2\frac{ym_{m,n}}{(4f_m)})-\frac{(ez_{m,n}+2f_s\alpha_{m,n})}{\Delta m_{m,n}})$$

Therefore the field in the aperture is given by:

$$\begin{aligned}Em(x_{m,n})&=(ex_{m,n}-\alpha_{m,n}xs_{m,n}-\beta_{m,n}\frac{-2xm_{m,n}}{4*f_m})e^{-j*\Phi_{m,n}}\\ Em(y_{m,n})&=(ey_{m,n}-\alpha_{m,n}ys_{m,n}-\beta_{m,n}\frac{-2ym_{m,n}}{4*f_m})e^{-j*\Phi_{m,n}}\end{aligned}\qquad (3.19)$$

From [8] the magnetic current density related is given by:

$$\begin{aligned}M(x_{m,n})&=2Em(y_{m,n})\\ M(y_{m,n})&=-2Em(x_{m,n})\\ \Delta_{m,n}&=\Delta_{m,n}ym\Delta_{m,n}xm\end{aligned}\qquad (3.20)$$

$\Delta_{m,n}$ is the square area between elements. Once determined the field distribution on the aperture with G.O. we must apply P.O.to obtain the far field.
The electric current density related is given by:

$$|L_\theta|=\left|\int\int_S \Delta_{m,n}e^{(j\frac{2\pi}{\lambda}\sin(\theta')(xa_{m,n}\cos(\varphi')+ya_{m,n}\sin(\varphi'))}(M(x_{m,n})\cos(\theta')\cos(\varphi')+M(y_{m,n})\cos(\theta')\sin(\varphi')\right|$$

$$|L_\varphi|=\left|\int\int_S \Delta_{m,n}e^{(j\frac{2\pi}{\lambda}\sin(\theta')(xa_{m,n}\cos(\varphi')+ya_{m,n}\sin(\varphi'))}(M(x_{m,n})\sin(\varphi')+M(y_{m,n})\cos(\varphi')\right|$$

Where N is the maximum number of elements per row and column.

We must take into consideration the relationship $R>\frac{2D^2}{\lambda}$, where D is main diameter. For the calculations is taken $R>>100000$ [cm]. As the polarization is parallel J_x and J_y are 0 (see Example 6.5 from [8]). More precisely from Eq.2.22.

$$E_\theta = \frac{(-j\frac{2\pi}{\lambda} e^{(-\frac{j2\pi}{\lambda}R)})}{4\pi R} L_\varphi \qquad (3.21)$$

$$E_\varphi = \frac{(j\frac{2\pi}{\lambda} e^{-\frac{j2\pi}{\lambda}R})}{4\pi R} L_\theta$$

At the end, we transform the fields to Cartesian coordinates. Using spherical-to-rectangular component transformation where $Er = 0$.

$$\begin{aligned} |Ex| &= |E_\theta \cos(\theta')\cos(\varphi') - E_\varphi \sin(\varphi')| \\ |Ey| &= |E_\theta \cos(\theta')\sin(\varphi') + E_\varphi \cos(\varphi'))| \\ |Ez| &= |-E_\theta * \sin(\varphi')| \end{aligned} \qquad (3.22)$$

We represent the pattern in tension. It means $20\log(|Ex|)$

The software programme is generated using the equation from Chapter 3.4.

A vertically polarized wave is incident and the co-polar radiation pattern can be established. As it can be expected the y component of the electric field is 0. The values of the cross-polar component are reported to the maximums of the co-polar value. There is cross-polar element in z due to asymmetries in this plane.

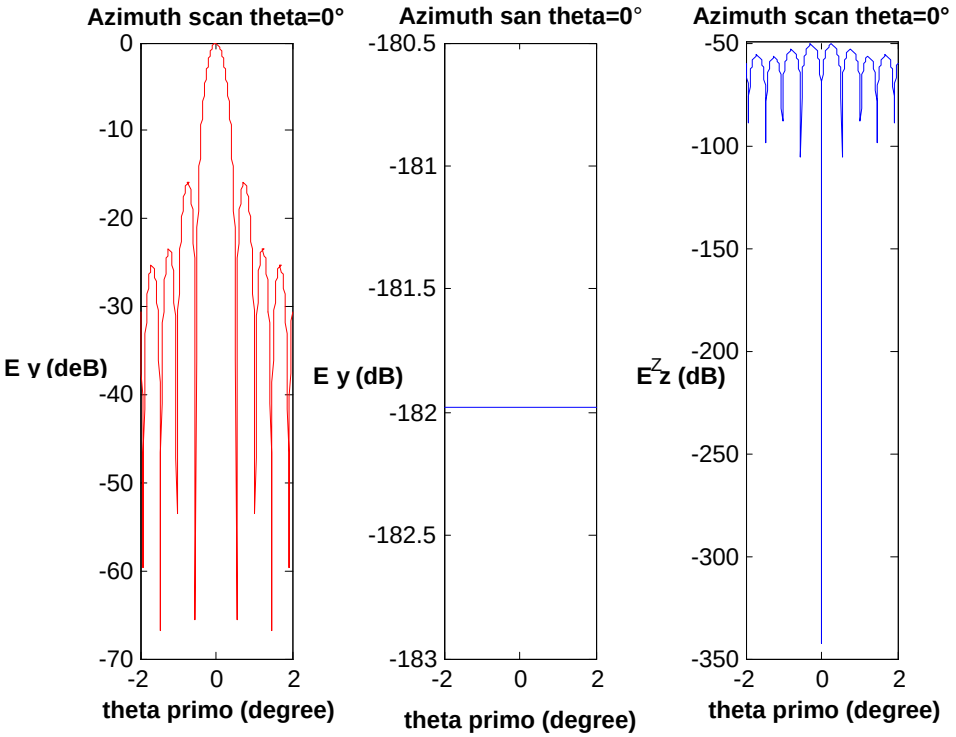

Fig. 3.49: Vertical Polarized pattern boresight

Azimuth beam scanning

Fig.3.50 shows an azimuth pattern cut, calculated when assuming that the array was linearly polarized. The cross-polar interference illustrated by E_y and E_z below, is the co-polar peak. The cross-polar lobes correspond closely to the co-polar side lobes in both form and position. As the beam is deflected from boresight, the cross-polar level increases and the main lobe moves off the main beam direction. The main cross-polar lobe is increasing in relative intensity when increasing the scan angle. When the main beam was scanned to approximately 10°, the beam width has remained the same.

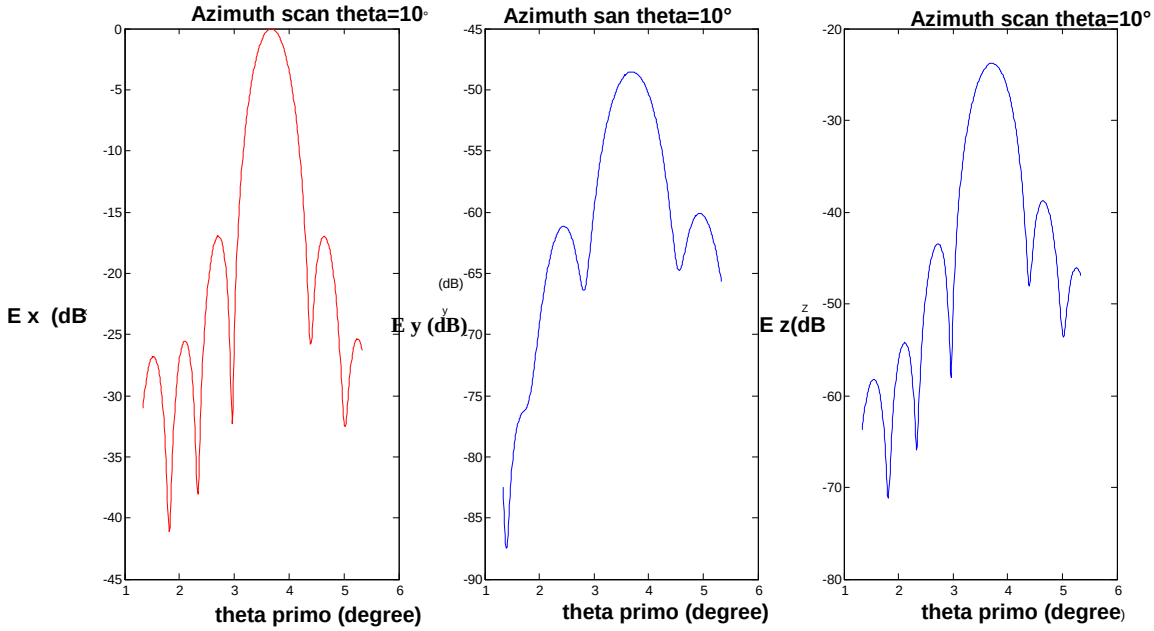

Fig. 3.51: Azimuth scan with vertical polarization

Elevation plane scan

Fig.3.52 shows an elevation cut through the boresight beam. It also shows that there is a clear asymmetry in the width of the side lobe structure and zero cross-polar interference. There is a bigger spillover for the elevation plane than the spillover for the azimuth plane. The side lobe level on the boresight side of the main beam tends to increase. In addition the main beam becomes, when scanned to the maximum angle, very asymmetrical.

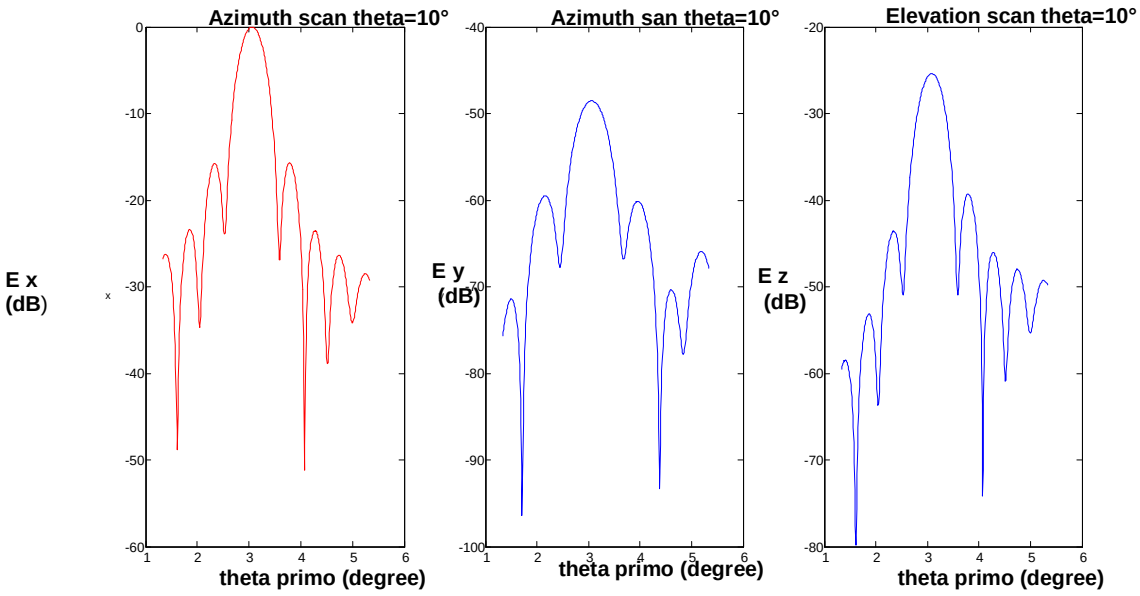

Fig. 3.52: Elevation scan with vertical polarization

To verifier the obtained results we compared the next figure with the obtained one from Pearson in [10]

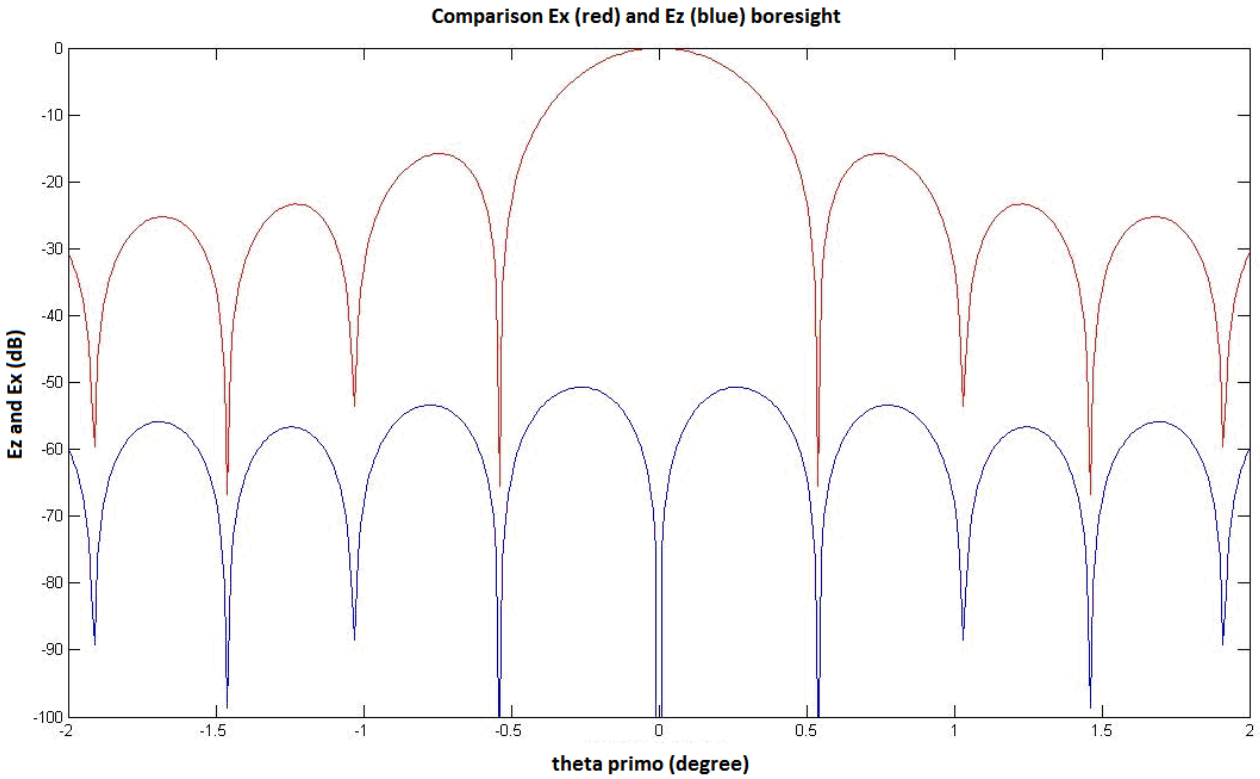

Fig. 3.53: Comparison elevation scan co-polar and cross-polar component with θ=0° and φ= 0

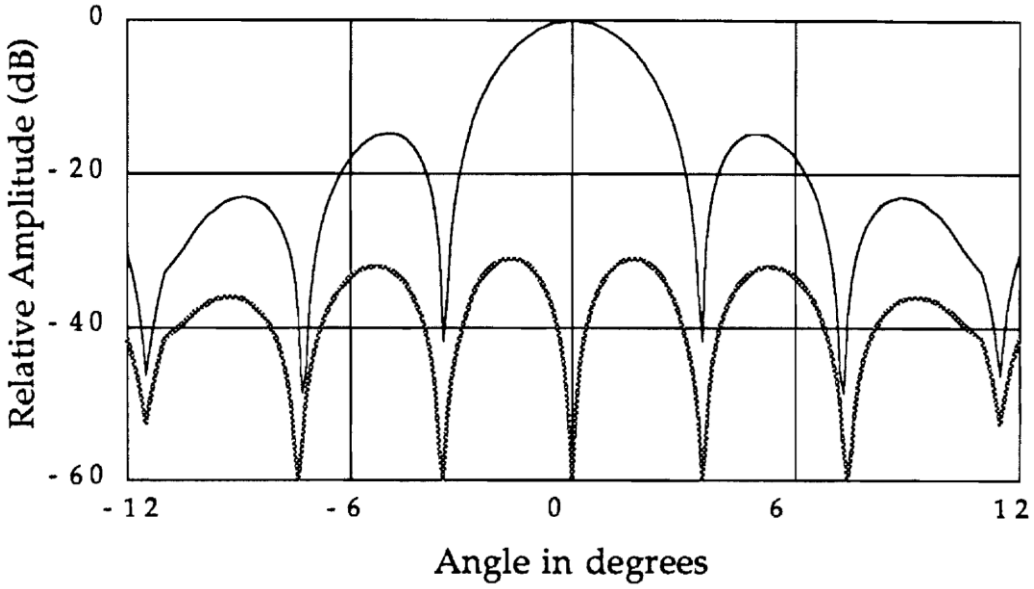

Fig. 3.54: Figure from [10] comparison elevation scan co-polar and cross-polar component

As well comparison is made for scan angles. In our case θ=3° φ=0° for Pearson θ=3° φ= 180°

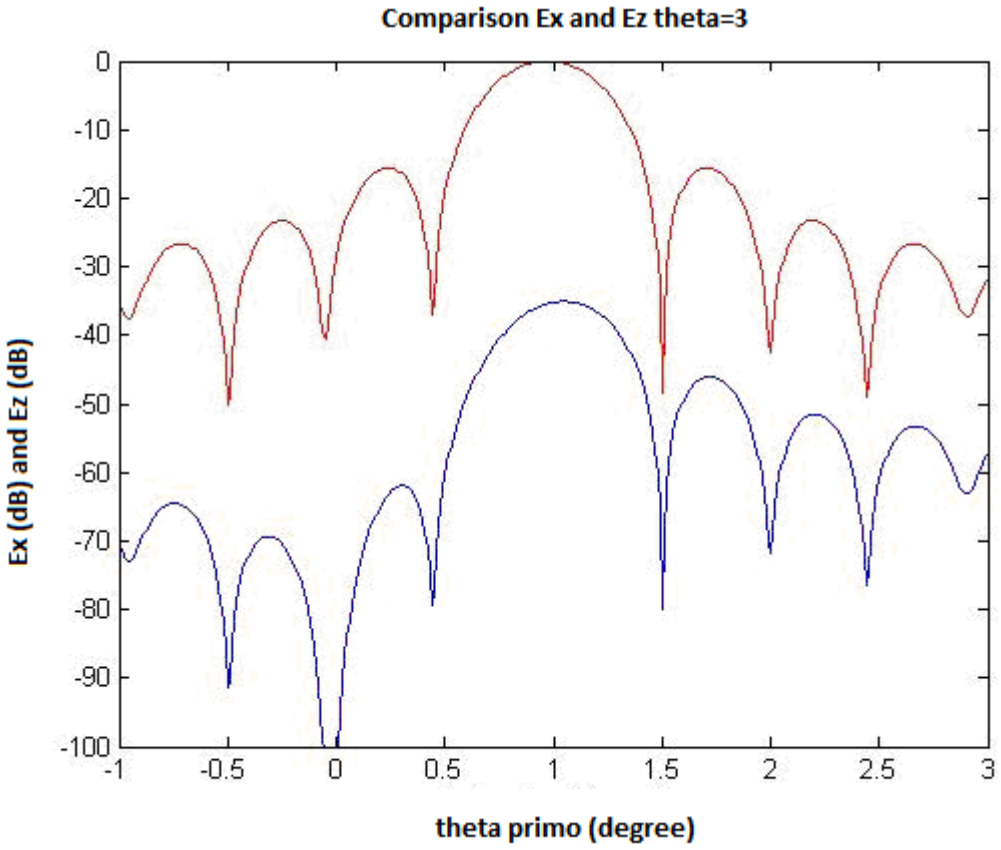

Fig. 3.55: Comparison elevation scan co-polar and cross-polar component with θ= 3° and φ= 0°

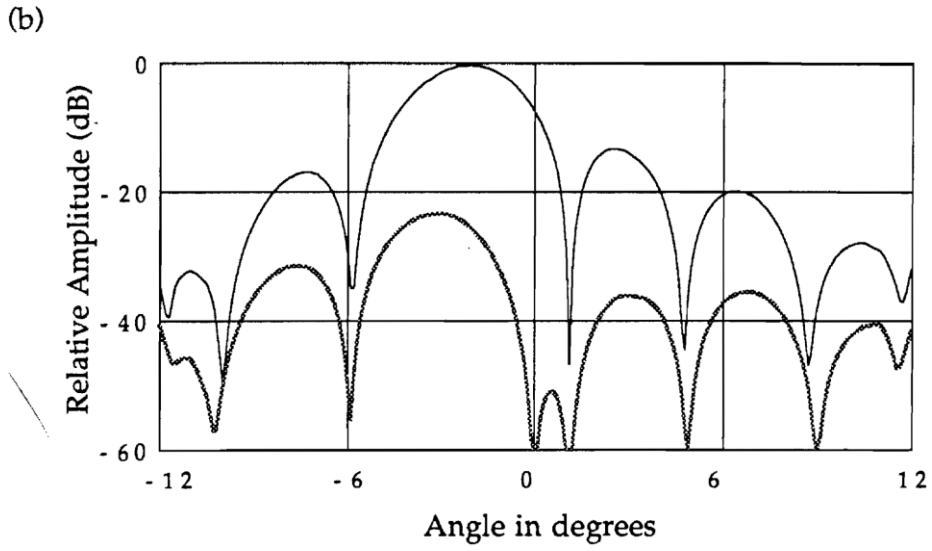

Fig. 3.56: Figure from [10] comparison elevation scan co-polar and cross-polar component

Multiple power pattern beams

The co-polar main lobe and first side lobe were plotted for 45 different beams scanned in elevation plane, using the same technique as the one applied in Chapter 3.3.9. The correction angles in this case are not considered for the elevation plane as it has been concluded that there is not a very important beam.

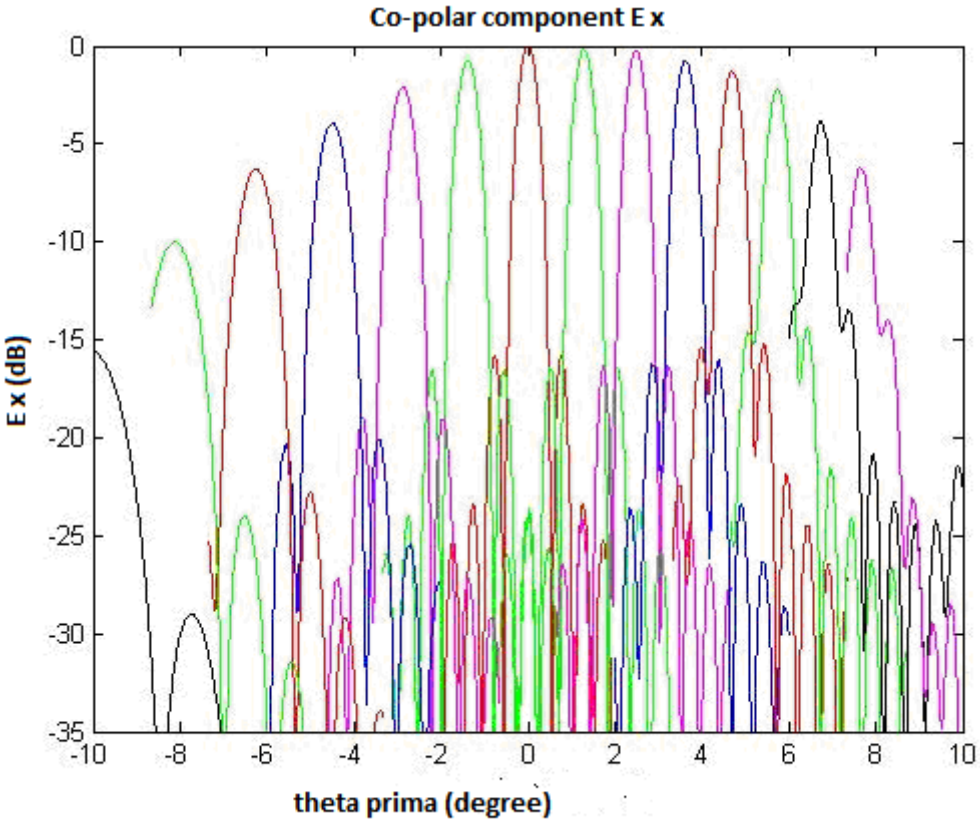

Fig. 3.57: E_x multiple power patterns with polarization

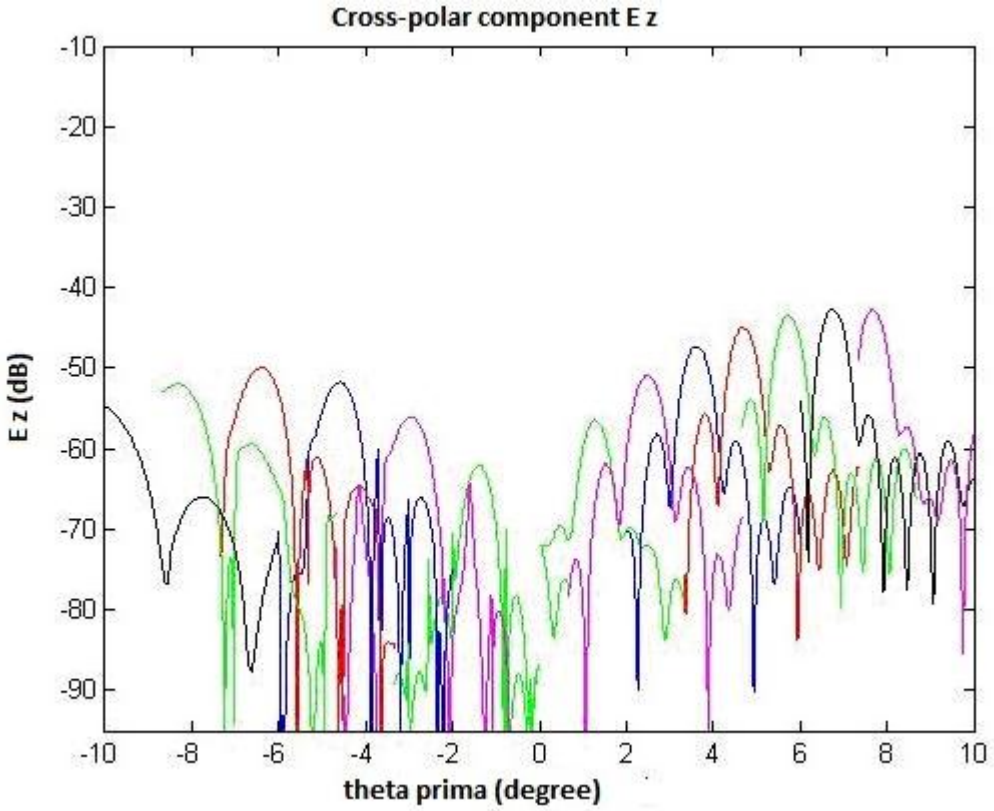

Fig.3.58: E_z multiple power patterns with polarization

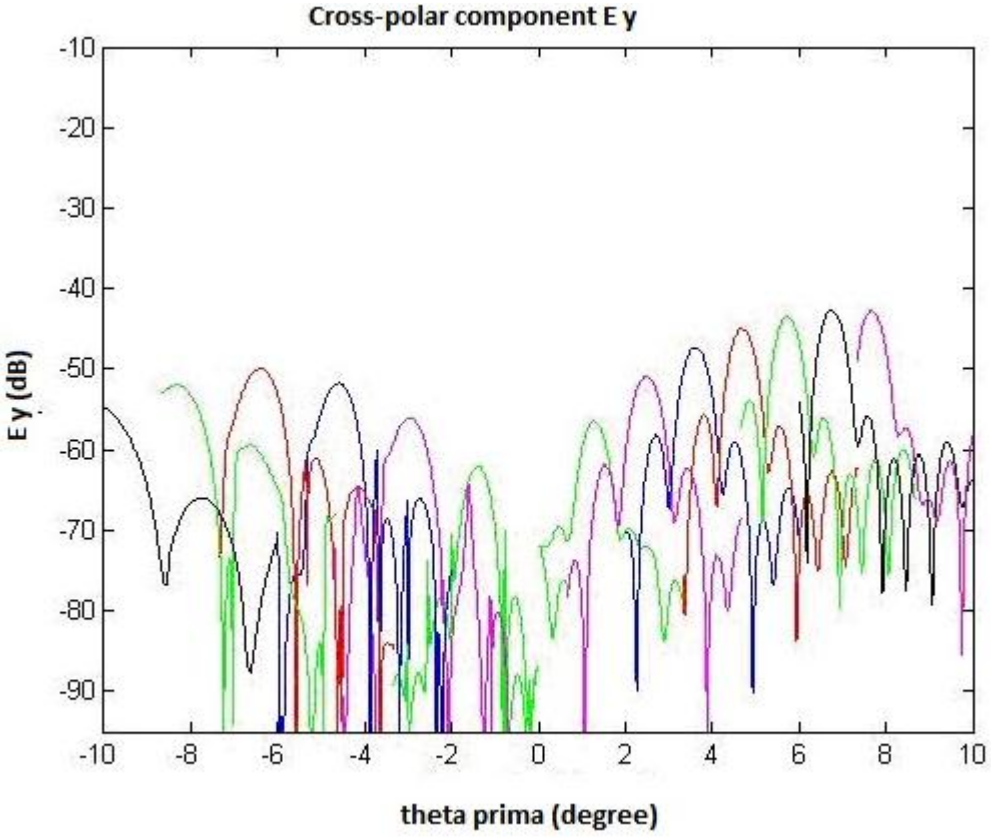

Fig.3.59: E_y multiple power patterns with polarization

The cross-polar component increases for the angles near the boresight, but decreases for bigger angles due to reasons of spillover and aberrations. There is more detailed study for different φ in Fig. 5 in Appendix B.

Comparison between scalar power pattern and co-polar component

A comparison is made between the scalar pattern and the co-polar component of the polarized power pattern. There is a complete coincidence between the pattern and the component when small angles are used.

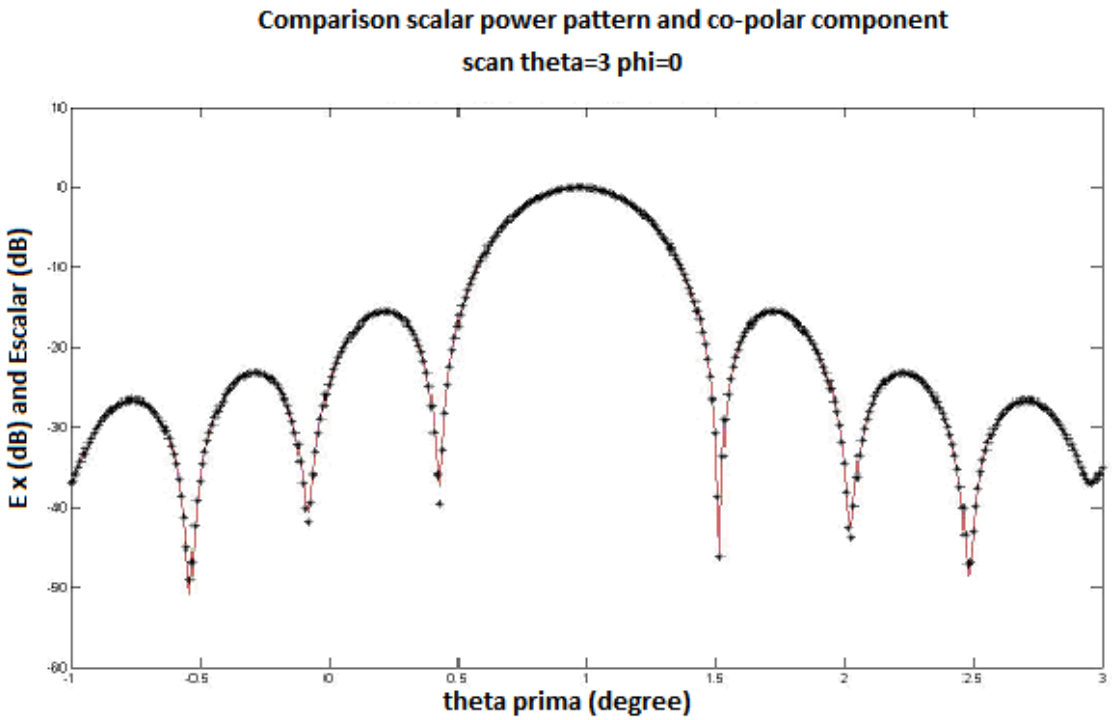

Fig. 3.60: Vertical Polarized pattern boresight

More illustrative figures are plotted in Appendix B (see Fig. 8 and 9) The multiple patterns are performed as previously explained in Chapter 3.3.9.

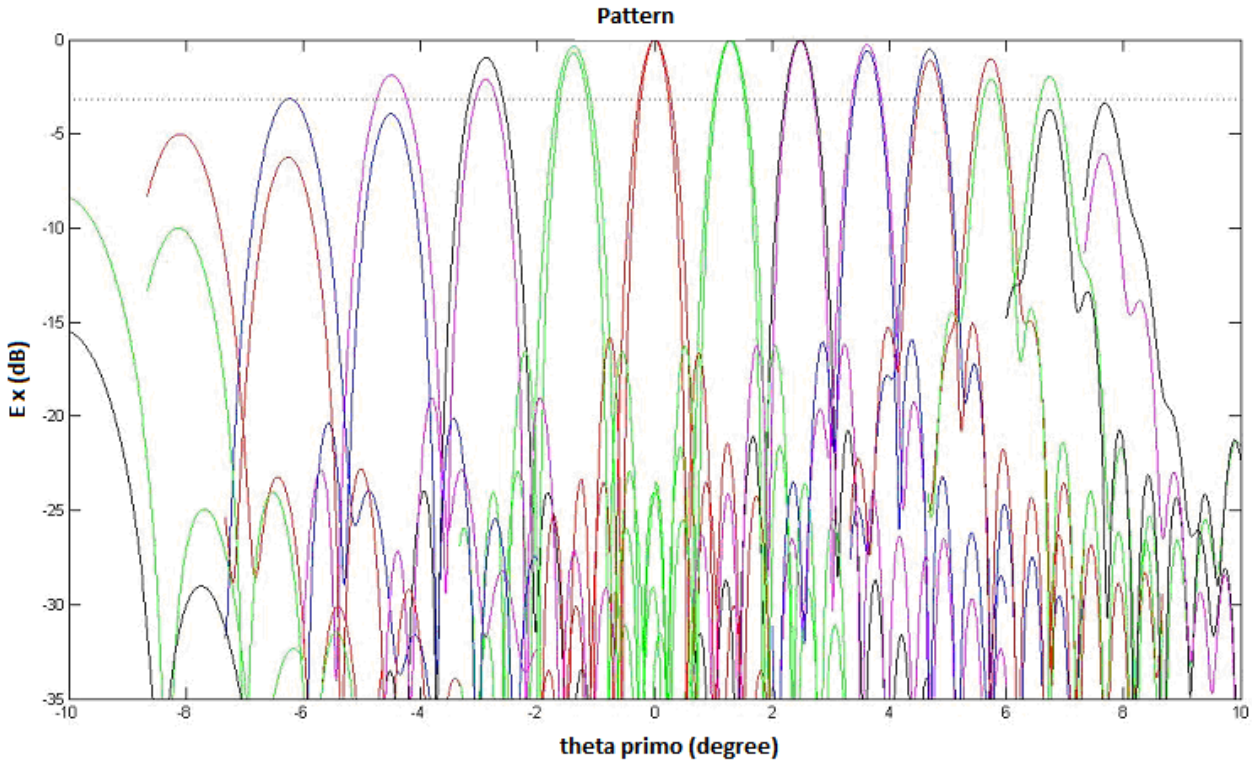

Fig. 3.61: Vertical Polarized pattern boresight

3.4. Conclusions

Due to aberrations and spillover, for a range of scan angles, phase distortion is observed. In boresight beam, an image is created at the focal point of the reflectors. In the scan mode this antenna architecture presents energy loss. Different pattern performances for elevation scan up, down ward and diagonal scan are discussed.

The linear relationship for the reflected angles is valid just for the elevation scan up and down wards, for all other cases nonlinear relationship is observed. The provided software calculates the angles, considering the maximum value of the pattern. The nonlinearity of the angles can be simulated with polynomial interpolations of fifth grade.

The co-polar lobes with vertical polarization correspond closely to the scalar power pattern side lobes in both form and position. There is a cross-polar component for angles of scan different from boresight.

We will make use of the explained theory in this chapter in future chapters.

4. Triangle and hexagonal configuration (GO). Plane Wave

4.1. Introduction

There is a change just in the shape of the array.Such change means that the paraboloids are determined in the same way and the ray tracing is exactly the same.
Two different cases are discussed: triangle and hexagonal configuration. Different aspects are contrast with the square array shape.

4.2. Triangle array configuration

The inputs are the same as the square configuration. One difference is that the number of circles and not the elements per side should be defined (see Chapter 3.3.1). The program calculates the total number of elements.
The designed software gives the opportunity to represent the system in 2 and 3 dimensions. The ray tracing is built using the equations from Chapter 3.2.

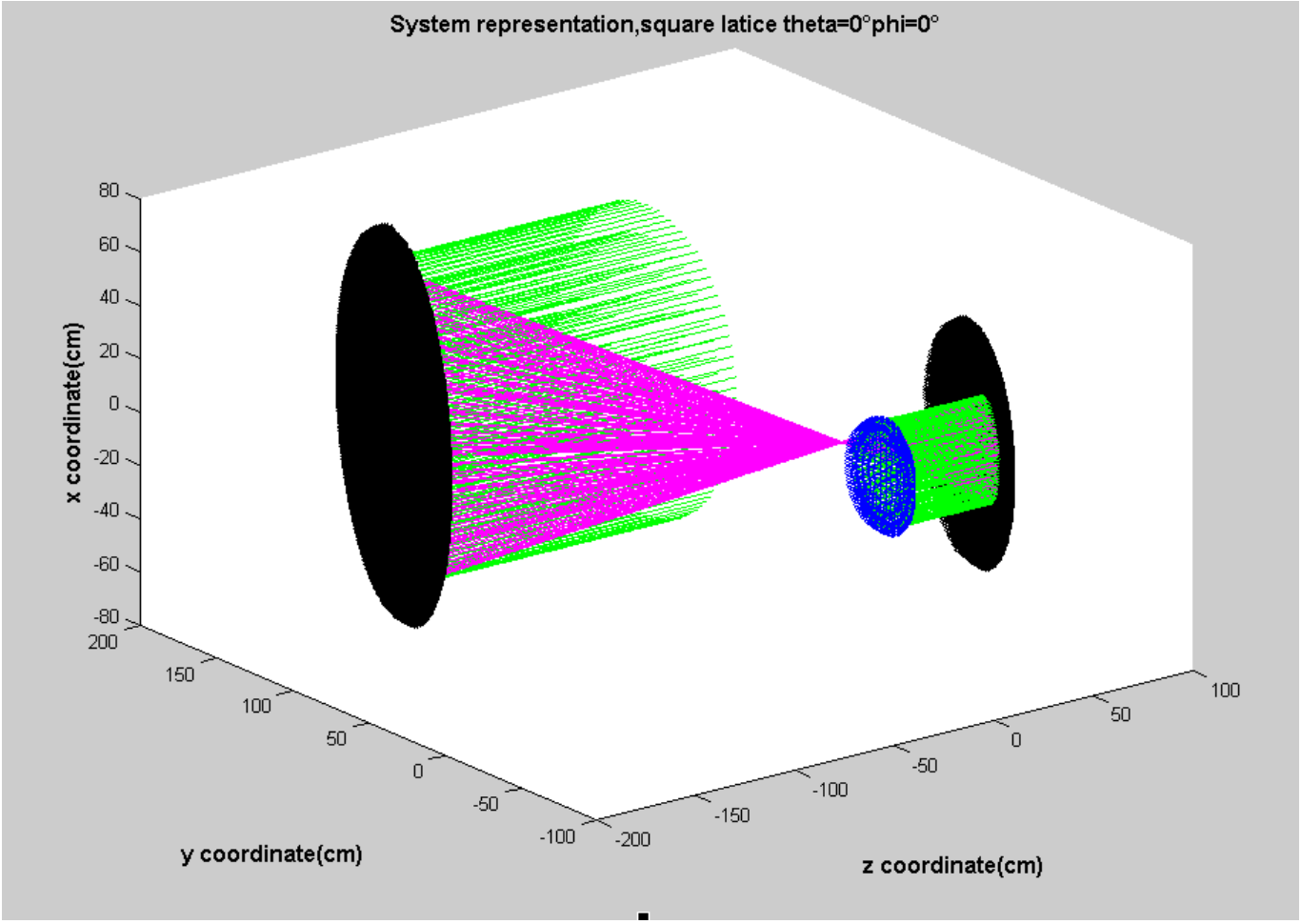

Fig. 4.1: 3D Representation of the system boresight

For better understanding of the circle number and the total elements number the next two figures are provided. With 3 circles we have a total of 43 elements and with 5 circles we have a total of 187 elements.

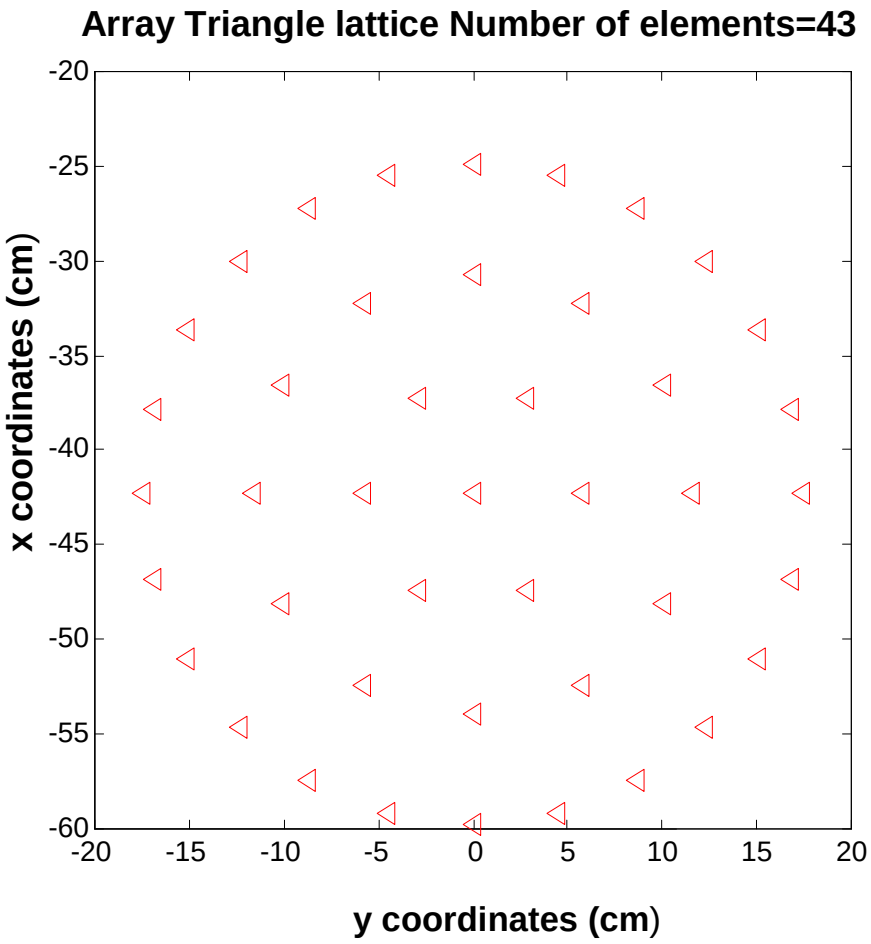

Fig. 4.2: Representation of the aperture 3 circle with 43 elements

Normally, 187 elements are used for the calculation of the different parameters. The interspacing between elements is not constant.

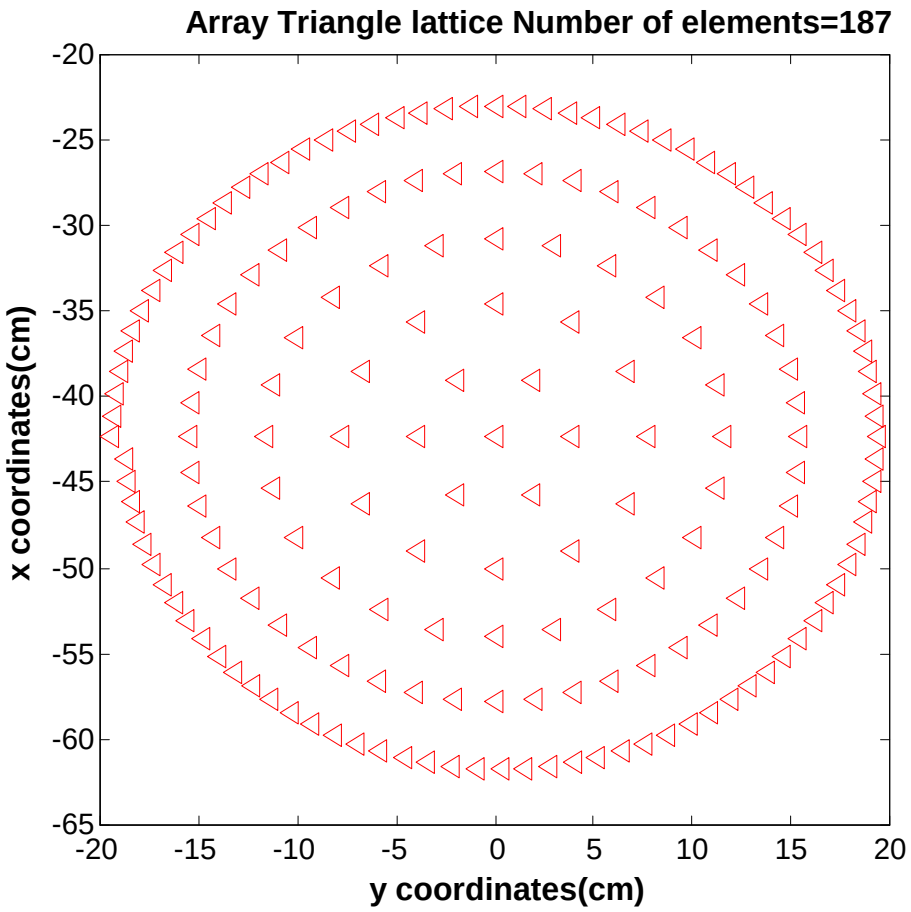

Fig. 4.3: Representation of the aperture 5 circle and 187 elements

The contrast between the square and triangle configuration is provided. Obviously, the number of elements in the case of the triangle is bigger than the square and the overall area is less.

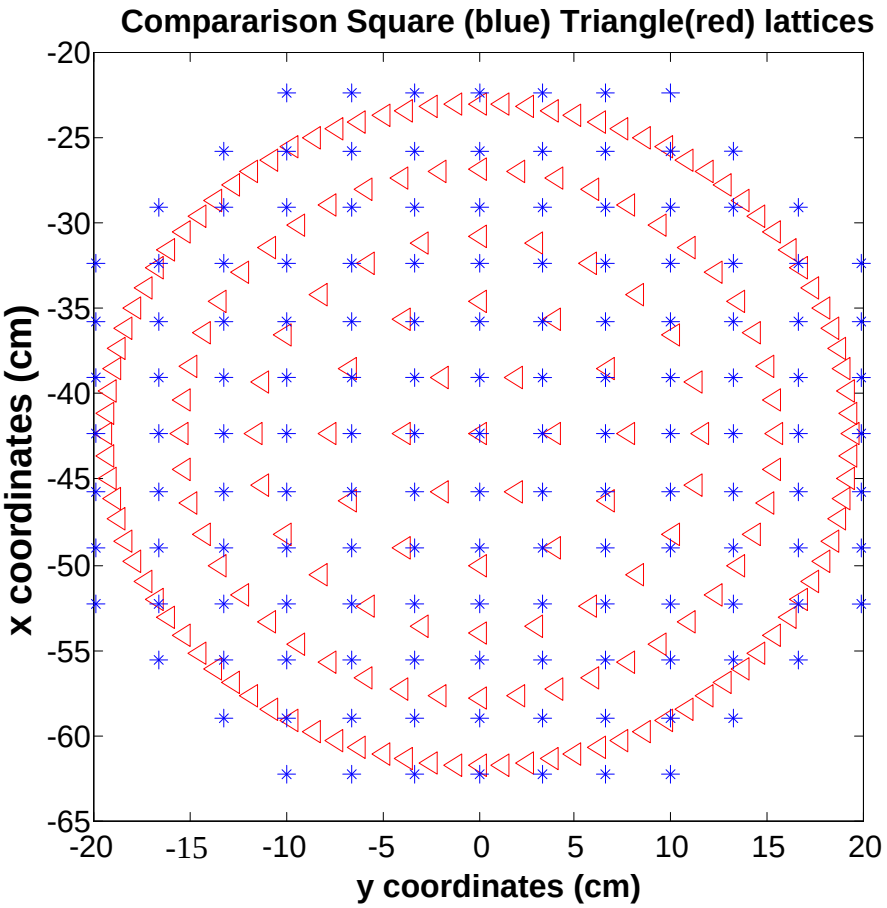

Fig. 4.4: Comparison between square configuration and triangle configuration

4.2.1. Aperture triangle configuration

As seen in the previous chapter the area between the elements in the aperture is important for the conservation of the energy. To observe the deformation in the area between elements, the vertices between them are represented in the next figures. The first one represents the image in the aperture for the boresight.

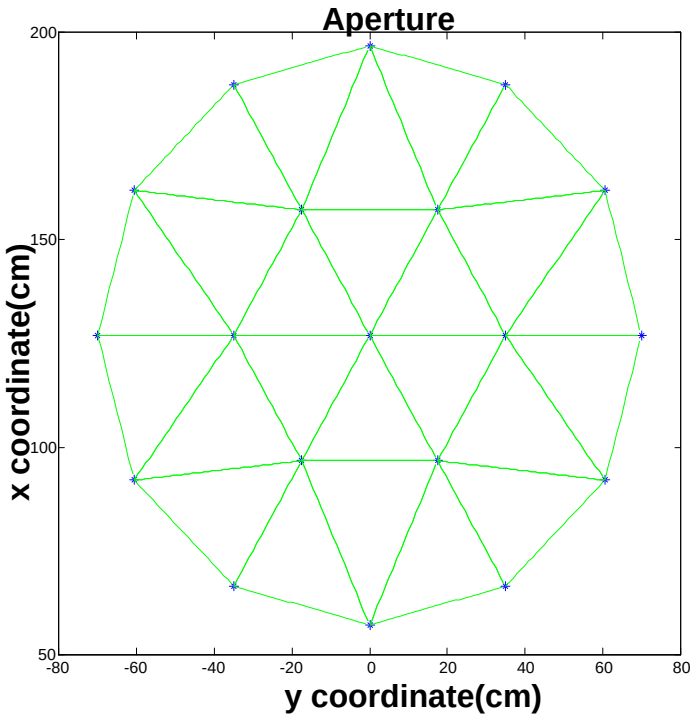

Fig. 4.5: Representation of the array two circle

The study of the aperture is shown taken into consideration two different scan angles. The same phenomenon is observed as in the square feed configuration. There is an expansion in the upward scan and reduction in the downward scan. In green is represented the boresight case and in blue – the different scan angles.

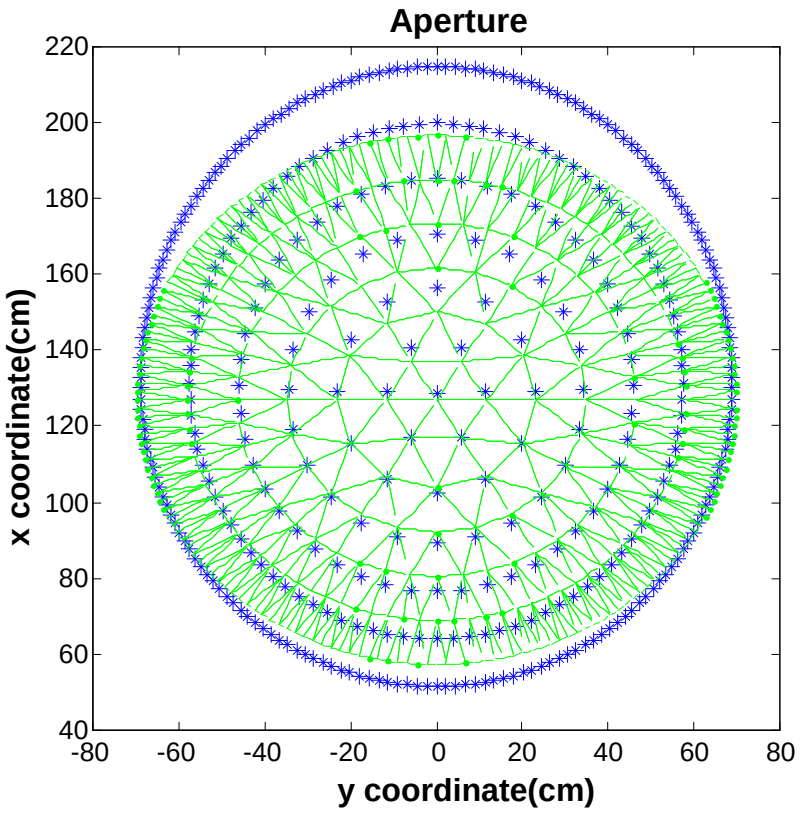

Fig. 4.6: Representation of the array 5 circle scan elevation plane upload

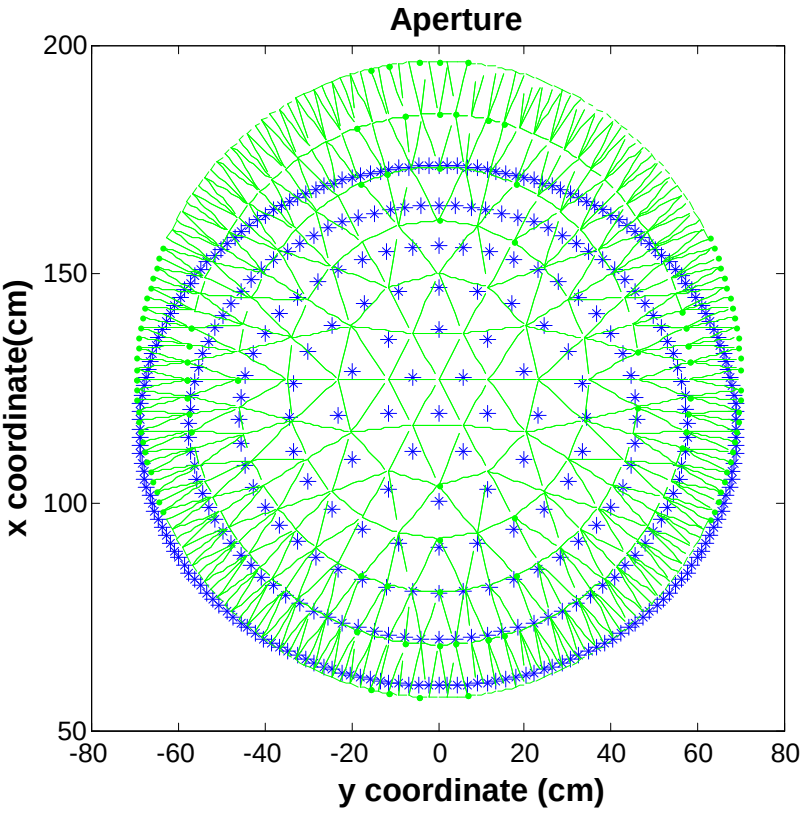

Fig. 4.7: Representation of the array 5 circle scan elevation plane download

For the diagonal scan there is a considerable deformation of the image in the antenna aperture. This will affect the phase distribution and the power pattern.

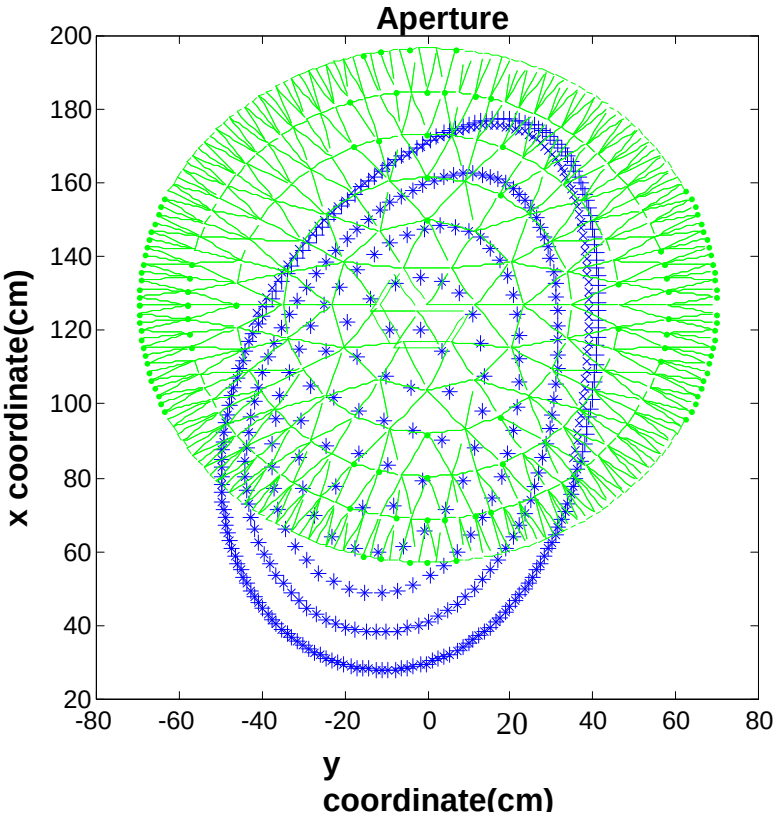

Fig. 4.8: Representation of the array 5 circle diagonal scan

4.2.2. Phase, path length error and aberration

The phase is calculated in the same way as in Chapter 3. The evaluation is made in the antenna aperture. As expected, the performance is similar. Please, note that the boresight case is in blue and the scan is in green. The considered scan angle is $\theta = 10^{o}$ and $\varphi = 0^{o}$. The direction of the phase tilt is in the sense of the scan.

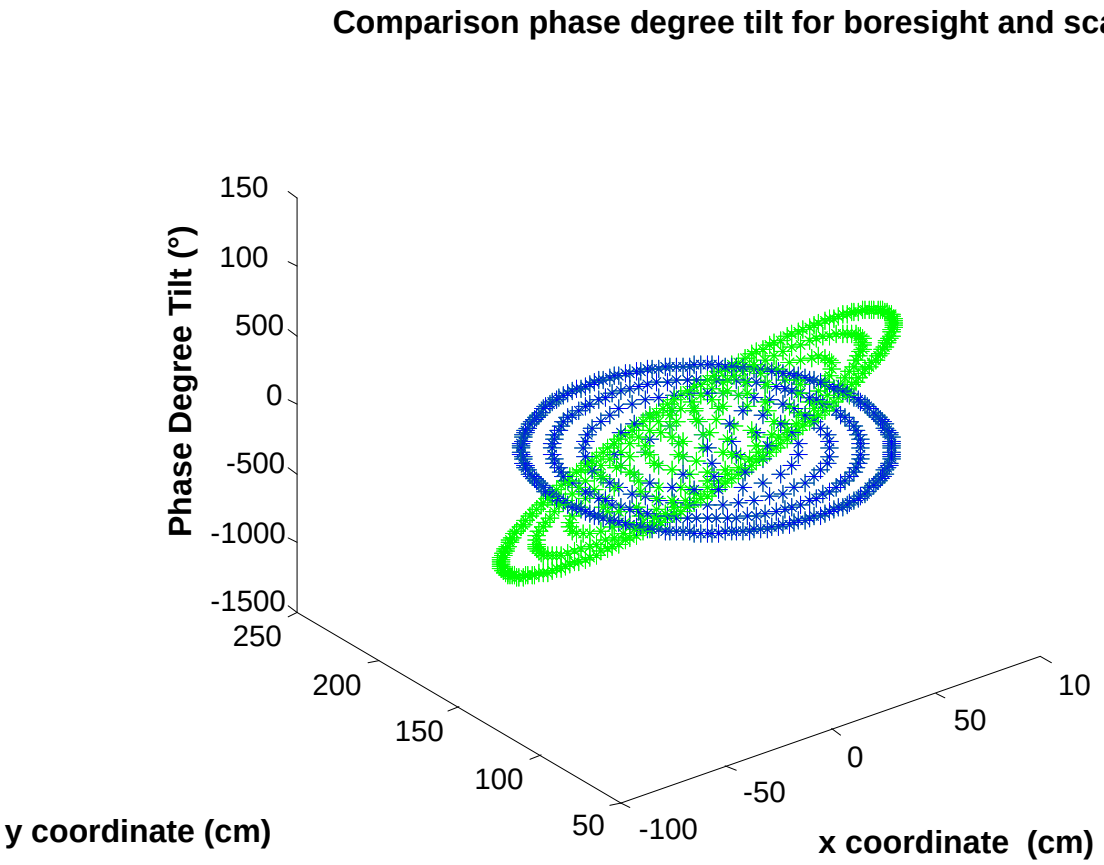

Fig. 4.8: Comparison phase degree tilt for boresight and scan

The aberration does not have a linear distortion as shown in the figure below.

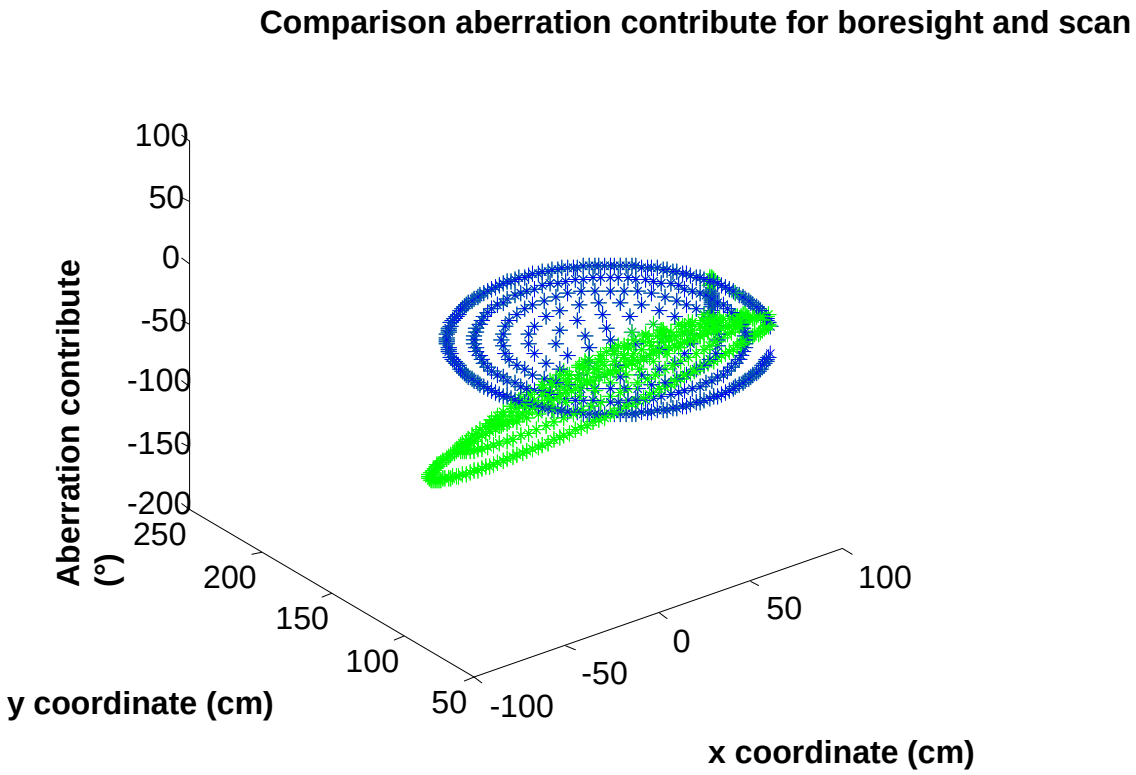

Fig. 4.9: Comparison aberration for boresight and scan

The caustic region explained in Chapter 3.3.4 (see Fig.3.12.) is one of the major reasons for phase aberrations. As a result of it, there is an important beam deformation for scan angles.

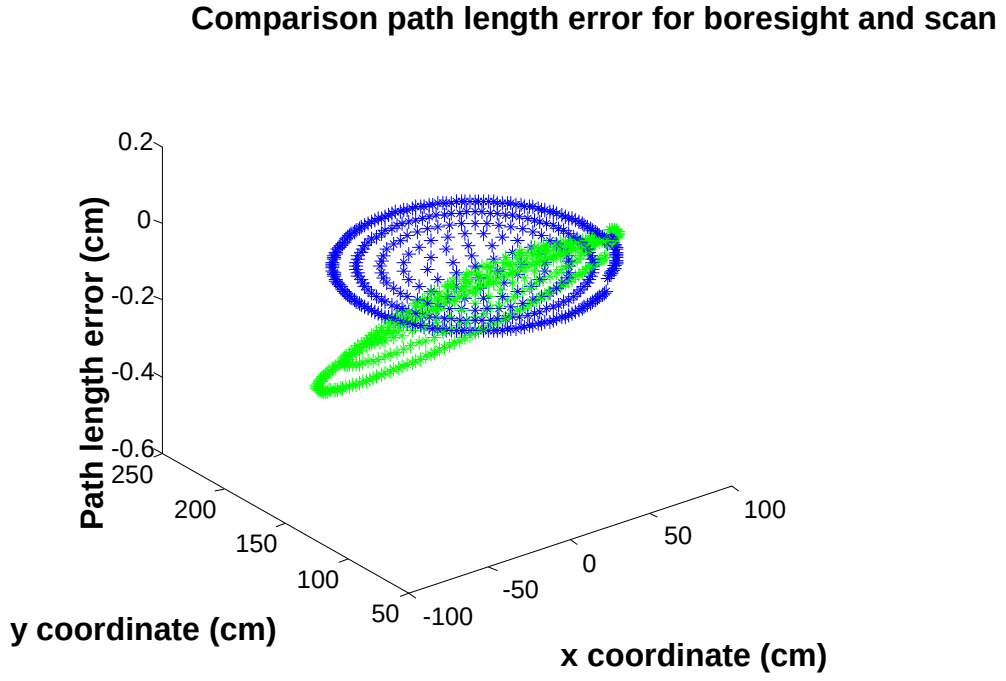

Fig. 4.10: Comparison path length error

The path lengths for the boresight are the same. When a scan is applied to the array there is a different path length for every ray depending of the angle of scan.

4.2.3. Scalar power pattern

The distance between elements is not equal, so the sum is over all the elements. Another difference from Eq. 3.18. is that we should divide it by the path length distance.

$$\left|P(\theta',\varphi')\right| = 20\log\left|\sum_{l=1}^{M} \begin{array}{l} Area_l * E(x0_{l,}\, y0_l) * \exp\left[-j\Phi(x'_{(l)}\ , y'_{(l)})\right]/(\mathrm{Los}_{(l)}+\mathrm{Lsm}_{(l)}+\mathrm{Lma}_{(l)})* \\ \exp\left[\, j2\pi(\, fm/\lambda)\sin\theta'(x'_{(l)}\cos\varphi'+ y'_{(l)}\sin\varphi')\right] \end{array}\right|$$

where M is the total number of elements. $E(x0_{l,}\, y0_l)$ is equivalent to the equation 3.18. For the next representation K=0 and C=0.

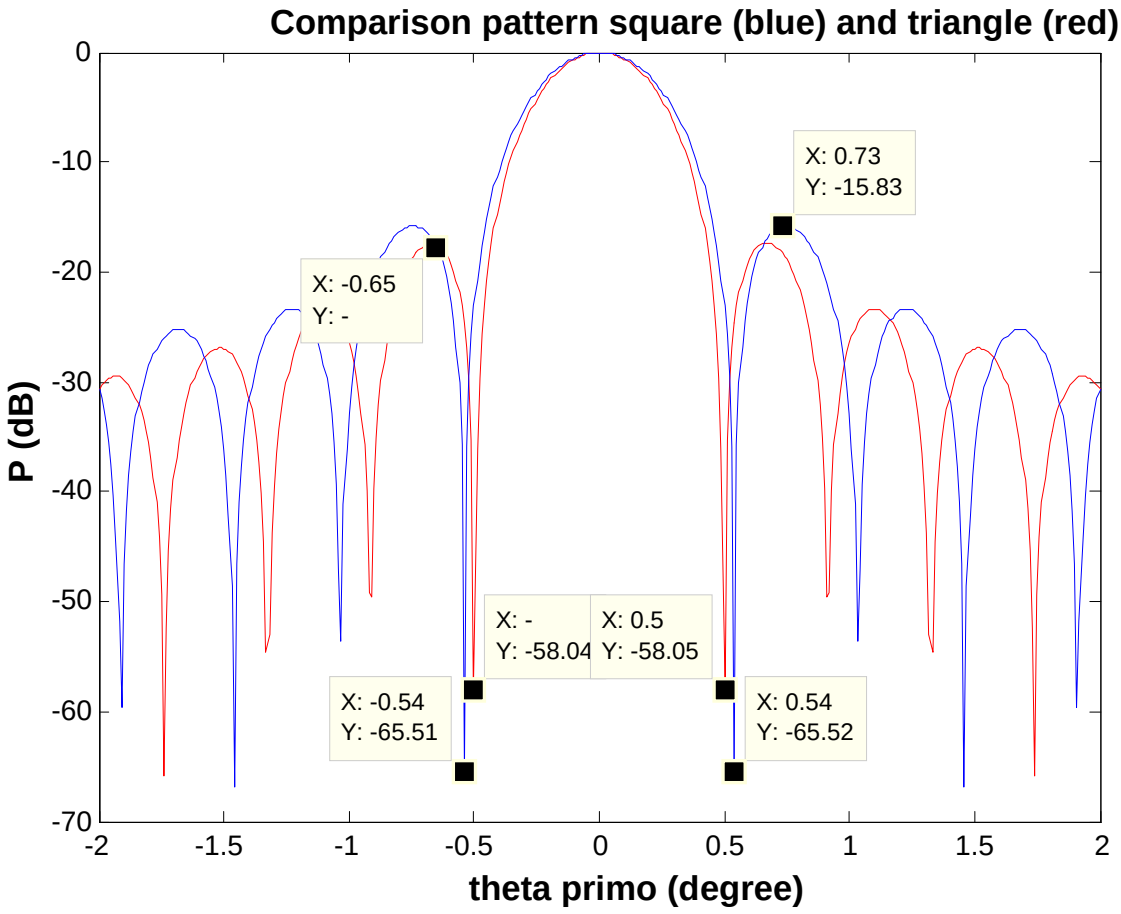

Fig. 4.11: Comparison scalar power pattern square (blue) and triangle (red) configuration boresight

The beam width is reduced from 1.08 degree to 1 degree. As the aperture is circular it is normal to obtain the same result as explained in Eq.2.1. Another gain is the

lower side lobe level -17.71 dB, while for the square configuration the side lobe level is of -15.83dB. The number of feeds used in the triangle configuration is 186, in contrast for square configuration where the number is just 145. The cost associated to the 41 elements must be considered.

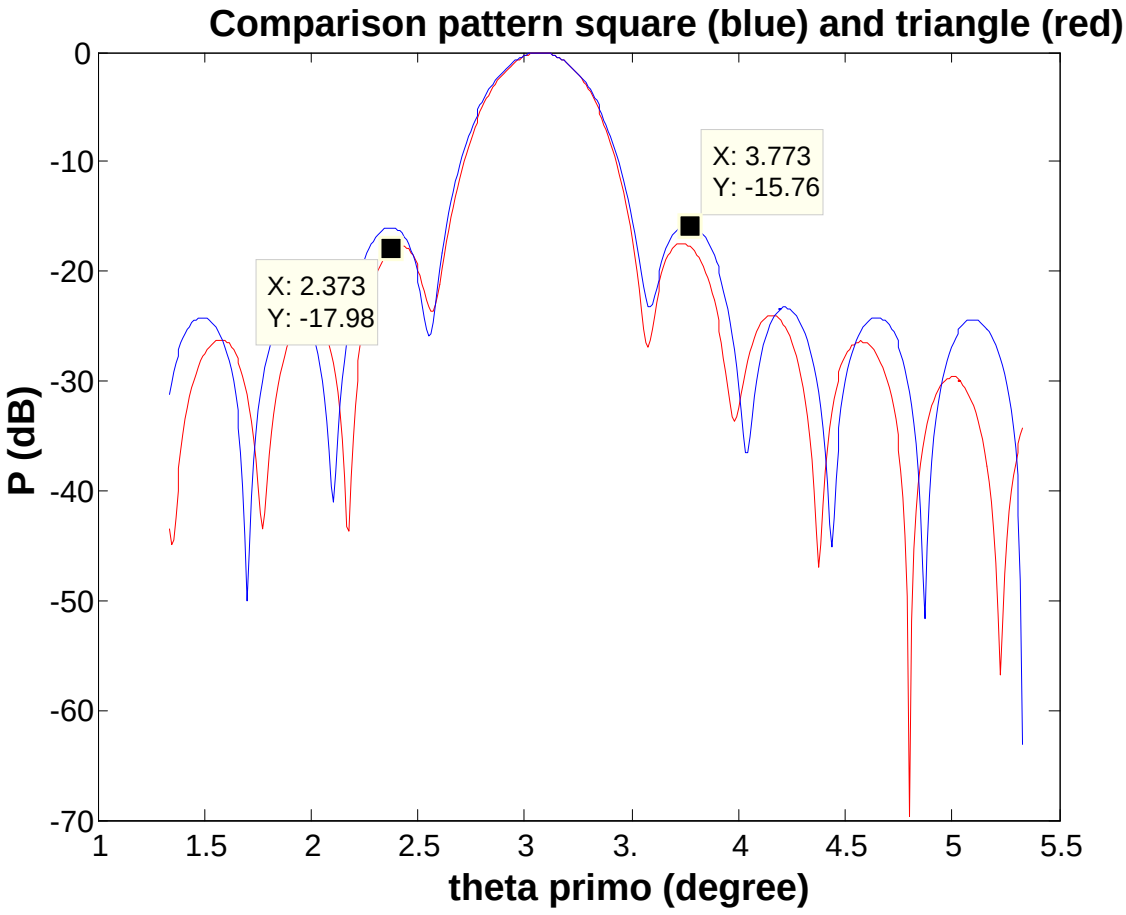

Fig. 4.12: Comparison scalar power pattern square (blue) and triangle (red) configuration scan

When scan is considered, for example in Fig. 4.12 the performance of the main beam is very similar to the one in square one. There is still gain in the side lobe level and in this way we can distinguish better the main beam from the side lobes. For the triangle configuration the side lobe level is of -17.98 dB

4.3. Hexagon array configuration

Every element of the hexagon array is equidistant. The user must introduce the number of hexagons. The total element number is computed by the software. All the rest of the parameters are declared in the same way as for the square

configuration. For example, for 7 hexagons there are 169 elements (as shown in Fig. 4.11.)

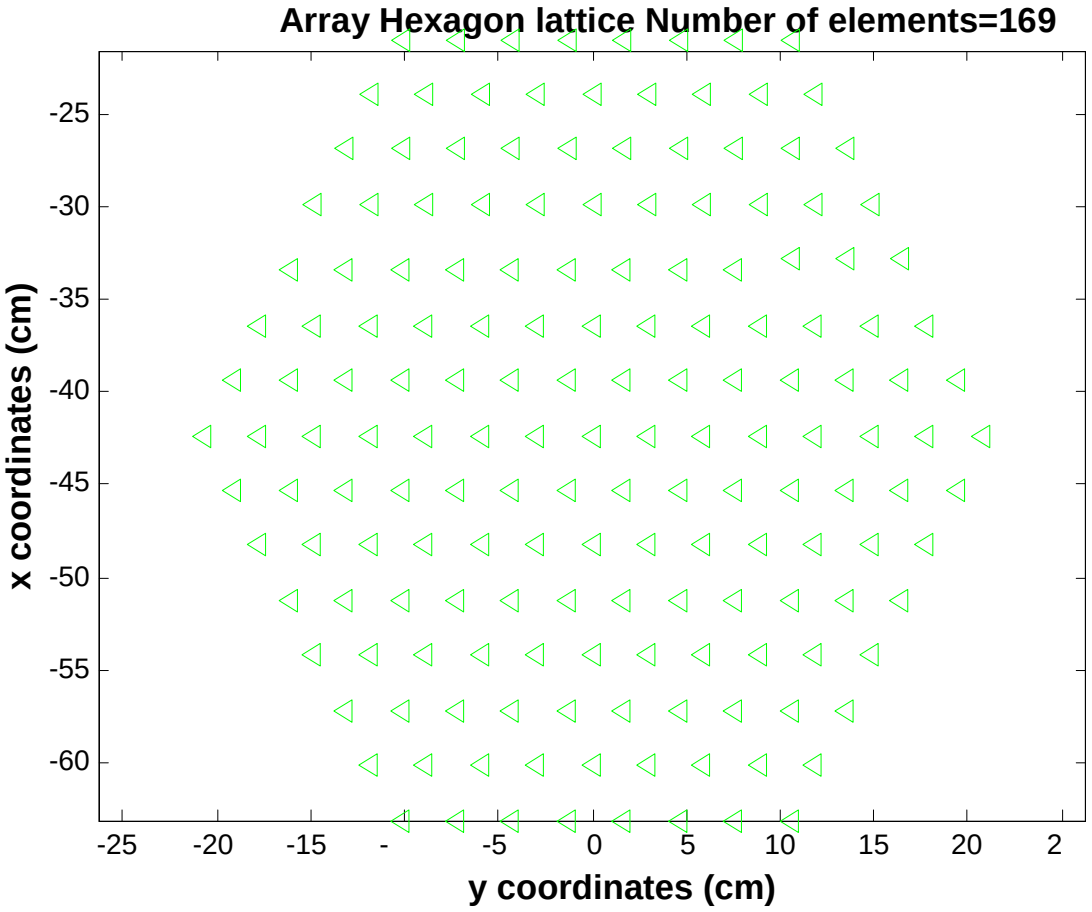

Fig. 4.13: Representation of the array 7 hexagons

The contrast between the two arrays configurations is shown in Fig. 4.12.

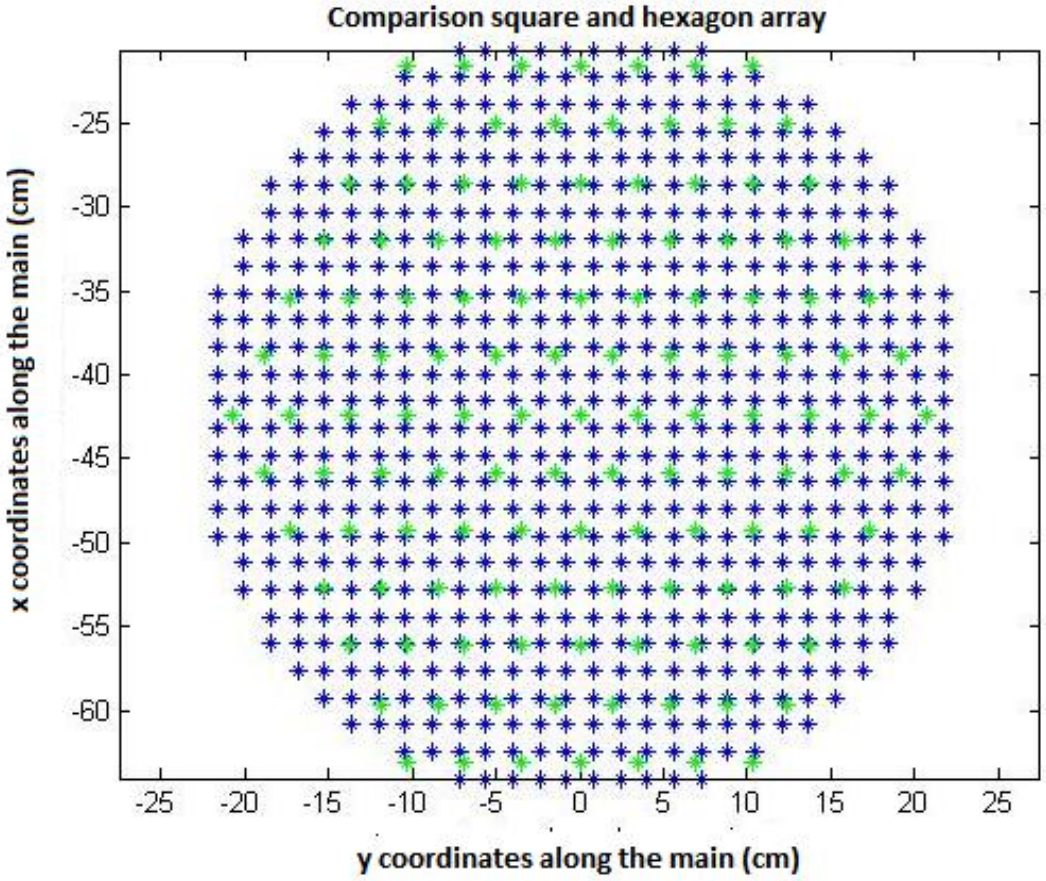

Fig. 4.14: Comparison of the arrays N=30 and 6 hexagons

It can be observed that the dimensions of the hexagon array are smaller in comparison with the one in square one.

The phase and path length study was omitted as the performance is very similar to the other two cases.

The scalar power pattern is represented and compared to the square configuration. As we do not have a perfect circle aperture, we obtain a beam width slightly larger than 1°, more precisely it is 1.08°, the same as the square array. The difference between the side lobe levels is 3.11dB for the first side lobe.

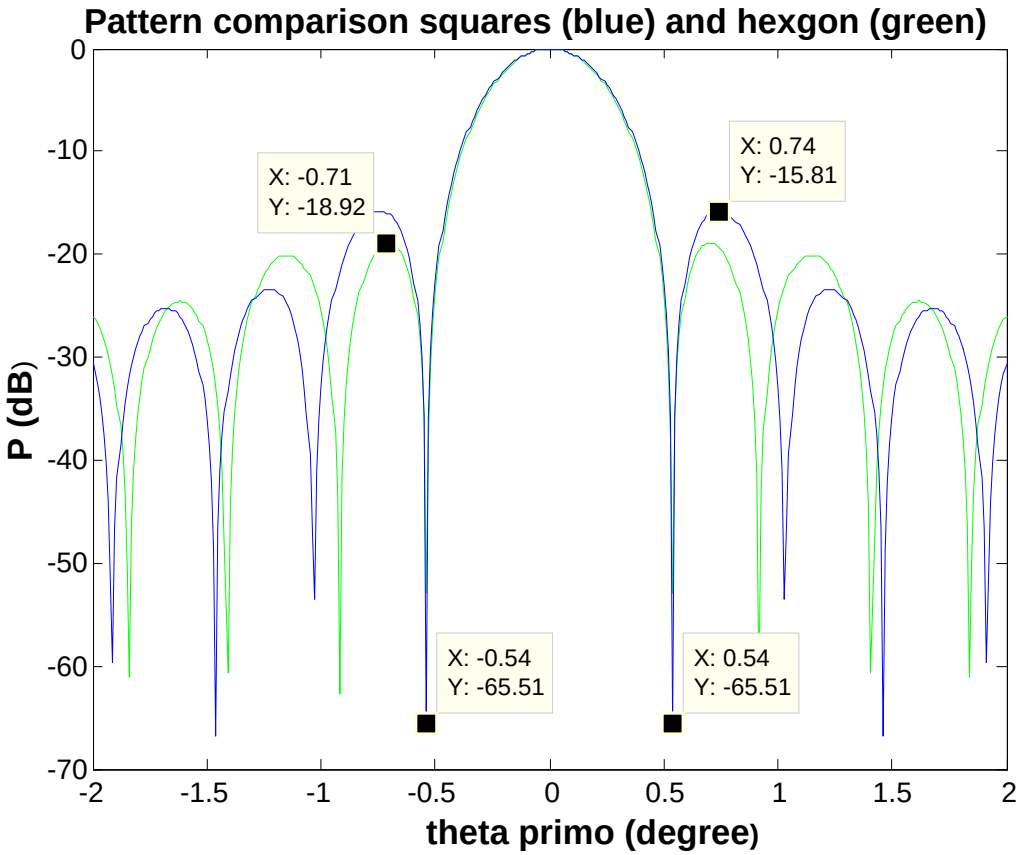

Fig. 4.15: Comparison square and hexagon scalar power pattern K=0 and C=0

Multiple scalar patterns are represented and compared to the square array configuration. For the hexagon array we have a gain in power for the scan angles, for example we have a gain of 2.24 dB in comparison with the square configuration for $\varphi = 0^{\circ}$ and $\theta = 16^{\circ}$. In the next figure if we consider Eq. 3.18 with K=0 an C=0

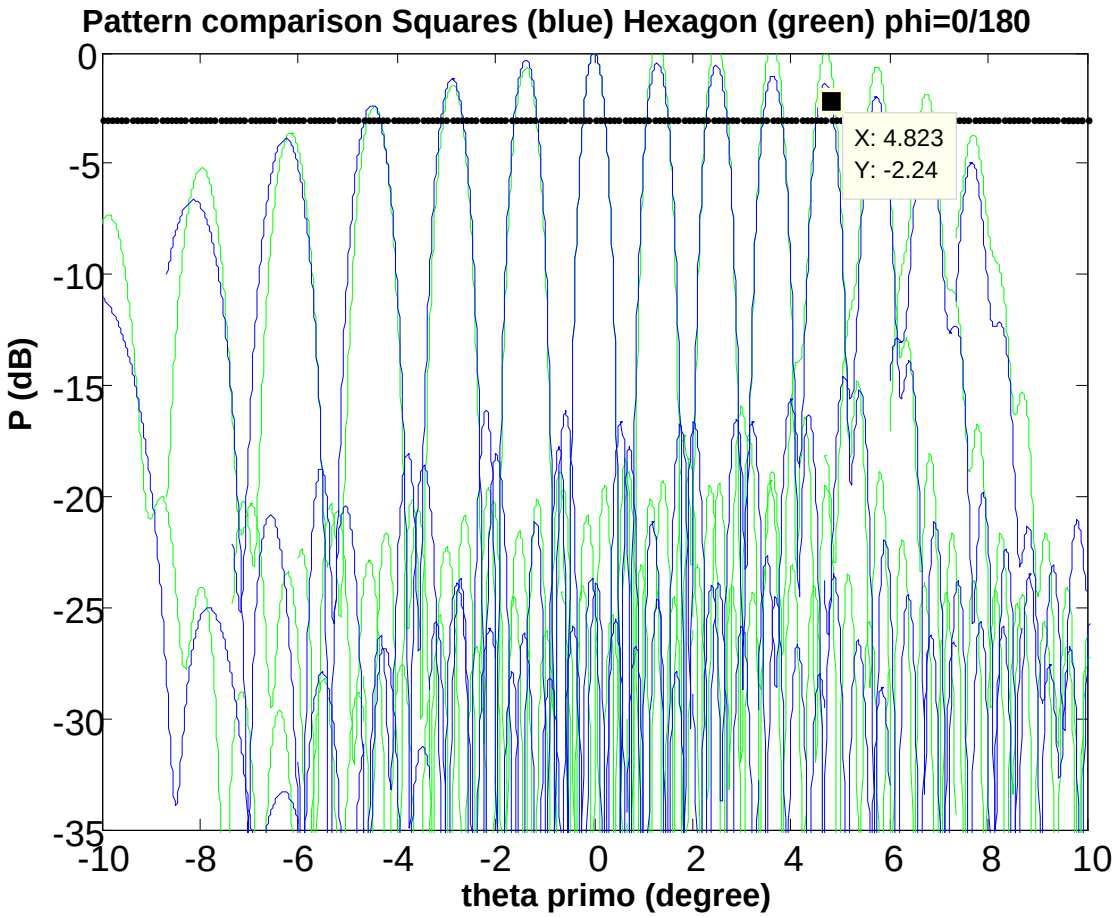

Fig. 4.16: Comparison square and hexagon multiple power pattern K=0 and C=0

4.4. Conclusions

In this chapter different array configurations are studied to obtain better performance of the antenna architecture. All of them are excited with planer wave and are studied considering that the wavelength is much smaller than the dimension of the dishes. The Geometrical Optics theory is applied.

The phase tilt is discussed, concluding that it has similar behaviour applying scan to the array.

For triangle configuration, bigger side lobe level difference is obtained. The inconvenience of this system is that the elements are not equidistant. The beam width is of 1º equal to the theorical value.

For the hexagon configuration, the side lobe level is bigger than for the case of the square configuration. This will permit to better distinguish the main beams from side lobe beams. For synthetic radiometry applications the hexagon array

configuration is used, due to its better scan performance. There is a considerable power gain for angles that are different from boresight.

5. Physical Optics. Plane wave

5.1. Introduction

Physical optics (P.O.) is considering the induced currents distribution on the sub reflector dishes. P.O is more often used in the analysis of electromagnetic scattering. The field is determined by calculating the radiation integral. The double integral calculus elevates the cost in terms of time. In our case this highly concerns us given that the dimensions of our system are very large. In terms of wavelength the time relation is quadratic with the antenna dimensions. The assumption that plane wave is incident is made. P.O is more accurate than G.O. Nevertheless, its disadvantage is that it is slower.

The reflectors dishes are meshed in small planar triangles. The analysis of the entire system, the sub and the main reflector are provided. In all cases just the boresight is considered. We make the assumption that when plane wave insides the system, the polarization is parallel (see Chapter.3.3.11. for more details)

5.2. Eclectic field irradiated of currents distribution

It is possible to describe an antenna in terms of its equivalent radiating currents in free space. We represent the electric field generated by this currents' distributions, considering Maxwell equations in linear, isotropic, with no dispersion and homogeneous space as was explained with more detail in Chapter 2.6 The equivalent radiating currents can be obtained in terms of field as discussed in [8].

$$\begin{aligned} \mathbf{J} &= 2\mathbf{n}\times\mathbf{H} = \mathbf{y}h_x + \mathbf{x}h_y \\ \mathbf{M} &= -2\mathbf{n}\times\mathbf{E} = 0 \end{aligned} \tag{5.1}$$

where $\mathbf{J}$ is evaluated from the incident field on small planar metallic surfaces. These surfaces have triangles shapes as shown in Fig. 5.1. As discussed in [12] the side of the triangle should be less then $10/\lambda$.

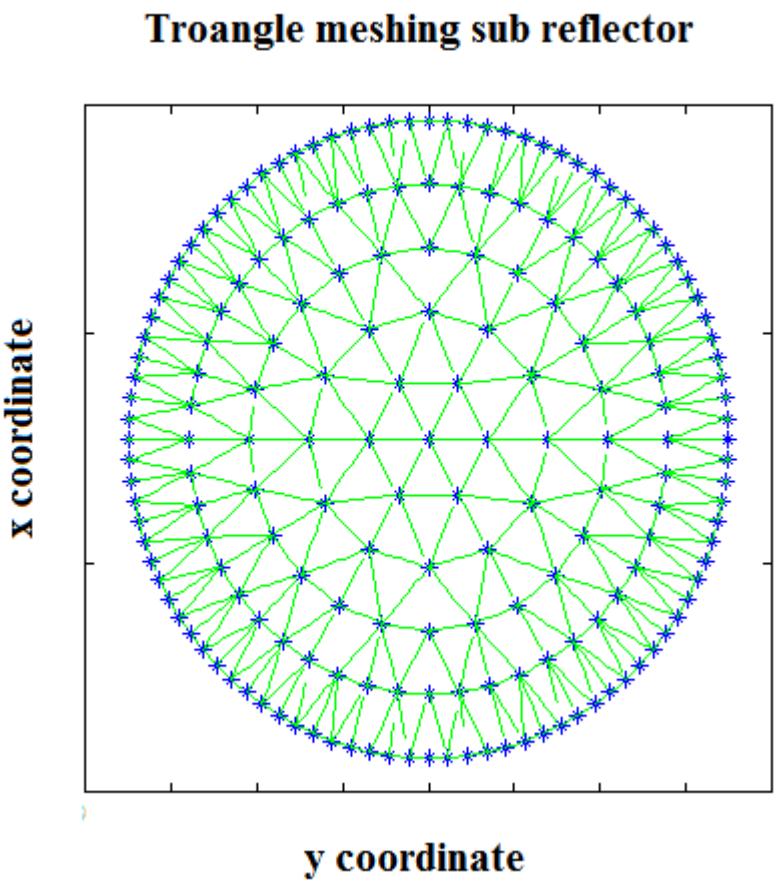

Fig. 5.1: Triangle meshing of the sub reflector

The approximation for arbitrary polygonal scattering surface reported in the work of Gordon [12] is used to evaluate the fields. The Helmholtz integrate which is a double integral evaluated over the surface can be reduced to line integral evaluated over the boundary of the surface by an easy application of Green’s theorem.

The analysis is made in transmission mode. The induced currents on the sub reflector are calculated and as well as the scattered field. Then the currents on the main reflector are computed considering the scattered field from the subreflector. There is always the hypothesis of far field. All the possible contributions are superimposed obtaining the total far field radiated by the system.

5.3. Total system analysis

The observation is made in a circle centred in the centre of the main reflector in a distance of 1800λ. For better representation the x axis is scaled. There are two angles for the maximum radiation, one in the desired direction and the other one at 180° of it.

When the entire system is considered, the representation of the power pattern is not the expected, due to hardware limitations. The number of triangles is 6 circles.

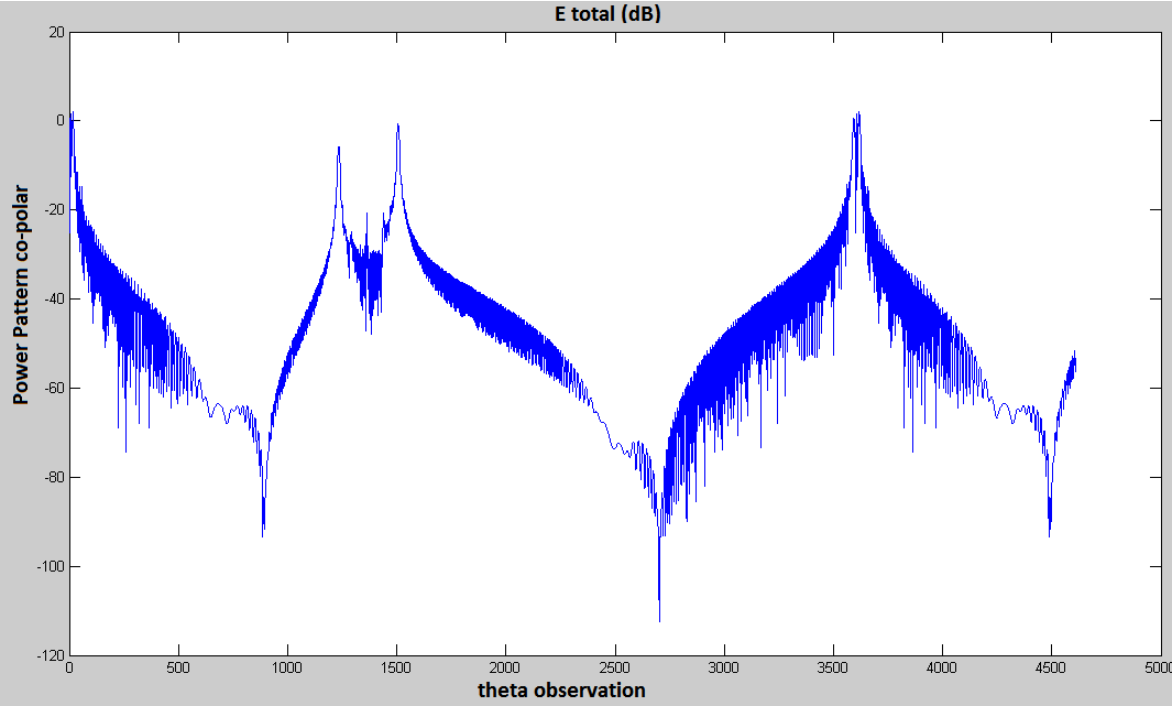

Fig. 5.2: Power Pattern co-polar component for the entire system

If we scale the entire system with 10, we do not obtain any improvement, as shown in the following figure.

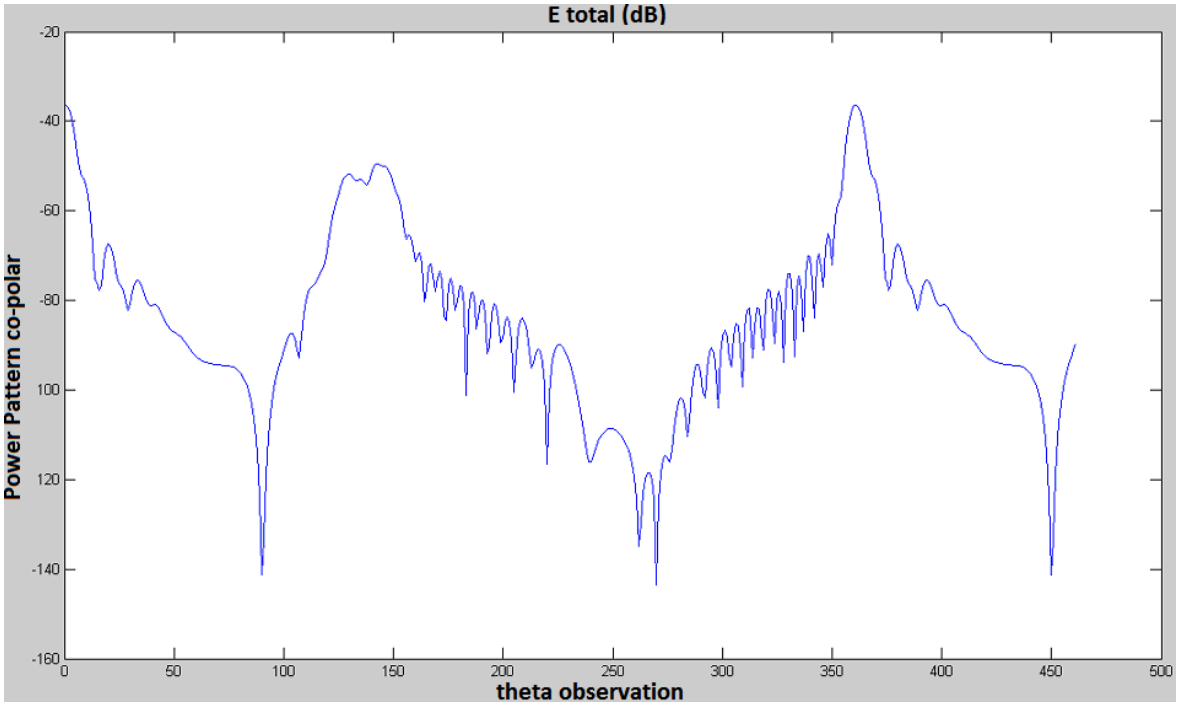

Fig. 5.3: Power Pattern co-polar component for the entire system scaled

If we scale the dishes with 10, we obtain the beam width of 10° (First Null Beam width) in the boresight direction just as we expected (see Eq.2.1). The reason is that if the focal length is larger in proportion, the dishes are flatter and the triangles can better approximate the paraboloid. If we consider one circle of triangles (6 triangles in total), we obtain a main beam of about 10°. If we increment two circles we obtain exactly 10° as shown in the figures below:

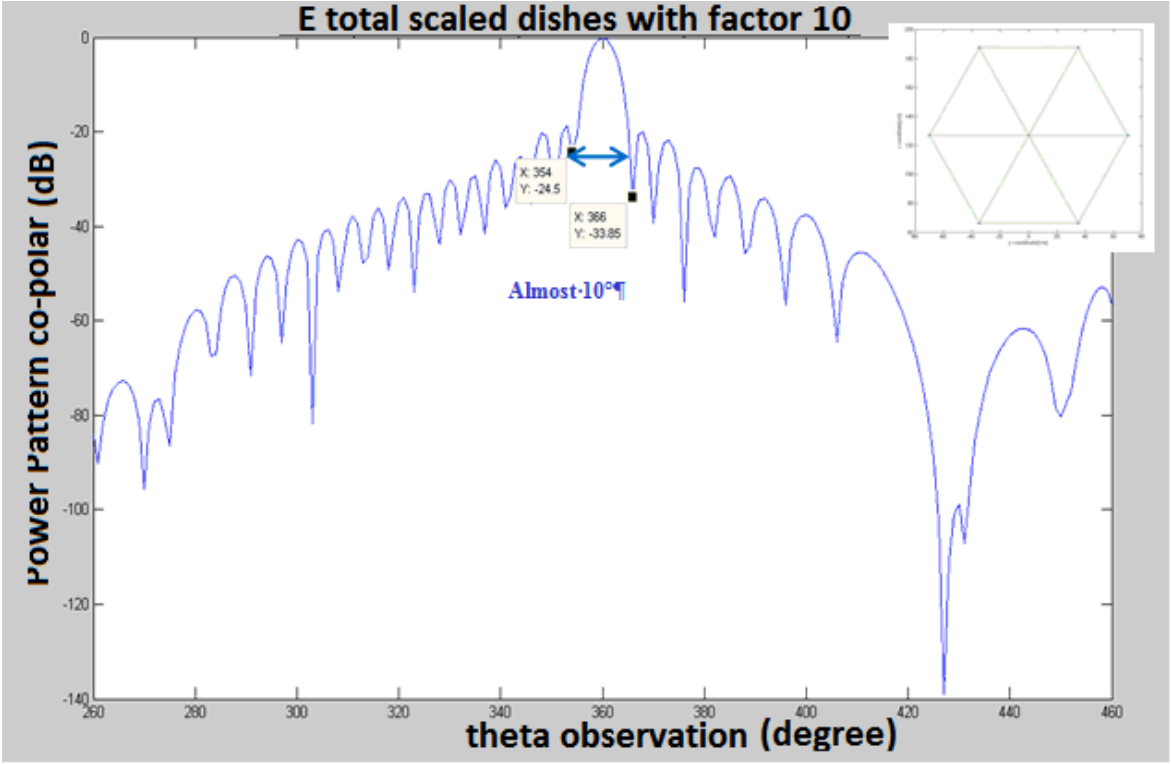

Fig. 5.4: Power Pattern co-polar component for the scaled system one circle

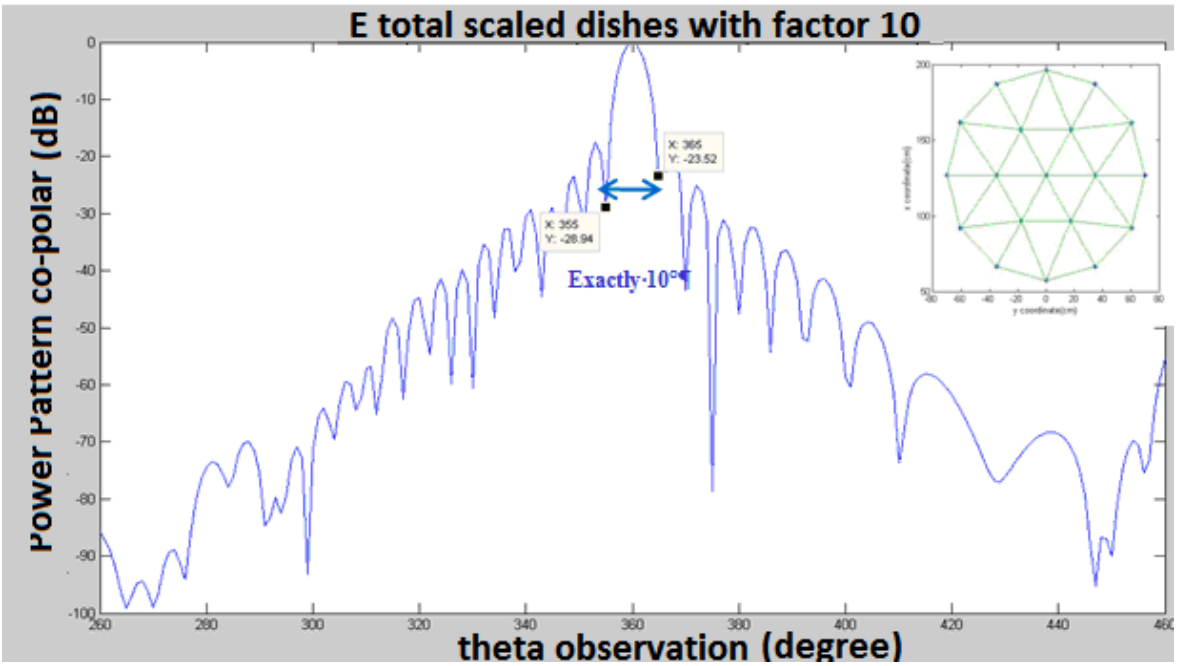

Fig. 5.5: Power Pattern co-polar component for the scaled system two circles

With the real dimensions of the system, there is a need to substantially increase the meshing circles. This leads to an unmanageable computational time.

The contribution of some of the triangles is studied as shown in the next figure. As the software is to be improved, the analysis is just qualitative. Fig.5.6. shows the

power pattern if we consider that just the triangles coloured in green illuminate the main, which is meshed as well with 6 triangles and they all participate in the calculus.

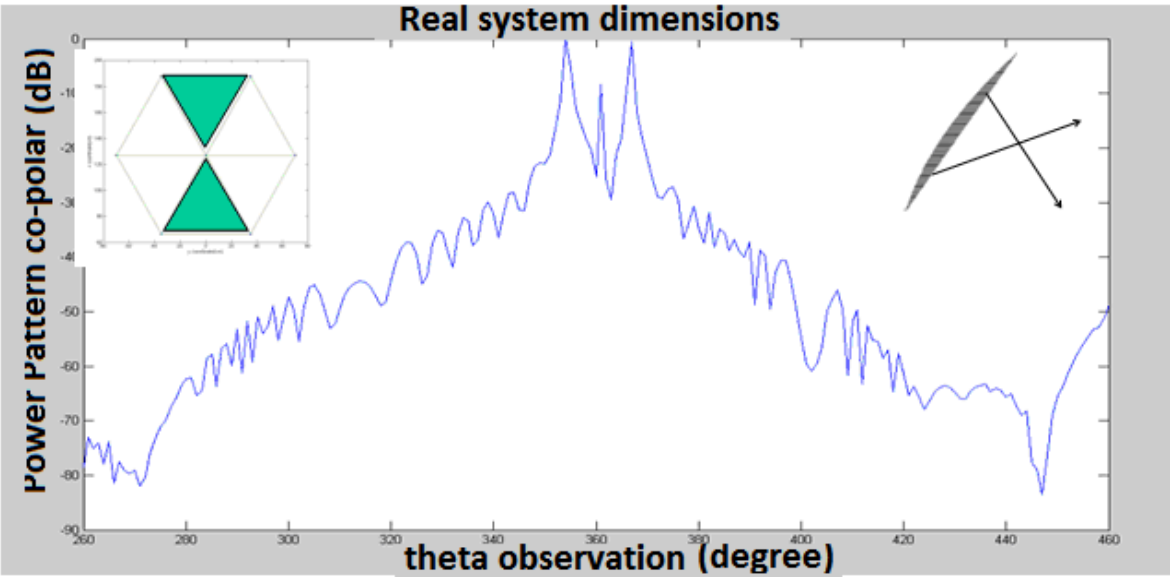

Fig.5.6: Power pattern for two triangles of the sub

As the power pattern considers the centres of the triangles, the two peaks are related to them. In the next figure there we consider four triangles of the subreflector.

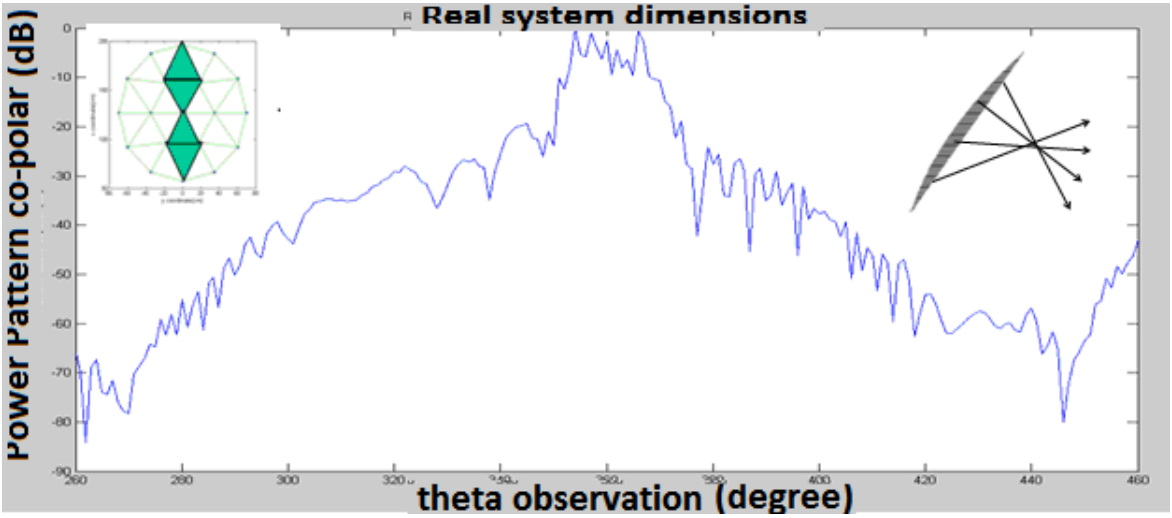

Fig. 5.7: Power pattern for four triangles of the sub

If we increase the number of considered triangles the pattern should be more precise. Instead it is worse

5.4. Analysis of the sub reflector

The power pattern is plotted for just the sub reflector. One circle of triangles is considered, meaning that the total number of triangles is 6. The observation is made at 1800λ in the first figure and the centre of the circle is the centre of the sub reflector. The co-polar direction is x axis. There is a cross-polar component as well due to the system asymmetry in the y axis.

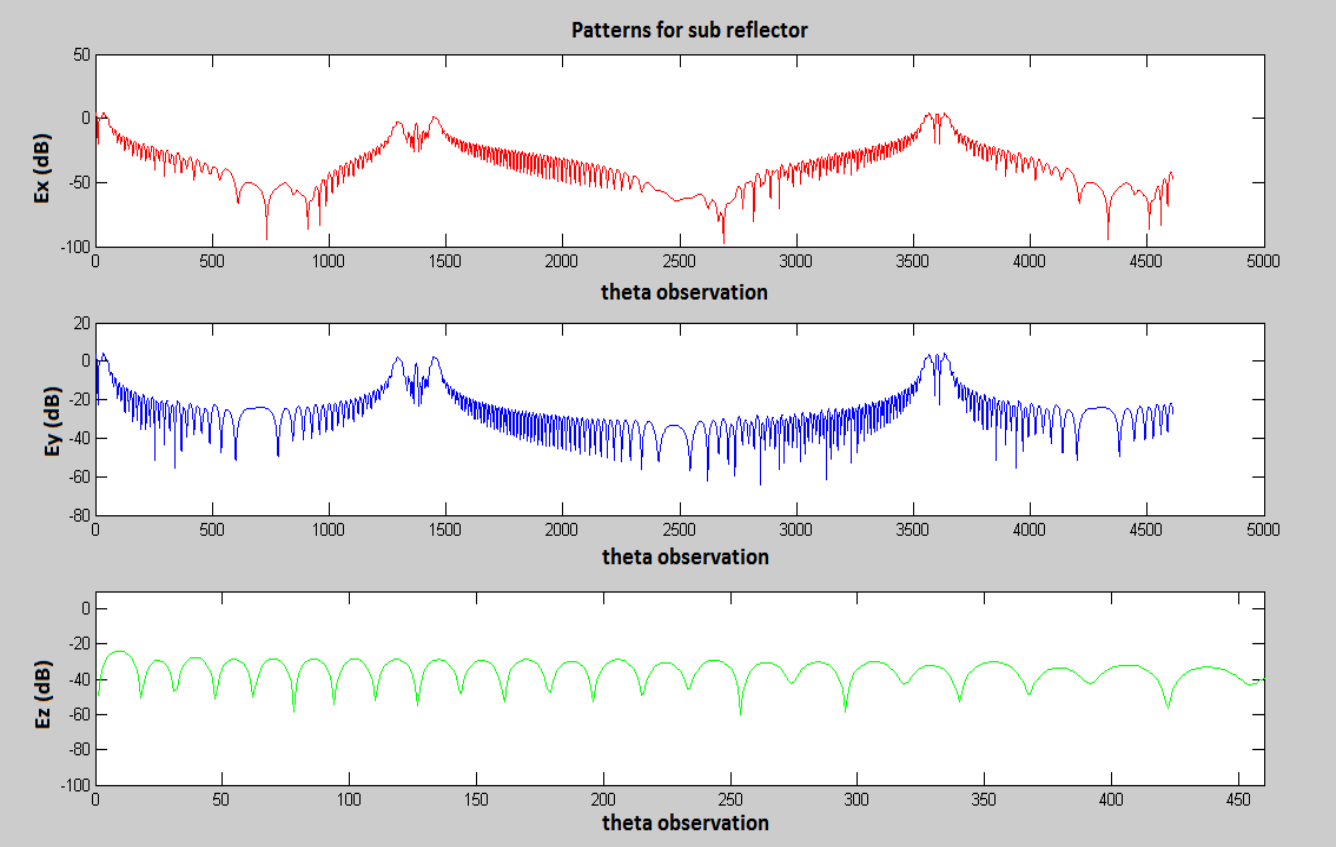

Fig. 5.8: Power pattern for four triangles of the sub 1800λ distance

The previous figure shows that the distance of observation is very important. In the next figure we increase it to 18000λ, so the main beam is better determined.
If we increase the number of circles, with 6 circles we have 187 elements. The area of one triangle varies from 8 cm^2 to 1.5. cm^2 . The difference is due to the fact that in the centre the triangles are bigger. With 8 circles, the area of each triangle varies from 4 cm^2 to 0.25 cm^2 .

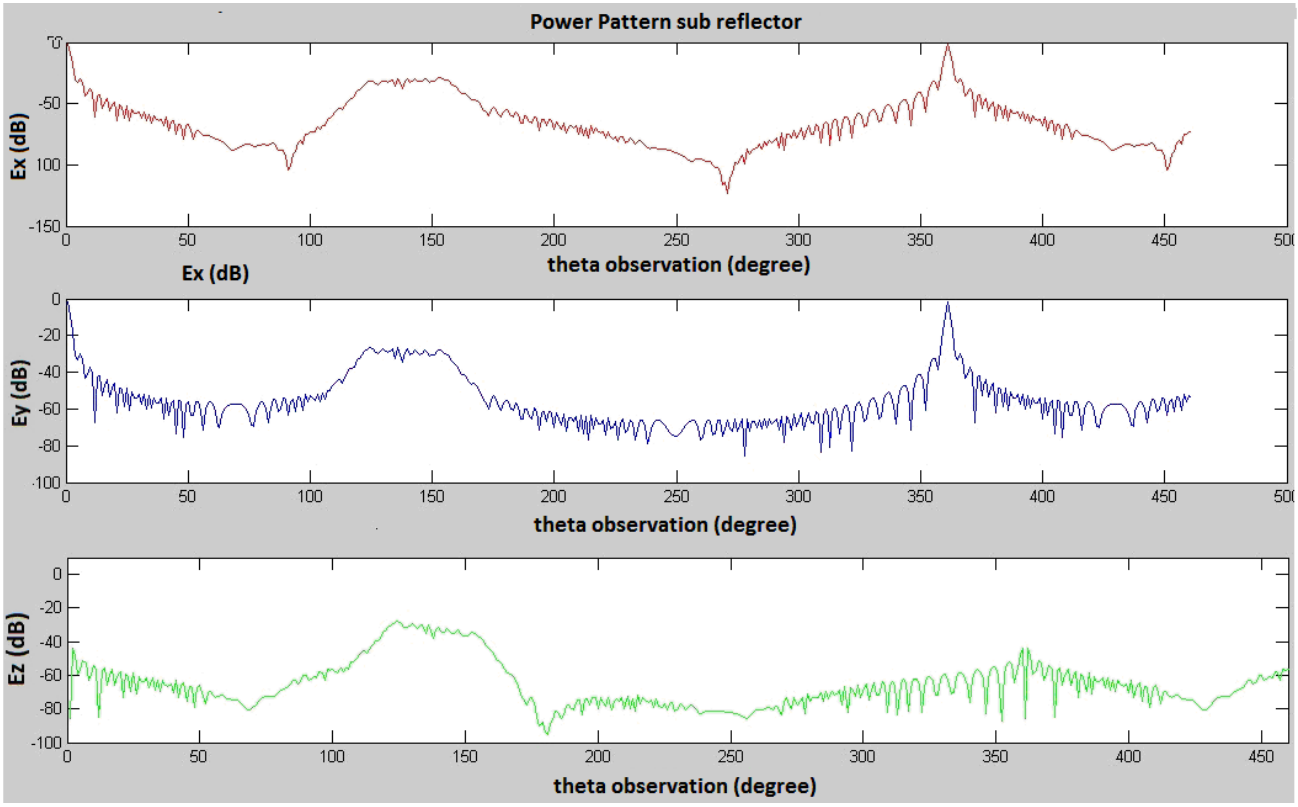

Fig. 5.9: Power pattern considering just the sub 18000λ distance

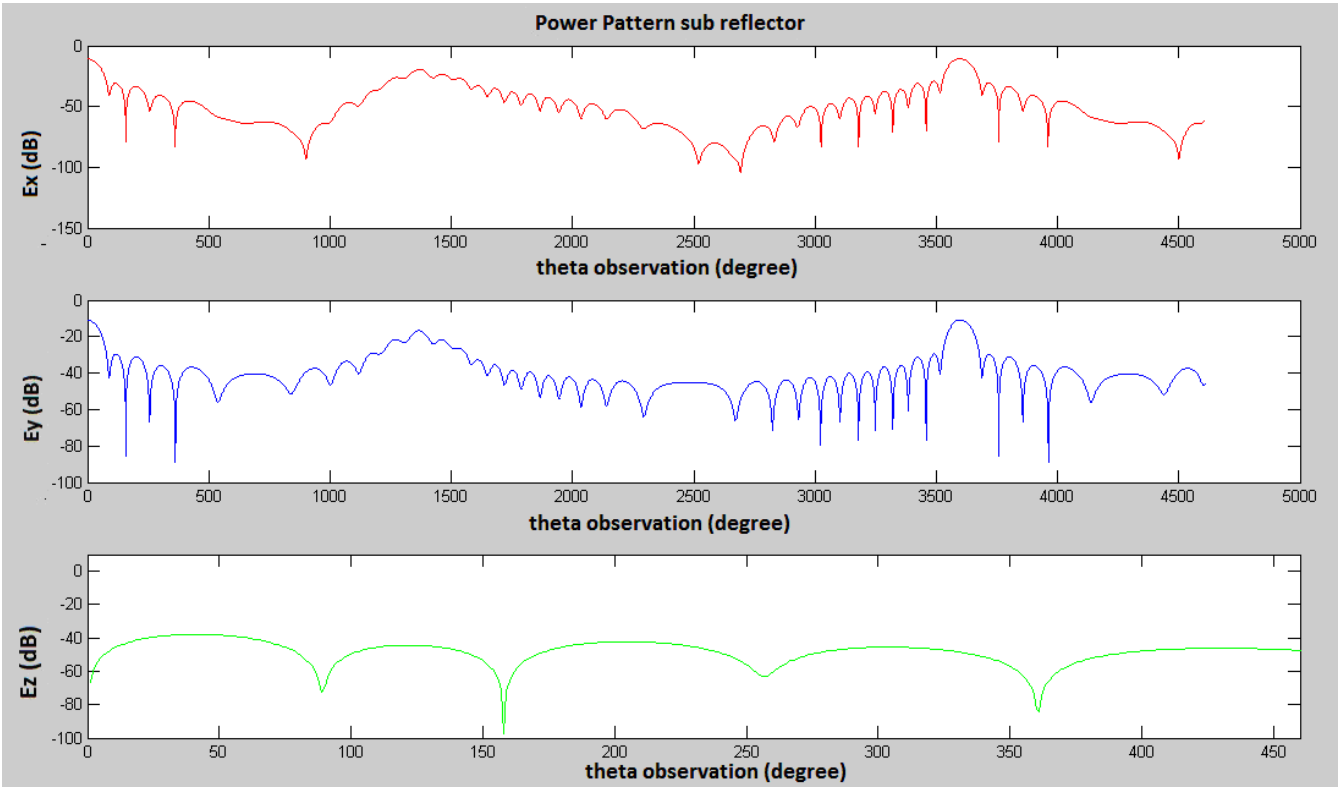

Fig. 5.10: Power pattern considering the sub scaled by 5. 6 triangles

We scale just the dishes by 5 in respect to the dimensions proposed by Fitzgerald [8]. Just one circle of triangles the area is of $9\,cm^2$. We start to see a pattern in the radiations sense.
The same analysis is done for the main reflector (see Appendix C)

5.5. Conclusions

Many applications of electromagnetic theory need analysis of the irradiated fields from structure with big dimensions like the one proposed in this work. The superficial integrals are substitute by integrals over the triangles lattice. This makes the software faster. It was discovered that due to the nature of the paraboloid the triangle should be very small to obtain proper results. When the number of triangles is substantially increased, there are memory limitations of the hardware. If the focal length remains the same and the dishes are scaled, the obtained beam has proportionally valid beam width. If the entire system is scaled, the power pattern does not improve.
We tried to decrease the computational difficulty, with the creation of a program that combines the G.O and P.O. theories: every triangle on the sub reflector illuminates just a part of the main reflector. Unfortunately the obtained results are still not satisfactory.
In the figures of this chapter it is shown that there are two angles for maximum radiation, which differs with 180°: one is in the desired direction and the other one is in the opposite one.

6. Spherical wave (G.O.)

6.1. *Introduction*

The spherical wave is simulated like a cone of rays that emerges from every feed. First, it was described just one element from the array. It illuminates the hall sub reflector. The number of rays is an input that the user of the software can determine.

Second, it was studied the whole array with hexagon geometry, as described in Chapter 4. Each element illuminates just a part of the sub reflector, the entire sub is covered.

6.2. *One element*

Study of just one element of the array is provided. At the beginning the system deployment is considered the same as Fitzgerald [1], where the only one element is position in the centre of the array (see Table 1). The next figure represents the 3D view of the system. We consider 6 rays to understand better the ray tracing. We can observe that from the feed to the sub reflector we have spherical wave, from the sub reflectorto the main reflector we have almost plane wave and from the spherical wave, which is convergent beyond the main aperture. In red are represented the rays that spillover the main dish.

If the array covers the entire sub, there is a lot of spillover, so it is considered to cover 85% of the sub reflector as shown in the figure below. Different representations for different percentages can be seen in Appendix C.

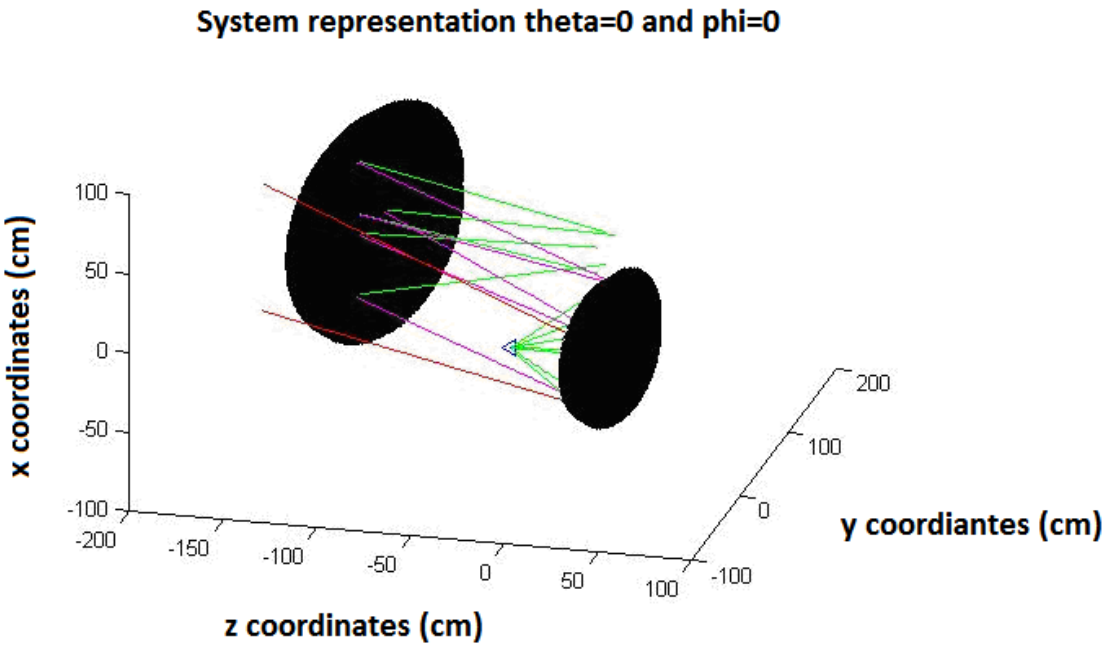

Fig. 6.2: 3D representation one feed Fitzgerald configuration 6 immerging rays

In the proposed software, analysis of 2D is provided (see Fig. 6.3 a). The cone's aperture image is of 5 circles considering the next configuration on the sub dish (see Fig. 6.3 b)). The obtained image in the main aperture is represented in Fig. 6.3 c).

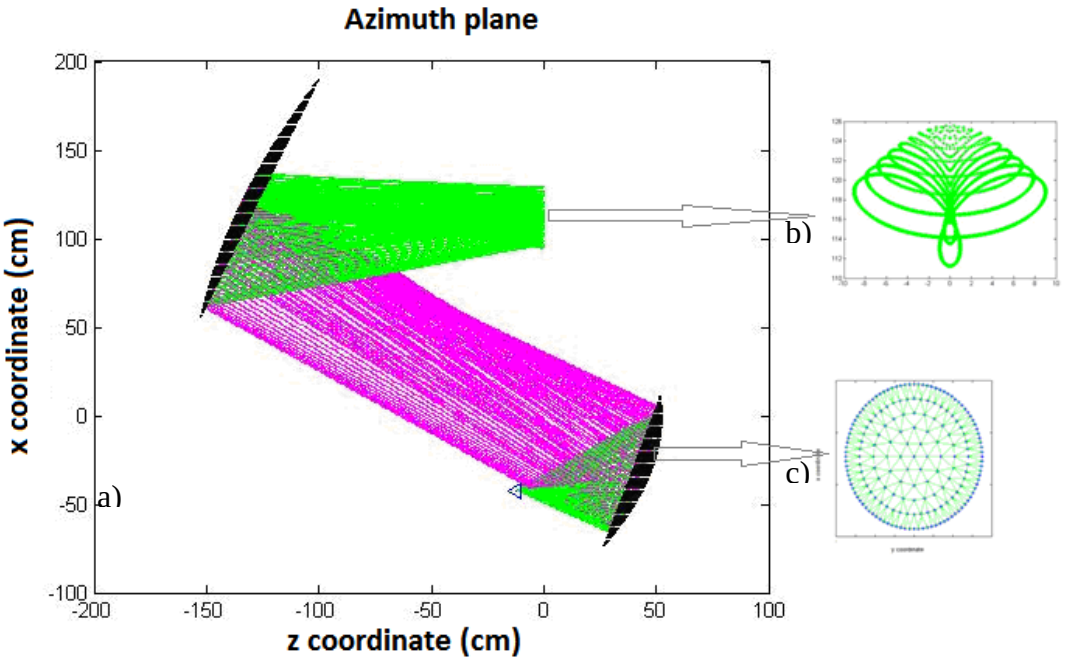

Fig. 6.3: a) Elevation plane, one feed (Fitzgerald configuration). b) Immerging rays on the sub reflector c) Image on the main aperture

As it was observed, if the array is positioned at –l the image of the array in the main aperture is not exact. The proposed solution is to position the feed at –fm, just under the main reflector. This way we have more accurate reproduction of the image in the aperture (see Fig.6.7.). In the green circle the image of the aperture is plotted, the blue stars are the triangles vertex and the red ones are the triangles centres. More detailed analysis of the aperture is exposed in the next chapter. Spillover is still observed if we illuminate the entire sub, for that reason we give certain directivity of the feed. In the figure below an 85% of the main has been illuminated.

The feed is placed at z0=-fm as shown in the figure and is positioned in the centre of the sub.

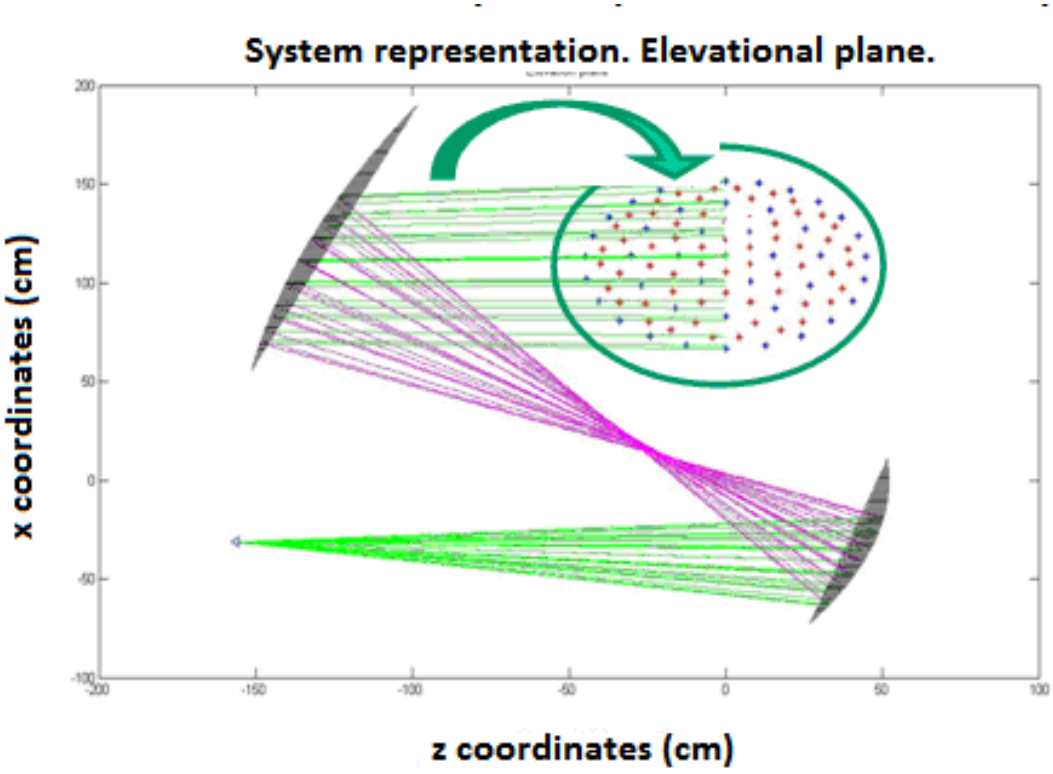

Fig. 6.4: Elevation plane one feed at focal length with representation of the aperture

The system is plotted in 3 dimensions as well in the following figure:

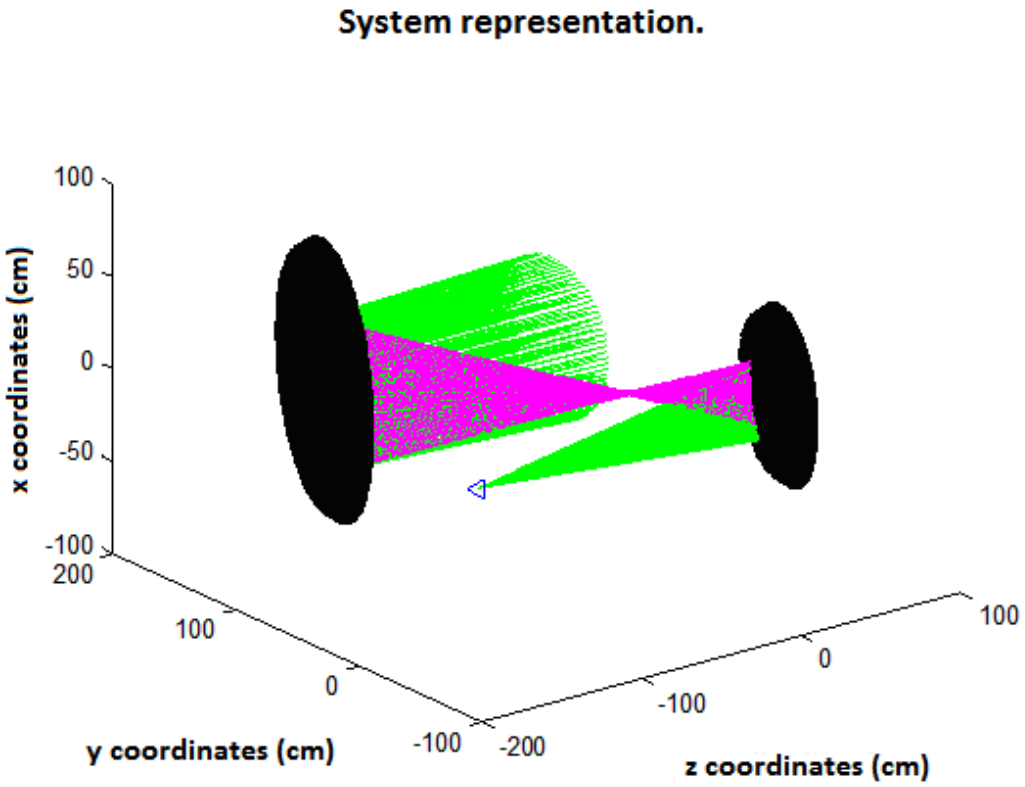

Fig. 6.5: 3D system representation one feed at focal length

6.2.1. Study of the aperture

When we consider the system configuration as explained in the paper of Fitzgerald [8] the following images in the aperture are obtained for different ray's number.

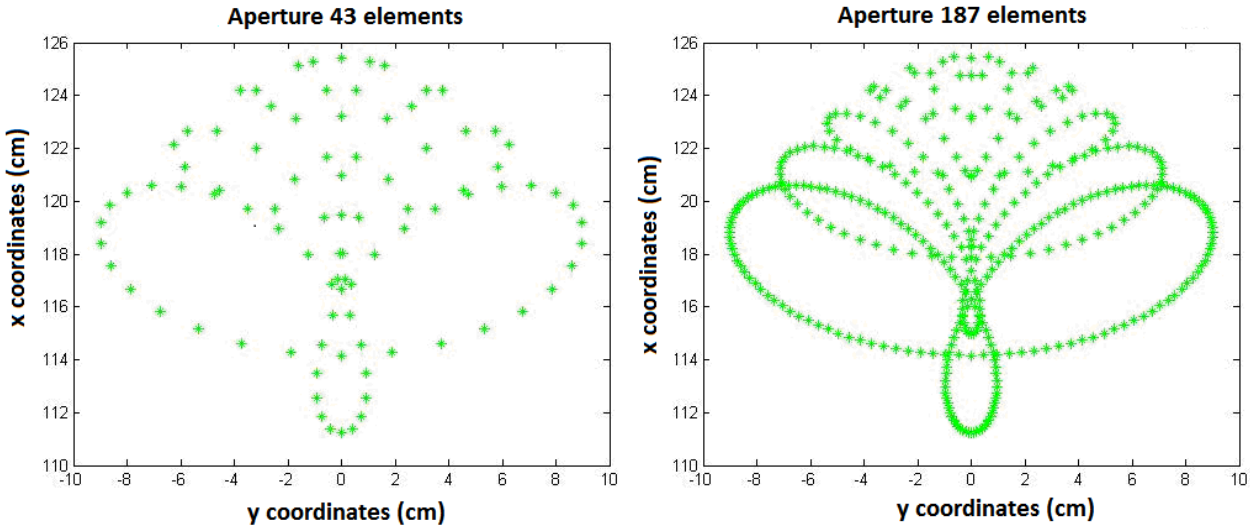

Fig. 6.6: Aperture for different rays' number z=-l and x=h

If we place the feed in front of the sub reflector, more precisely in the coordinate x=h2 (see Fig. 3.2.), the image in the aperture is plotted in the Fig. 6.6. The gray circle behind it represents the real main aperture.

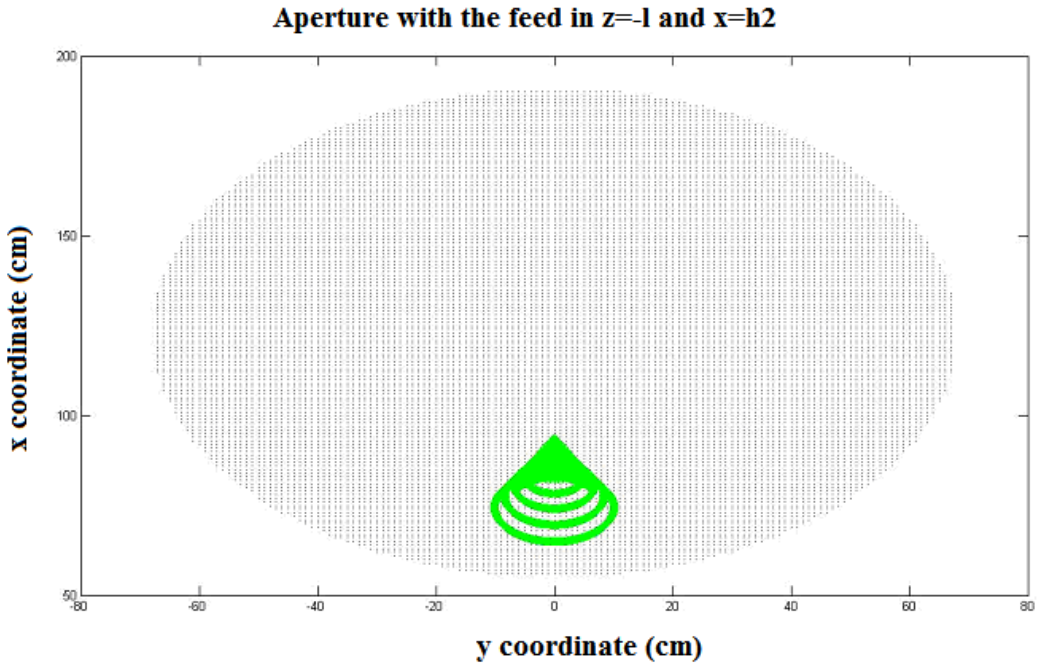

Fig. 6.7: Aperture with the feed in z=-l and x=h2

This configuration does not satisfy us, as the real image on the aperture is very important. As a solution, the feed was plotted at –fm just below the main as was explained in the previous chapter, and the next image was obtained.

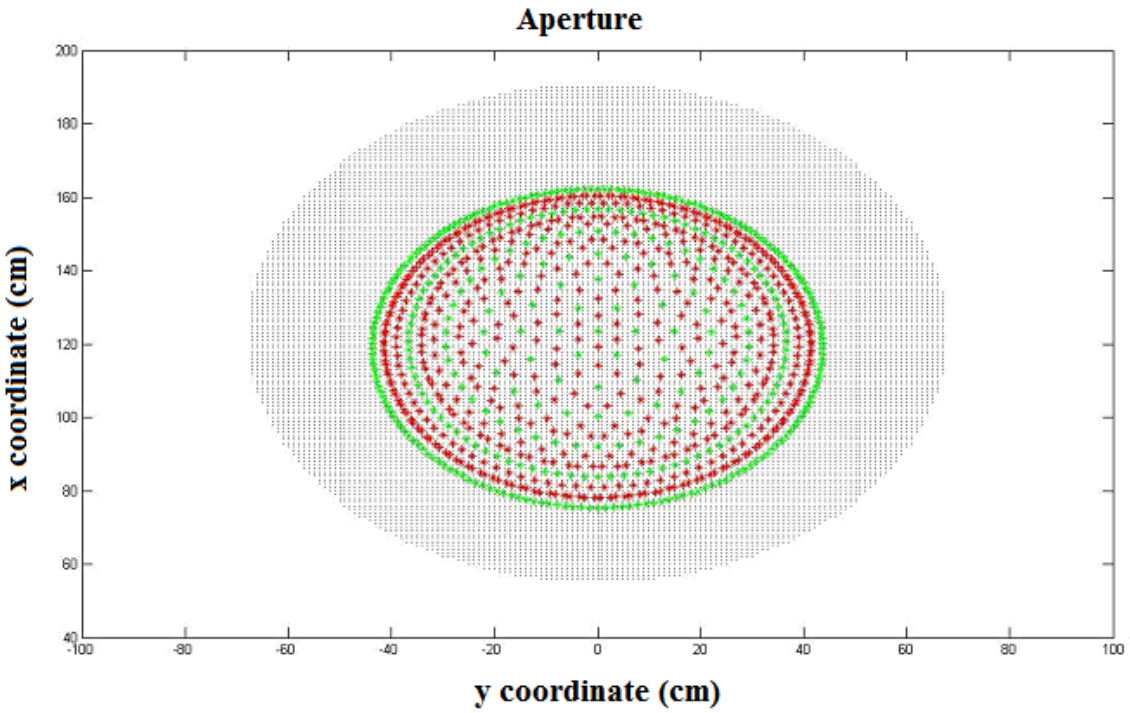

Fig. 6.8: Aperture with the feed in z=-fm and x=h2

More precisely the feed is in 210λ distance from the sub reflector. The percentage that was covered was 75%. As it is shown, not the entire main is covered. If we plot the system and the aperture, we have full illumination of the main dish.

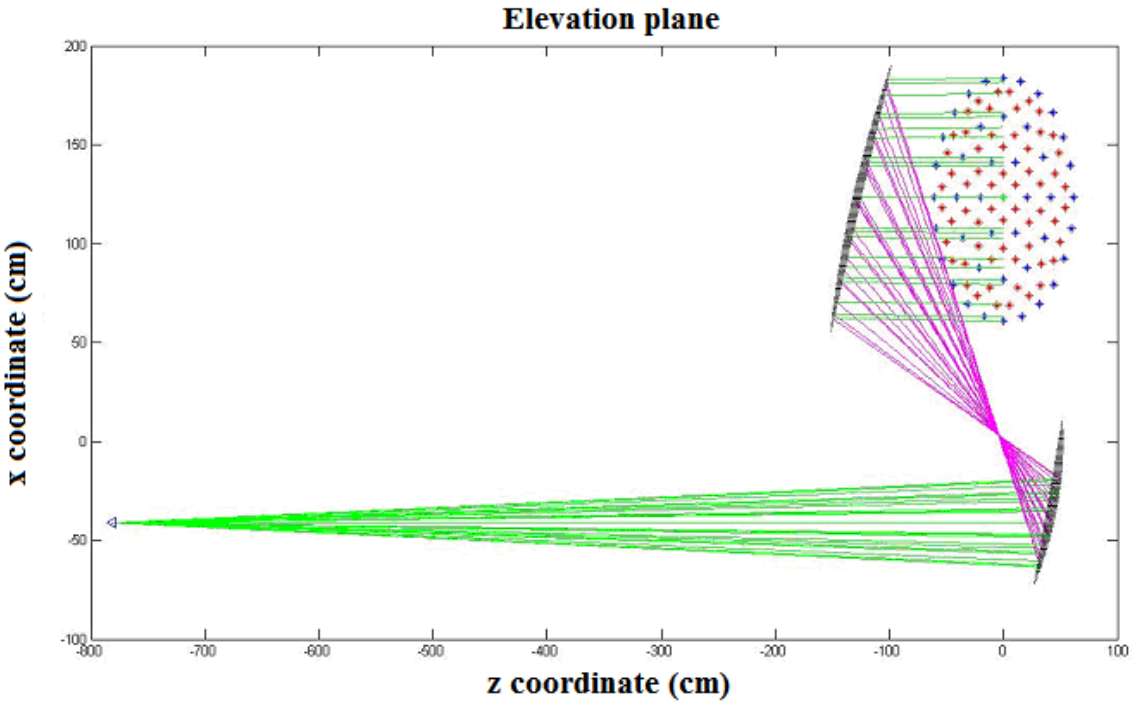

Fig. 6.8: System representation with the feed in z=-4*fm and x=h2

The hypothesis that the feed is at -100*fm is made to verify the plane wave condition, due the fact that the emerged rays are parallel between them. We observe that the system magnifies the image, the same was observed in Chapter 3. The rays are confocal at the focal plane and the far field pattern is the same as in the plane wave conditions.

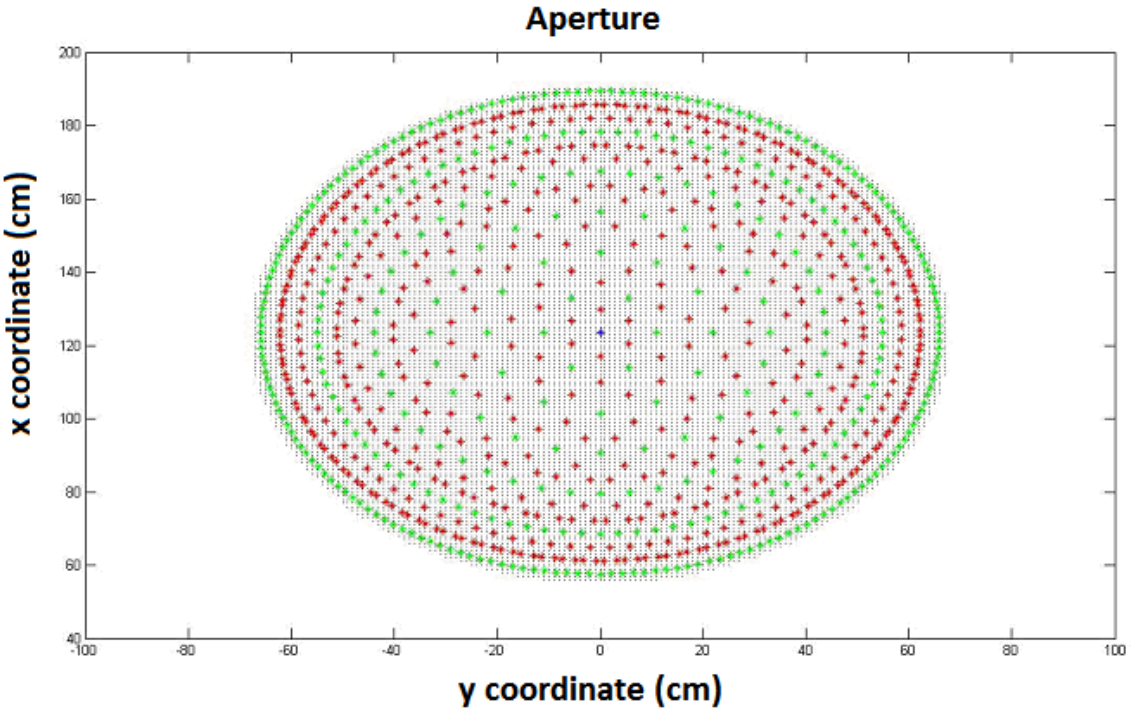

Fig. 6.9: Aperture with the feed in z=-100*fm and x=h2

The formulas for the power pattern are:

$$\left|P(\theta',\phi')\right| = 20\log\left|\sum_{l=1}^{M} Area_l * E(x'_l, y'_l) * \exp\{-jF(x'_{(l)}, y'_{(l)})\} / (Los_{(l)} + Lsm_{(l)} + Lma_{(l)}) * \exp\{j2\pi(fm/l)\sin\theta'(x'_{(l)}\cos\phi' + y'_{(l)}\sin\phi')\}\right|$$

where M is the total number of reflected rays and the power pattern is represented in the figure bellow:

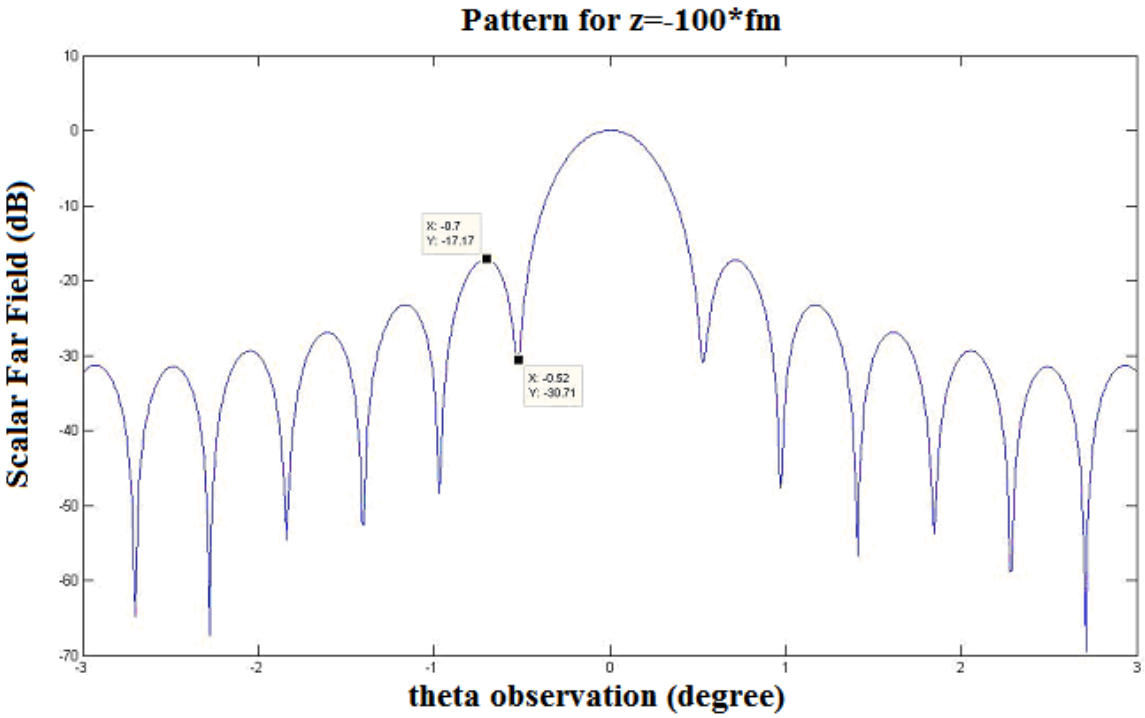

Fig. 6.8: Scalar power pattern with the feed in z=-100*fm and x=h2

6.3. Hexagon configuration. Spherical wave

Different positions of the array are discussed to define the best position. Every feed illuminates a portion of the sub reflector, in such way that the sub reflector is covered entirely. The spherical wave was simulated in the same way as in the case of one element (See Chapter 6.2). The scalar power patterns and the phase distribution are represented.

6.3.1. Aperture view

If the position of the array is the same as in Chapter 3, the observed image in the main aperture is shown below. The considered array's element distribution is represented in Fig 6.10 b). In the next figures, the reflected rays are plotted in green and the main aperture is in black.

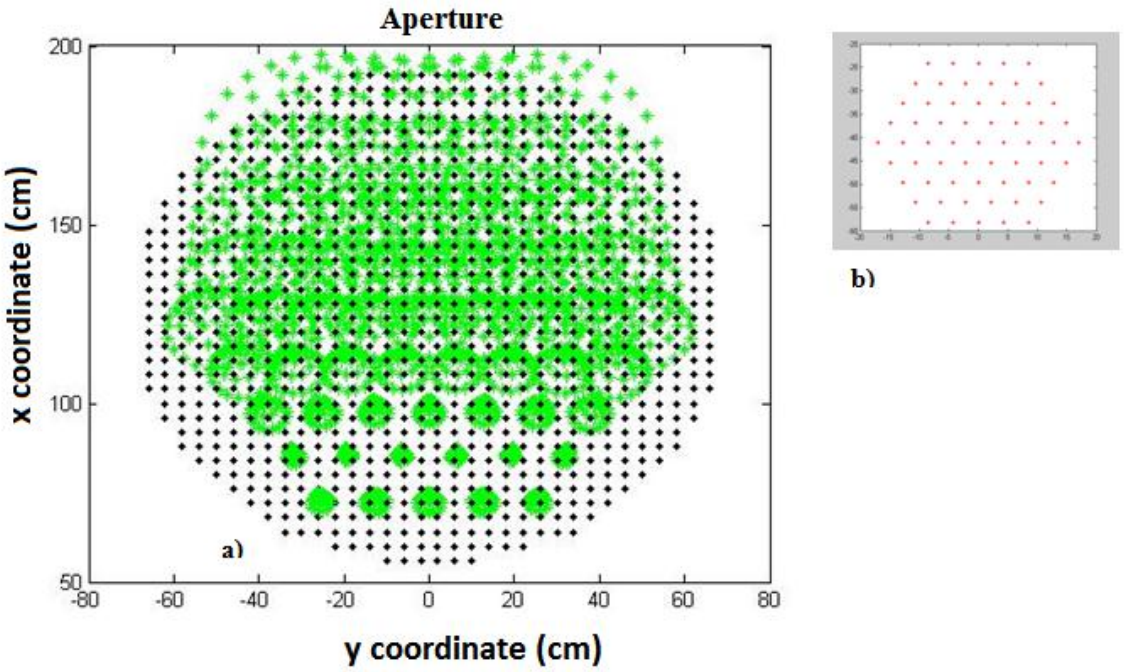

Fig. 6.10: a) Aperture feed at z=-l and x=h b) the correspondent array distribution 61 elements

The upper part of the main reflector expands the image meanwhile the down part reduces it.

If we place the array at 210λ from the sub reflector, just below the main dish and its centre is positioned in front of the sub reflector's centre, we obtain a better image, although there is some spillover. The same feed distribution was applied. More concentration of rays is presented in the centre of the main aperture.

The upper part of the main reflector expands the image, meanwhile the down part reduces it.

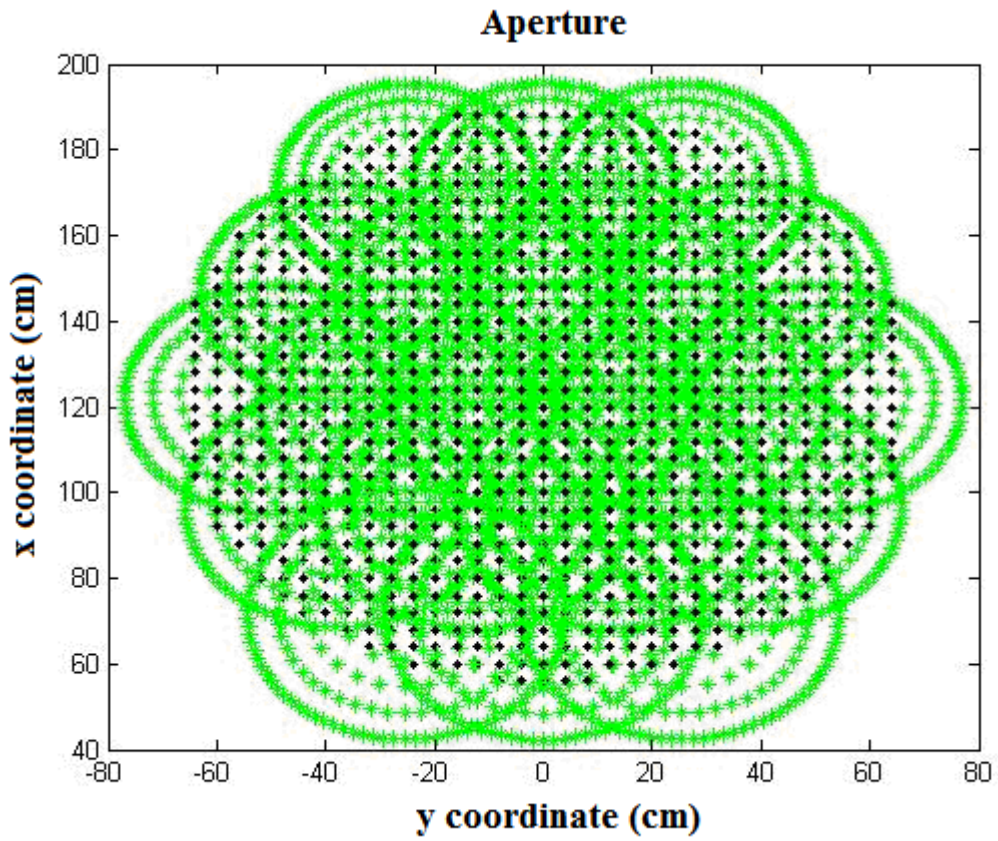

Fig. 6.12: Aperture feed at z=-fm and x=h2 (Fitzgerald) [8]

The representation of the spillover is plotted in Appendix C (Fig.13).

6.3.2. Phase distribution

First, the phase for just one feed is plotted at 210λ distance from the sub reflector. The bar diagram is plotted as well.

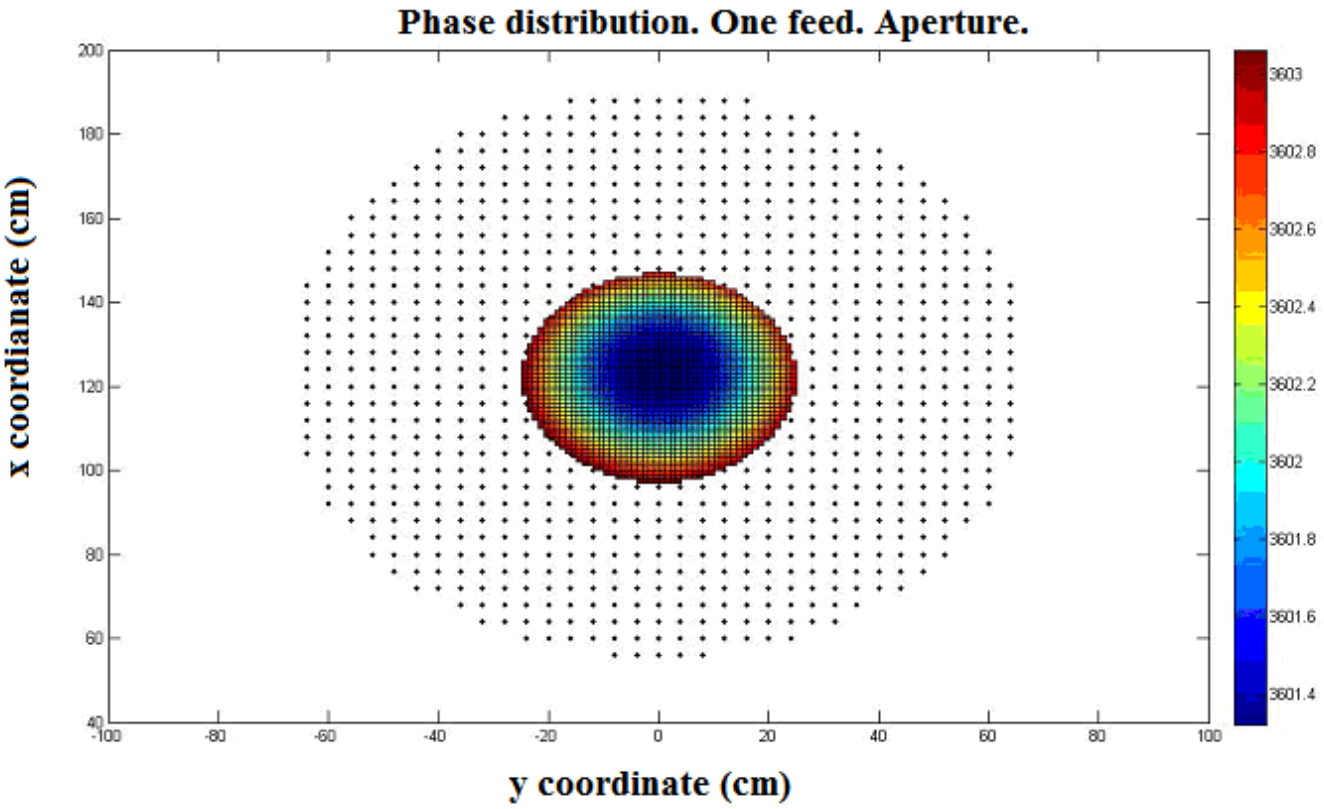

Fig. 6.13: Phase distribution. One feed

Second, the entire array is considered and it was observed there is phase interference between the elements.

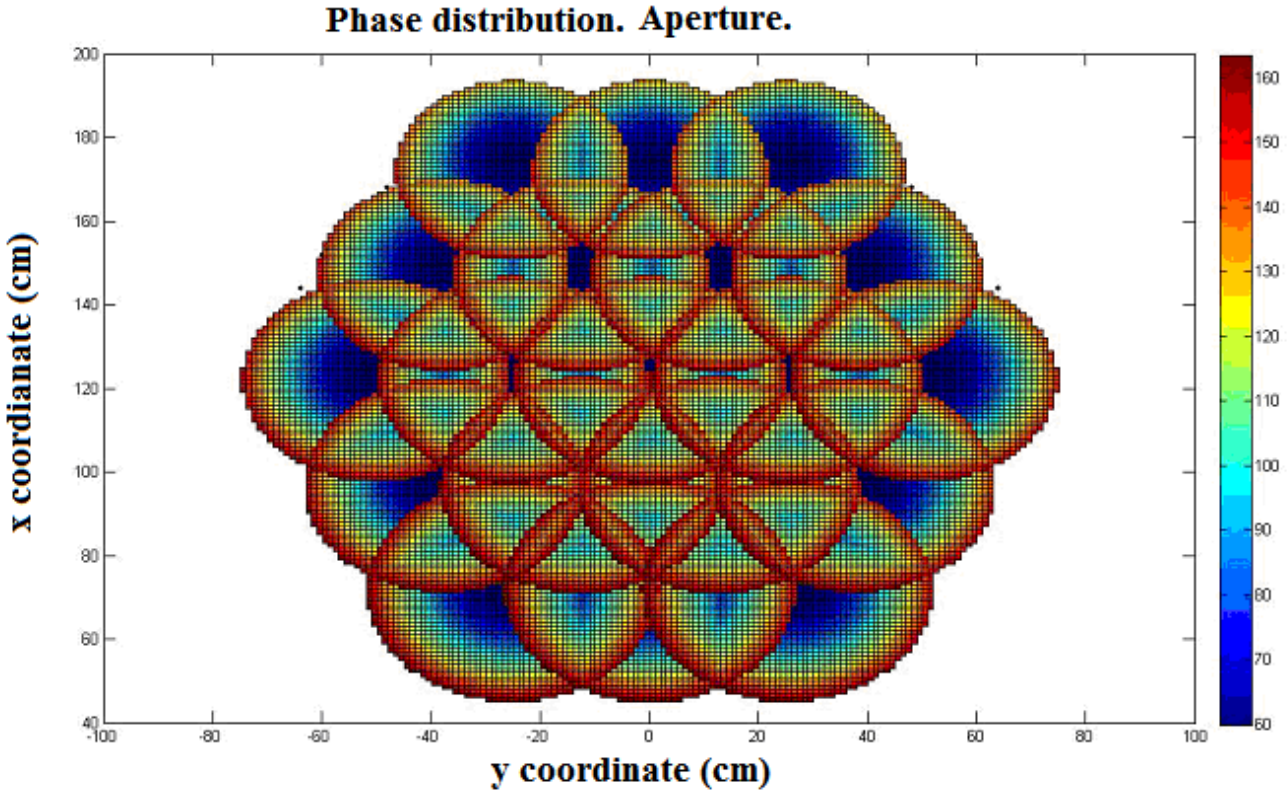

Fig. 6.14: Phase distribution. Entire array.

If we consider the entire array and we apply elevation scan with $\theta = 10^{o}$, the obtain phase distribution is as follows:

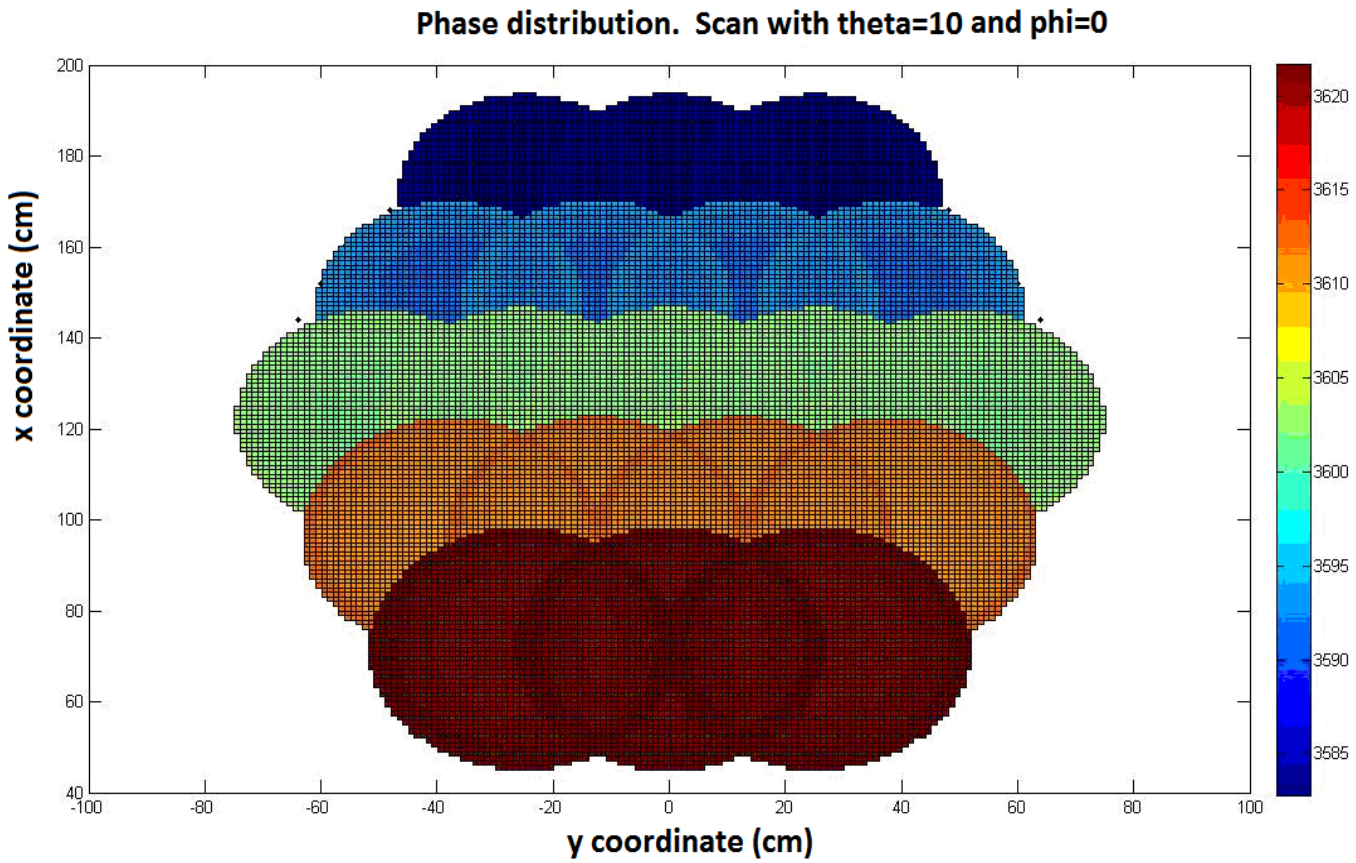

Fig. 6.15: Phase distribution. Entire array

II we plotted the phase distribution in degrees we observe figure below.

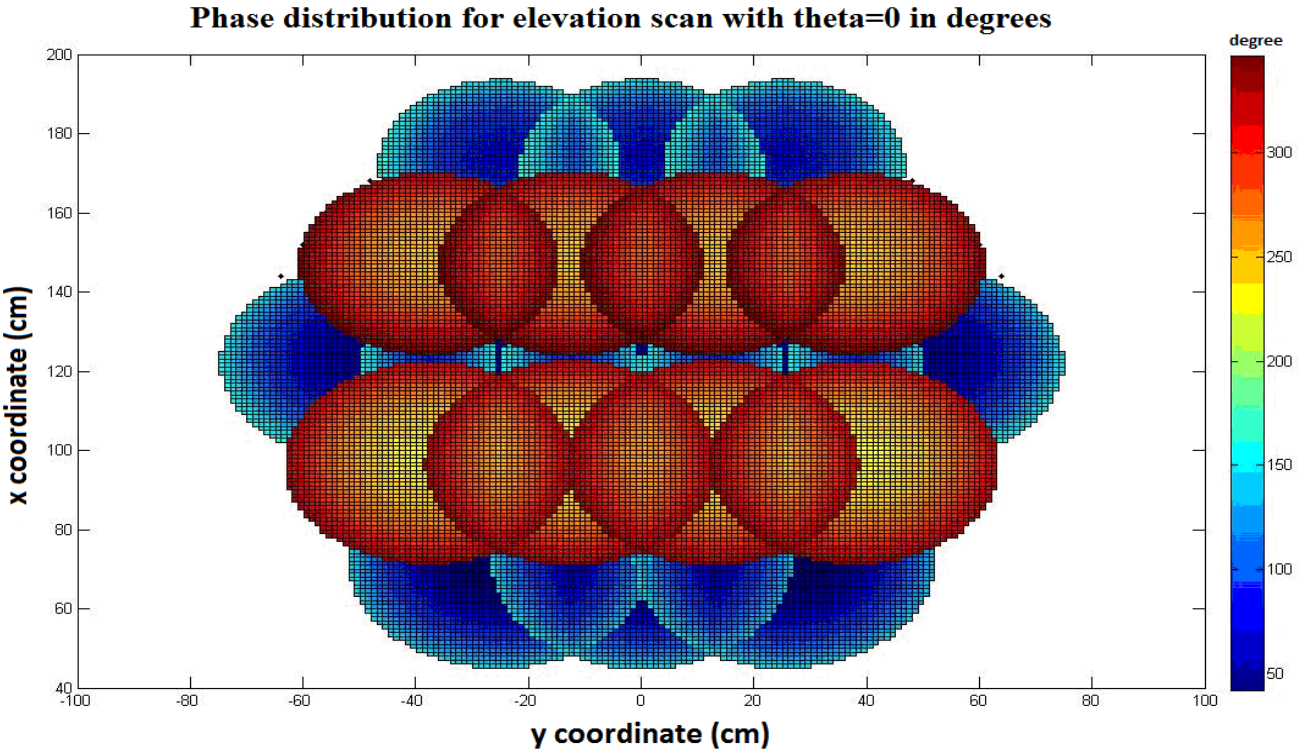

Fig. 6.16: Phase distribution. Entire array

6.3.3. Scalar power pattern

The pattern was implemented in two different ways: one is by considering the area as the previous cases, and the other one is with the command in MatLab griddata. The array was considered with 169 elements, it is shown in Fig. 6.17 a) below:

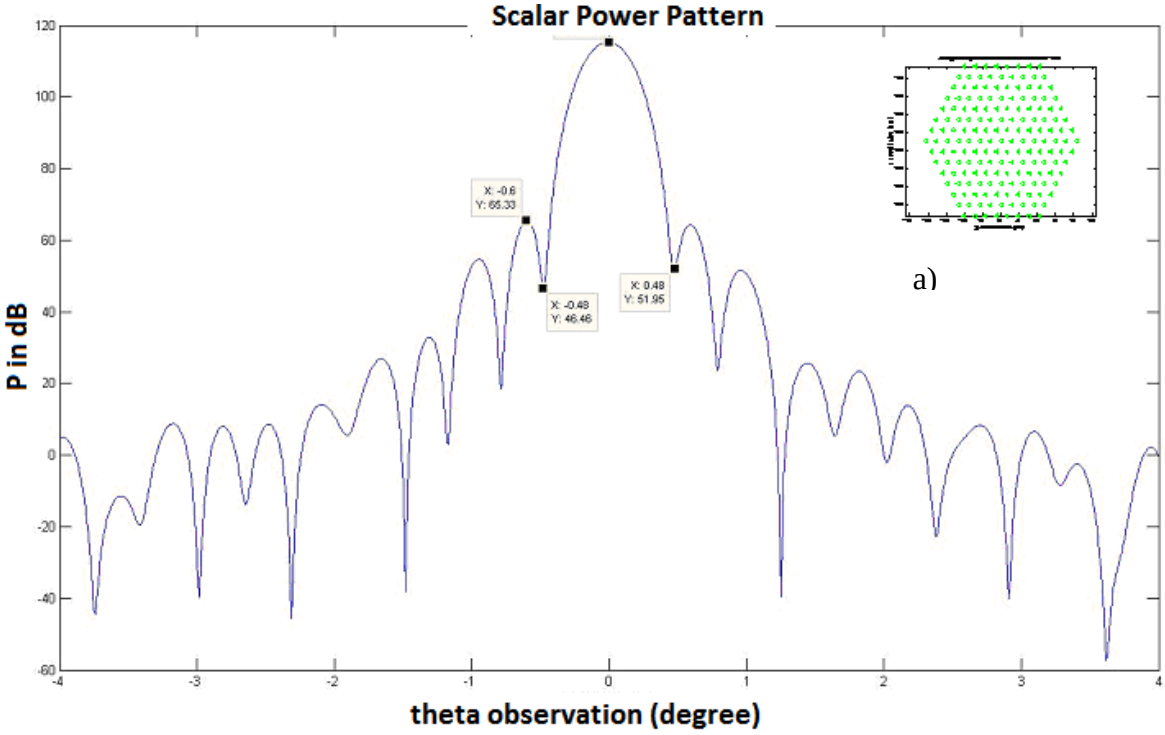

Fig. 6.17: Scalar power pattern with area

Griddata gives an independence from the position of the reflected rays on the aperture. This means that if we change the configuration of the array from hexagon to triangle, the program will be able to calculate the scalar power pattern as well.

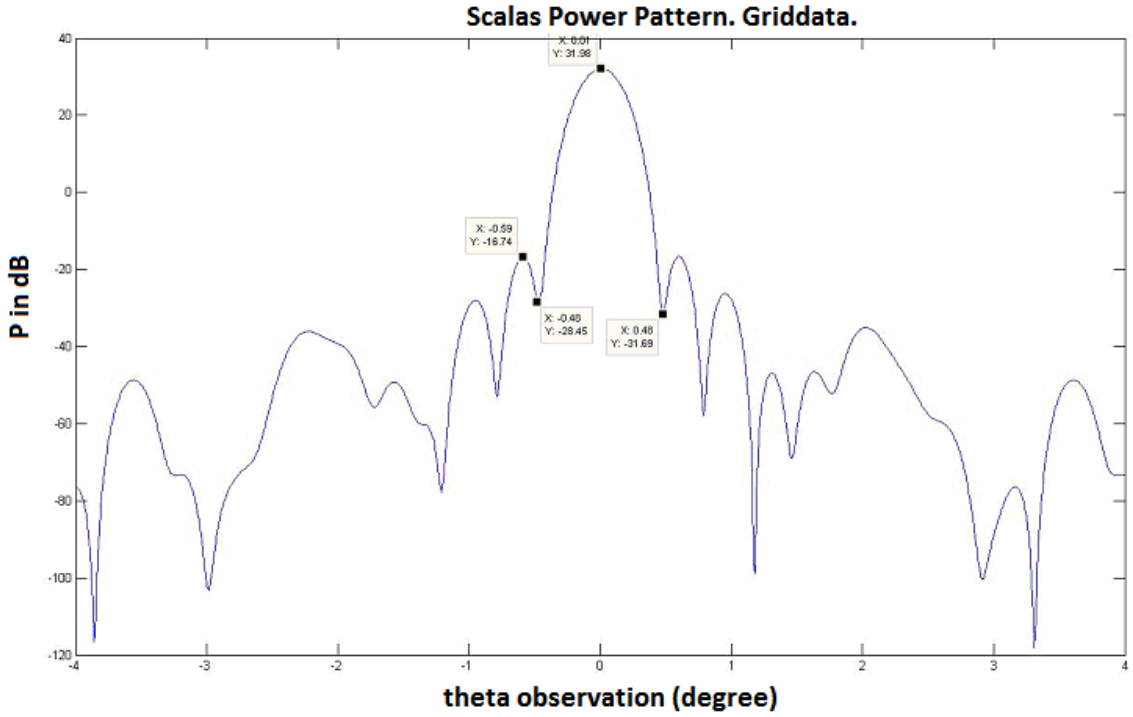

Fig. 6.18: Scalar Power Pattern with Griddata

As the two different methods are contrasted, it was observed that the one that calculates the area is more precise than the one that uses griddata. For further applications the area method will be applied.

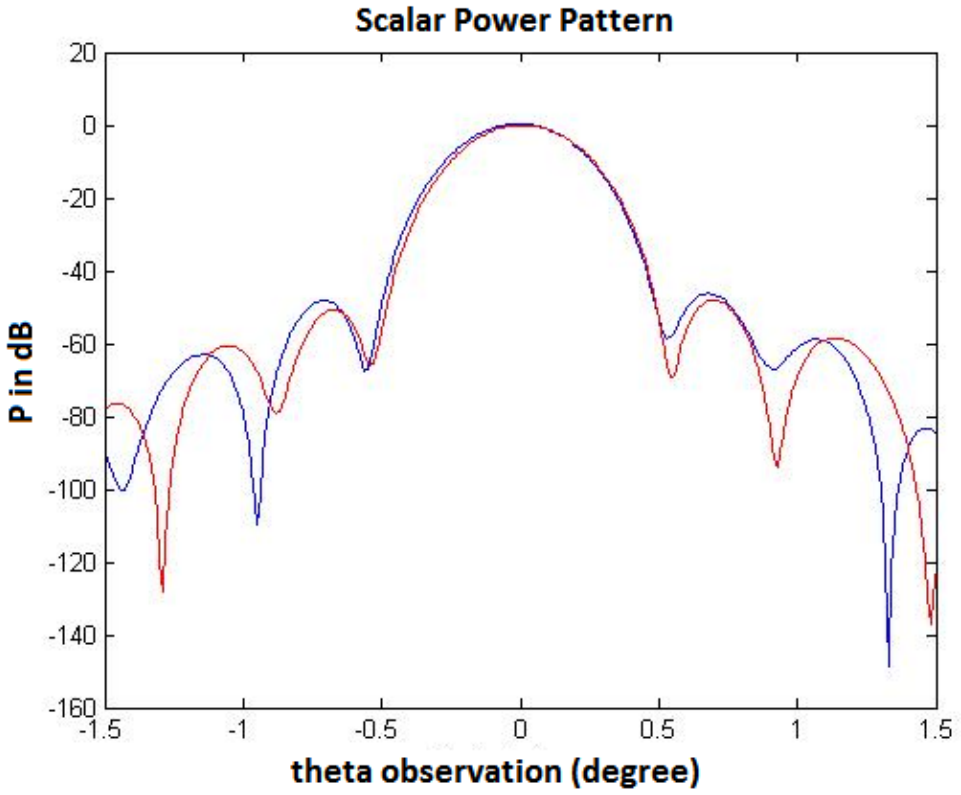

Fig. 6.19:Comparison griddata.(red) and area (blue)

There is a taper effect non-uniform field sampling distribution, as observed, the reason is that there are more concentration of rays in the centre of the main aperture, as discussed previously.

As it is seen in the previous chapter, there is phase distortion in the main aperture. This affects the scalar pattern in case of a scan, as shown in the next figure.

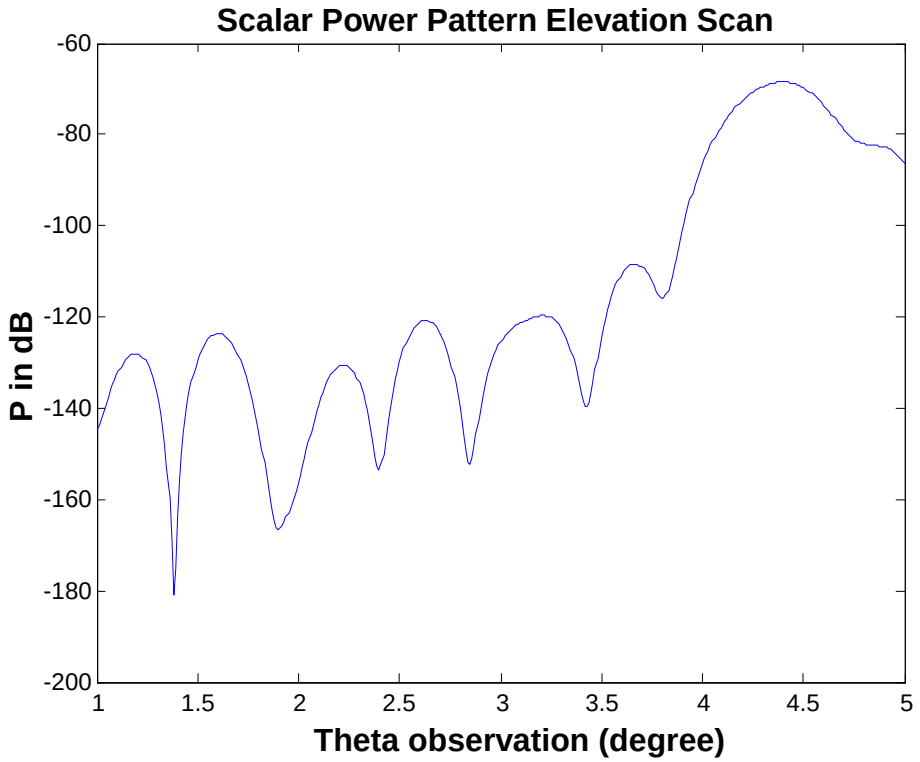

Fig. 6.20: Power Pattern distortion for scan angles

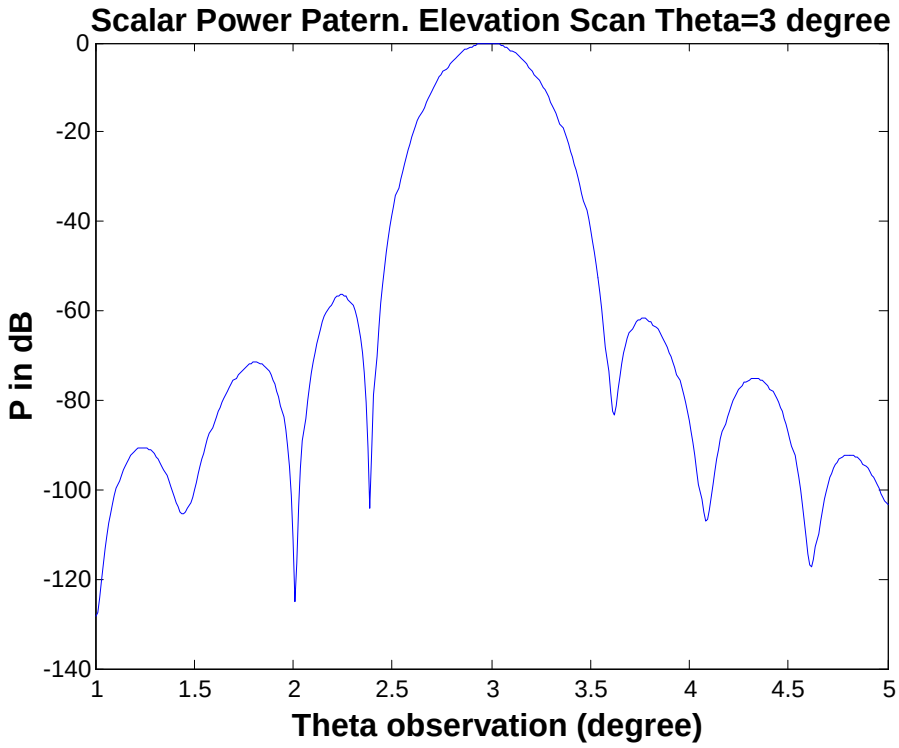

Fig. 6.21: Power Pattern for scan angle with correction

One solution is proposed by A.R. Cherrette [20]. To improve the degraded pattern, we apply the conjugate field matching method (CFM), in which we set the excitation as the conjugated field in the desired direction:

$$E_{feed} = E^{*}(\theta = \theta_{beam}, \phi = \phi_{beam})$$

The obtained result is shown in the following figure.

6.4. CST Simulation

CST Microsoft Studio is commercial software with a number of applications for antenna analysis. It was decided to implement the system in CST and to compare it with the created software.

6.4.1. *Patch antenna*

The patch antenna is represented in the following figure:

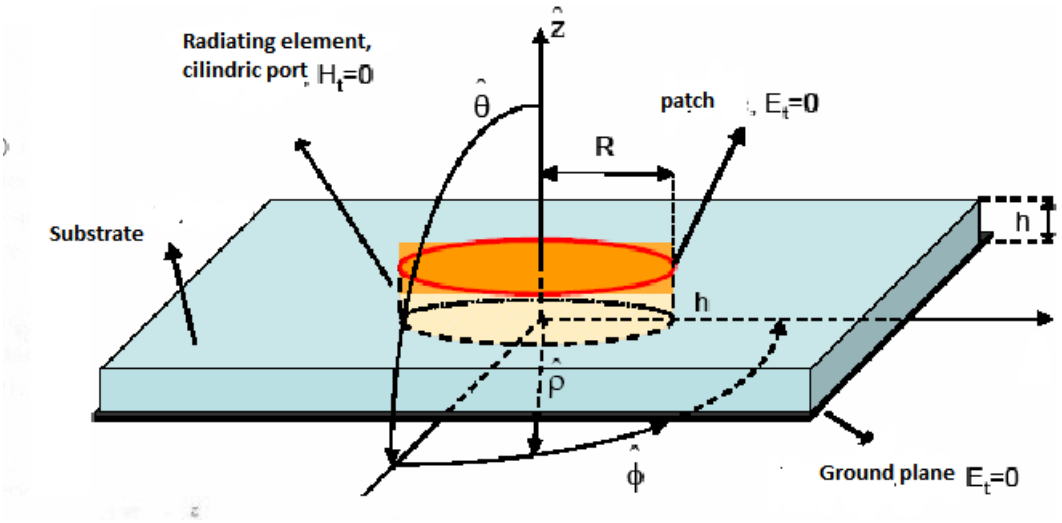

Fig. 6.22: Patch antenna general representation [11]

The orientation of the port is made considering the desired parallel polarization. To be in resonance with the work frequency, the patch antenna should have the following dimensions:

$$d = \frac{\lambda}{2}$$

Where:

$$\lambda = \frac{\lambda_0}{\sqrt{\varepsilon_{r\,dielc}}}$$

The dielectric is Teflon (red) of 0.8 λ large and 0.05 λ of width, metal (p.e.c) of 0.312 λ of diameter and 0.0018 λ (gray) and a port (see Fig.6.20 b))The ground plane is the same dimension as the dielectric.

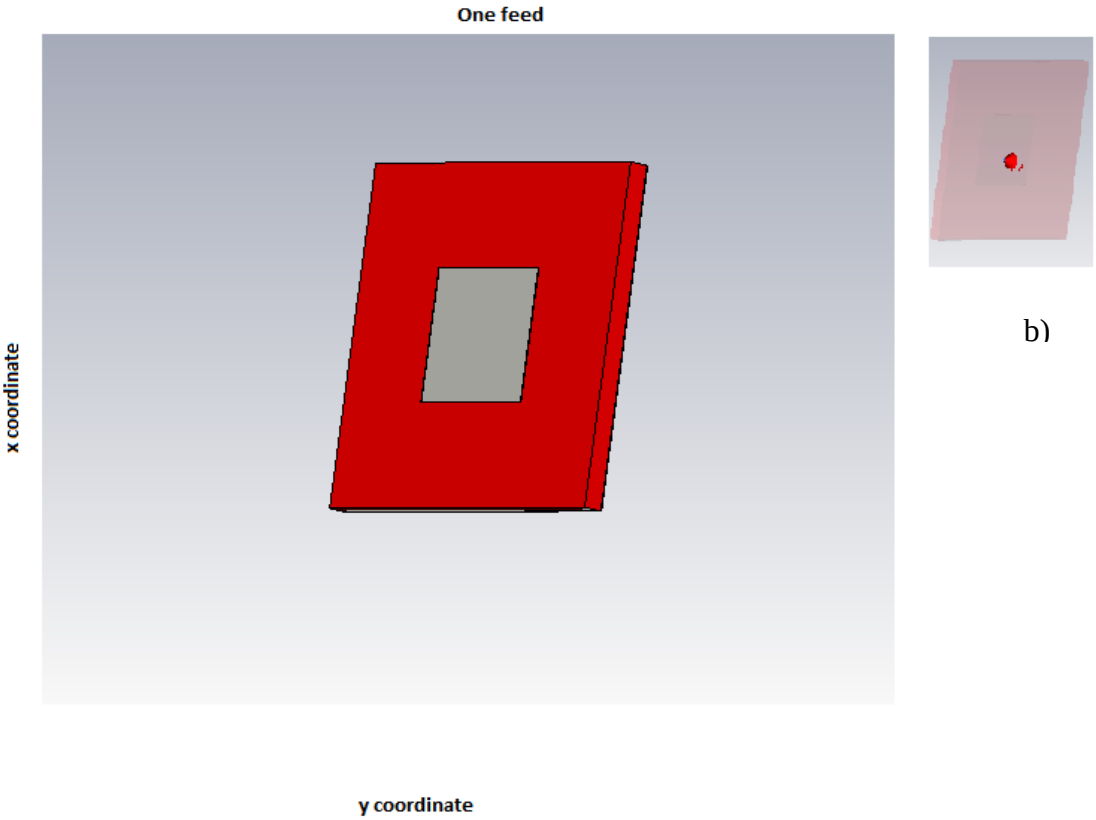

Fig. 6.23: a) One feed representation. b) port of the feed

6.4.2. Element factor

To find the element factor of the array 19 elements are plotted as shown in Fig. 6.20 The ground and dielectric are the same for all elements. The array was excited with spherical wave. It is observed that as the distance between elements is much grater than 1λ there are a lot of grating lobs as shown in Fig.6.21.

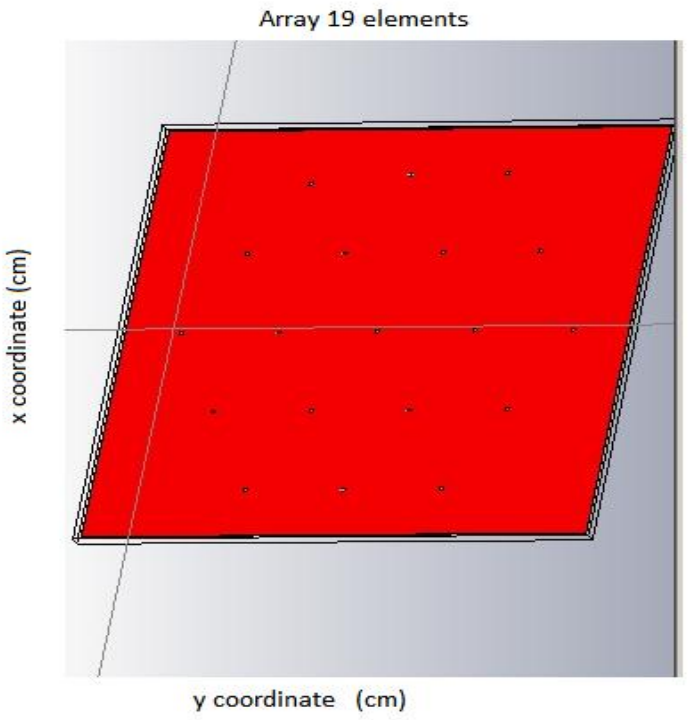

Fig. 6.24: CST Array view.

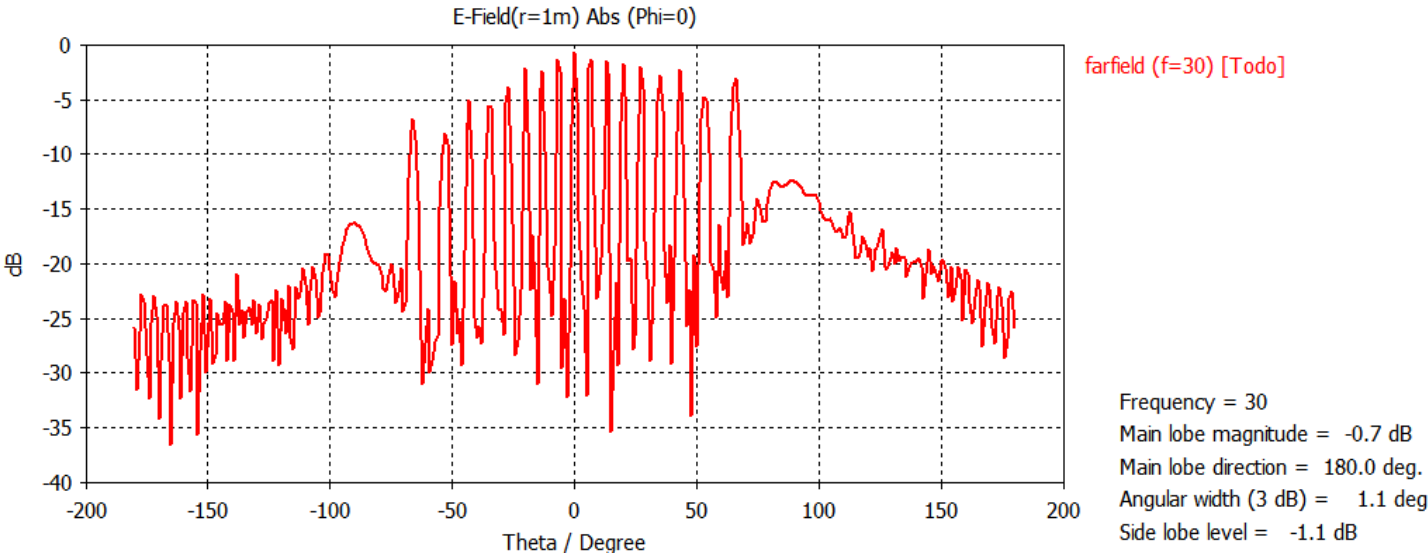

Fig. 6.25: CST E-Field element factor.

The array was exited with equal amplitude distribution. In Appendix C in Fig. 12 amplitude tapering is considered with K=1 and C=0 (see Eq. 3.18.)

When the element factor of the array is added to the power pattern formula and it is compared to the previous one, the power pattern remains the same. The reason is that with this configuration the elements are too far from each other and they do not interfere between them (see Fig.6.23).

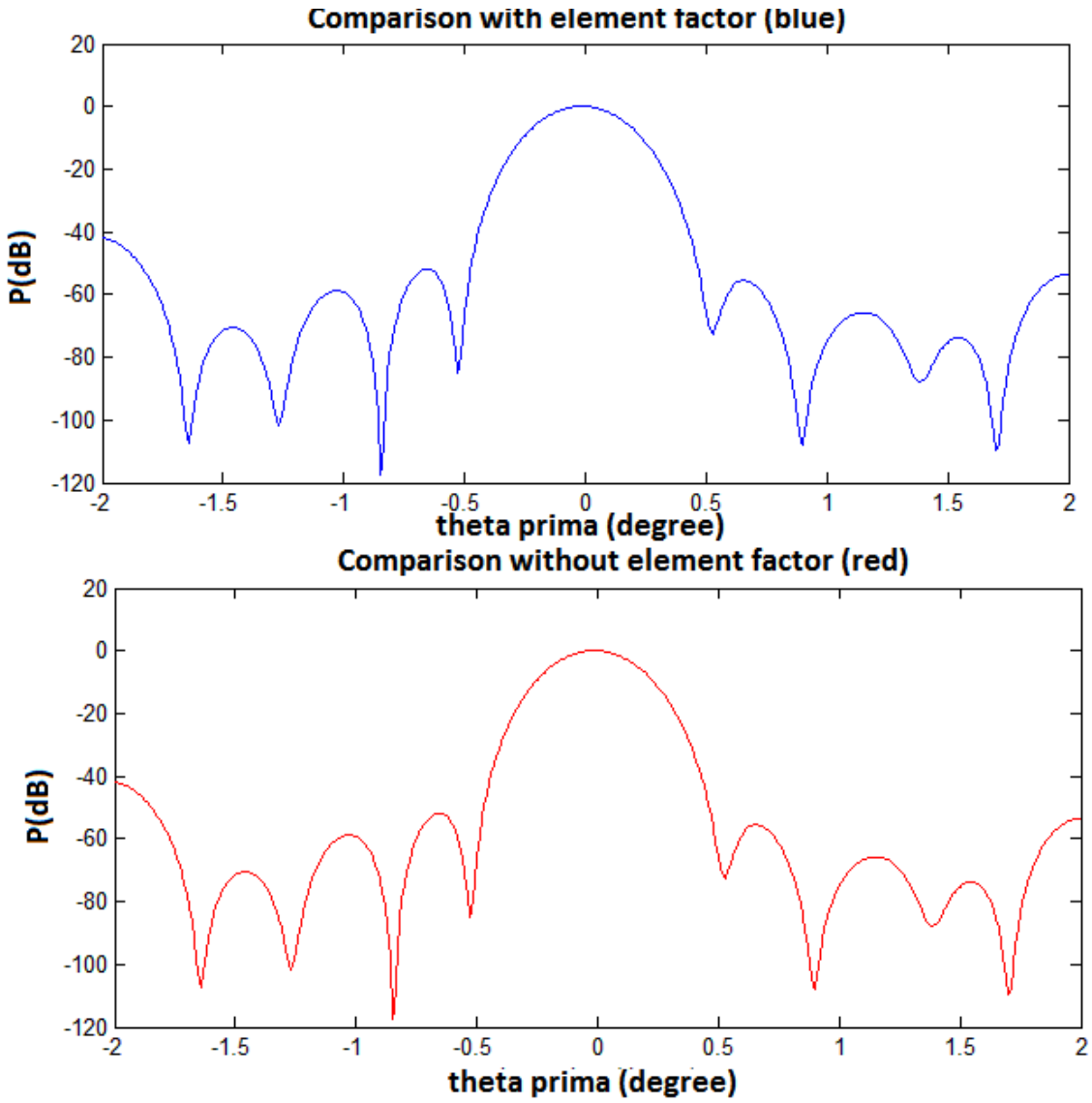

Fig. 6.26: Power pattern comparison

6.4.3. Entire system representation

The entire system was implemented in CST Microsoft Studio. To reduce computational cost, the array elements are designed as shown in the next figure. With the designed structure, the programs go out of memory. There are 9 000 000 000 sampling points.

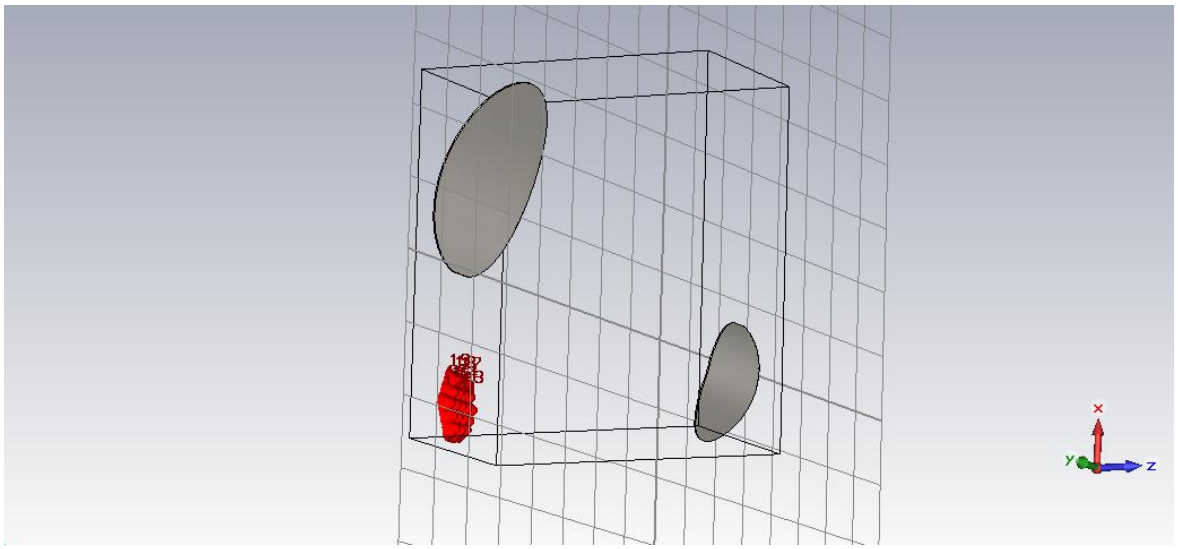

Fig. 6.22: CST System representation.

We also tried to implement the antenna architecture in another commercial software-Grasp, but this structure is not supported, as the second sub reflector could not be determined as a paraboloid. It was tried as well to use an ellipse or hyperbola with eccentricity equal to 1, but it was not possible.

6.5. Conclusions

In Geometrical Optics, spherical wave is represented like a cone that emerges from a feed. All the other parameters are the same as in the previous chapters. The study is provided for one feed and for the hexagon array configuration.

It is shown that for one feed is better to cover just 85% of the sub dish, because if the entire sub reflector is considered, there is intolerable spillover. Another observation that is made is that to cover the entire main reflector, the feed should be positioned below it.

For hexagon array configuration, directivity on the cones is applied in order to ensure total illumination of the sub reflector. The image in the main aperture is plotted. If the array is in the same position as in Fitzgerald [8], it is shown that the main reflector is not completely covered, so it is decided to place it in a focal length distance from the sub reflector (below the main reflector). In this case there is some spillover and concentration in the centre of the main aperture. To obtain independence of the array configuration in the area calculus, the software is

improved using the function griddata. Besides, the results calculated with the area are better than the ones with griddata.

The large dimensions of the structure at the high frequency make impossible the implementation of the structure in CST Microsoft Studio. The only way at the present movement to study the program is with the created software, due to computational limitations.

7. Radiometry

7.1. Introduction

Matter emits spontaneously electromagnetic radiation. Its energy depends on the physical temperature of the body. Radiometers measure the Earth brightness temperature at different frequencies and polarizations. Emission models predict the dependence of the brightness temperature with parameters as ocean salinity, soil moisture, etc.

The simplest case of a radiometric configuration is the total power radiometer. In addition, a total power radiometer does not apply interferometry, thus provides a direct measurement of the quantities of interest.

In this chapter it is demonstrated that with Synthetic Radiometry is possible to be obtained better accuracy in the observation: narrower beams. The cost is the high computational effort.

7.2. Basic Operation

A radiometer measures the *Visibility function*, from which the brightness temperature map will be reconstructed. This map will contain information about the key parameters involved in Earth observation. A radiometer receives electromagnetic waves through one antenna or through an array of two or more antennas, which can be sorted along one spatial direction or lie in a two-dimensional plane. The antenna receivers are each connected to a receiving circuit that performs a conversion of the electromagnetic energy received at the antenna input into different forms of energy at the output of the instrument that serve to quantify the received electromagnetic energy. The antenna array synthesises an equivalent aperture antenna, this technique of employing an antenna array in space for simulating an aperture antenna is called "*aperture synthesis*".

The concept of aperture synthesis relies on *interferometry* since signals measured by each receiving elements of the antenna configuration get mixed (or cross-correlated) to produce images having the same spatial or angular resolution as an

instrument of the size of the entire array. For each antenna pair, depending on its orientation and distance in between elements for a given working frequency, the measured quantity turns into an output, which is one component of the Fourier Transform of the spatial distribution of the brightness of the observed object. This component is measured for a specific spatial frequency, which is known as “baseline”. The estimated brightness map of the source is then obtained in terms of inverse Fourier transform over the spectrum of spatial frequencies with respect to these measurements.

The total amount of electromagnetic energy radiated by the Earth is due to solar electromagnetic radiation. In a first approximation we can describe the whole electromagnetic energy detected by the radiometer as part of the energy exchanged from the Sun with the Earth. Solar energy is in a first instance reflected, refracted and absorbed at the Earth's atmosphere (at interface 1 in figure Fig. 7.1 below).

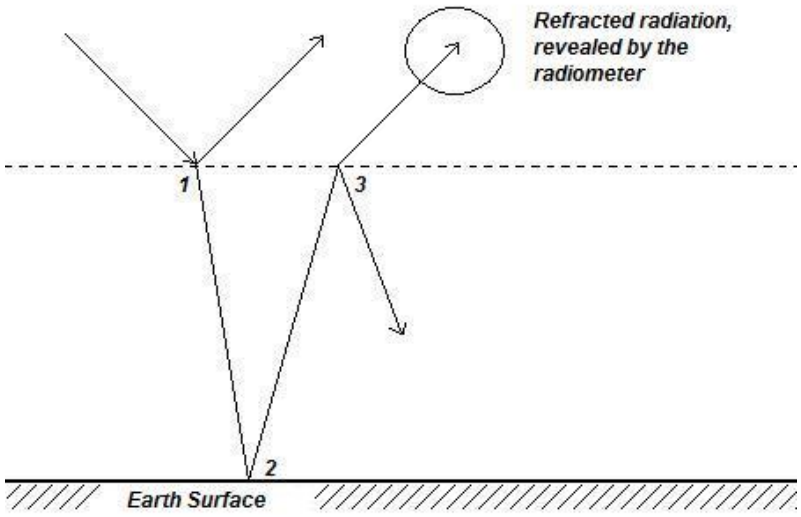

Fig.7.1: Interaction of radiation at the boundaries [13]

The refracted part affects the Earth's surface, where it meets a new interface (interface 2), on which occur, in turn, the processes of absorption and reflection.

The reflected part of energy will then again be subject to the processes of reflection, refraction and absorption at the atmosphere (interface 3). The latter part, refracted by the atmosphere, is thus part of energy detected by the radiometer.

As follows, this idealized model will be adopted to differentiate between the quantities measured by the instrument and the amount of energy actually radiated from the Earth.

Brightness is the power emitted by a body in a solid angle by unit surface and relates the electromagnetic radiated energy to temperature. This relationship is of fundamental importance, since the measured quantities by a radiometer are always related to as brightness temperatures having units of measurements [K].

7.3. Visibility function

The basic measurement performed by an aperture synthesis interferometric radiometer is called Visibility function. The term derives from optical interferometry and in case of aperture synthesis it indicates the cross correlation of the voltage outputs of the receivers of an interferometric radiometer. Each pair of the antenna array forming the synthetic aperture measures a sample of the Visibility function. The first step is to implement the visibility function according to its theoretical definition.

Considering a simple example from [21] of two antennas the visibility function can be described as:

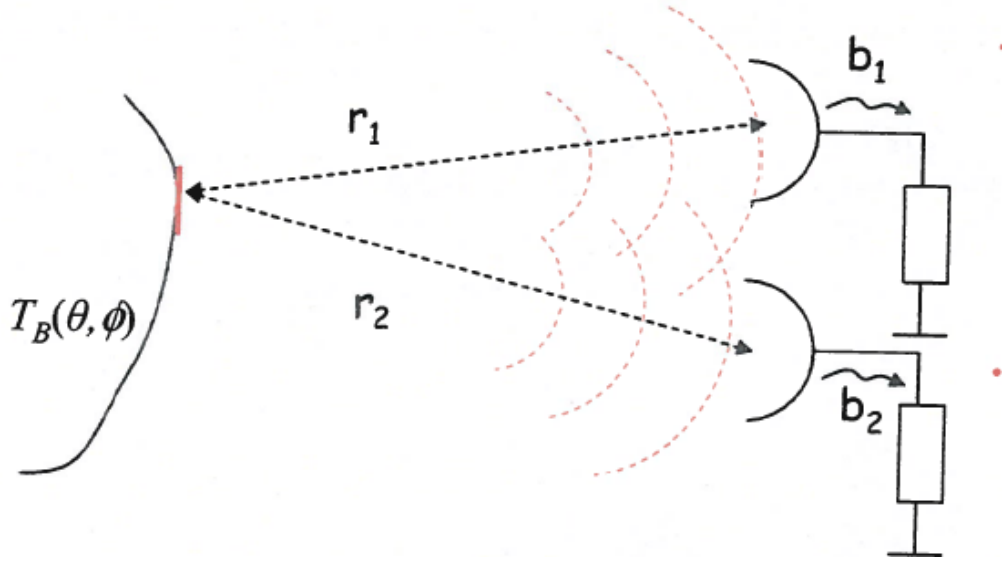

Fig.7.2: Visibility function for two antennas [21]

The power spectral density is defined by the Antenna temperature:

$\overline{|b_1|^2} = kT_{A1}$ and $\overline{|b_2|^2} = kT_{A2}$, where k is the

$$V_{ij}(u,v) = \frac{1}{\sqrt{\Omega_1 \Omega_2}} \iint_{4\pi} T_B(\theta,\varphi) F_{n1}(\theta,\varphi) F^*_{n2}(\theta,\varphi) e^{jk(r_2 - r_1)} d\Omega$$

Phase difference $u = \frac{x_2 - x_1}{\lambda}$ and $v = \frac{y_2 - y_1}{\lambda}$. $F_{n_i}(\theta,\varphi)$ is the power pattern of one feed. $T_B(\xi,\eta)$ is the brightness temperature.

It is useful to express the previous equation in terms of direction cosines by the following substitution:

$$d\Omega = \sin\theta d\theta d\phi = \frac{da}{r^2}$$

The observation index are ξ and η declared as:

$$\xi = \sin\theta\cos\phi$$
$$\eta = \sin\theta\sin\phi$$
$$d\Omega = \sin\theta d\theta d\phi = d\xi d\eta \Big/ \sqrt{1-\xi^2-\eta^2}$$

So,

$$V_{1,2}(u,v) = \frac{1}{\sqrt{\Omega_1 \Omega_2}} \iint_{\xi^2+\eta^2<1} \frac{T_B(\xi,\eta) F_{n1}(\xi,\eta) F_{n2}{}^*(\xi,\eta)}{\sqrt{1-\xi^2-\eta^2}} e^{-j2\pi(u\xi+v\eta)} d\xi d\eta$$

And more general:

$$V(u,v) = \iint_{\xi^2+\eta^2<1} \frac{T_B(\xi,\eta)\left|F_n(\xi,\eta)\right|}{\Omega_a \sqrt{1-\xi^2-\eta^2}} e^{-2\pi(u\xi+v\eta)} d\xi d\eta$$

The modified brightness temperature map is retrieved by (Fourier) inversion of the measured Visibility function. This is a four dimensional matrix. It is a complex values matrix. Where i and j are the feed index.

We call G matrix to the factor:

$$G_{ij}(\xi,\eta)=\frac{1}{4\pi}\frac{T_B(\xi,\eta)}{\sqrt{1-\xi^2-\eta^2}}F_{n_i}(\xi,\eta)F_{n_j}{}^{*}(\xi,\eta)$$

7.4. Antenna temperature

For convenience the mathematical formulation of estimation of the brightness temperature is recalled**.**

$$[T]=[G]^{+}[V]$$

Where:

$$[G]^{+}=[G]^{*}([G]^{*}[G]^{*})^{-1}$$

The calculation, based on the choice of the number of samples, can take some computational time. In fact, taking more samples in ξ and η, the size of the matrix increases.

7.5. Computational results

7.5.1. Y array

First, we will consider the Y shaped array as shown in the figure, as this is the configuration of MIRAS ESA's first interferometric synthetic radiometer.

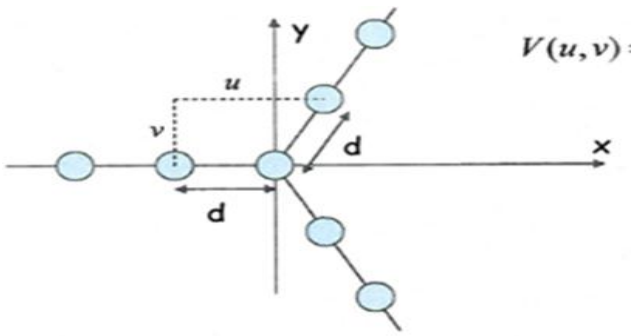

Fig.7.3: Y shape array representation

The observation range for the G matrix is of 2.29 degrees (theta). If T_B is constant as in the case below ($T_B = 240K$) the antenna temperature is constant over the whole scenario.

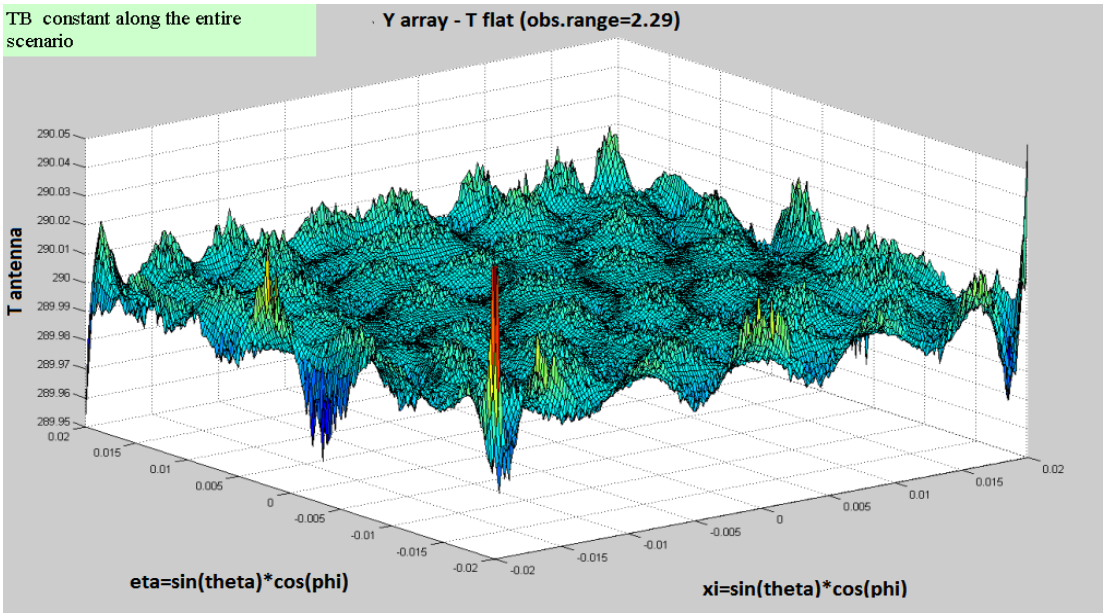

Fig. 7.4: Y array antenna temperature with constant

If $T_B = \delta_{ij}$ (Kroneker's Delta) and the observed range for the G matrix is of 2.29 degree again. The observed range of G matrix (θ, φ) is very important for the good representation. The direction is boresight. There is clear main lobe in the desired direction.

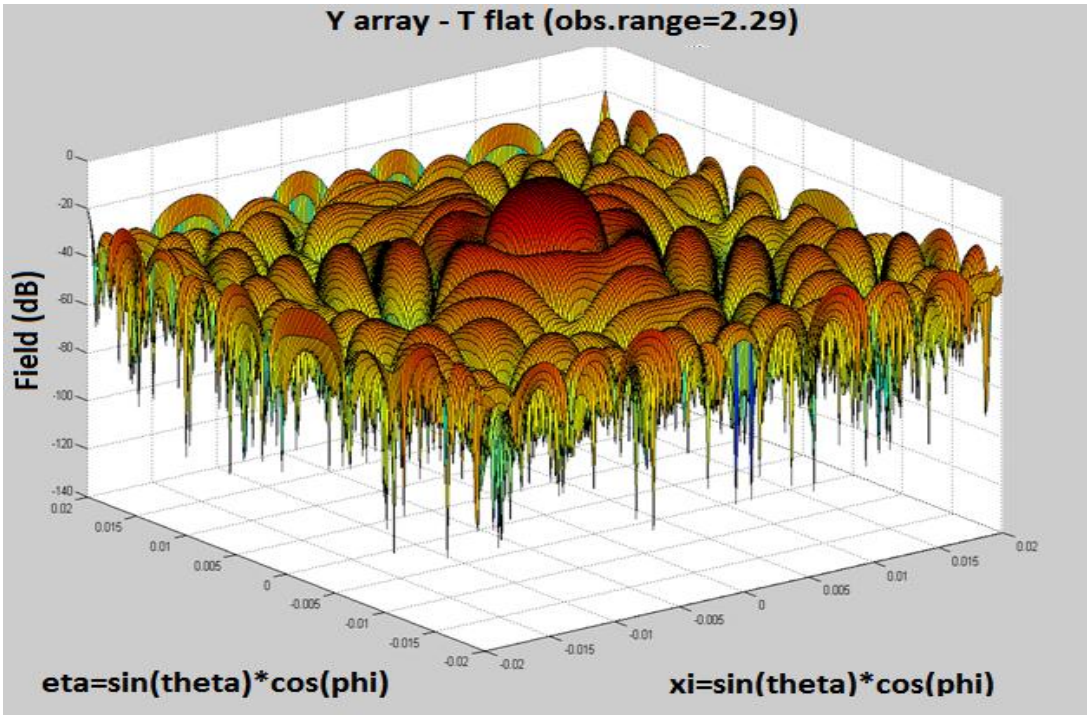

Fig. 7.5: Y array antenna temperature with $T_B = \delta_{ij}$

7.5.2. Real Radiometry vs. Synthetic Radiometry. Hexagon configuration

To understand the differences between Real and Synthetic Radiometry the spatial resolution is discussed. The theory of Real Radiometry is to consider the Fourier Transform for every feed. As shown in the example below we consider it uniform, and then we add all the feed elements.

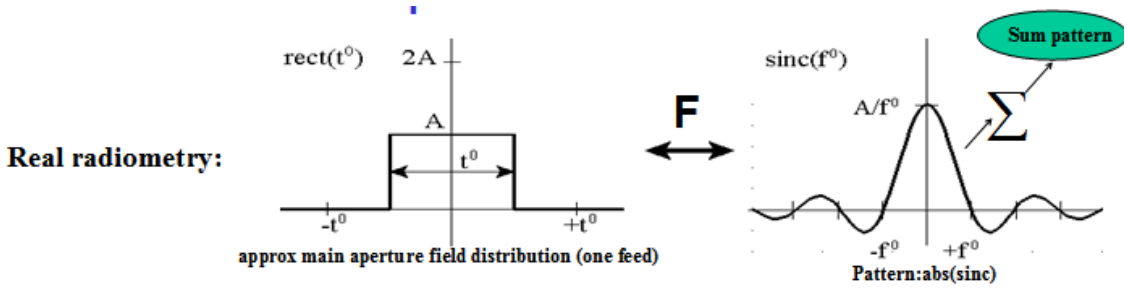

For the Synthetic Radiometry we consider the correlation between every two elements, then we apply Fourier Transform and in the end we add all the convolutions. The process is illustrated below:

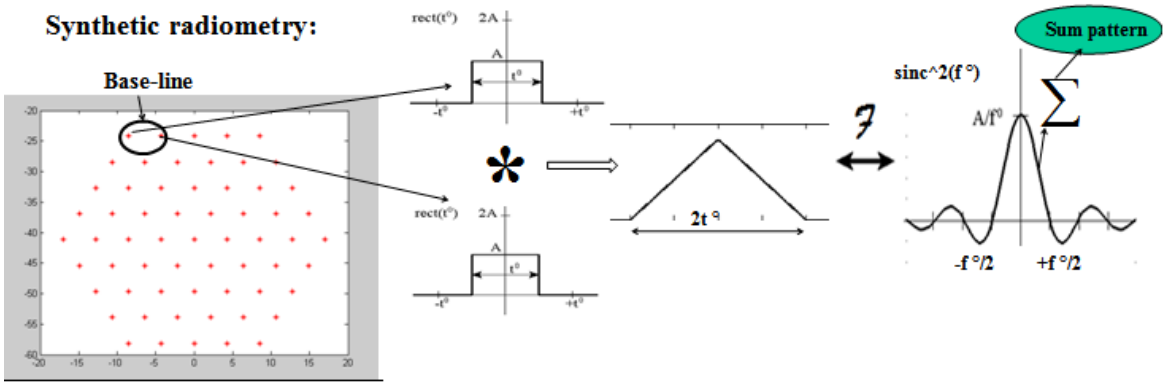

If we consider 61 elements we obtain pattern of 1.16 degrees, with real radiometer theory.

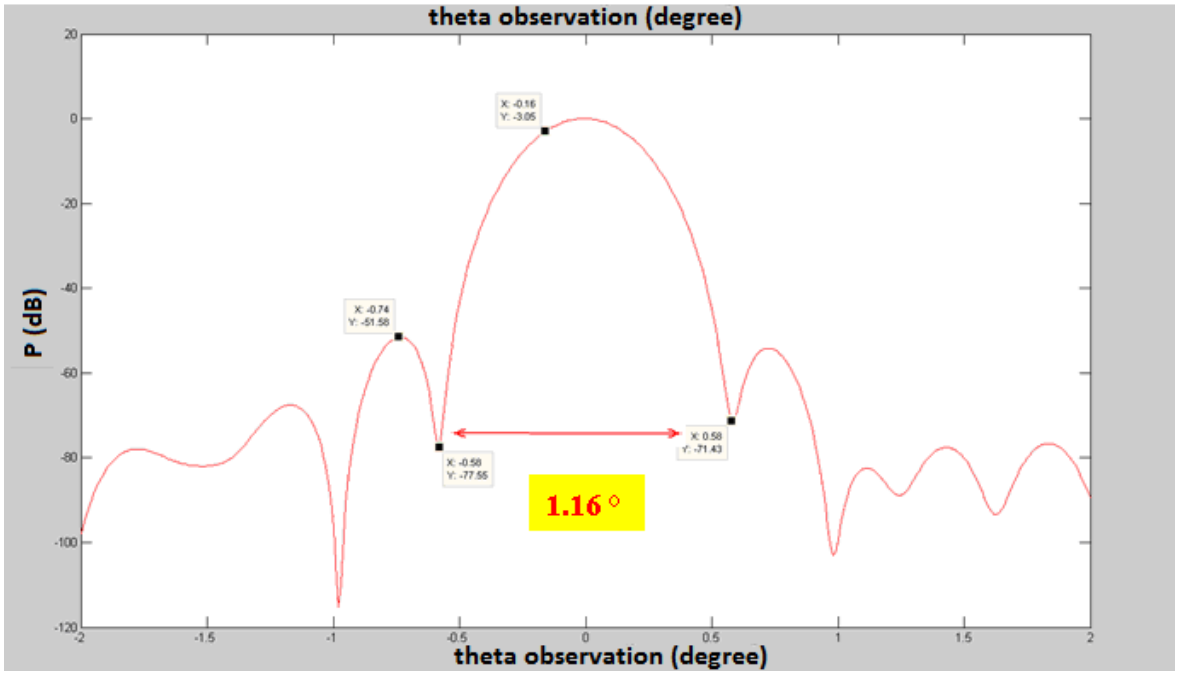

Fig. 7.6: Real Scalar Pattern a) aperture view b) array view

If we consider the synthetic scalar pattern we should consider the observation angle for the G matrix to obtain the best power pattern. For 2.26 degrees of observation we obtain a beam width of 0.46°.

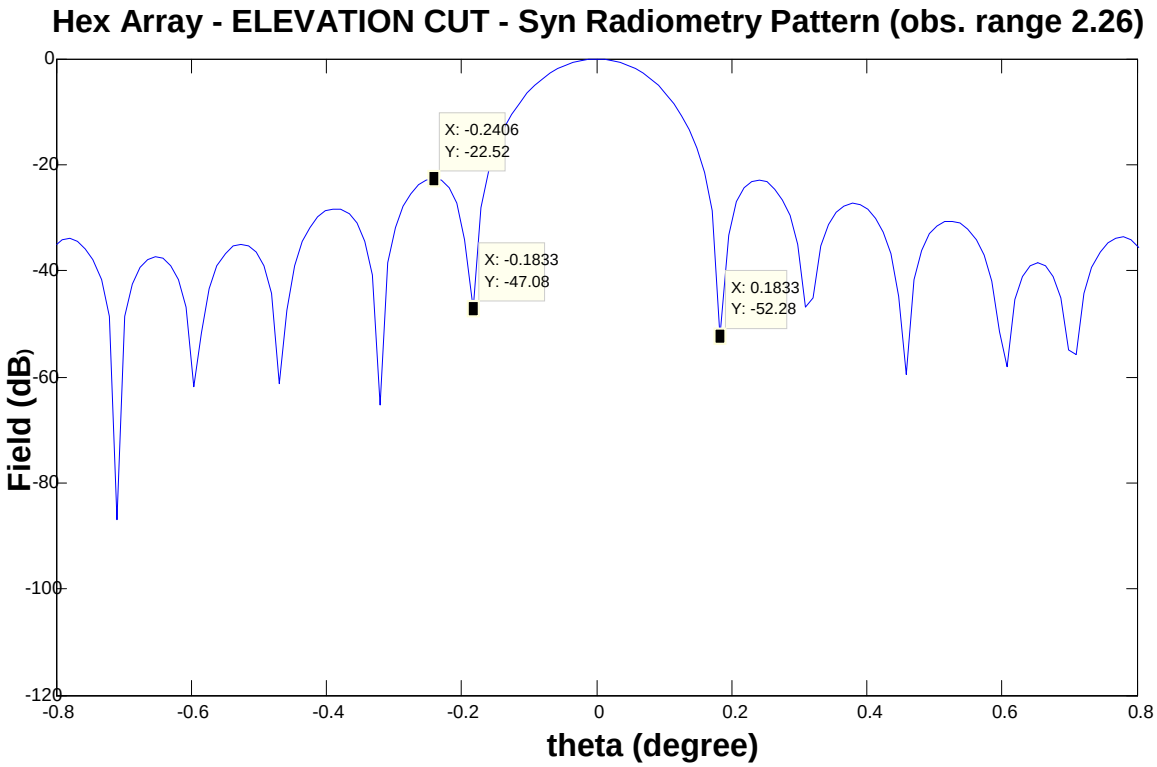

Fig. 7.7: Scalar power pattern hexagon configuration with 2.26 degrees of observation angle for G matrix boresight.

This value is less than the halved one obtained with the real radiometer.

We have more power distribution in less angle of illumination. The side lobe level is 22dB below the main lobe level.

The azimuth view of the pattern is presented below.

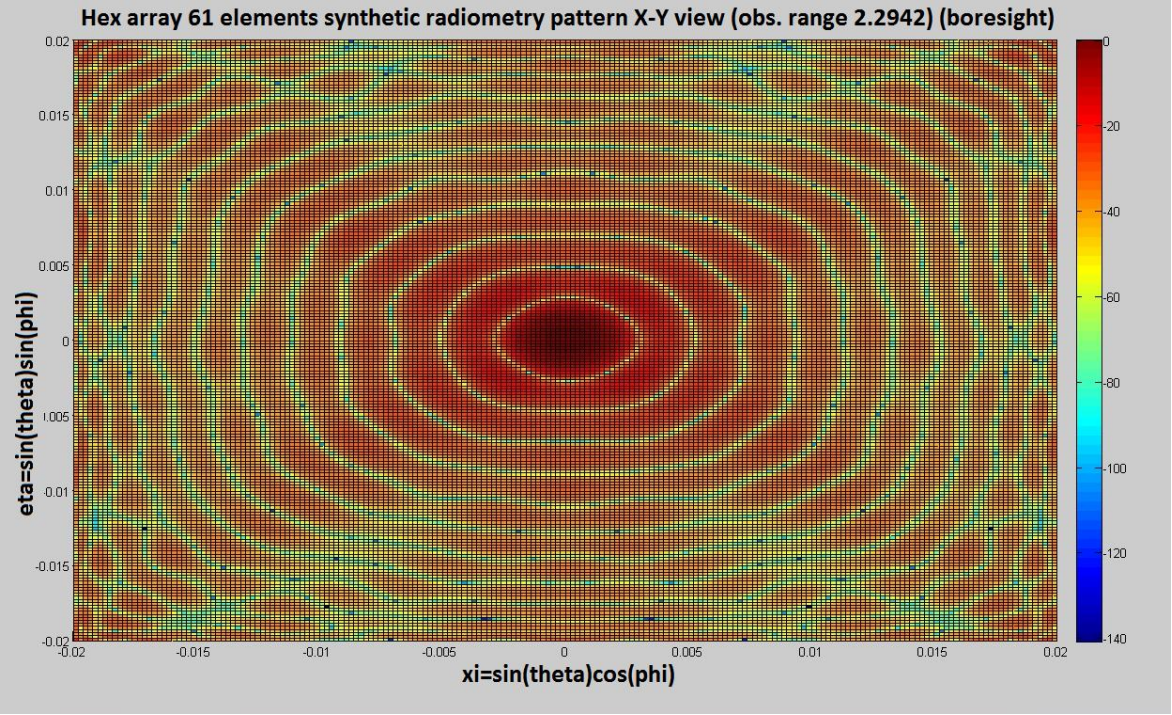

Fig. 7.9: X-Y view for boresight

7.5.3. *Equivalence between Y-shaped array and hexagon configurations. Feeds distributions and spacing*

Ingasi Corbella discussed in [21] that the Y-shape and hexagon configurations are equivalent. This is verified in this chapter. The exactness of the equivalence depends of the inter-spacing d.

The synthetic patterns are plotted in the following figure. The observation range for the G matrix is 4.5 degrees.

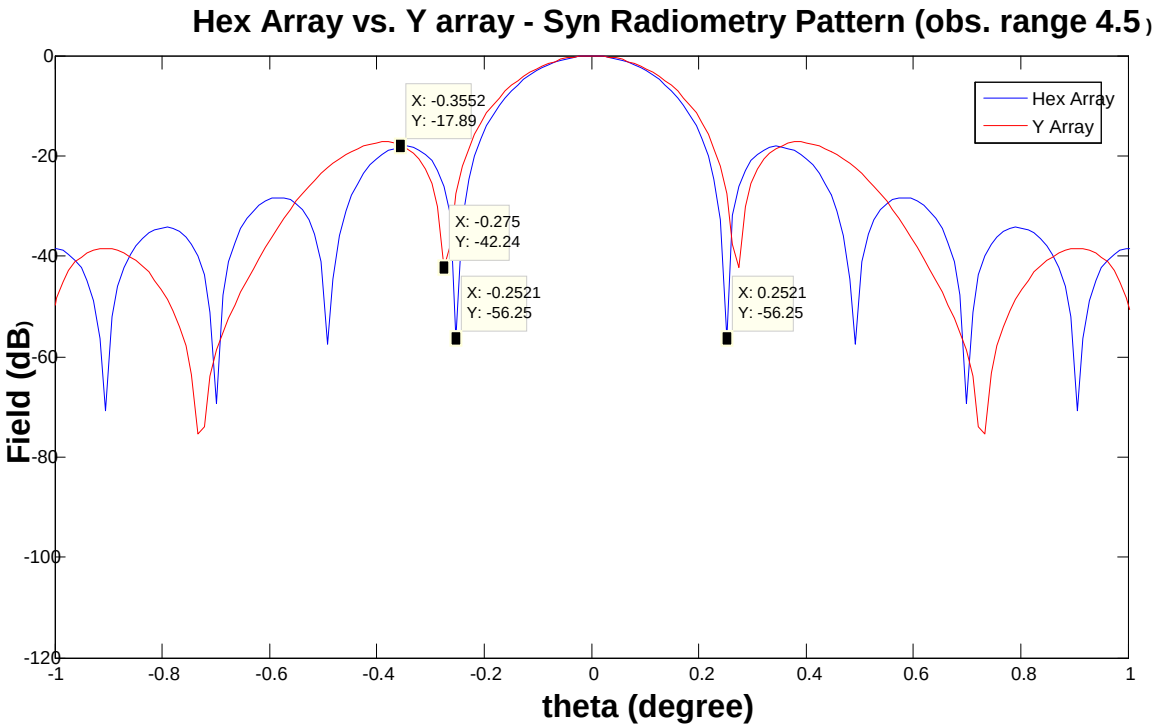

Fig. 7.13 Y-shape / Hexagonal comparisons for the default case (61 hex. Array elements)

If we decrease the inter-spacing the equivalence is verified. This way we increase the array elements and consecutively the computational request.

8. Conclusions and future work

8.1. English version

8.1.1. Conclusions

The work primarily examines the techniques based on Fourier Transform (F.T.) and develops effective methods that permit to analyze two-dimensional antenna alignments with double parabolic reflector of imaging type.

The technique for the study of an antenna system at high frequencies can be of two types: **Geometrical and Physical Optics**. The Geometrical Optics is based on ray tracing analysis. One ray, which emerges from the feed, represents the plane wave meanwhile the spherical wave is represented by a cone.

The Physical Optics is a theory that considers the induced currents, where the field are represented by radiation integrals of the surface currents. These methods are different in how they describe the diffraction, the computational efficiency and accuracy of the field. All the techniques have advantages and disadvantages. The choice between them strictly depends on the **application requirements.**

In **G.O.** the **spherical wave** is represented like a cone that emerges from a feed. The study is provided for one feed and for the hexagon array configuration. It is shown that for one feed is better to cover just 85% of the sub dish, because if the entire sub reflector is considered there is an intolerable spillover. Another observation that is made is that in order to cover the entire main reflector the feed should be positioned below it.

For the **plane wave**, it is well known that there is one F.T. from the aperture to the far field, but there is another one in the focal point. As the number of F.T. is even, we can conclude that **every feed participates in the formation of the pattern.** If the feed is excited with **plane wave**, after the sub reflector to the main reflector there is **spherical wave** and **plane wave** is presented from the main to the aperture.

First, the feeds are distributed in **square configuration**. Due to aberrations and spillover, for a range of scan angles, phase distortion is observed. In the **scan**

mode this antenna architecture presents **energy loss**. For elevation scan up the observed main beam is narrower then downward. The **linear relationship for the reflected angles** is valid just for the elevation scan up and down wards, for all other cases nonlinear relationship is observed. The **nonlinearity of the angles** can be simulated with polynomial interpolations of fifth grade. When the polarization is examined, the **co-polar lobes** with vertical polarization correspond closely to the **scalar power pattern** side lobes in both form and position. There is a cross-polar component for angles of scan different from the boresight.

Hexagon and triangle configurations are studied to obtain better performance of the antenna architecture. The phase tilt has similar behaviour applying scan to the array as the square case. For triangle configuration, bigger side lobe level difference is obtained. The inconvenience of this system is that the elements are not equidistant. The beam width is of 1°, equal to the theoretical value. For the hexagon configuration, the side lobe level is bigger than for the square case. This will permit to better distinguish the main beams from side lobe beams. There is a considerable **power gain** for angles different from the boresight.

In the **P.O. case** the superficial integrals are substituted by integrals over the triangles lattice. This makes the software faster. It was discovered that due to the nature of the paraboloid, the triangle should be very small to obtain proper results. When the number of triangles is substantially increased, there are **memory limitations** of the hardware. If the **focal length remains** the same and the **dishes are scaled** the obtained beam has a proportionally valid beam width, because the triangles cover better the less curved surface of the paraboloids. The software needs **future improvements**.

The big dimensions of the structure at high frequency made impossible the implementation of the structure in **CST Microsoft Studio**. The only way that we find achievable to study the program is with the created software at the present moment, due to **computational limitations**.

The application of the hybrid antenna is for **synthetic radiometer**, which measures **brightness temperature.** The equivalence between the Y-shaped array and the hexagon is demonstrated. This equivalence depends on the interspacing between elements (baseline). Considering the theoretical results, we can confirm that the implemented antenna with dimensions of 260cm high and 210cm large can substitute the interferometric synthetic radiometer MIRAS, which with dimensions of 800cm large. Obviously the complexity of the interconnections with the hybrid antenna with an array and double reflector is less.

8.1.2. Future work

The obtained results are theoretical, simulated by designed software. They are contrasted with the existed theoretical work in this area. There is interest from the European Space Agency for its **construction** with hexagon array as an interferometric synthetic radiometer.

Another improvement can be the **bicollimated** offset Gregorian dual reflector antenna proposed by Rao [22]. With this method the limited angle of view is doubled with some deformation of the dishes.

Definitely more precise analysis of the array configuration should be provided, for example the coupling model.

At the present moment the P.O. designed software has memory limitations due to the fact that the meshing of the dishes should be with many and very small triangles which increase the computational cost. With the improvement of the technologies there is possibility for future solutions.

Similar is the situation with the CST simulation, due to the dimensions of the structure.

This technology is interesting for space communications; therefore another application can be for telecommunication purposes. This project has shown good theoretical results, which can be proven in the future with the construction of the antenna architecture.

8.2. Spanish version

8.2.1. Conclusiones

El trabajo examina sobre todo las técnicas basadas en la Transformada de Fourier y desarrolla métodos efectivos para permitir el análisis de array planos con doble reflector parabólico de tipo Imaging.

Las técnicas para el estudio de un sistema de antenas de alta frecuencia puede ser de dos tipos: Óptica Geométrica y Física. La Óptica Geométrica está basada en el análisis de los rayos. La onda plana se representa con un rayo que sale de un alimentador, mientras que la onda esférica se representa por un cono.

La Óptica Física es una teoría que considera las corrientes inducidas donde el campo es representado por integrales de superficie. Estos métodos son diferentes en relación a la difracción, la eficiencia computacional y la precisión del campo. Todas las técnicas tienen sus ventajas e inconvenientes, la elección entre ellas depende estrictamente del uso requerido.

Se ha representado en G.O la onda esférica como un cono que sale del alimentador. El estudio es presentado para un alimentador y para la configuración del array entero. Está demostrado que para un feed debe cubrir solo 85% del reflector de sub, porque si se considera todo el reflector hay un desbordamiento intolerable. Otra observación que se ha hecho es que para cubrir el main reflector el alimentador debe ser posicionado debajo de él.

Para onda plana, se conoce que hay una F.T. de la apertura al campo lejano, pero existe también otra en el punto focal. Como el número de F.T. es par, podemos concluir que cada alimentador participa en la formación del diagrama de radiación. Si el array se alimenta con onda plana, después del sub reflector al main reflector hay onda esférica y desde el main a la apertura hay onda plana.

Primero, los alimentadores son distribuidos en una configuración cuadrada. Es observada la distorsión de la fase, debido a aberraciones y desbordamiento, para un rango de ángulos de barrido. En este caso la antena presenta pérdida de energía. Para barrido en el plano de elevación hacia arriba, el haz de radiación es mas estrecho que para el caso de barrido hacia abajo. La relación linear para ángulos reflectados es válido solo para el plano de elevación, para el resto de los casos una relación no linear es observada. La no linealidad puede ser simulada

mediante polinomios de interpolación de quinto grado. En el caso del campo polarizado paralelamente, los lóbulos co-polares corresponden al diagrama de radiación en posición y forma. Se presenta una componente cross-polar para ángulos diferentes de boresight.

Las configuraciones triangular y hexagonal son estudiadas para obtener un mejor funcionamiento de la antena. La inclinación de la fase tiene un comportamiento similar al del caso de un array cuadrado.

Se ha obtenido para el caso de triángulos una diferencia entre los niveles del primer lóbulo secundario mayor. El inconveniente en este caso es que los elementos no son equidistantes. El ancho del haz de radiación es de 1°, igual al valor teórico. Para la configuración hexagonal, el nivel de los lóbulos secundarios es mas bajo que en el caso del array cuadrado. Esto va a permitir distinguir mejor el haz principal de los lóbulos secundarios. Hay una considerable ganancia de potencia para ángulos diferentes del boresigth.

En el caso de P.O. las integrales de superficies vienen sustituidas de integrales sobre los lados de los triángulos. Esto hace el programa de software más rápido. Fue descubierto que, debido a la forma del paraboloide los triángulos deben ser muy pequeños para obtener unos resultados apropiados. Cuando el número de triángulos es incrementado sustancialmente hay limitaciones de memoria. Si la longitud focal resta la misma y se escalan los reflectores, el ancho de haz obtenido tiene un valor valido, esto es debido al hecho de que los triángulos cubren mejor las superficie menos curvada del paraboloide. El software necesita un mejoramiento.

Las grandes dimensiones de la estructura a alta frecuencia hace imposible la implementación de la estructura en CST Microsoft Studio. La única forma que hemos encontrado factible para realizar el estudio, ha sido mediante el software creado en el presente momento, debido a limitaciones computacionales.

Las aplicaciones de la antena híbrida es para radiómetro sintético, que mide la temperatura de brillo. La equivalencia entre el array de forma de Y y el array hexagonal depende del espaciado entre los elementos (baseline). Teniendo en cuenta los resultados teóricos obtenidos se puede confirmar que el sistema con dimensiones 260cm por 210 cm puede sustituir el radiómetro sintético interferométrico MIRAS, que es de dimensiones de 800cm. Obviamente la

complejidad de las interconexiones es menor con la antena híbrida con array y doble reflector.

8.2.2. Trabajo futuro

Los resultados obtenidos son teóricos, simulados por un software diseñado y son contrastados con trabajos teóricos que existen en este campo. Hay un gran interés por parte de la Agencia Espacial Europea, en la futura construcción de un array hexagonal como un radiómetro inerferométrico sintético.

Una mejora del sistema puede ser la antena Gregoriana bicollimada propuesta de parte de Rao [22]. Con este método, el ángulo de observación que en este sistema es muy pequeño, puede ser aumentado con algunas deformaciones de la superficie de los reflectores.

Definitivamente, un análisis mas preciso del array debe ser realizado, como por ejemplo el modelo de acopiamiento.

En el presente momento, el software diseñado para el análisis con P.O. tiene limitaciones por la memoria que requiere, debido al hecho que el mallado está formado por un numero de triángulos elevado, lo que aumenta el coste computacional. Con la mejora en las tecnologías (CPU, memoria) se pueden llegar a obtener soluciones a este problema.

La situación es similar con la simulación en CST, debido a las grandes dimensiones de la estructura.

Esta tecnología es interesante para las comunicaciones satelitales, otras aplicaciones pueden ser para usos de telecomunicación. Este proyecto ha dado unos resultados teóricos buenos, que pueden ser confirmados con la construcción del sistema.

References

[1] W.D. Fitzgerald, "Limited Electronic Scanning with an offset-feed near-field Gregorian System"
[2] Corrado Dragone, "Scannable Antenna Arrangement Capable of Producing a Large Image of a Small Array with Minimal Aberrations"
[3] Corrado Dragone "A First-Order Treatment of Aberrations in Cassgrainian and Gregorian Antennas"
[4] J.B.L Rao "Bicollomated Near Field Gregorian Reflector Antenna"
[5] J.W. Goodman, "Introduction to Fourier Optics ", New York: McGraw-Hill, 1968
[6] A.K Bhattacharya "Phased Array Antenas"
[7] José Luis Masa, Jorge Ruiz, "Antenas y Circuitos de Alta Frecuencia". Asignatura de Master de Escuela Politécnica Superior de la UAM
[8] Constantin A. Balanis, "Advanced Engineering Electromagnetics"
[9] Carray Rappaport, Antonio Garcia Pino "Zooming and Scanning Gregorian Confocal Dual Reflector Antennas"
[10] Robert Anthony Pearson , "An Array-Fed dual reflector antenna for limited sector electronic beam scanning", PhD Thesis University College London
[11] Ramiro José López Colino, "Integración de una antena plano TX/RX de apuntamiento variable con desfasadores digitale y matrices de Butler para comunicaciones WiMAX a 3.5GHz " ,Proyecto fin de Carrera UAM
[12] Francesco Russo, "Interali di Reazione per Funzioni di Base di gradi dimensioni per Analisi di Reirradiazione Elettromagnetica mediante Metodo dei Momenti " ,Tesi di Laurea di Universita` degli studi di Siena.
[13] Christian Sciannella ,"Analysis of Periodic and Aperiodic Aperture Synthesis Interferometric Radiometers", ESTEC Internship Final Report
[14] Constantin A. Balanis, " Antenna Theory", Chapman &Hall
[15] W.B. Gordon: "Far-field approximations to the Kirchoff-Helmholtz representations of scattered fields", IEEE Trans. Antennas Prop., vol 23, pp. 590-592, July 1975
[16] Antenna Configuration Trade-off Study for Future Broadband Satellite Networks ESA-ESTEC ITT 01.1EE.30 - AO/1-4007/01/NL/LvH
[17] The Visibility Function in Interferometric Aperture Synthesis Radiometry Ignasi Corebllа, Nuria Duffo, Marce Vall Llossera
[18] Ignasi Corbella "Interferometric Aperture Synthesis Radiometry For Earth Observation" Prof. Universidad Politécnica de Catalunya
[19] Y.T Lo , S.W. Lee "Antenna Handbook" Volume II
[20] A R Cherette "Compensation on reflector antenna surface distortion using an array feed"
[21] Ignasi Corbella ,Course on Interferometric Radiometry, 2007
[22] Rao, ''Bicollimated Offset Gregorian Dual Reflector Antenna System''

Appendix

Appendix A

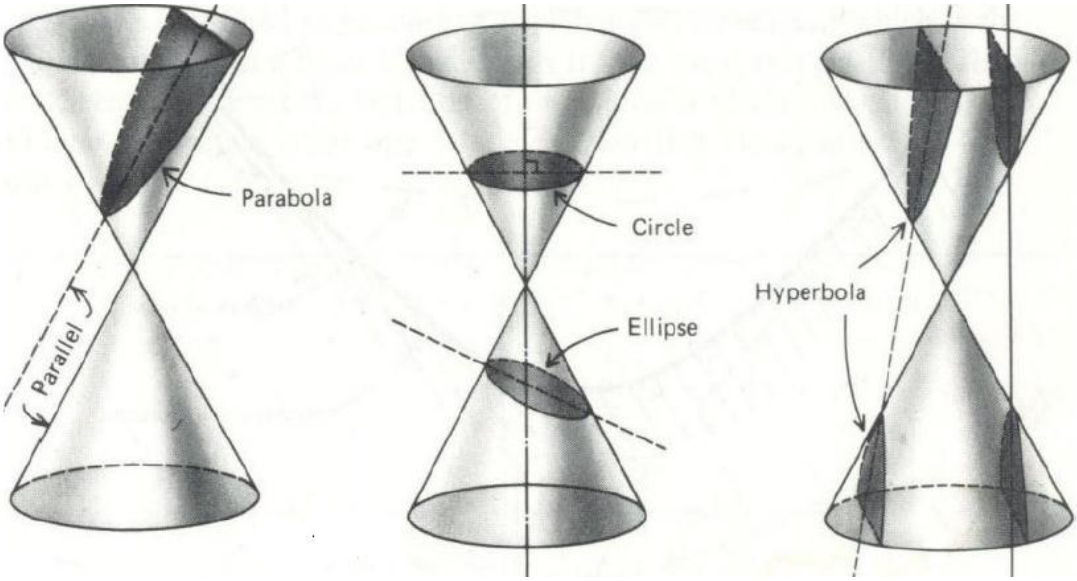

Reflector antennas utilize curvatures called conic sections (see Fig. 1 below). In addition to the parabola, the other shapes are the circle, the ellipse, and the hyperbola.

The most useful reflector is the parabola, shown in Fig. 3. The parabola has the valuable property, by which rays of light or RF emanating from the focus, are all reflected to parallel paths forming in this way a narrow beam. All paths from the focus to a plane across the aperture, or a parallel plane at any distance, have the same length. Since all the rays have the same path length, they are all in phase and the beam is coherent. This behaviour is reciprocal — rays from a distant source are reflected to a point at the focus. The axis of symmetry for the parabola is the axial line through the vertex and the focus; if we spin the parabolic curve around this axis, we get the familiar parabolic dish.

The multiple-reflector systems were originally developed as optical telescopes, long before the radio Thus, a quick overview of telescope designs is discussed. All

of them have the same important property — ray paths must all have the same length.

The Gregorian telescope (James Gregory, 1634), see Fig. 5, adds an elliptical sub reflector to reshape the beam, shortening the telescope, and moves the focus to a convenient point behind the centre of the reflector. An ellipse has two foci, with the useful property by which a ray emanating from one focus is reflected to pass through the other focus, as shown in Fig. 2. If most of the ellipse is removed, then rays from the first focus appear to radiate from the second, but the angle may be changed by adjusting the curvature of the ellipse. For an antenna, we may place an efficient feedhorn with a narrow beam at the first focus and choose an ellipse that reshapes the beam into a broad one to illuminate a deep dish. The broad beam appears to come from the second focus, so we must make the second focus coincident with the focal point of the main parabolic reflector.

Figure 5b

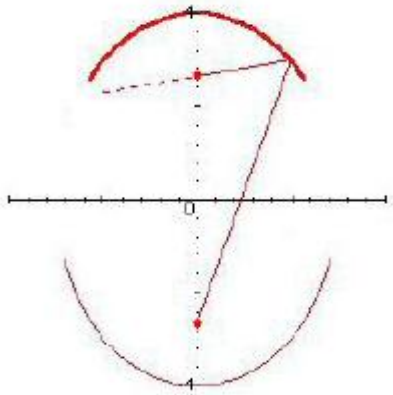

The Cassegrain telescope (attributed to M. Cassegrain, 1672, although he is not known to have published anything) in Fig. 6 has a hyperbolic sub reflectorrather than an elliptical one, but still has the same function. The hyperbola consists of two mirror-image curves and also has two foci, as shown in Fig. 3. The curves are between the two foci. For a reflector only one curve is needed. Rays emanating from the focus on the convex side of the curve are reflected by the hyperbola so that they appear to come from the other focus which is behind the reflector. The focus behind the reflector, on the concave side, is referred to as a virtual focus, because the rays never reaches it. Since the rays appear to radiate from the virtual focus, we must make it coincident with the focal point of the main parabolic

reflector. The curvature of the hyperbola may also be adjusted to reshape the beam as required.

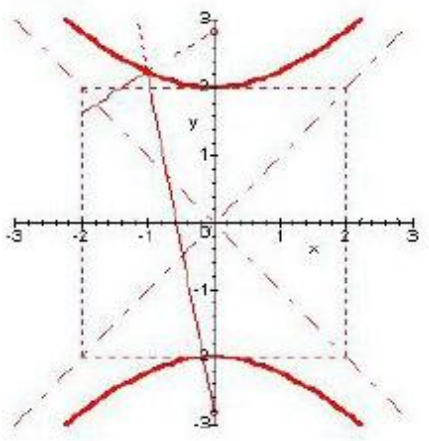

Appendix B

M=3

θ	φ	θ' expected	φ' expected	θ' measured	φ' measured
0		0		0	
4	0	1.33333333	-180	1.33333333	-180
8	0	2.66666667	-180	2.46666667	-180.2
12	0	4	-180	3.6	-180.2
16	0	5.33333333	-180	4.73333333	-180.2
20	0	6.66666667	-180	5.76666667	-180.2
24	0	8	-180	6.8	-180.2
28	0	9.33333333	-180	7.93333333	-180.2
0		0		0	
4	45	1.33333333	-135	1.33333333	-133.4
8	45	2.66666667	-135	2.56666667	-132
12	45	4	-135	3.7	-130.6
16	45	5.33333333	-135	4.93333333	-129
20	45	6.66666667	-135	6.06666667	-127.6
24	45	8	-135	7.3	-126
28	45	9.33333333	-135	8.43333333	-124.8
0		0		0	
4	90	1.33333333	-90	1.33333333	-87.8
8	90	2.66666667	-90	2.66666667	-85.8
12	90	4	-90	4	-83.8
16	90	5.33333333	-90	5.43333333	-81.6
20	90	6.66666667	-90	6.86666667	-79.8
24	90	8	-90	8.4	-77.8
28	90	9.33333333	-90	9.93333333	-76
0		0		0	
4	180	1.33333333	0	1.43333333	0.2
8	180	2.66666667	0	2.86666667	0
12	180	4	0	4.5	0.2
16	180	5.33333333	0	6.23333333	0.2

20	180	6.66666667	0	8.16666667	0.2
24	180	8	0	10	0.4
28	180	9.33333333	0	11.3333333	0.2

Table B Expected and Observed angles

Different scan angles system representation in azimuth plane

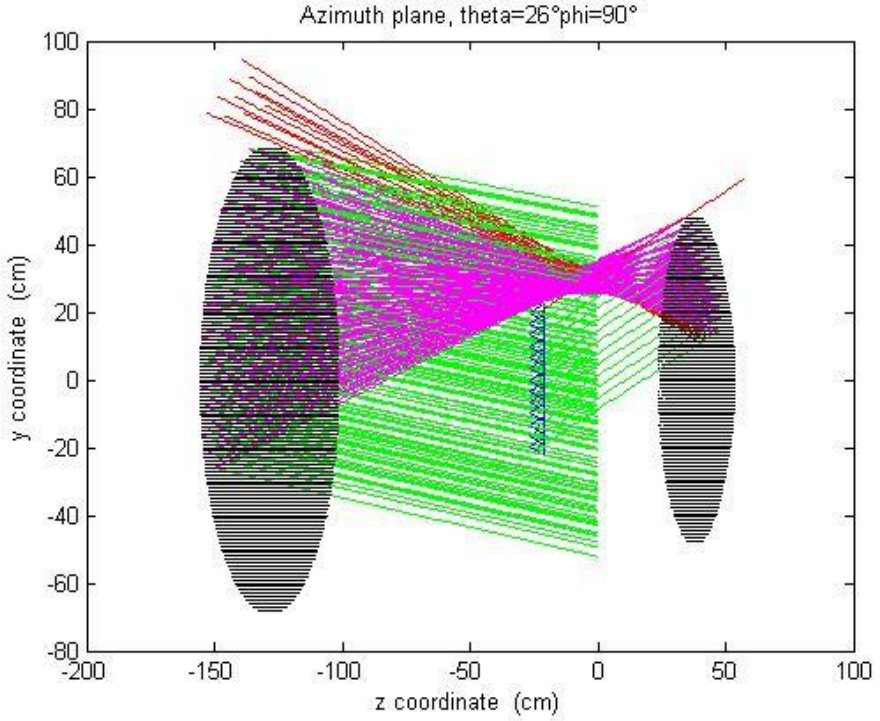

Fig.1 Azimuth plane theta=26° and phi=90°

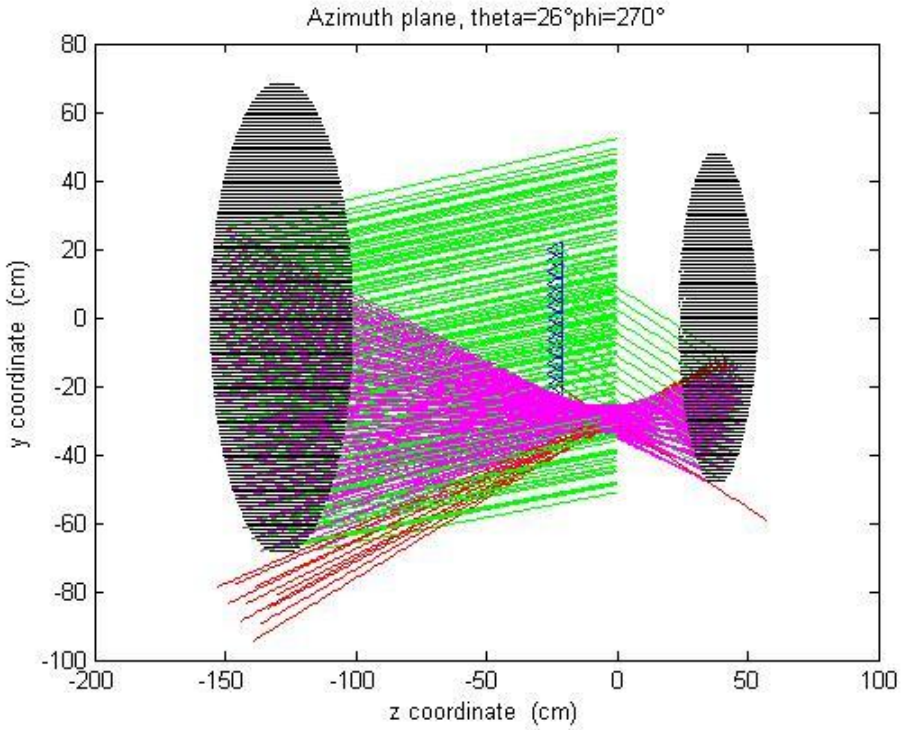

Fig.2 Azimuth plane theta=26° and phi=270°

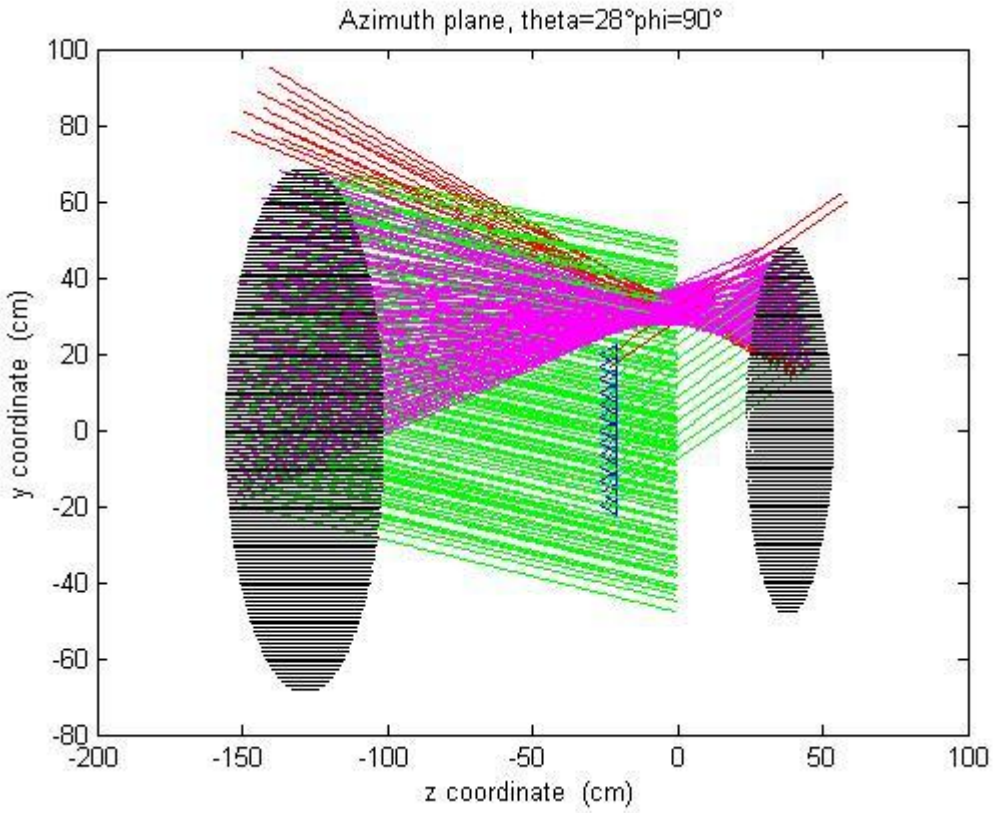

Fig.3 Azimuth plane theta=20° and phi=90°

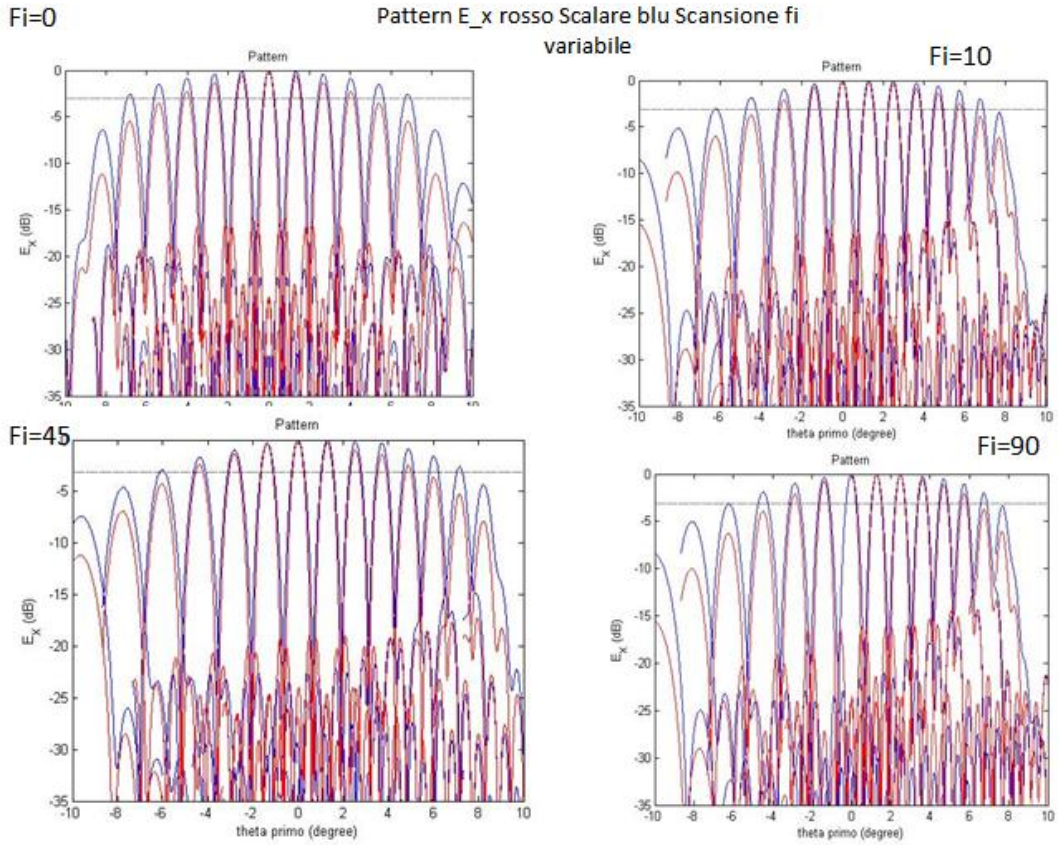

Fig. 4: Comparison co-polar component scalar pattern

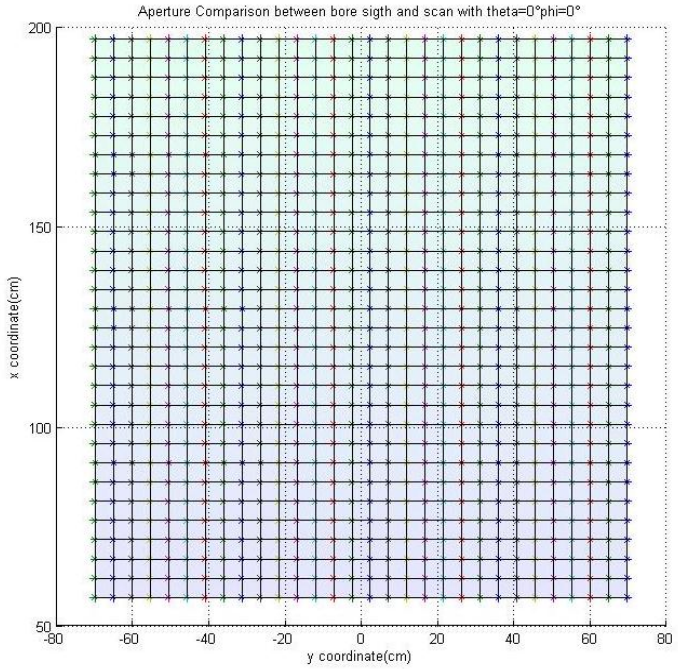

Fig. 5: Aperture with N=30

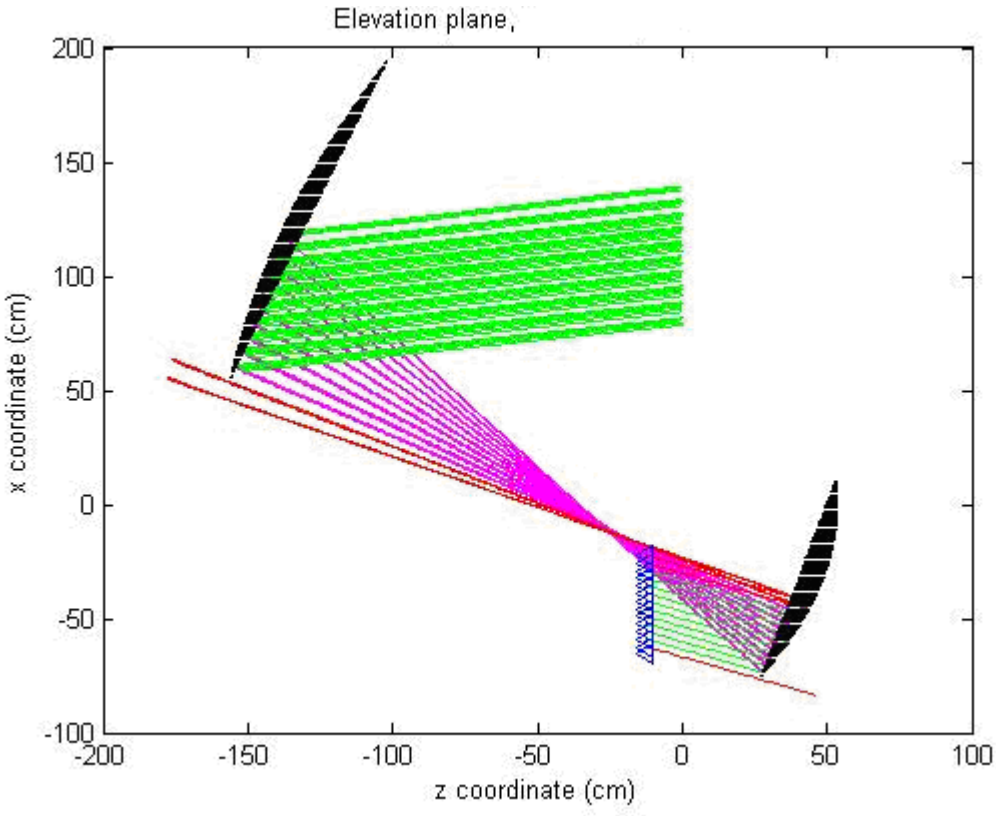

Fig.6: Block for theta=28° and phi=180°

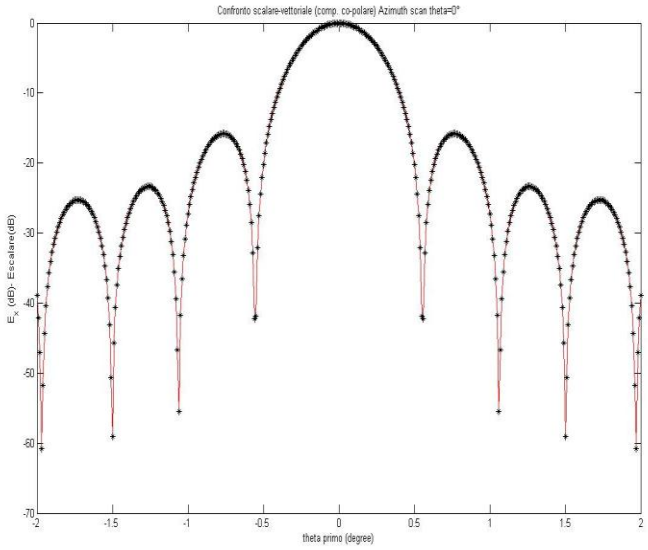

Fig 7. Comparison co-polar component scalar patter boresight

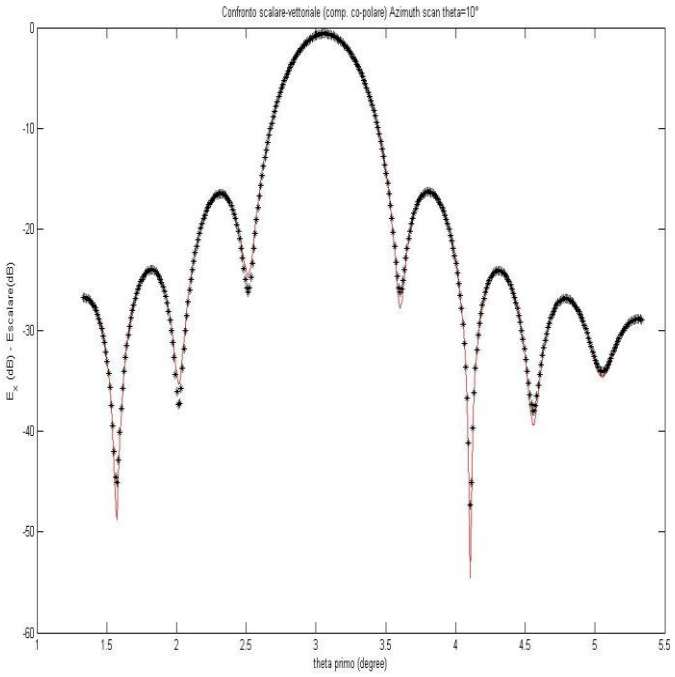

Fig 8. Comparison co-polar component scalar patter scan

Appendix C

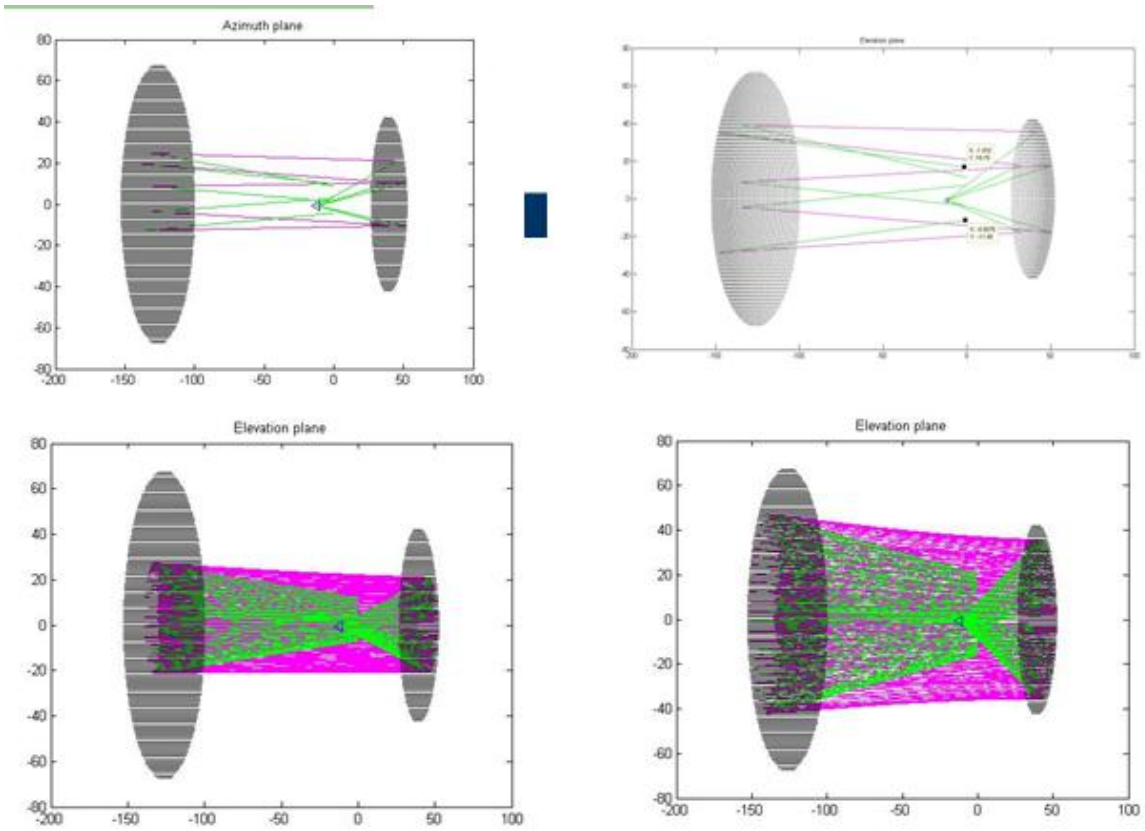

Fig 9. One element study

Analysis main reflector

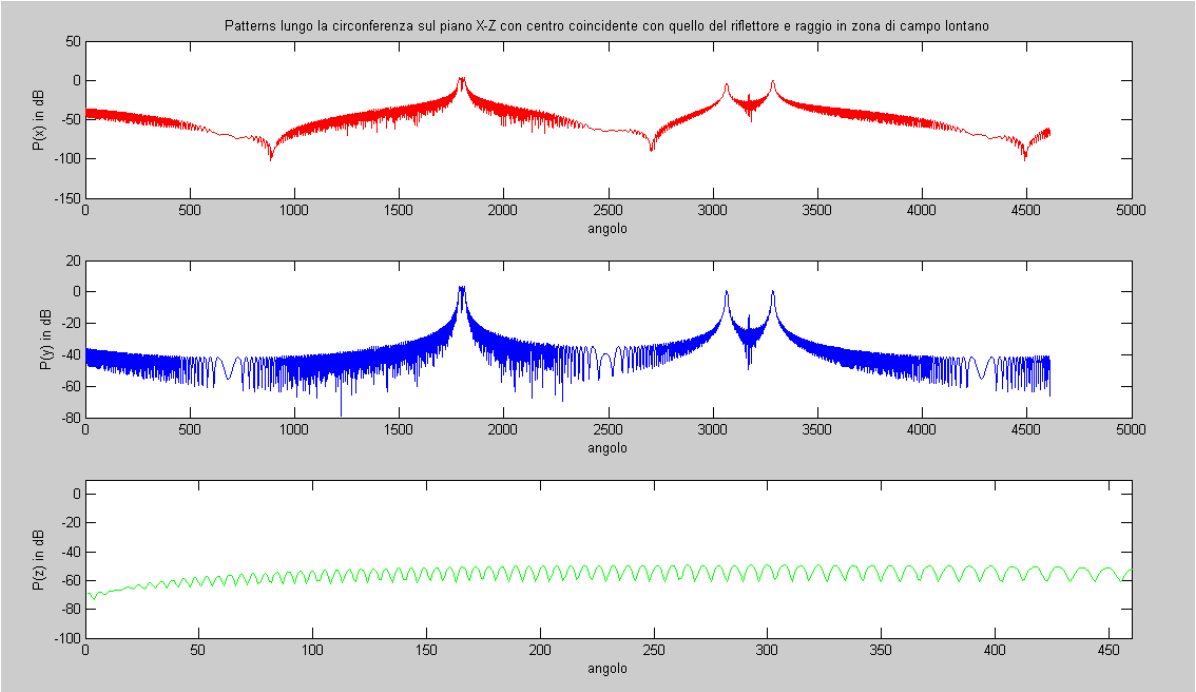

Fig 9. All the system

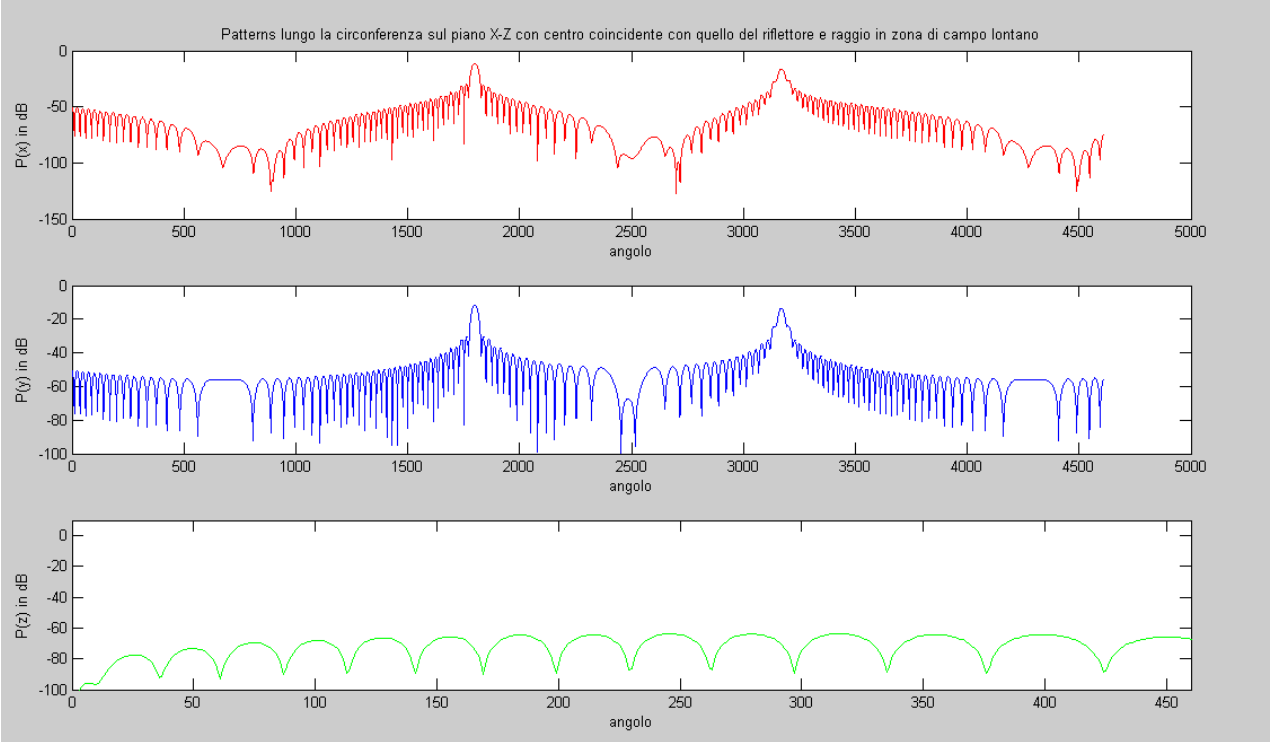

Fig 9. the dishes scaled with 5

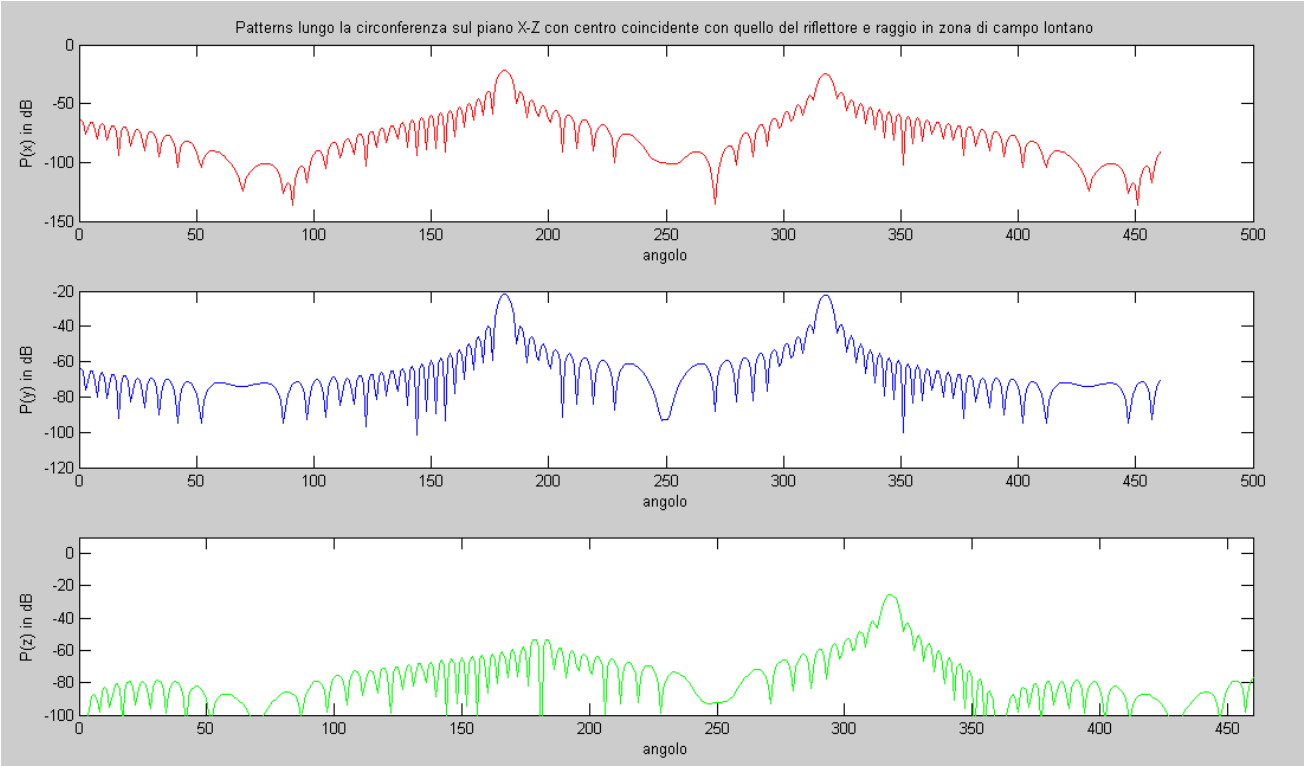

Fig 10. the dishes scaled with 10 area of 1.7 to 0.8 sq.cm

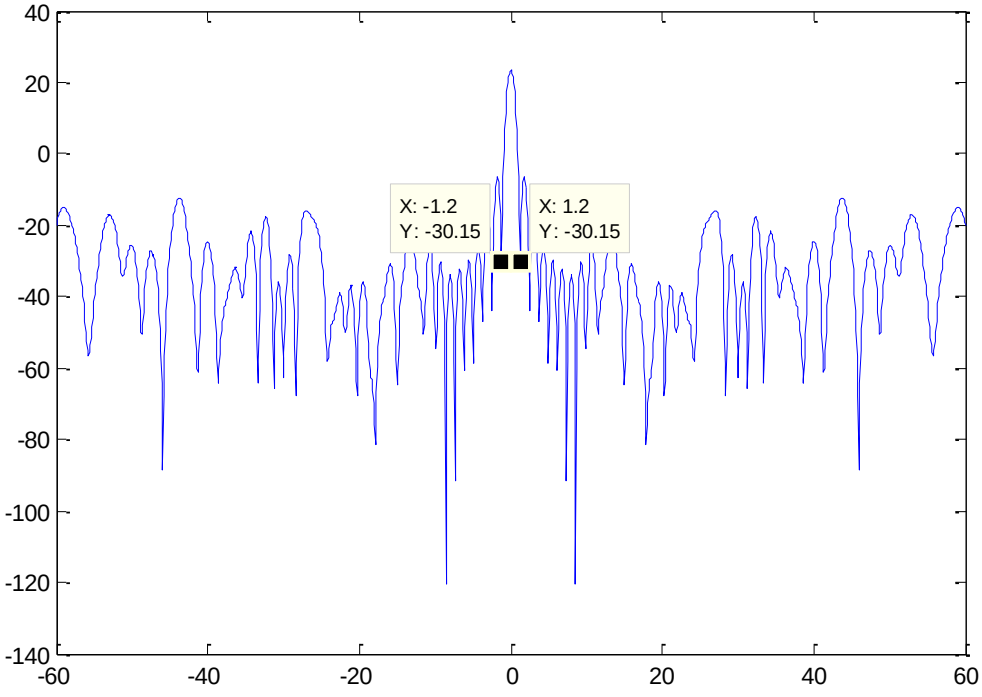

Fig 11. Hexagon configuration spherical wave large range of view

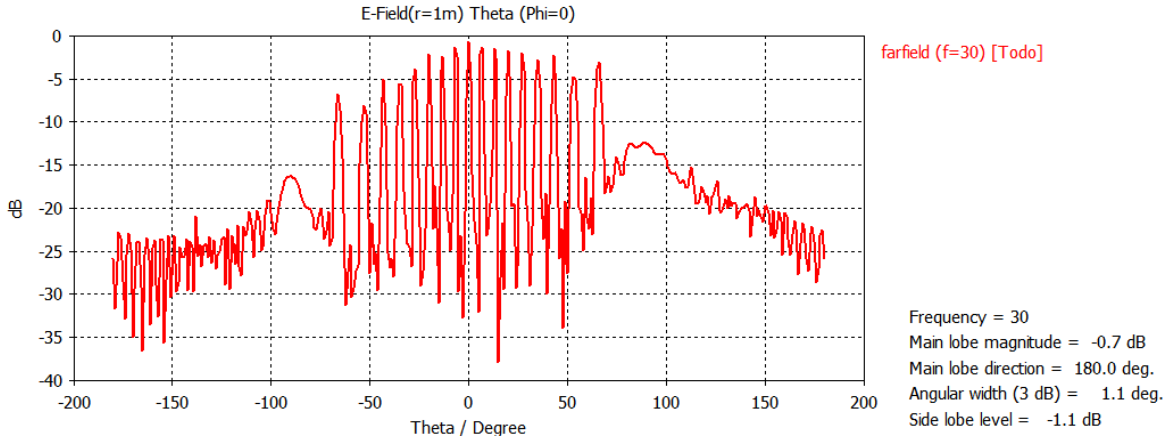

Fig 12. E field amplitude taper 19 elements

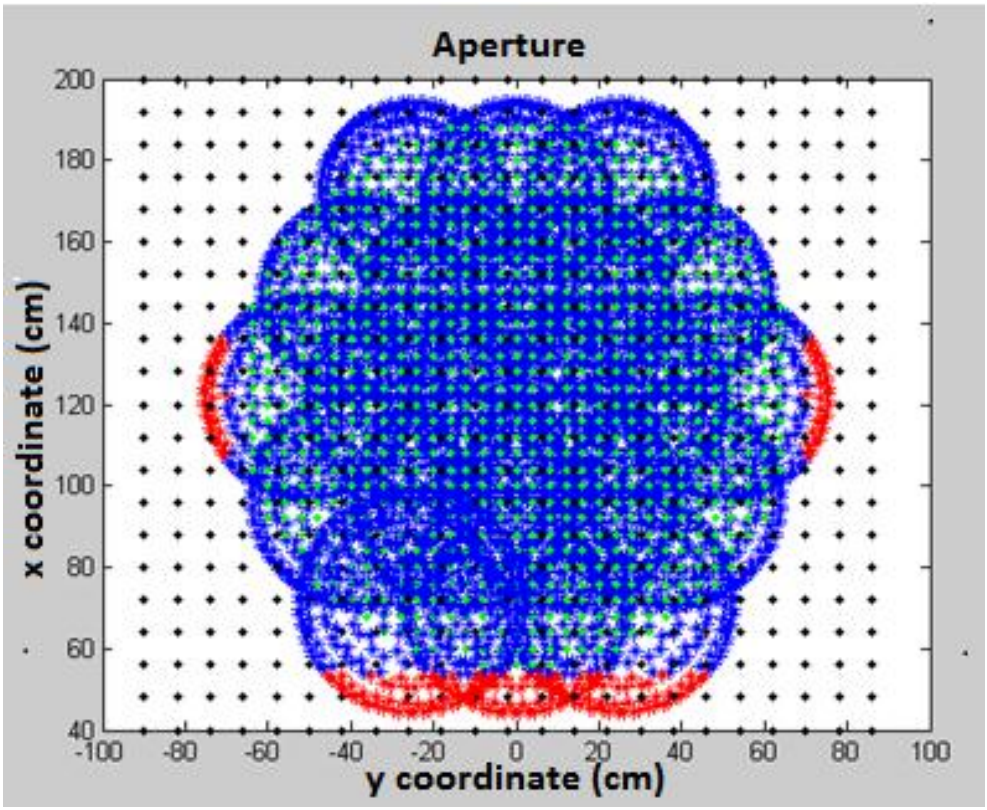

Fig 13. Spillover (red) Aperture (blue)

Presupuesto

1) Ejecución Material

- . Compra de ordenador personal (S.O. incluido)

  2.000 €
- . Compra de impresora láser

  400 €
- . Material de officinal

  200 €
- . Licencia Sofware CST Microwave Studio (1 año)

  1500 €
- . Licencia Sofware Matlab (1 año)

  1500 €

- Total de ejecución material

  5.600 €

2) Gastos generales

- . 16% sobre ejecución material

  896 €

3) Beneficio Industrial

- . 6% sobre ejecución material

  336 €

4) Honorarios Proyecto

- . 1200 horas a 15 €/ hora

  18.000€

5) Material fungible

- . Gastos de impresión

  200 €
- . Encuadernación

4 €

- . Total de material fungible

204 €

6) Subtotal del presupuesto

- . Subtotal Presupuesto

25.036

7) I.V.A. aplicable

- . 17% Subtotal Presupuesto

4.256,12€

8) Total presupuesto

- . Total Presupuesto

29.292,12 €

Madrid, Ocrtubre 2011

El Ingeniero Jefe de Proyecto

Fdo.: Bogdana Lachezarova Tsonevska

Ingeniero Superior de Telecomunicación

PLIEGO DE CONDICIONES

Este documento contiene las condiciones legales que guiarán la realización, en este proyecto, de unas anetenas híbridas. En lo que sigue, se supondrá que el proyecto ha sido encargado por una empresa cliente a una empresa consultora con la finalidad de realizar dicho sistema. Dicha empresa ha debido desarrollar una línea de investigación con objeto de elaborar el proyecto. Esta línea de investigación, junto con el posterior desarrollo de los programas está amparada por las condiciones particulares del siguiente pliego.

Supuesto que la utilización industrial de los métodos recogidos en el presente proyecto ha sido decidida por parte de la empresa cliente o de otras, la obra a realizar se regulará por las siguientes:

Condiciones generales

1. La modalidad de contratación será el concurso. La adjudicación se hará, por tanto, a la proposición más favorable sin atender exclusivamente al valor económico, dependiendo de las mayores garantías ofrecidas. La empresa que somete el proyecto a concurso se reserva el derecho a declararlo desierto.

2. El montaje y mecanización completa de los equipos que intervengan será realizado totalmente por la empresa licitadora.

3. En la oferta, se hará constar el precio total por el que se compromete a realizar la obra y el tanto por ciento de baja que supone este precio en relación con un importe límite si este se hubiera fijado.

4. La obra se realizará bajo la dirección técnica de un Ingeniero Superior de Telecomunicación, auxiliado por el número de Ingenieros Técnicos y Programadores que se estime preciso para el desarrollo de la misma.

5. Aparte del Ingeniero Director, el contratista tendrá derecho a contratar al resto del personal, pudiendo ceder esta prerrogativa a favor del Ingeniero Director, quien no estará obligado a aceptarla.

6. El contratista tiene derecho a sacar copias a su costa de los planos, pliego de condiciones y presupuestos. El Ingeniero autor del proyecto autorizará con su firma las copias solicitadas por el contratista después de confrontarlas.

7. Se abonará al contratista la obra que realmente ejecute con sujeción al proyecto que sirvió de base para la contratación, a las modificaciones autorizadas por la superioridad o a las órdenes que con arreglo a sus facultades le hayan comunicado por escrito al Ingeniero Director de obras siempre que dicha obra se haya ajustado a los preceptos de los pliegos de condiciones, con arreglo a los cuales, se harán las modificaciones y la valoración de las diversas unidades sin que el importe total pueda exceder de los presupuestos aprobados. Por consiguiente, el número de unidades que se consignan en el proyecto o en el presupuesto, no podrá servirle de fundamento para entablar reclamaciones de ninguna clase, salvo en los casos de rescisión.

8. Tanto en las certificaciones de obras como en la liquidación final, se abonarán los trabajos realizados por el contratista a los precios de ejecución material que figuran en el presupuesto para cada unidad de la obra.

9. Si excepcionalmente se hubiera ejecutado algún trabajo que no se ajustase a las condiciones de la contrata pero que sin embargo es admisible a juicio del Ingeniero Director de obras, se dará conocimiento a la Dirección, proponiendo a la vez la rebaja de precios que el Ingeniero estime justa y si la Dirección resolviera aceptar la obra, quedará el contratista obligado a conformarse con la rebaja acordada.

10. Cuando se juzgue necesario emplear materiales o ejecutar obras que no figuren en el presupuesto de la contrata, se evaluará su importe a los precios asignados a otras obras o materiales análogos si los hubiere y cuando no, se discutirán entre el Ingeniero Director y el contratista, sometiéndolos a la aprobación de la Dirección. Los nuevos precios convenidos por uno u otro procedimiento, se sujetarán siempre al establecido en el punto anterior.

11. Cuando el contratista, con autorización del Ingeniero Director de obras, emplee materiales de calidad más elevada o de mayores dimensiones de lo estipulado en el proyecto, o sustituya una clase de fabricación por otra que tenga asignado mayor precio o ejecute con mayores dimensiones cualquier otra parte de las obras, o en general, introduzca en ellas cualquier modificación que sea beneficiosa a juicio del Ingeniero Director de obras, no tendrá derecho sin embargo, sino a lo que le correspondería si hubiera realizado la obra con estricta sujeción a lo proyectado y contratado.

12. Las cantidades calculadas para obras accesorias, aunque figuren por partida alzada en el presupuesto final (general), no serán abonadas sino a los precios de la contrata, según las condiciones de la misma y los proyectos particulares que para ellas se formen, o en su defecto, por lo que resulte de su medición final.

13. El contratista queda obligado a abonar al Ingeniero autor del proyecto y director de obras así como a los Ingenieros Técnicos, el importe de sus respectivos honorarios facultativos por formación del proyecto, dirección técnica y administración en su caso, con arreglo a las tarifas y honorarios vigentes.

14. Concluida la ejecución de la obra, será reconocida por el Ingeniero Director que a tal efecto designe la empresa.

15. La garantía definitiva será del 4% del presupuesto y la provisional del 2%.

16. La forma de pago será por certificaciones mensuales de la obra ejecutada, de acuerdo con los precios del presupuesto, deducida la baja si la hubiera.

17. La fecha de comienzo de las obras será a partir de los 15 días naturales del replanteo oficial de las mismas y la definitiva, al año de haber ejecutado la provisional, procediéndose si no existe reclamación alguna, a la reclamación de la fianza.

18. Si el contratista al efectuar el replanteo, observase algún error en el proyecto, deberá comunicarlo en el plazo de quince días al Ingeniero Director de obras, pues transcurrido ese plazo será responsable de la exactitud del proyecto.

19. El contratista está obligado a designar una persona responsable que se entenderá con el Ingeniero Director de obras, o con el delegado que éste designe, para todo relacionado con ella. Al ser el Ingeniero Director de obras el que interpreta el proyecto, el contratista deberá consultarle cualquier duda que surja en su realización.

20. Durante la realización de la obra, se girarán visitas de inspección por personal facultativo de la empresa cliente, para hacer las comprobaciones que se crean oportunas. Es obligación del contratista, la conservación de la obra ya ejecutada hasta la recepción de la misma, por lo que el deterioro parcial o total de ella, aunque sea por agentes atmosféricos u otras causas, deberá ser reparado o reconstruido por su cuenta.

21. El contratista, deberá realizar la obra en el plazo mencionado a partir de la fecha del contrato, incurriendo en multa, por retraso de la ejecución siempre que éste no sea debido a causas de fuerza mayor. A la terminación de la obra, se hará una recepción provisional previo reconocimiento y examen por la dirección técnica, el depositario de efectos, el interventor y el jefe de servicio o un representante, estampando su conformidad el contratista.

22. Hecha la recepción provisional, se certificará al contratista el resto de la obra, reservándose la administración el importe de los gastos de conservación de la misma hasta su recepción definitiva y la fianza durante el tiempo señalado como plazo de garantía. La recepción definitiva se hará en las mismas condiciones que la provisional, extendiéndose el acta correspondiente. El Director Técnico propondrá a la Junta Económica la devolución de la fianza al contratista de acuerdo con las condiciones económicas legales establecidas.

23. Las tarifas para la determinación de honorarios, reguladas por orden de la Presidencia del Gobierno el 19 de Octubre de 1961, se aplicarán sobre el denominado en la actualidad "Presupuesto de Ejecución de Contrata" y anteriormente llamado "Presupuesto de Ejecución Material" que hoy designa otro concepto.

Condiciones particulares

La empresa consultora, que ha desarrollado el presente proyecto, lo entregará a la empresa cliente bajo las condiciones generales ya formuladas, debiendo añadirse las siguientes condiciones particulares:

1. La propiedad intelectual de los procesos descritos y analizados en el presente trabajo, pertenece por entero a la empresa consultora representada por el Ingeniero Director del Proyecto.

2. La empresa consultora se reserva el derecho a la utilización total o parcial de los resultados de la investigación realizada para desarrollar el siguiente proyecto, bien para su publicación o bien para su uso en trabajos o proyectos posteriores, para la misma empresa cliente o para otra.

3. Cualquier tipo de reproducción aparte de las reseñadas en las condiciones generales, bien sea para uso particular de la empresa cliente, o para cualquier otra aplicación, contará con autorización expresa y por escrito del Ingeniero Director del Proyecto, que actuará en representación de la empresa consultora.

4. En la autorización se ha de hacer constar la aplicación a que se destinan sus reproducciones así como su cantidad.

5. En todas las reproducciones se indicará su procedencia, explicitando el nombre del proyecto, nombre del Ingeniero Director y de la empresa consultora.

6. Si el proyecto pasa la etapa de desarrollo, cualquier modificación que se realice sobre él, deberá ser notificada al Ingeniero Director del Proyecto y a criterio de éste, la empresa consultora decidirá aceptar o no la modificación propuesta.

7. Si la modificación se acepta, la empresa consultora se hará responsable al mismo nivel que el proyecto inicial del que resulta el añadirla.

8. Si la modificación no es aceptada, por el contrario, la empresa consultora declinará toda responsabilidad que se derive de la aplicación o influencia de la misma.

9. Si la empresa cliente decide desarrollar industrialmente uno o varios productos en los que resulte parcial o totalmente aplicable el estudio de este proyecto, deberá comunicarlo a la empresa consultora.

10. La empresa consultora no se responsabiliza de los efectos laterales que se puedan producir en el momento en que se utilice la herramienta objeto del presente proyecto para la realización de otras aplicaciones.

11. La empresa consultora tendrá prioridad respecto a otras en la elaboración de los proyectos auxiliares que fuese necesario desarrollar para dicha aplicación industrial, siempre que no haga explícita renuncia a este hecho. En este caso, deberá autorizar expresamente los proyectos presentados por otros.

12. El Ingeniero Director del presente proyecto, será el responsable de la dirección de la aplicación industrial siempre que la empresa consultora lo estime oportuno. En caso contrario, la persona designada deberá contar con la autorización del mismo, quien delegará en él las responsabilidades que ostente.